CALIBRATION REPORT

FOR THE

THERMAL EMISSION SPECTROMETER

(TES)

FOR THE MARS OBSERVER MISSION

642-TBD

VOL. 1

Philip R. Christensen

Department of Geology

Arizona State University

Tempe, AZ 85287-1404

10/9/92
10./14/92
1/11/93
3/8/93
4/21/93
6/25/93
6/30/93
7/6/93
8/9/93
1/6/95

Table of Contents

1.0 Calibration Plan 1
1.1 Introduction 1
1.2 Relevant Instrument and Test Fixture Properties 1
1.2.1 Spectrometer Data Structure 1
1.2.2 Albedo Bolometer Data Structure 2
1.2.3 Thermal Bolometer Data Structure 2
1.2.4 Internal Reference Surface Properties and Instrumentation 2
1.2.5 External Target Properties and Instrumentation 3
1.2.6 Internal Instrument Temperature Instrumentation 5
1.3 Bench-Level Test Conditions and Overview 7
1.4 Thermal Vacuum Test Conditions and Overview 8
2.0 Bench -level Testing 9
2.1 Field of View 9
2.2 Out-Of-Field Response 13
2.2.1 Intermediate Out-of-Field Region 13
2.2.2 Far Out-of-Field Response 16
2.3 Spectral Characterization 16
2.3.1 Spectrometer Spectral Line Shape 16
2.3.2 Albedo Bolometer Spectral Response 17
2.3.3 Thermal Bolometer Spectral Response 17
3.0 Spectrometer Radiometric Calibration 19
3.1 Data Processing and Analysis 19
3.2 Instrument Response Function Versus Instrument Temperature and Heater State 21
3.3 Determination of Instrument Response Linearity and Offset 23
3.4 Determination of Reference Surface Emissivity (ref_emiss) 27
3.5 Absolute Calibration (calib_simple) 30
3.6 Signal-to-Noise Performance 32
3.7 Spectrometer Gain Analysis 33
3.8 Spectrometer Heater Performance Analysis 34
3.9 Determination of In-flight Calibrated Radiance 36
3.9.1 Definition of In-Flight Calibrated Radiance 36
3.9.2 Instrument Response Function 37
3.9.3 Instrument Energy 38
4.0 Albedo Bolometer Radiometric Calibration 39

4.1 Radiometric Performance 39
4.2 Signal-to-Noise Performance 39
5.0 Thermal Bolometer Radiometric Calibration 40
5.1 Radiometric Performance (from S. Chase - 8/11/93 Report) 40
5-1-1. Linearity of Radiometric Transfer Functions (slopes) 40
5-1-2. Temperature Dependence: 43
5-1-3. Internal Reference Surface (IRS) 44
5.2 Signal-to-Noise Performance 51
6.0 Time History of Instrument Response 52
Figure Captions 54
Appendix A - Software Analysis Tools 60
Appendix B - In-Flight Noise Anomaly 61

1.0 CALIBRATION PLAN

1.1 INTRODUCTION

Thermal Emission Spectrometer (TES) instrument was calibrated and tested prior to shipment to General Electric at the Santa Barbara Research Center (SBRC). Specifications for these tests are provided in the Mars Observer Calibration Document (642-_). The primary tests performed were: 1) field-of-view definition and co-alignment of all three instrument sub-sections; 2) out-of-field response for all three sub-sections; 3) spectrometer spectral line shape; 4) albedo bolometer spectral response; 5) thermal bolometer spectral response; 6) spectrometer radiometric calibration; 7) albedo bolometer radiometric calibration; 6) thermal bolometer radiometric calibration. In addition to these calibrations, and extensive set of tests were performed under ambient and vacuum conditions to verify instrument functional performance, including all actuators, the command and signal processors, and the command and data links. Each of the calibration tests are described in the subsequent sections.

1.2 RELEVANT INSTRUMENT AND TEST FIXTURE PROPERTIES

1.2.1 Spectrometer Data Structure

The voltage output from the interferometer is initially ±5 V digitized at 16 bit resolution. These data are processed on-board the TES instrument using an integer, prime-factors DFT. As a result of the cosine transforms applied to these data, the resulting spectral data are real numbers representing the signal amplitude as a function of wavenumber. The units of these transformed voltage values will be refered to as TES Numbers (TN). The spectral data are stored and telemetered in fixed point format. For each detector output there is a sign bit and 11 data bits, with an assumed decimal point in front of the first data bit. All spectral bands for a given detector have a single exponent that is stored separately.

1.2.2 Albedo Bolometer Data Structure

The albedo bolometer data are stored as signed 14-bit integers in 2's complement format. A maximum value of 0x 1FFF corresponds to +5.0 volts output from the albedo detector. A minimum value of 0x0 corresponds to -5.0 volts.

1.2.3 Thermal Bolometer Data Structure

The thermal bolometer data are stored as signed 14-bit integers in 2's complement format. A maximum value of 0x 1FFF corresponds to +5.0 volts output from the thermal bolometer detector. A minimum value of 0x0 corresponds to -5.0 volts.

1.2.4 Internal Reference Surface Properties and Instrumentation

The internal reference surface was formed with parallel groves machined with 45° inclined surfaces with a height of 1.52 mm and a spacing of 3.05 mm (Fig. 1-1). The reference surface was machined from aluminum alloy 6061-T651 with a protective coating of black anodize. The surface was coated with "CAD-A-LAC black" paint to a thickness of 2.5 mil, and cured for four hours at 70 °C.

The internal reference surface was instrumented with YSI thermisters, delivered from the manufacturer with a stated absolute accuracy of 2% in resistance corresponding to ±0.2 °C for temperatures from 0 to +40° and ±0.4 °C from -40 to 0 °C. These thermisters were imbedded in the underside of the reference surface at locations shown in Figure 1-2. Resistance from these thermisters were digitized through the TES telemetry. This resistance is converted to temperature using the formulas given in Table 1-1. The digitization of the resultant temperatures is 0.167 °C at -16.6 °C, 0.109 °C at 1.1 °C, and 0.097 °C at 25 °C.

Table 1-1 Internal Reference Surface Temperature Derivation

YSI Thermisters:

$$\text{temperature} = \frac{5398.94}{\ln\left(254898 * \frac{r}{1000}\right)} - 341.0$$

r = measured resistance (ohms)

The relative temperature error between the three reference surface temperature readings was determined using temperature measurements taken within ~1.5 minutes after instrument turn in ambient conditions (test acta4). Typical values for the mean and sigma of the three thermisters (orbit 2, ICKs 129-147) are given in Table 1-2. From these results it is apparent that the three thermisters give identical readings within the digitizatioin and standard deviations.

Table 1-2 Mean and Sigmas of Reference Surface Temperatures

Reference Thermister	Mean (°C)	Sigma (°C)
PTR-1	25.543	0.050
PTR-2	25.456	0.092
PTR-3	25.494	0.055

1.2.5 External Target Properties and Instrumentation

The two calibration blackbodies (BCU-1 and BCU-2) were identical, 7.25" diameter, 15° half-angle cones (Fig. 1-3a and 1-3b) that were used within the thermal vacuum chamber (Fig. 1-3c). Each blackbody was instrumented with two pairs of platinum thermisters placed at the front and back of the cone surface (Fig. 1-3a). Only one of each pair was used during calibration; the second was for redundancy. These thermisters were calibrated prior to shipment from the manufacturer to an absolute accuracy of 0.1 °C (±0.5% resistance). The formulas used in converting the measured

resistance to temperature are given in Table 1-3. The digitization of these telemetry points varies from ~0.01 °C at -190°C to 0.02 at 35 °C. Typical values for the mean and sigma of the front and back thermisters in BCU-1, determined on test tvk26, orbit 2, ICKs 127-156, are given in Table 1-4. As can be seen, the temperature stability is within the digitization level over >1 minute time periods. In addition, the front and back temperatures agree to within 0.2 °C for both the cold, "space" blackbody (BCU-1) and the hot, "planet" blackbody (BCU-2).

Table 1-3 External Blackbody Target Temperature Derivation

Platinum Thermisters:

$$\text{Temperature} = \frac{-b + \sqrt{d}}{2a}$$

$$a = -r_0 * \frac{\alpha * \beta}{1000}$$

$$b = r_0 * \alpha + \frac{r_0 * \alpha * \beta}{1000}$$

$$c = r_0 - r$$

$$d = b^2 - 4 * a * c$$

r = measured resistance (ohms)

$\alpha = 0.0038$

$\beta = 1.889$

BCU-1 Front $r_0 = 1003.78$

BCU-1 Back $r_0 = 1000.25$

BCU-2 Front $r_0 = 999.25$

BCU-2 Back $r_0 = 1000.52$

Lplate $r_0 = 998.64$

Table 1-4 Mean and Sigma of External Calibration Target Temperatures Test tvk26

Thermister	Mean	Sigma
BCU-1 Front	-190.629	0.000
BCU-1 Back	-190.834	0.000
BCU-2 Front	34.700	0.000

BCU-2 Back	34.525	0.000

1.2.6 Internal Instrument Temperature Instrumentation

Sixteen temperatures internal to the TES instrument were instrumented and can be transmitted on ground command. The location of these temperature telemetry points is given in Table 1-5. All of these thermisters were YSI except those mounted on the detector packages and internal electronics which were Fenwall. The absolute accuracy of the Fenwall resistors is the same as the YSI resistors. The formulas used in converting the measured resistance to temperature for these thermisters are given in Table 1-6. The digitization of these telemetry points is typically 0.1-0.2 °C at 5 °C. Mean and sigmas for telemetry points on the power supply (sensor 9), field stop (sensor 11), beamsplitter (sensor 13), and secondary mirror (sensor 16), determined for test tvk26, orbit 2, ICK 127 to 136, are given in Table 1-7. As can be seen from this table, the temperatures are stable to within the digitization levels.

Table 1-5 Internal Temperature Telemetry Points

Sensor	Location
1	Albedo Detector Package
2	Bolometer Detector Package
3	Spectrometer Detector Package
4	Bolometer Blackbody Reference
5	Internal Reference Temp 1
6	Internal Reference Temp 2
7	Internal Reference Temp 3
8	Bolometer Blackbody Reference (spare)
9	Electronics
10	Power Supply
11	Telescope Field Stop
12	Interferometer Fixed Mirror
13	Interferometer Beamsplitter
14	Interferometer Motor
15	Primary Mirror
16	Secondary Mirror

Table 1-6 Internal Instrument Temperature Derivation

Optical Surfaces:

YSI Thermisters; - see Table 1-2

Electronics:

Fenwall Thermisters:

$$\text{temperature} = 40.36 - 79.547 * \log\left(\frac{r}{1000}\right)$$

r = measured resistance

Table 1-7 Mean and Sigma of Selected Internal Telemetry Temperatures

Telemetry Point	Mean (°C)	Sigma (°C)
Electronics (#9)	11.74	0.082
Field Stop (#11)	2.94	0.055
Beamsplitter (#13)	3.14	0.051
Secondary Mirror (#16)	0.696	0.077

1.3 Bench-Level Test Conditions and Overview

Bench-level testing of the TES instrument was performed in two phases. One phase consisted of piece-part and system-level testing of the spectral performance of each sub-section. These tests were performed under ambient conditions. The second phase consisted of field of view and out-of-field tests conducted before and after vibration and thermal-vacuum testing to determine and confirm the field-of-view and co-alignment of the three instrument sub-sections. This phase of testing was completed between May and October, 1991.

1.4 THERMAL VACUUM TEST CONDITIONS AND OVERVIEW

The TES was radiometrically calibrated in thermal vacuum at SBRC between Sept. 13 and Oct. 11, 1991. Calibration data were collected at instrument temperatures of -20, -10, 0, +10, +20, +30, and +40 °C with detector heaters on and off. At each instrument state, one of the two calibration target blackbodies (BCU2; the ""planet" view) was set to target temperatures of 130, 160, 200, 240, 270, 310, and 325 K, while the second blackbody (BCU1; the "space" view) was held at a temperature near 83 K. For each instrument-planet target state (calibration test set) a series of observations were made to provide instrument calibration, performance, and operational baseline data. Albedo calibrations were performed once at each instrument temperature when the planet blackbody was at 270 K..

Figure 1-4 shows the timeline of major events the occurred during thermal vacuum instrument calibration. The initial tests include a series of ambient tests to establish a link to bench-level testing done prior to thermal vacuum testing. These tests were followed by a required hot plateau test and thermal balance test. The original plan called for the completion of the detector-heaters-on tests, followed by heaters-off tests. Problems with ice condensation on the cold blackbody and noise produced by the thermal bolometer heater resulted in a modification of this test plan as indicated in Figure 1-4. Overall, however, all of the test and calibration objectives set for this program were achieved.

The observational conditions and parameters for the calibration data set are summarized in Tables 1-8 through 1-16 at the end of this report. Table 1-8 gives the set of sequences collected at each point in the calibration matrix. Table 1-9 gives a detailed listing of the set of observations within each of the TV*xnn* sequences (where *x* refers to the sequence version and *xx* refers to the run number). Each calibration test set has a unique run number. Included in Table 1-9 are the number of observations collected at each viewing position (planet, reference, space), the instrument gain state, image motion

compensation state, and scan length. During the course of the calibration activity, refinements and modifications were made to the calibration sequences which led to different sequence versions; Table 1-10 summarizes these differences. Table 1-11 gives the date, file name, starting orbit, and number of gain states used to observe the planet target for each calibration test set. Table 1-12 gives the actual instrument and target temperatures for each of the calibration data sets (files TV*xnn*) including; 1) the internal instrument reference surface temperature, taken as the average of the three internal thermisters mounted on the reference surface; 2) the aft optics temperature using the thermister mounted on the beamsplitter; and 3) the planet blackbody temperature, given as the average of the two thermisters internal to the blackbody. Table 1-13 lists the data content and file number of the data archive tapes. Table 1-14 gives the filename and test condition of each test performed on the integrated TES instrument, sorted by test type; Table 1-15 gives a chronological listing of the tests performed at SBRC; Table 1-16 gives a chronological listing of test performed at GE and Cape Canaveral.

2.0 BENCH -LEVEL TESTING

2.1 FIELD OF VIEW

Field of view location data were acquired using the precision "Cline" collimator at SBRC. Thermal and visual sources were projected through a 1 mrad wide by 40 mrad long slit into the TES aperture. The TES was manually rotated to move the slit at 1 mrad spacing across the focal plane; 33 points were measured from -16 to +16 mrad in elevation, 41 points were measured from -20 to +20 mrad in azimuth. The detailed discussion of the field of view measurements is given in the TES Field of View Procedure, SBRC drawing #151620.

The data initially collected and contained on the working data sheets, computer files, and plots were referenced to an arbitrary zero point on the collimator. For the final field of view positions, taken immediately prior to shipment from SBRC, the axes of the TES alignment cube corresponded to +0.25 mrad in elevation and +0.10 mrad in azimuth. relative to the arbitrary collimator axis

These offsets have been included in all of the data presented below, such that the field of view positions are referenced to the TES alignment cube.

Three ICKs were collected and averaged at each spatial location. Using these data the final field of view positions were determined using the following processing (scripts fov_az and fov_el):

1) Data were corrected for instrument drift using first and last points collected at location 0.
2) Minimum response was determined and set to zero; all other values were offset by this value.
3) Maximum response was determined and scaled to 1.0; all other values were then scaled.
4) Location of half-power points were determined using these processed values.

Initial bench measurements taking on August 15, 1991 (test FVC1 and FVD1) showed excellent alignment of the three instrument subsections. Following final instrument assembly and torque down of the aft optics cover on September 4, 1991, the alignment of the albedo and thermal bolometers, relative to the spectrometer, was found to have shifted by ~1 mrad in elevation. After extensive testing it was determined that this shift was stable and no further movement was ever detected. Measurements were made before and after the acceptance and qualification level vibration testing and before and after thermal vacuum testing and no discernible changes in alignment were observed.

The results from the final pre-shipment bench alignments tests performed on 10/14/91 (tests FVO8 and FVN5) are given in Figures 2-1 and 2-2; the location of the half-power and center points are given in Tables 2-1, 2-2, and 2-3, the half-power points are illustrated in Figure 2-3 (data in files fvo8.dat_relative_to_alignment_cube, fvn5.dat_relative_to_alignment_cube, and fov_data_relative_to_alignment_cube). (Note: scanning the TES pointing mirror in the $+\theta$ direction (toward the fore limb) rotates the detector array in a clockwise direction projected against the limb as viewed in Fig. 2-3;

rotation to the -θ direction (aft limb) produces a counterclockwise rotation). Finally, the results from a detailed 2-dimensional spot scan are illustrated in Figure 2-4 for spectrometer detectors 2 and 5.

Table 2-1 Elevation Half Power Points - From Test FVO8 Relative to TES Alignment Cube

	Albedo Bolometer		Thermal Bolometer		Spectrometer	
Detector	Left (mrad)	Right (mrad)	Left (mrad)	Right (mrad	Left (mrad)	Right (mrad)
1	4.59	13.29	4.99	14.15	5.97	14.20
2	-5.25	3.51	-4.85	4.19	-3.36	4.82
3	-14.75	-6.05	-14.58	-5.59	-12.46	-4.45
4	4.47	13.06	4.59	13.72	5.92	13.90
5	-5.39	3.32	-4.97	4.11	-3.33	4.77
6	-14.64	-6.24	-14.64	-5.57	-12.50	-4.48

Table 2-2 Azimuth Half Power Points - From Test FVN5 Relative to TES Alignment Cube

	Albedo Bolometer		Thermal Bolometer		Spectrometer	
Detector	Low (mrad)	High (mrad)	Low (mrad)	High (mrad	Low (mrad)	High (mrad)
1	0.40	8.54	0.40	8.50	0.40	8.33
2	0.25	8.48	0.25	8.22	0.47	8.48
3	0.49	8.82	0.35	8.44	0.44	8.44
4	-9.27	-1.10	-8.99	-0.90	-9.16	-0.71
5	-9.57	-1.03	-9.57	-1.29	-9.31	-0.77
6	-9.35	-1.03	-9.35	-0.88	-9.02	-0.88

Table 2-3 Field of View Center Points - From Tests FVO8 and FVN5 Relative to TES Alignment Cube

	Albedo Bolometer		Thermal Bolometer		Spectrometer	
Detector	Elevation (mrad)	Azimuth (mrad)	Elevation (mrad)	Azimuth (mrad)	Elevation (mrad)	Azimuth (mrad)
1	8.94	4.47	9.57	4.45	10.08	4.36
2	-0.87	4.36	-0.33	4.23	0.73	4.47
3	-10.40	4.65	-10.08	4.39	-8.45	4.44
4	8.76	-5.18	9.15	-4.94	9.91	-4.93
5	-1.03	-5.30	-0.43	-5.43	0.72	-5.04
6	-10.44	-5.19	-10.11	-5.11	-8.49	-4.95

Once the TES was delivered to GE it was aligned on the spacecraft using the alignment cube for reference. Table 2-4 gives the measured pre-flight orientation of the TES alignment cube relative to the spacecraft axes taken from Table 1 of the System Optical Alignment For the Mars Observer Satellite document dated Aug. 6, 1992. The angles presented in Table 2-1 represent rotations about the specified axis in a right-handed coordinate system. An attempt to verify this alignment will be made using Mars as a point source at MOI -23 and -18 days.

Table 2-4 TES Alignment Relative to the Spacecraft Axes

Axis	Measured Preflight Position (mrad)
θ X	0.0977
θ Y	0.174
θ Z	-0.291

Using the offsets between the TES alignment cube and the spacecraft axes given in Table 2-4, the position of the center of each TES field of view relative to the spacecraft coordinate system can be calculated. This final transform will not be done until the pre-launch predictions have been verified using the Mars approach observations.

2.2 Out-Of-Field Response

2.2.1 Intermediate Out-of-Field Region

Out-of-field response test was done to determine the percentage of the total energy received by each detector that fell outside of the half-power points. The calibration requirements for each instrument sub-section are given in Table 2-5.

Table 2-5 Design Normalized Enclosed Energy

Sensing Area	Design Response to Extended Source		
	Spectrometer	Albedo Bolometer	Thermal Bolometer
6.5 mrad Square	0.7	0.7	0.5
8.3	0.9	0.9	0.8
12	0.95	0.96	0.9
16	0.99	0.995	0.95
24	0.998	0.999	0.98

Data for these tests were collected using a 2 x 2 mrad slit that was manually scanned across the focal plane from -19.2 to +19.2 mrad in elevation with a spacing of 2.45 mrad (17 points). At each elevation position, the TES pointing mirror was scanned from -14.7 to +14.7 mrad in azimuth with a spacing of 2.45 mrad (13 points) (test FVA1). Five ICKs were collected at each grid position with the aperture open and 5 ICKs with it blocked to use for background energy subtraction.

Figure 2-5 shows 3-dimensional examples of the intermediate out-of-field energy for 1 detector in each instrument sub-section. As can be seen, there is some apparent

electronic cross-talk between detectors. However, the vertical (energy) axis of these plots is greatly exaggerated and the actual magnitude of the out-of-field energy is close to the design specification.

The quantitative determination of the percent of enclosed energy was made in the following manner:

1) Data were averaged and shutter closed observations subtracted.
2) Beginning with the nominal center point of each detector, the measured energy was determined as a function of the size of the enclosed area, beginning with a 1x1 bin size (2x2 mrad) and extending outward to 3x3 (6.9x6.9 mrad), etc. A bi-directional, linear interpolation was performed to determine the energy in the 0.45 mrad gaps between slit locations.
3) A linear convergence smoothing algorithm was applied to smooth the data between the measured points. Figure 2-6 shows a comparison of this smoothing algorithm for the raw and processed data for the albedo detector 2; Figure 2-7 shows the results for the albedo and thermal bolometer detectors.
4) The average of the smoothed data from all six detectors was used to determine the system performance, shown in Table 2-6. This analysis explicitly assumes that all of the out-of-field energy is contained in an area 40 x 30 mrad in size. Any energy outside this area would result in lower percentages than given in Table 2-6.

Table 2-6 Measured Normalized Enclosed Energy

Sensing Area	Measured Response to Extended Source (Average of 6 Detectors)		
	Spectrometer	Albedo Bolometer	Thermal Bolometer
6.5 mrad Square	0.66 ±0.06	0.56	0.51
8.3	0.85 ±0.08	0.75	0.70
12	0.93 ±0.08	0.96	0.91

16	0.95 ±0.09	0.98	0.95
24	0.97 ±0.09	0.99	0.98

The spectrometer data collected during test FVA1 were saturated in the center positions of each detector. An attempt was made to use these results by scaling to the line-slit data, but this approach did not prove successful. Instead, the line-scan data used in Section 2-1 had to be used to estimate out-of-field response.

Figure 2-8 illustrates the method that was used. What is desired is the energy enclosed in a sensing area of size L x L. As seen in this figure, what is measured is the total energy enclosed in Strip 1, given by:

$$\text{Strip 1 Energy} = \text{Total Energy} - (2 * A)$$

However, this energy over-estimates the sensing-area energy by an amount equal to the energy enclosed in the two areas "B" (Fig. 2-8a). Thus:

$$\text{Sensing-Area Energy} = \text{Total Energy} - (2 * A) - (2 * B)$$

Because the energy in area B cannot be measured directly in this technique, it must be assumed that 2 * B = 2 * C (Fig. 2-8b). Ideally,

$$(2 * C) = \text{Strip 2} - D$$

However, because D is not directly knowable, it is assumed that the energy distribution in Strip 2 is uniform, in which case:

$$(2 * C) = \text{Strip 2} * \left(\frac{40 \text{ mrad} - L}{40 \text{ mrad}}\right)$$

Thus:

$$\text{Sensing-Area Energy} = \text{Total Energy} - (2*A) - \left[\text{Strip 2} * \left(\frac{40 - L}{40}\right)\right]$$

Table 2-7 gives a comparison of the enclosed energy determined from this method for the thermal bolometer detector 2, with that given using the 2-dimensional grid from Table 2-6. Line-slit data are from test FVO8. As seen from this comparison, the agreement is within 9%. Therefore, the line-slit technique was used to determine the spectrometer out-of-field results given in Table 2-6, assuming a 9% uncertainty.

Table 2-7 Comparison of Line-Slit and 2-Dimensional Methods

Thermal Bolometer Detector 2 (Test FVO8)

Sensing Area	Measured Response to Extended Source	
	Line-Scan	2-D
6.5 mrad Square	0.55	0.51
8.3	0.76	0.70
12	0.92	0.91
16	0.95	0.95
24	0.96	0.98

2.2.2 Far Out-of-Field Response

The energy from an extended area covering ±200 mrad in elevation and azimuth was measured during bench testing (test GOOF). Measurements were taken using a 40 x 32 mrad source that was scanned across an area 200 mrad by 200 mrad in azimuth and elevation. At each grid point, 5 ICKs were collected with the aperture open and 5 ICKs with it blocked to remove the background. This study was performed to look for obvious problems and search for regions of significant out-of-field contribution; no attempt was made quantify the energy in this area because the contributions were small compared to both the magnitude and the fluctuations in the background energy. Examples from each instrument sub-section are given in Figure 2-9. No significant out-of-field energy was detected.

2.3 Spectral Characterization

2.3.1 Spectrometer Spectral Line Shape

Data were collected to measure the spectral line shape. This test consisted of illuminating each detector with the output slit of a Perkin Elmer monochrometer capable of generating a 3 cm^{-1} wide slit. The center wavenumber of this slit was stepped in 1 cm^{-1} increments from 795 to 805 cm^{-1}. The TES-processed spectral data was sampled at 800 for each

observation and these data were collected and plotted versus the center wavenumber of monochrometer position. In this manner it possible to simulate illuminating the TES with 10 cm-1 data and measuring the effective spectral line shape. This test was repeated at 1250 cm^{-1} where the monochrometer was varied from 1245 to 1255 cm^{-1}. The analysis is complicated by the fact that the monochrometer input was 3 cm^{-1} wide, rather than infinitely narrow in an ideal case. However, preliminary analysis of these data showed good agreement with both the predicted line shape and the increase in width with increase detector distance from the optical axis (see TES Functional Requirements Document for predicted effects). Detailed analysis of these data had not been performed at the time of the Mars Observer failure and was not completed.

2.3.2 Albedo Bolometer Spectral Response

Not completed.

2.3.3 Thermal Bolometer Spectral Response

The initial effort to characterize the spectral response of the thermal bolometer channels focused on piece-part determinations of the transmission, absorption, and response of the individual components. However, due primarily to the late delivery of the thermal bolometer detector package, this effort was unsuccessful. In particular, no good characterization of the detector response was ever made. A similar detector was sent to the NOSC Lab for characterization against a NSTL standard; however, this characterization extended only to 25 μm and was not done on the flight component.

The alternative method that was chosen to provide some estimate of the spectral characterization used the bolometric data taken at seven planet blackbody temperatures. Stated another way, how much deviation from flat response is needed to produce a non-linear response function?

To test this simulated response function was constructed that allowed the linearity of spectral response $F(\lambda)$ to be varied:

$$V = V_{planet} - V_{space} = \sum_{4.5}^{100\,\mu m} F(\lambda)\left[B_{planet}(\lambda) - B_{space}(\lambda)\right]\Delta\lambda$$

where V_{planet} and V_{space} are the measured voltages from the planet and space blackbody targets, B_{planet} and B_{space} are the Planck radiance values at the temperatures measured for the planet and space blackbodies, and $\Delta\lambda$ is 2 μm.

For this simulation the same seven planet temperatures used during the normal calibration sequence were used. To see the effect, $F(\lambda)$ was assumed to be equal to 1.0 at 4.5 μm and 0.2 at 100 μm, a rather dramatic non-linearity, but probably of the same general slope as the actual instrument function. Figure 2-10 shows this altered response function plotted together with the unaltered case with $F(\lambda)=1.0$ over the same spectral range. Looking closely it is possible to see a slight bowing of the altered curve, but it is still quite linear. As will be seen later none of the TES channels shows non-linearities of this magnitude. We can conclude that the TES does not have gross non-linearities of the magnitude simulated although it could easily have isolated response features that would be undetectable given only the seven blackbody temperature measurements. In fact, other $F(\lambda)$ functions were tried that had large discontinuities, but the resulting transfer functions were more linear than that shown in Figure 2-10.

The error introduced by assuming linearity when, in fact, the spectral shape has the non-linearity indicated in Figure 2-10 can be determined by normalizing the two curves and solving for the temperature difference corresponding to the radiance differences at the same value of Plsig-Spsig. The normalized plots are shown in Figure 2-11. This was done by fitting third-order polynomials to the two curves and solving for the Plrad-Sprad values corresponding to mid-scale output where the departure of the two curves is greatest. The third-order equation for the linear curve is:

$$Y_1 = 2.9438E\text{-}5+3.1035X_1+7.138X_1^2 - 248.09X_1^3 \qquad \text{Linear curve}$$

$$Y_{nl} = -1.5439E\text{-}4+2.909X_{nl}+23.154X_{nl}^2 - 533.58X_{nl}^3 \qquad \text{Non-linear curve}$$

where Y is Plsig-Spsig and X is Plrad-Sprad.

Letting Y=3E-2 (mid-scale) and solving for X gives,

$X_1 = (\text{Plrad-Sprad})_1 = 9.518E\text{-}3$ watts/etc.

$X_{nl} = (\text{Plrad-Sprad})_{nl} = 9.777E\text{-}3$ watts/etc.

Subtracting the space radiance in each case and solving for the corresponding planet temperatures gives:

$\text{Plrad}_1 = 9.449E\text{-}3$ watts/etc.

$\text{Plrad}_{nl} = 9.708E\text{-}3$ watts/etc.

Solving for the corresponding planet temperatures, assuming blackbody functions, is,

T_{pl}=269.5K

T_{pnl}=271.4K

The error caused by the assumed gross non-linearity of spectral response is 1.9K. Because none of the TES channels shows this degree of non-linearity we must assume that the spectral response is flatter than this. However, for calibration purposes it might be a good idea to assume some rolloff in spectral response since the one piece of information we do have, the detector spectral response measurements, shows a slight rolloff in responsivity.

3.0 SPECTROMETER RADIOMETRIC CALIBRATION

3.1 DATA PROCESSING AND ANALYSIS

The measured output voltage ($V_{measured}$, in units of TES Numbers (TN)) from the TES spectrometer as a function of wavenumber is given by:

$$V_{measured} = \{(E_{emitted} + E_{reflected}) - E_{instrument}\} * f \quad (1)$$

where $E_{emitted}$ is the energy emitted by the target, $E_{reflected}$ is the energy emitted by the environment and reflected off of the target, $E_{instrument}$ is the energy emitted by the instrument, and f is the instrument response function, which may be signal dependent. Expanding Eq. 1 gives:

$$V_{measured} = \{\varepsilon_t B(T_t) + R_t \varepsilon_{env} B(T_{env}) - \varepsilon_i B(T_i)\} * f \quad (2)$$

where ε_t and ε_i are the emissivities of the target and instrument respectively, and $B(T_t)$, $B(T_{env})$, and $B(T_i)$ are energies, given by the Planck function, emitted from the target, environment, and instrument respectively (subsequently referred to simply as B_t B_{env}, and B_i).

In the thermal vacuum chamber three independent spectral measurements could be made: 1) the temperature-variable (planet) blackbody; 2) the fixed, cold (space) blackbody; and 3) the TES internal reference surface. These observations give three independent values of $V_{measured}$ at each calibration test set:

$$V_{planet} = \{\varepsilon_{planet} B_{planet} + R_{planet} B_{env} - (\varepsilon_i B_i)_{planet}\} * f_{planet} \quad (3a)$$

$$V_{space} = \{\varepsilon_{space} B_{space} + R_{space} B_{env} - (\varepsilon_i B_i)_{space}\} * f_{space} \quad (3b)$$

$$V_{reference} = \{\varepsilon_{reference} B_{reference} + R_{reference} B_{env} - (\varepsilon_i B_i)_{reference}\} * f_{reference} \quad (3c)$$

where the subscripts planet, space, and reference refer to observations and properties of these three targets. For the purpose of the TES calibration, the external calibration targets (planet and space blackbodies) are considered sufficiently blackbody in nature to set ε_{planet} and ε_{space} equal to unity and R_{planet} and R_{space} equal to zero. Simplifying Eq. 3 with these assumptions gives:

$$V_{planet} = \{B_{planet} - (\varepsilon_i B_i)_{planet}\} * f_{planet} \quad (4a)$$

$$V_{space} = \{B_{space} - (\varepsilon_i B_i)_{space}\} * f_{space} \quad (4b)$$

$$V_{reference} = \{\varepsilon_{reference} B_{reference} + R_{reference} B_{env} - (\varepsilon_i B_i)_{reference}\} * f_{reference} \quad (4c)$$

In Equation 4 seven variables can be directly measured: V_{planet}, V_{space}, $V_{reference}$, T_{planet}, T_{space}, T_{env}, $T_{reference}$, and T_{bc}, leaving seven unknowns, $(\varepsilon_i B_i)_{planet}$, $(\varepsilon_i B_i)_{space}$, $(\varepsilon_i B_i)_{reference}$, $\varepsilon_{reference}$, f_{planet}, f_{space}, $f_{reference}$ and four equations. Clearly some additional simplifying assumptions are required.

The basic problem stems from the fact that the large differences in signal strength between planet, space, and reference views may result in small, non-linear variations in the instrument response function, the magnitude of which must be determined. In addition, the very process of observing targets at widely differing temperatures can produce changes in instrument temperature (B_i). These changes can occur over relatively short time intervals, be non-linear between successive space views, and are further complicated when the detector heaters are operated due to heater cycling over short (<1 minute) intervals. In order to determine the most appropriate set of approximations, a number of studies and tests have been performed.

For each approach three analysis approaches are possible: 1) use the mean of all planet and reference observations, together with the mean of all space observations taken before the associated planet or reference observations; 2) use only the first few (3) planet and reference observations, together with the last three space observations taken as close

in time as possible to the associated planet or reference observations. This approach attempts to minimize temperature drifts; and 3) use the mean of all planet and reference observations, together with the mean of all space observations taken both before and after the associated planet or reference observations. These three methods are referred to as: 1) before_full; 2) before_mini; 3) both_full. In the nomenclature developed, space1 and s1 refer interchangeably to the space view preceding the planet view; space2 and s2 refer to the space view between planet and reference views; space3 and s3 to the space look after the reference view; s12 to the mean of s1 and s2; and s23 to the mean of s2 and s3.

3.2 Instrument Response Function Versus Instrument Temperature and Heater State

An initial analysis was performed to determine the approximate variation in spectrometer performance as a function of instrument and detector temperature. These results were then used to correct for the slight variations in instrument temperature during the precise calibration studies done at "fixed" instrument temperatures. For this study, the simplifying assumption was made that the instrument response function was independent of signal strength. Using Eq. 4, this assumption results in:

$$V_{planet} = \{B_{planet} - (\varepsilon_i B_i)\} * f \quad (5a)$$

$$V_{space} = \{B_{space} - (\varepsilon_i B_i)\} * f \quad (5b)$$

$$V_{reference} = \{\varepsilon_{reference} B_{reference} + R_{reference} B_{env} - (\varepsilon_i B_i)\} * f \quad (5c)$$

with three equations and three unknowns (f, $\varepsilon_i B_i$, and $\varepsilon_{reference}$) (assuming that $R_{reference}$ equals 1 - $\varepsilon_{reference}$). For this analysis only the both_full case was modeled.

Examples of the instrument response functions derived from this analysis are shown for detector 2 for both the heater on and heater off cases (Fig. 3-1). (Note: the units of instrument repsonse used throughout are TN/(W cm^{-2} str^{-1} cm^{-1})). Instrument set-point temperatures were varied from -20 to +30 °C; the planet blackbody temperature was set at ~270 K. Variation in instrument temperature produces a large change in response with the heater off as both the detector temperature and instrument temperature

vary over ~35 °C. The heater-on case shows less variation. These variations can be explained as follows: with the heater on the detector performance is nearly constant but the ~35 °C variation in instrument temperature produces some variation in interferometer alignment. with the heater off, both the detector and instrument vary in temperature so both the alignment and detector performance vary, producing a greater variation in performance with instrument temperature, as both detector performance and interferometer alignment degrade with decreasing temperature. Overall, the performance is best near room temperature, where the spectrometer was aligned and the detector performance is nearly optimal.

Figure 3-2 shows the same instrument response data versus detector temperature. Only data from Detector 2 are shown, for each of 15 wavenumber channels sampled every 10 (~105 cm^{-1}) channels beginning at channel 1 (148 cm^{-1}) and covering the full TES spectral range, and plotted . These data more clearly show the strong variation in response between detector temperatures of ~-10 to 10 °C and the weaker variation between 10 and 22 °C for the heater-off case.

In flight, the noise in the instrument response function (f) from a single reference surface observation will be reduced by combining multiple determinations over a time period of 1-14 days. However, the statistical variations in f must be separated from the expected variations in f due to variations in instrument temperature. This separation will be done by fitting a function (most likely a second-order polynomial) to the complete set of instrument response data from the time period of interest.

An important result from this study is the comparison of heater-off to heater-on case for variable instrument temperatures. For instrument temperatures of 0 to 30 °C there is little difference in performance between the two conditions. Thus, given the major problems encountered with temperature stability and noise when the heater is on (see Section 3-8), there appears to be no significant advantage to operating the TES with the detector heater on.

3.3 Determination of Instrument Response Linearity and Offset

The primary objective of the TES radiometric testing was to determine the variation in instrument response with incident energy. This variation was initially studied using the external planet and space targets, whose temperatures and emissivities were believed to be well known. Initial studies used the both_full method to maximize SNR, while minimizing the effect of instrument temperature drift during data acquisition.

Each set of "constant" instrument temperature tests, consisting of either six or seven blackbody temperatures, was processed together. (V_{planet} - V_{space}) was determined, along with the corresponding (B_{planet} - B_{space}) values using the measured blackbody temperatures. A linear least squares fit was performed, weighted by the computed values of σV_{planet} and σV_{space}. The values of σ for the temperatures of the blackbodies were too small to be significant and were not included. Two cases were investigated: 1) used a linear fit that was not forced to pass through the origin; 2) used a linear fit forced that was forced through the origin.

For the heater-off tests, an initial study was performed to determine the relative importance of correcting the response for instrument/detector temperature. Figure 3-3 shows an example of the raw (V_{planet} - V_{space}) data for a single detector (Det. 2), a single wavenumber (983 cm^{-1}), and a single instrument set-point temperature (~0 °C). Figure 3-4 shows the y-axis offsets as a function of wavenumber for the unforced case with an unforced linear fit for each of the five instrument temperature sets. Figure 3-5 shows the y-axis offsets after the correction was made for detector temperature. In those cases where the detector temperature did not vary significantly over the test set (e.g. tvn20-tvn38) the uncorrected y-axis offsets vary from 0 to ~0.7, with the maximum occurring at ~600 cm^{-1}. Once the data were corrected for detector temperature variations, all of the y offset data have a similar dependence on wavenumber and similar amplitudes, indicating that the correction for detector temperature was appropriate and necessary. Corrections

for instrument temperature have been made in all of the analyses discussed in the following sections.

The y-offset errors were converted to irradiance using the instrument response functions computed for the best-fit linear model (Figure 3-6) (note: thre data in Figures 3-6, 3-7, 3-10, and 3-12 were originally computed in irradiance - these figures have not been recomputed in radiance units as was done for all other energy figures in this report). In correcting the data for instrument temperature the response was modified downward to be consistent with the lowest temperature used in temperature correction; thus the instrument response calculated from the linear best fit is generally lower than that calculated when the instrument viewed the 270K planet blackbody and was subsequently warmer. Figure 3-7 shows the resulting y-axis residuals, i.e. (V_{planet} - V_{space}) measured versus (V_{planet} - V_{space}), for the linear best fits, converted to radiance (note: in this case the response function for the TBB = 270K case was used to convert to radiance). Figures 3-7a-d gives the data from the unforced fit; Figures 3-7e-h gives data from the forced fit. Comparison curves are shown for the tvk14-tvk28 series corresponding to 0.3 and 0.8% of a blackbody at 270K for the unforced (Fig. 3-7b) and forced cases (Fig. 3-7f).

Assuming no calibration was performed on the data beyond the simplest approach of observing space and the reference blackbody, then the forced-fit results represent the errors in absolute calibration that would result. These errors are equivalent to a ~0.3% error in absolute calibration for a surface at 270 K . Figure 3-8 shows a schematic, highly exaggerated view of the residuals, for a given wavenumber, as a function of (Vplanet - Vspace), as determined from Figure 3-7.

As seen in Figures 3-6 and 3-7, the y-axis residual errors while remarkably small. However, they are systematic and therefore were investigated further. Possible causes for these errors include any combination of: 1) variations in instrument temperature during the collection of a set of planet and space observations, in which case the $\varepsilon_i B_i$ terms (Eq. 5) would not cancel; 2) systematic errors in the measurement of the blackbody

temperatures; 3) an energy term that was not correctly removed by differencing Vspace from Vplanet; or 4) non-linearities in instrument response with signal level. Each of these is discussed below.

Possible variations in instrument temperature during a suite of measurements were studied by processing the before_full and before_mini data in an identical manner to the both_full data processed above. The results for these two cases, for an instrument temperature of ~0 °C (tvk14-tvk28), are shown in Figure 3-9. The y-axis offsets and residuals for these cases are essentially identical to the both_full case, as seen by comparison of Figures 3-9a and b with Figure 3-5b, effectively eliminating instrument temperature variations as a possible cause.

The presence of errors in the blackbody temperature thermisters are a possible cause of the apparent y-axis offset that was investigated extensively. An unforced, linear best-fit was used to determine the slope of the response function at each wavenumber. Assuming that the response function should pass exactly through the origin, this slope was then used with the y-offset term set to zero to calculate model points. The residual in the x-axis was then determined, shown in Figure 3-10 for an instrument set-point temperature of 0 °C (tvk14-tvk28). These residuals are assumed to represent the error in absolute temperature between the two blackbodies. Figure 3-11 shows the relationship between the y- and x-axis residuals.

The x-axis residuals can be nearly reproduced by a small error of ~2.5 K in the relative temperature between the two blackbodies for the lowest (130 K) planet blackbody temperatures (Fig. 3-12). However, this modeling requires much larger temperature errors for intermediate planet temperatures and fails completely for the highest planet temperatures. Thus, while blackbody temperature errors may play a role in producing the observed deviations from a linear response, they are not the sole explanation.

The possible energy terms that might remain after calculating Vplanet - Vspace was limited by design in the experimental setup. Both target blackbodies were identical, were placed at small (30°), symmetric angles off of the nadir position, and were placed close to the TES aperture to minimize the amount of external energy that could be observed through the TES aperture. A possibility would be subtle differences in the emissivity of one of the blackbodies so that different amounts of instrument energy were reflected back onto the detector. For a given, nearly constant instrument temperature, however, the magnitude of this reflected component should remain approximately constant over the set of blackbody temperatures. The result would be a constant shift in the y-axis values. The resulting best fit line would have a different y-offset, but would have the same y residuals. This prediction was confirmed by analysis. Thus, unless implausible mechanisms, such as a temperature-dependent variation of the emissivity of one the blackbodies is invoked, differences in target emissivity cannot explain the observed residuals. No other possible energy terms have been investigated.

Finally, it is possible (likely ?) that non-linearities exist in the instrument response. Figure 3-13 shows the magnitude of raw data measured from the interferometer. Comparison of Figures 3-12 and 3-13 shows some consistency in the residual error with signal strength, with large signal levels producing responses slightly below the best-fit line. It is important to note, however, that the Fourier transform process assumes a linear response, so that any non-linearities have been transform in a complex manner throughout the entire spectrum and cannot be easily corrected.

In conclusion, no convincing, single mechanism has been found to account for the observed, systematic residual errors from a simple, linear response. However, because the overall magnitude of the errors in very small and because the most likely cause due to non-linearities in response has been transformed through the spectrum, it is concluded that no corrections will be made to the instrument data in flight to attempt to remove these small residual errors. The instrument response function will be assumed to be

linear with signal strength and have zero offset (i.e. $(B_{planet} - B_{space}) = 0$ when $(V_{planet} - V_{space}) = 0$).

3.4 Determination of Reference Surface Emissivity (REF_EMISS)

The next study was done to determine the emissivity of the internal reference surface. The intent of this activity was to transfer the calibration from the external target blackbodies to the internal reference surface, under the fundamental assumption that the external blackbodies have an emissivity of unity.

Based on the results from the linearity study, the simplifying assumption was made that the instrument response function was linear with signal strength. Solving for f, $\varepsilon_i B_i$, and $\varepsilon_{reference}$ gives:

$$f = \frac{V_{planet} - \overline{V}_{s12}}{B_{planet} - \overline{B}_{s12}} \tag{6a}$$

$$\varepsilon_i B_i = \overline{B}_{s12} - \frac{\overline{V}_{s12}}{f} \tag{6b}$$

$$\varepsilon_{reference} = \frac{\left(\frac{V_{reference}}{f} + \varepsilon_i B_i - B_{env}\right)}{(B_{reference} - B_{env})} \tag{6c}$$

for the before_full case.

Unfortunately, in practice $B_{reference}$ is very close to B_{env} so that the denominator of Eq. 6c is small and $\varepsilon_{reference}$ is very sensitive to noise in $V_{reference}$ and of limited value. Ignoring the effect of reflected environmental emission, which is reasonable given the high expected emissivity of the reference surface and the fact that the TES internal cavity with the cover closed is itself close to a blackbody cavity, leads to:

$$\varepsilon_{reference} = \frac{\left(\frac{V_{reference}}{f} + \varepsilon_i B_i\right)}{B_{reference}} \tag{6d}$$

Using the observed spectra and measured temperatures and allows f, $\varepsilon_i B_i$, and $\varepsilon_{reference}$ to be determined from the appropriate set of Equation 6 for each of the three cases. Figure 3-14 shows the derived reference surface emissivity for all detectors for

T_{inst} = 0 °C, T_{BB} = 270 K, heaters off (test set tvk22). This test was selected under the assumption that the best transfer from the external to internal blackbodies could be done when these two blackbodies were close in temperature.

Figure 3-14a shows an expanded view of the reference surface emissivity determined for single scan, imc off data for each of the five good detectors calculated using the average of the three reference surface temperature measurements. Also shown is the average of the five detectors, which, given the calibration method, should provide a better representation of the reference surface emissivity. Figure 3-14b shows the similar case for single scan, imc on. For completeness, Figures 3-14c and 3-14d show the cases for double scans, imc off and imc on respectively.

The reference surface emissivity derived and illustrated in Fig. 3-14 is within 0.1% of unity, with the major excursions occurring near 425 and 1000 cm^{-1}. These features are unusual in that they have a higher emissivity than the average, a behavior atypical for potential absorption features associated with the reference surface coating. Further study suggests that these features are actually absorption bands in the cold (space) blackbody. Using the space and planet blackbody observations alone it is possible to determine the emissivity of one blackbody assuming the emissivity of the other one is unity using:

$$V_{space} = (\varepsilon_{space} B_{space} + (1 - \varepsilon_{space}) B_I - B_I) * f \tag{7a}$$

$$V_{planet} = (B_{planet} - B_I) * f$$

solving for ε_{space} gives:

$$\varepsilon_{space} = \frac{\frac{V_{space}}{V_{planet}} (B_{planet} - B_I)}{B_{space} - B_I} \tag{7b}$$

Figure 3-15 shows the emissivity of the space blackbody determined in this manner. As seen in this figure, the same spectral features are present near 425 and 1000 cm^{-1} as were observed in Fig. 3-14. Because the reference surface was not used for any

of the derivations it is apparent that these features must be present on one (or both) of the calibration blackbodies, rather than on the reference surface.

The conclusion, therefore, is that the emissivity of the reference surface is indistinguishable from unity, to within the noise levels of the instrument, and unit emissivity will be used for all in-flight calibrations.

The next study investigated the best choice of reference surface temperature. Figure 3-16a again gives the reference surface emissivity determined using the measured planet blackbody temperature, T_{planet} = -4.90 °C, and the average of the three reference surface thermister temperatures, T_{ref}(average) = 0.938 °C (test set tvk22 - note: this figure is same as Figure 3-14a and the spectral features near 425 and 1000 cm^{-1} can be ignored). Figures 3-16b, c and d show the emissivity calculated using only temperature sensor 1 (0.952 °C), sensor 2 (1.109 °C), and sensor 3 (0.754 °C) respectively. As can be seen, the average temperature provides the closest values to unity emissivity and will be used for in-flight calibration.

Figure 3-17 shows a similar set of plots for the case of T_{planet} = -4.981 °C and T_{ref}(average) = -5.677 °C (test set tvk9). Figure 3-17a shows the reference surface emissivity using the average reference surface temperature, while Figures 3-17b, c and d show the emissivity calculated using only temperature sensor 1 (-5.671 °C), sensor 2 (-5.531 °C), and sensor 3 (-5.827 °C) respectively. In this set the average temperature does not provide a good result for the emissivity, but no other combination of temperature sensors provides a better result. The deviations seen in Figure 3-17 are most likely due to the small deviations from a perfectly linear response as discussed in the previous section, rather than errors in the temperature of the reference surface.

The reference surface emissivity was also derived using data collected with the spectrometer detector heaters on. T_{inst} = 0 °C, T_{BB} = 270 K, heaters on (test set tvl22) for the "both_full" case. These emissivity derived for this case deviated by up to 0.5%

from unity. These problems, however, are typical for "heaters-on" observations (see Section 3-8) and the heaters will not be operated at Mars.

In summary, data taken under conditions where the internal reference surface and the external "planet" blackbody were nearly the same temperature give a reference surface emissivity of unity to within the noise levels of the instrument. This high emissivity is likely due in part to the fact the instrument acts as a blackbody cavity with the cover closed viewing the reference surface. In this state the entire cavity is approximately isothermal. This condition will, however, be true in operation at Mars and the results obtained here should be valid for flight conditions. For all future studies, the reference surface emissivity will be taken to be unity for both single and double scans.

3.5 ABSOLUTE CALIBRATION (CALIB_SIMPLE)

The next step was to perform a complete end-to-end calibration test. This test involved the following steps:

1) The instrument response and instrument energy were determined using observations of the cold external blackbody and the internal reference surface. Based on the results of Section 3.3, the assumption that $f_{reference} = f_{planet} = f_{space}$ was used, along with the assumption that the instrument was perfectly linear and the transfer function goes through the origin. The reference surface emissivity determined in Section 3.4 was used, together with the average of the three reference surface temperatures.

2) Measurements of the external "planet" blackbody were converted to radiance (actually irradiance).

3) The ratio of B_{planet} radiance (measured) to B_{planet} (predicted) from the Planck function using the average of the two planet blackbody thermister temperatures was determined, along with the difference between these two determinations. The difference provides and estimate of the absolute radiance error that results from the calibration

4) The brightness temperature of the planet blackbody was determined to provide an estimate of the effective absolute temperature error in the calibration. This brightness

temperature was then used to determine the apparent emissivity of the target, again to provide an estimate of calibration error.

Solving Eq. 4 and using the mean of the space views before and after planet views ($\overline{B}_{s12}$; $\overline{V}_{s12}$) gives:

$$B_{planet} = \overline{B}_{s12} + (V_{planet} - \overline{V}_{s12})\left(\frac{\varepsilon_{reference}B_{reference} - \overline{B}_{s23}}{V_{reference} - \overline{V}_{s23}}\right) \quad (8)$$

The results of this analysis are shown in Figures 3-18 through 3-21. Figure 3-18 shows the difference between the TES-calculated and the Planck emission for all detectors for T_{inst} = 0 °C, T_{BB} = 270 K, heaters off (test set tvk22). Figure 3-19 shows this difference for detector 2 for all blackbody temperatures for T_{inst} = 0 °C. Figure 3-19a shows the full set of cases. As seen in this figure, the absolute radiance error is worst for temperatures farthest from ~270 K and the sign of the error varies from positive for planet temperature <270 K to negative for planet temperature >270 K. These errors are consistent with those found in Section 3.3 and illustrated schematically in Figure 3-8.

Figures 3-19b-h shows each individual case compared to a "best-fit" fraction of the radiance from a blackbody at the appropriate temperature. These curves are intended merely to illustrate the magnitude of the radiance error for each blackbody temperature.

Figure 3-20 shows the brightness temperature derived for each planet blackbody case for T_{inst} = 0°C. Also shown as a straight line is the measured planet blackbody temperatures using the average of the two thermistors. As can be seen from these figures there relatively small errors in the derived temperature. The NEΔT is only ~3°C for the worst case (127.3 K case).

The same method was used to determine and compare the TES-derived to Planck emission with spectrometer detector heaters on. These data are shown in Figure 3-21 in the same format as presented in Figure 3-20 for the heaters off case. As can be seen comparing Fig 3-21 to Fig. 3-20, the absolute calibration is worse in the heaters-on case, and there is more noise and structure in the derived temperature data.

3.6 SIGNAL-TO-NOISE PERFORMANCE

The signal-to-noise (SNR) of the TES was investigated using the standard deviations, derived in the standard way, as a measure of the noise in instrument. This approach produces an upper limit to the noise levels, and a lower limit to the SNR, because other sources of variance may be present that are unrelated to the instrument itself. The most likely of these is due to variations in the energy from the various targets observed due to cyclic variations in their temperature.

Figure 3-22 shows the sigma values computed for the T_{inst} = 0°C case with spectrometer heater off for the space target (space1 & 2) (Fig. 3-22a); the reference target (ref1) (Fig. 3-22b); the planet target with imc off (Fig. 3-22c); and the planet target with imc on (Fig. 3-22d). The same cases for with the spectrometer heater on are shown in Figure 3-23. These (and other) figures show the following trends:

1) For the heater off cases, there is an increase in noise levels of typically 20 to 40% from low wavenumbers (~400 to 800 cm^{-1}) to high wavenumbers (~1000 to 1400 cm^{-1}). In some cases there is a pronounced jump in noise levels near 900 cm^{-1}; in other cases the variation is roughly linearly, and in some instances it is roughly sinusoidal, decreasing again at the highest wavenumbers (> ~1400 cm^{-1}).
2) The sigmas are lowest for the reference views, with average values around 0.07.
3) The sigmas for the space views are roughly constant for a given instrument temperature, with average values of approximately 0.12.
4) The sigmas on the planet views vary somewhat with planet temperature. However, this variation does not appear systematic; for instrument temperatures of -20, -10, and 0° C, there is little variation, although the highest instrument temperatures have the highest sigmas. Conversely, for instrument temperatures of +10 and +20 °C the sigmas decrease by a factor ~3 and ~5 respectively as the planet temperature increases from 130 K to 325 K. Typical values are ~0.1-0.15.

5) Imc produces some additional noise, both as an approximately 25% increase in the base noise level and in greater variability in the noise spectrum.

6) The spectrometer heater does introduce additional noise. For the reference views, which have the lowest noise (~0.07) for heater off, the typical values range from ~0.15 to 0.2 with heater on, with a pronounced increase in noise toward high wavenumbers (Fig. 3-23). Observations of cold targets (both space and cold planet) have higher sigmas that observed for warm targets (reference and warm planet). These trends are easily seen in Figure 3-23b, where there is a systematic decrease in the sigma from average values near 0.4 for a planet temperature of 130 K to ~0.12 for a planet temperature of 325 K. This effect should not be due to physical changes in the instrument when viewing targets of different temperature because it was not observed for the heater off case. Instead, it appears that there is a scene-energy-dependent noise source.

3.7 Spectrometer Gain Analysis

The TES spectrometer has four internal gain settings that nominally are: 1, 2.5, 4, and 8. A concerted attempt was made to achieve these values using 1% precision resistors. The actual value of the gain is stored in the Instrument Parameter Tuning Table on-board the instrument. The values in this table are used in the flight software to divide the measured signal prior to transmission to Earth. The parameters in this table are adjustable on ground command.

The actual instrument gain setting were evaluated in two ways; 1) the gains were cycled through all four settings for the reference view for each instrument/planet case; and 2) for those cases where the signal levels permitted, the planet target was viewed at all of the gain settings that would not saturate.

Figure 3-24 shows the results comparing the signals from the external planet blackbody at the four gain settings. The instrument setpoint temperature was +30°C, heaters were off, and the planet blackbody temperature was 310 K (test tvn27). In

calculating the signal transmitted from the instrument, the nominal gains of 1, 2.5, 4, and 8 were used. Therefore, if the actual gains have these values, then the ratios shown in Figure 3-24 should equal one.

Figure 3-24 shows significant deviation from unity that is most likely due to temperature variations that have not been properly removed. Figure 3-25 gives the ratio of gain 2/gain 1, 3/1, and 4/1 for the signals from the reference surface at a temperature of 22.3 °C. The data in this figure do not appear to suffer from the types of problems seen in Figure 3-24. As seen in figure 3-25, the actual gains agree with the nominal set point gains to within 0.1%. Given this result, the nominal gains will be used for standard processing unless in-flight data indicate a variation in relative gain values.

3.8 Spectrometer Heater Performance Analysis

The initial indication of noise related to the spectrometer detector heater was obtained during radiance calibration studies done with the heater on. Virtually all computed parameters that involved dividing one set of observations by another, such as instrument response function or emissivity, show a characteristic spectral shape (Fig. 3-26). Subsequent analysis has shown that this spectral shape can be also be produced by ratioing observations taken less than 10 ICKs apart, indicating that some instrument condition is varying of time-scales of this duration or less.

Figure 3-27 shows the time variation in the raw data for two wavenumbers (1503.5 and 1608.6). The observed variability appears random. However, when 10 ICK time averages are computed for these two wavenumbers to remove some of the random noise (Figure 3-28) it is apparent that there are systematic fluctuations is signal strength that are strongly correlation between wavenumbers. Figure 3-28a shows this effect for two wavenumbers for a single detector; Figure 3-28b shows the comparison for a single wavenumber measured by two different detectors (2 & 3), and demonstrates that these systematic fluctuations are correlated between different detectors as well.

The non-random nature of these fluctuations can be further illustrated using the time variations in all wavenumbers simultaneously. This was done by ratioing spectra acquired a different time intervals. If the variations are correlated between wavenumbers, then for two time periods in which two spectral channels have nearly identical values, such as at ICKs 42 and 52 in Figure 3-28, then all wavenumbers should have similar values at the two times and the ratio of the spectra should be approximately unity. Exactly this behavior is observed in Figure 3-29 for the ratio of ICK 42 to ICK 52. For time periods where wavenumbers 1503 and 1608 differ (e.g. ICK 82 versus ICK 42 in Fig. 3-28) then the spectral ratios reflect variations at all wavenumbers, as is observed (dotted curve in Figure 3-29).

It is apparent from Figure 3-29 that the signal fluctuations are highly correlated in wavenumber. Most importantly, the spectral shape of these correlated fluctuations mimics the spectral signature observed in Figure 3-26. It is proposed, therefore, that the variation in some instrument property, over time scales of ~10-20 ICKs, is responsible for producing a correlated change in response with the spectral character shown in Figure 3-29.

Figure 3-30 shows the 10 ICK averages for the identical sequence of data shown in Figure 3-28, but with the spectrometer detector heater off. As seen in this figure, there is a much weaker correlation between different wavenumbers than was seen with the heater on. Figure 3-31 shows the ratio of the raw spectral data for ICKs 62, 102, 122, and 152 relative to ICK 42. Comparison with Figure 3-29 shows that the spectral shape is much flatter with the detector heater off (Fig. 3-31) than with heater on (Fig. 3-29).

The short time scale (20-40 seconds) observed for correlated variations between channels would appear to rule out physical changes in the temperatures of the targets, as does the fact that the problem is correlated with spectrometer heater state. Physical changes in the temperature of the detectors themselves is possible, though unlikely. Figure 3-32?? shows a comparison of the 10 ICK averages for wavenumber 1503 for

detectors 2 and 3 (Fig. 3-32a) and detectors 2 and 5 (Fig 3-32b). These comparisons were chosen because detectors 2 and 3 share common electronics, whereas 2 and 5 do not. As seen in these figures, the correlation is as good between all three detectors as it is for different spectral channels within a single detector. Thus, the noise source must be common to all detectors and the mechanism for producing the observed variability must be produced outside of the detectors, their preamps, or their postamps. Possibilities include power supply noise that is enhanced when the heater circuits are active, or possibly noise produced by oscillations in the heater circuit itself.

Based on this study the spectrometer heater will not be operated in flight. In addition, electronic noise in the spectrometer data is observed whenever the bolometer heater is operated. This problem appears to be related to electronic oscillations in the bolometer heater. Because of this problem the bolometer heater will not be used in flight either.

3.9 Determination of In-Flight Calibrated Radiance

3.9.1 Definition of In-Flight Calibrated Radiance

The measured signal (V_{planet}) viewing Mars, as a function of frequency (ν), is given by:

$$V_{planet}(\nu) = \left[\sum_{p=1}^{n} \{\varepsilon_p(\nu) B(T_p, \nu)\} - B(T_I, \nu) \right] * f(\nu) \qquad (9)$$

where: n = number on surface components, p

ε_p = planet emissivity of surface component p

Tp = temperature of surface component p

B = Planck function radiance

T_I = Instrument temperature

f = instrument response function

Solving for the calibrated radiance ($\sum_{p=1}^{n} \varepsilon_p(\nu) B(T_p, \nu)$) gives:

$$\text{Calibrated Radiance} = \sum_{p=1}^{n} \varepsilon_p(\nu) B(T_p, \nu) = B(T_I, \nu) - \frac{V_{planet}(\nu)}{f(\nu)} \qquad (10)$$

To compute calibrated radiance, both f and $B(T_I, \nu)$ must be determined as outlined previously. The objectives in flight are: 1) to minimize the noise on these functions by taking advantage of their repetitive and predictable forms; and 2) to develop an effective means for interpolating the background energy ($B(T_I)$ between calibration observations .

3.9.2 Instrument Response Function

The instrument response function (f) should be a slowly varying function except for the small variations due to changes in instrument temperature. As long as space and reference view are obtained close together in time (within several ICKs) then these two terms can be used directly to calculate f given by:

$$f(\nu) = \frac{V_{ref}(\nu) - V_{space}(\nu)}{\varepsilon_{ref}(\nu)B(T_{ref}, \nu) - B(T_{space}, \nu)} \tag{12}$$

where $\varepsilon_{ref}(\nu)$ was derived from SBRC thermal vacuum testing and found to be unity at all frequencies (see Section 3-4), T_{ref} is from the average of the three reference surface temperatures, and T_{space} is 3 K (probably the best known parameter of the entire TES experiment).

The noise in the instrument response function (f) from a single pair of reference/space observations can be reduced by combining multiple determinations over a time period of TBD (~7) days. However, the statistical variations in f must be separated from the expected variations in f due to variations in instrument temperature. This separation will be done by fitting a function (most likely a second-order polynomial) to the complete set of instrument response data from the time period of interest. The spectrometer detector telemetry temperature will be used for instrument temperature.

The value of f used in Eq. 2 for each planet measurement is then determined from the functional form of f, again using the spectrometer detector temperature for each measurement.

3.9.3 Instrument Energy

The instrument energy, $B(T_I)$, is obtained by viewing space, which provides an excellent target of known (low) temperature and unit emissivity. For each space view (ignoring the dependence on ν):

$$V_{space} = [B(T_{space}) - B(T_I)] * f$$

$$B(T_I) = B(T_{space}) - \frac{V_{space}}{f} \qquad (13)$$

The noise in an individual space view can be reduced in one of two ways:

Method 1:

Simply smooth (filter) the $B(T_I)$ data over frequency. These data should have very little inherent spectral structure because the instrument energy comes from a cavity that is essentially blackbody in nature. Thus, the spectral "variations" are primarily due to noise and can be removed by smoothing with no loss in accuracy.

Method 2:

Compute $B(T_I)$ for each ν and and determine a best fit TI to get an "effective" instrument temperature. In the simplest case this best fit could be done by inverting the Planck function to calculate $T_I(\nu)$ over an appropriate range of frequencies where the signal-noise-was high enough to get a reasonable determination. If the internal instrument temperatures are nearly isothermal, then a uniform weighting (average) of the derived instrument temperatures should provide a reasonable estimate of the average instrument temperature. If not, then a more sophisticated weighting scheme could be used. In any case the "effective" instrument temperature would be used in the Planck function to compute a noise-free $B(T_I)$ term. This method is essentially a smoothing operation as well, except in this case the "smoothing" function is the Planck function. The advantage is that it provides a physically plausible function for

smoothing; the disadvantage would come if the instrument was not isothermal and the associated computational complexities and potential radiance errors introduced by representing the instrument energy by a series of Planck functions.

Once the background energy is determined at each space observation by either method, this energy must be interpolated for all of the intervening planet observations and used with f to determining the calibrated radiance for each planet observation. In either case the instrument energy for each planet view will be determined using a functional fit to the instrument energies determined for the nearest, bounding space views. Initially, a simple linear interpolation between bounding space values will be used; with time in orbit, a more complex function will be determined to account for repetitive, periodic variations in instrument temperature. For Method 1, the interpolation would be between the smoothed, derived instrument energy. For Method 2, the interpolation would be between the derived instrument temperature(s). This later method has the advantage of more accurately representing the variable (instrument temperature) that is actually changing.

4.0 ALBEDO BOLOMETER RADIOMETRIC CALIBRATION

4.1 RADIOMETRIC PERFORMANCE

Not completed.

4.2 SIGNAL-TO-NOISE PERFORMANCE

At the time of the loss of Mars Observer, a detailed analysis of the albedo channel SNR performance had not been completed. This detailed study has not been performed. However, initial analysis was done to verify that the instrument met its functional requirements with a SNR of ~1500.

5.0 THERMAL BOLOMETER RADIOMETRIC CALIBRATION

5.1 RADIOMETRIC PERFORMANCE (FROM S. CHASE - 8/11/93 REPORT)

Introduction

This report summarizes the analysis of the TES bolometric channel calibration data. The data were analyzed in three areas:

1. Linearity: Determine slope and offsets of radiometric transfer functions for each channel at each of six instrument temperatures.
2. Temperature dependence: Determine temperature vs. gain function for each channel
3. Internal Reference Surface (IRS): Determine accuracy of IRS calibration for determination of in-orbit planet radiances.

All of the analysis to be described was performed in MathCad 3.1 for the Macintosh. Two data files (channel data and temperatures) were used as input for each instrument temperature calibration run.

Data used in the analysis were averages of ICKs 17-32 (Space), 37-164 (Day) and 199-214 (RefB). The IRS temperatures corresponding to RefB were the averages of Auxtemps 1,2 and 3.

5-1-1. Linearity of Radiometric Transfer Functions (slopes)

All channels were found to be quite linear over the seven planet blackbody temperatures. Table 5-1 contains slopes (least-squares regression straight line) and offsets and Pearson's r (correlation coefficient[1]) for each of the six detectors at each instrument temperature. Slopes are in units of watt-cm^{-2}-ster^{-1} (planet-space radiance) and offsets are in signal units (planet-space signal).

Table 5-1. Bolometer Channel Slopes and Offsets (least-squares fit)

Channel	1	2	3	4	5	6

[1] Pearson's r is not defined in MathCad, but I think it is similar to a Chi-Square correlation coefficient.

-20C						
Slope	143.685	146.575	155.929	144.159	145.065	147.706
Offset	-1.220	-1.689	-2.452	0.043	-1.414	-0.069
Corr	1.0	1.0	1.0	1.0	1.0	1.0
-10C						
Slope	149.777	152.884	162.409	150.774	151.347	154.310
Offset	-7.499	-7.291	-7.989	-7.423	-9.117	-6.840
Corr	1.0	1.0	1.0	1.0	1.0	1.0
0C						
Slope	157.292	160.381	170.095	159.957	159.133	163.34
Offset	-1.297	-1.684	-2.645	-1.016	-1.174	0.504
Corr	1.0	1.0	1.0	1.0	1.0	1.0
+10C						
Slope	163.455	166.697	176.507	167.373	165.908	170.753
Offset	4.566	3.406	1.662	5.549	3.880	7.108
Corr	1.0	1.0	1.0	1.0	1.0	1.0
+20C						
Slope	168.367	171.447	181.014	172.896	171.357	176.753
Offset	7.845	7.041	5.638	10.304	6.966	10.506
Corr	1.0	1.0	1.0	1.0	1.0	1.0
+30C						
Slope	170.049	173.012	182.390	175.141	173.413	179.151
Offset	6.859	7.541	6.778	8.094	6.635	8.973
Corr	1.0	1.0	1.0	1.0	1.0	1.0

When these least-square fit transfer functions were used to check agreement of the reference surface data errors of up to 8% in radiance were encountered that were attributed to monotonic changes in instrument temperature (and hence gain) that were occurring during the calibration run. It was assumed that the temperatures, and gains, changed in such a way that the transfer functions were still linear.

To check out this assumption the slopes of the (IRS signal-space)/(IRS radiance-space) curves were calculated by a method that more nearly represents the actual data taking sequence. In this method, the radiance corresponding to the IRS temperature is used, and

the curve is assumed to go through zero. This is a fairly good assumption based on the data fit to a curve shown in the table above. The slopes computed in this manner are shown in Table 5-2.

Table 5-2. Bolometer IRS Slopes Calculated at a Planet Temperature of 270K

Channel	1	2	3	4	5	6
-20C Slope	142.856	145.794	154.94	143.327	144.194	147.057
-10C Slope	148.85	151.814	161.291	149.766	150.544	153.413
0C Slope	156.698	159.817	169.533	159.665	158.563	163.044
+10C Slope	162.458	165.777	175.691	166.175	164.952	169.528
+20C Slope	167.926	170.963	180.490	172.36	170.880	176.342
+30C Slope	170.203	173.178	182.354	175.537	173.608	179.605

Comparing these slopes to those in Table 5-1. show differences of less than 1%. Moreover, Table 5-3, below shows IRS slopes at each planet blackbody temperature (in this case for +30C instrument temperature). The change in slope is less than 1% over the run suggesting that the instrument temperature, and therefore the gain, was quite stable.

A more likely explanation is simply the manner in which the data were plotted. This will be illustrated in Section 5-1-3.

Table 5-3. Channel Slopes at Each Planet Blackbody Temperature (+30C Run)

$Slope_{n,1}$·RadK
169.835
170.306
170.341
170.42
170.504
169.095
170.203

$Slope_{n,3}$·RadK
182.378
182.769
182.715
182.77
182.84
181.756
182.354

$Slope_{n,5}$·RadK
173.211
173.676
173.743
173.829
173.795
172.528
173.608

$Slope_{n,2}$·RadK
173.061
173.525
173.513
173.549
173.611
172.06
173.178

$Slope_{n,4}$·RadK
175.264
175.76
175.863
175.881
175.968
173.669
175.537

$Slope_{n,6}$·RadK
179.155
179.755
179.752
179.773
179.847
177.907
179.605

5-1-2. Temperature Dependence:

Pyroelectric detectors have a responsivity dependence on temperature. Figure 5-1. shows this dependence for all six channels for a relatively constant planet blackbody temperature at 238K. The abscissa is IRS temperature (the average of the three temperature sensors).

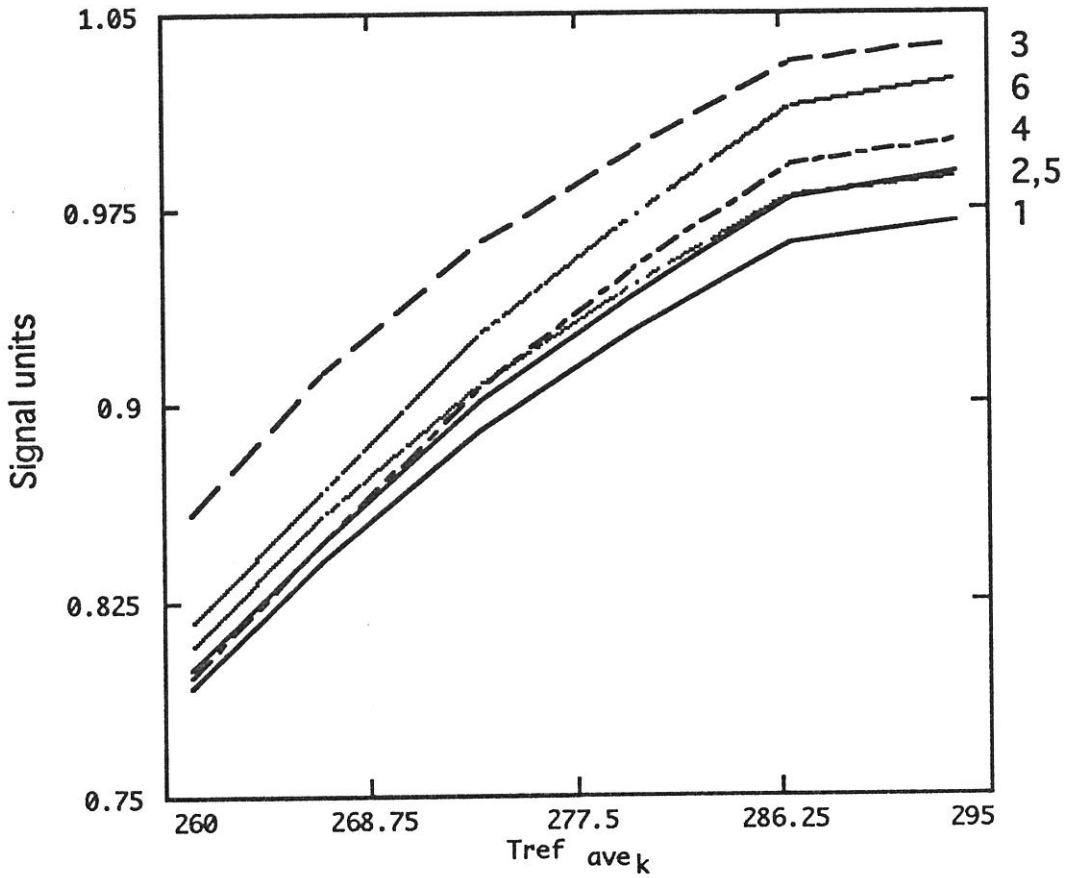

Figure 5-1. Temperature Dependence of Bolometer Channel Responsivities

The slope of these curves is about 0.00617 signal units per K.

5-1-3. Internal Reference Surface (IRS)

Based on the discussion in Section 5-1-1, the agreement of the planet radiance to that of the IRS radiance at a corresponding temperature to the IRS was calculated. The calculated planet-space radiance was determined by dividing the planet-space signal by the IRS slope. The ratio of the calculated value to the measured value is shown in Figure 5-2 for an instrument temperature of +30C.

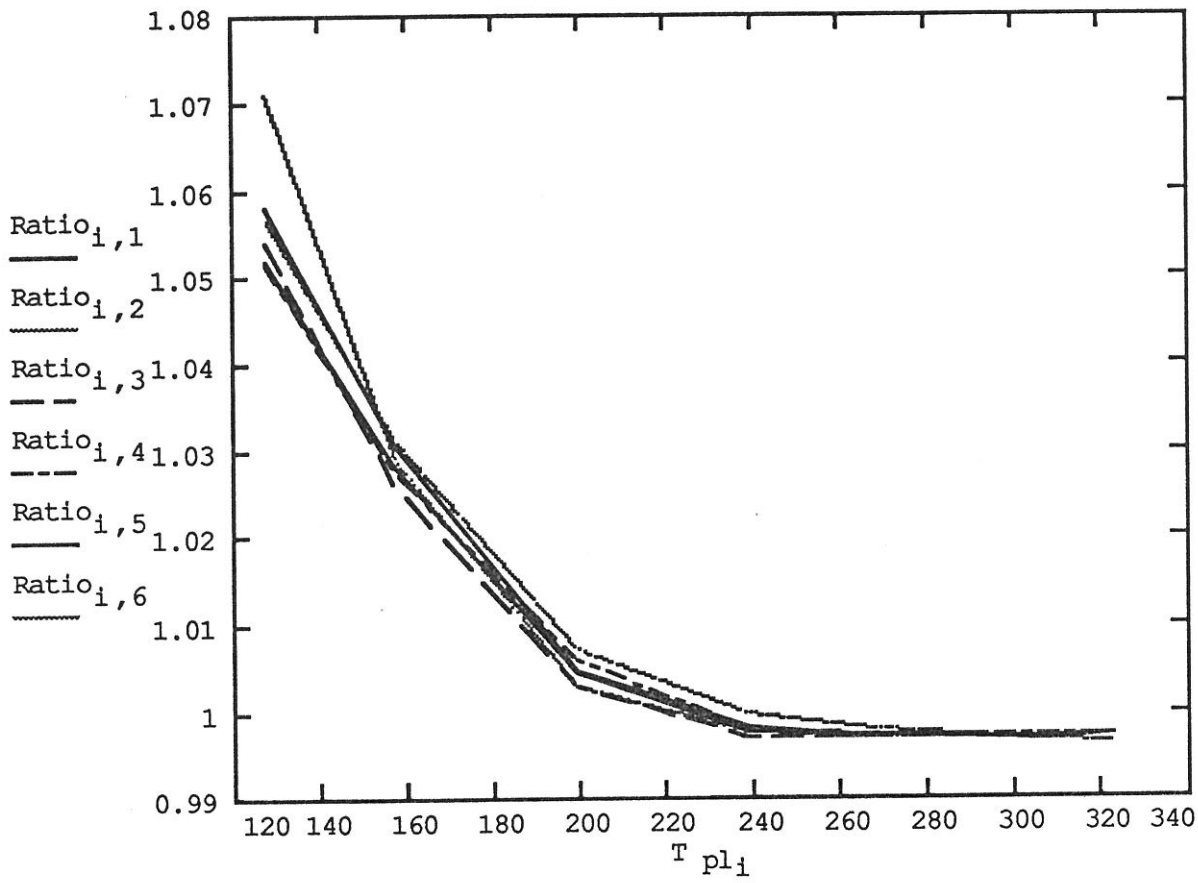

Figure 5-2. Ratio of Radiance Error at Each Planet Temperature

These ratios are seen to grow at low planet temperatures because the planet radiance is decreasing in proportion to a fixed radiance error. This is the type of error I believe we were seeing in the previous analysis.

However, when the ratio of the radiance difference to a fixed radiance at 270K is plotted the resulting error is much smaller. This can be seen in Figure 5-3.

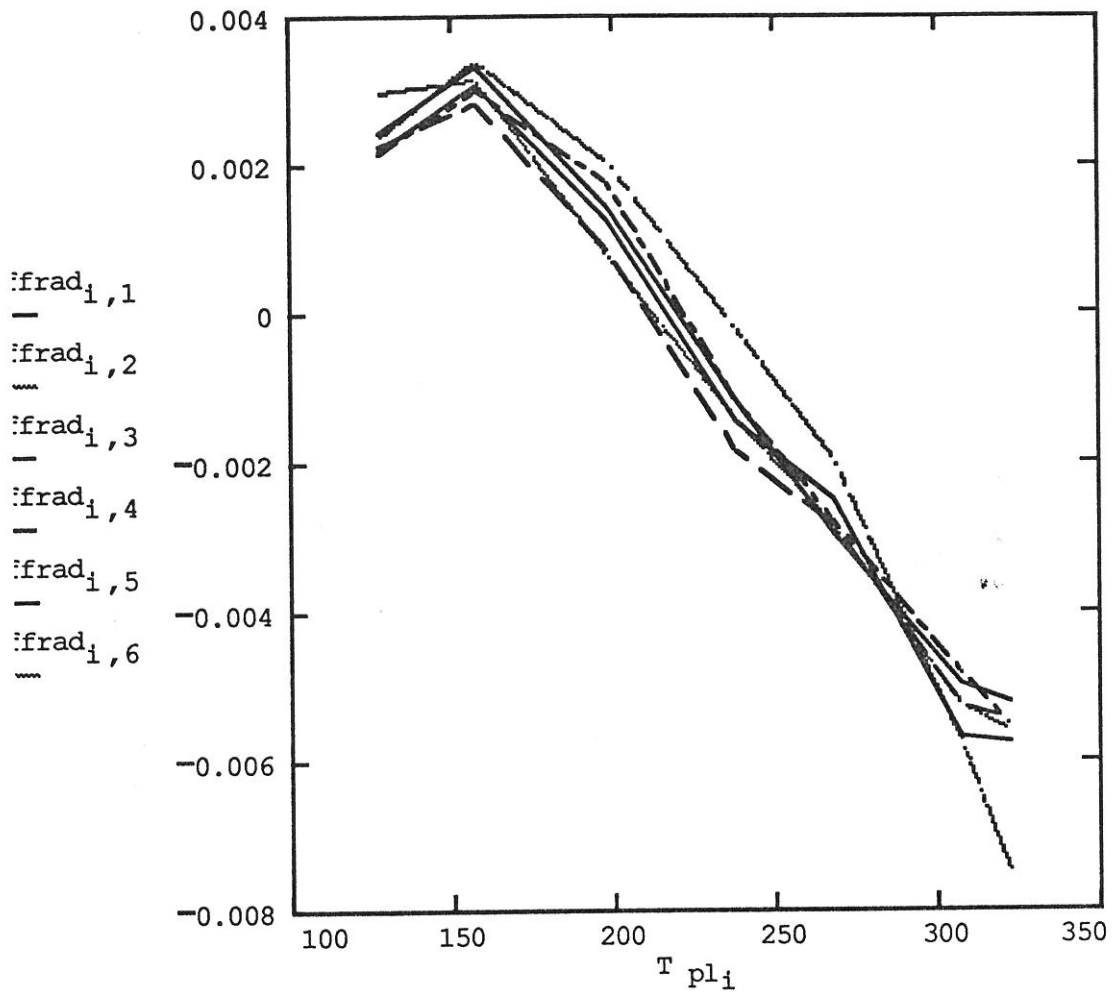

Figure 5-3. Ratio of Radiance Difference to the Radiance at 270K, for +30C Instrument Temperature

Plots at different instrument temperatures are different shapes, but the errors are comparable. These plots for all instrument temperatures are shown in the following figures.

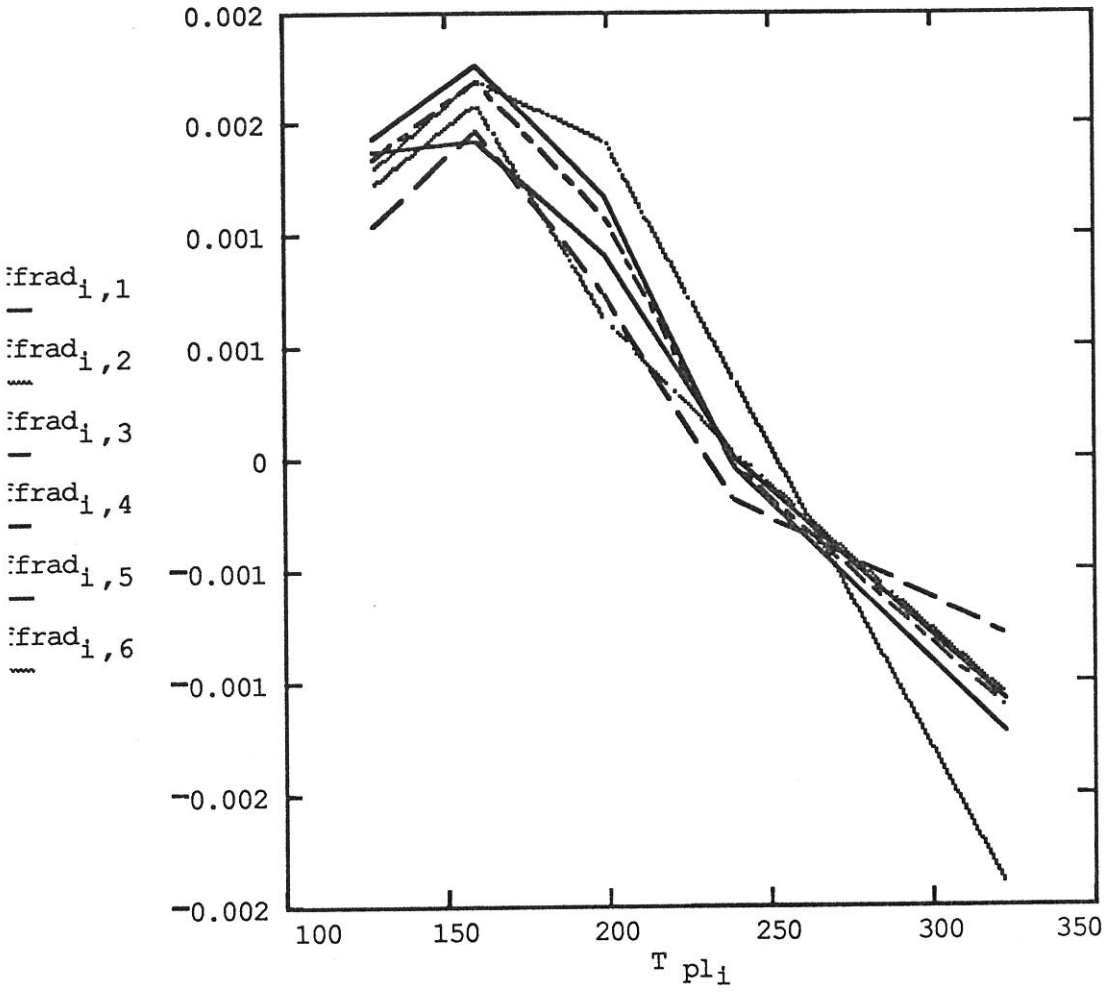

Figure 5-4. Ratio of Radiance Difference to the Radiance at 270K, for +20C Instrument Temperature

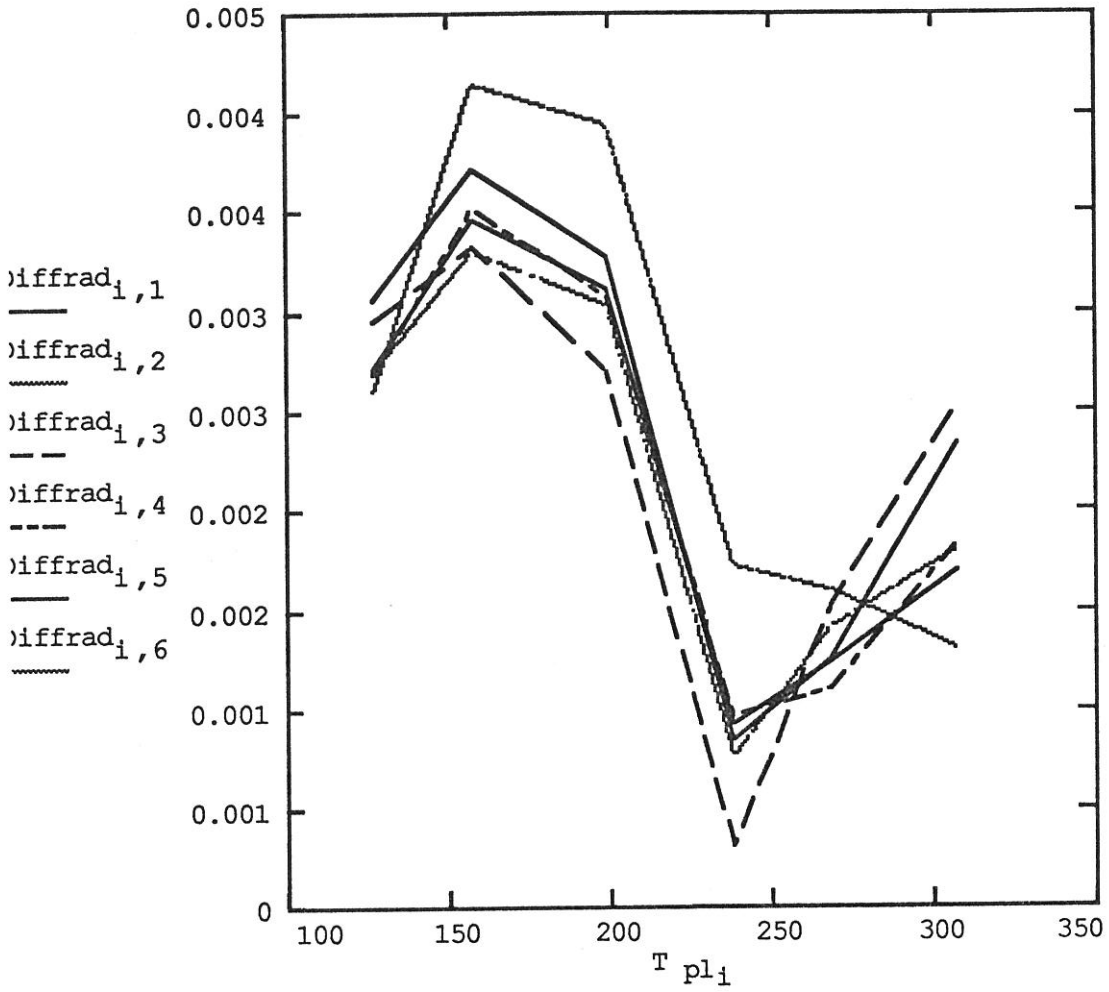

Figure 5-5. Ratio of Radiance Difference to the Radiance at 270K, for +10C Instrument Temperature

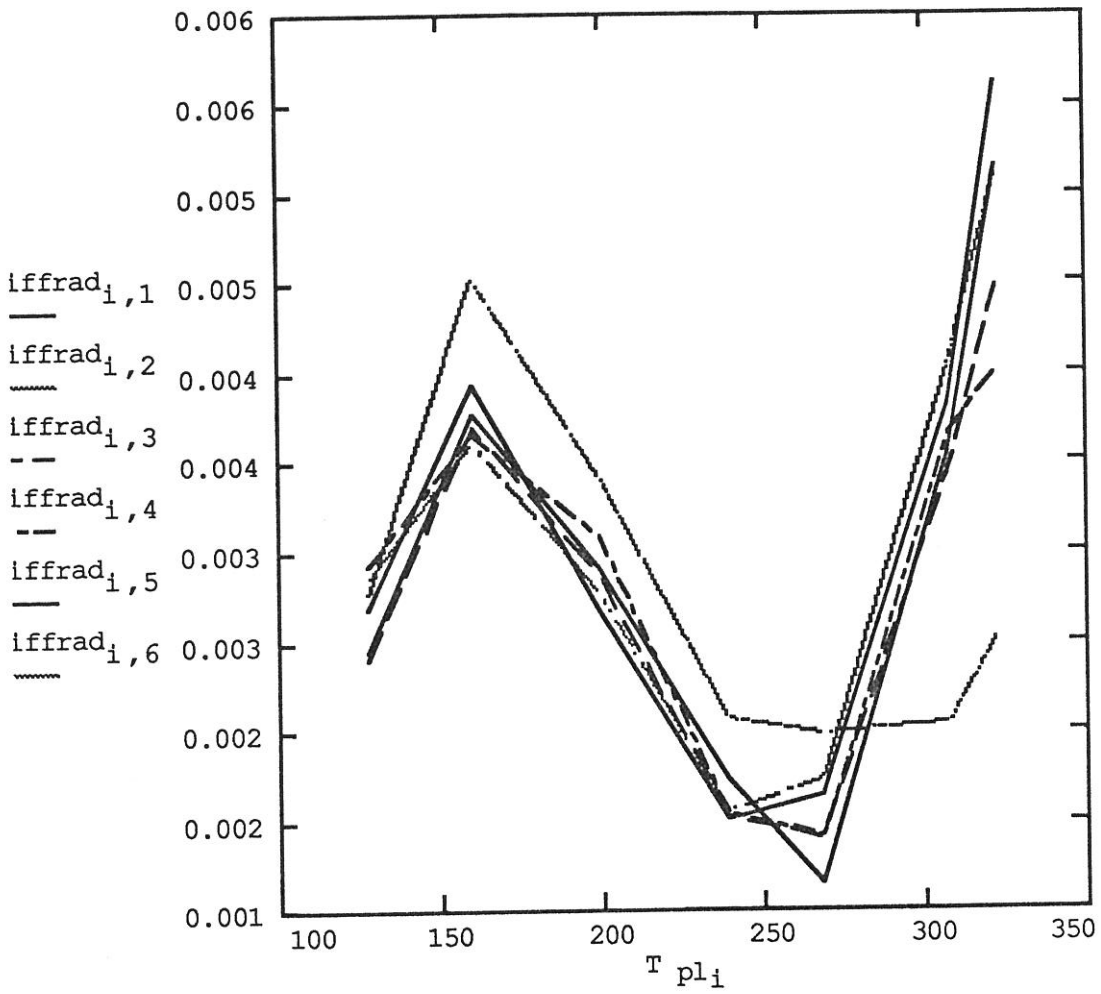

Figure 5-6. Ratio of Radiance Difference to the Radiance at 270K, for +0C Instrument Temperature

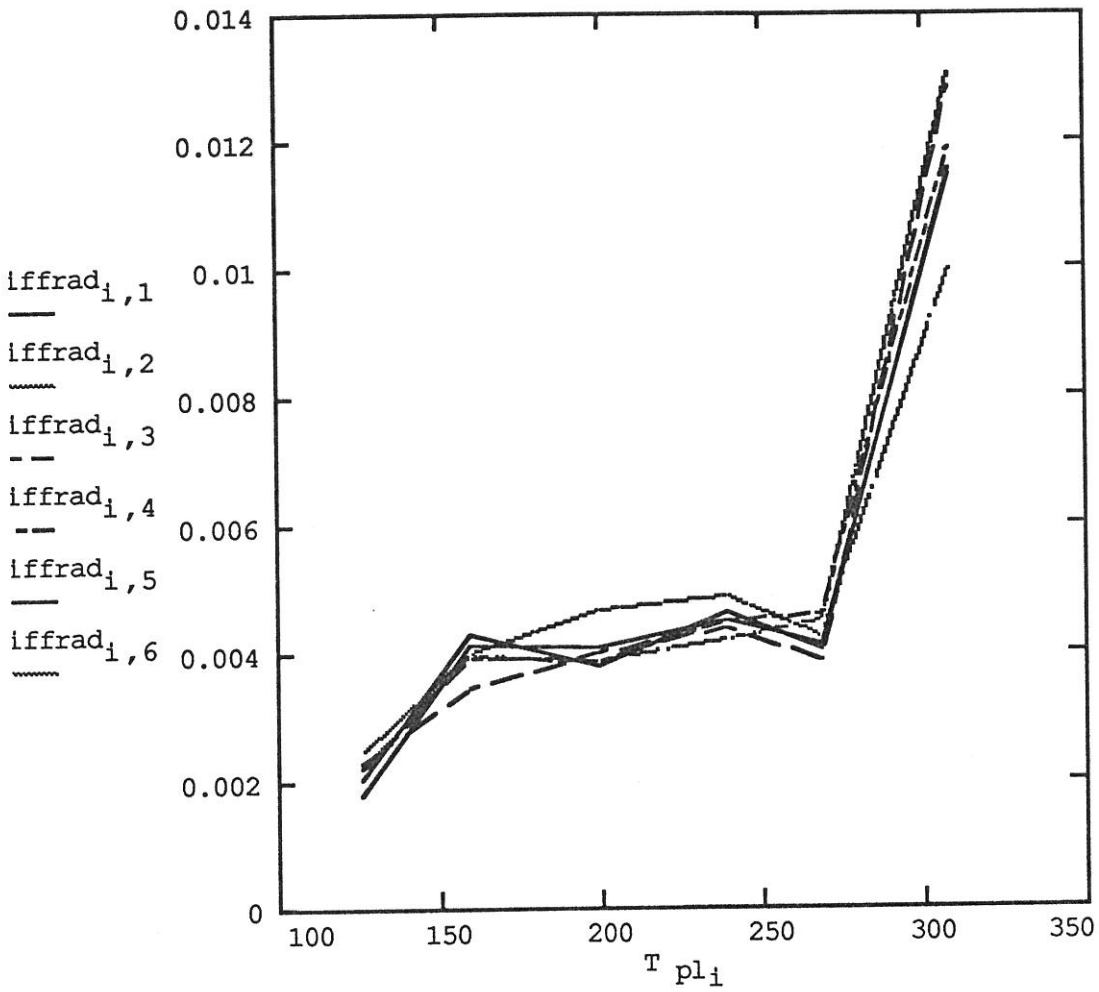

Figure 5-7. Ratio of Radiance Difference to the Radiance at 270K, for -10C Instrument Temperature

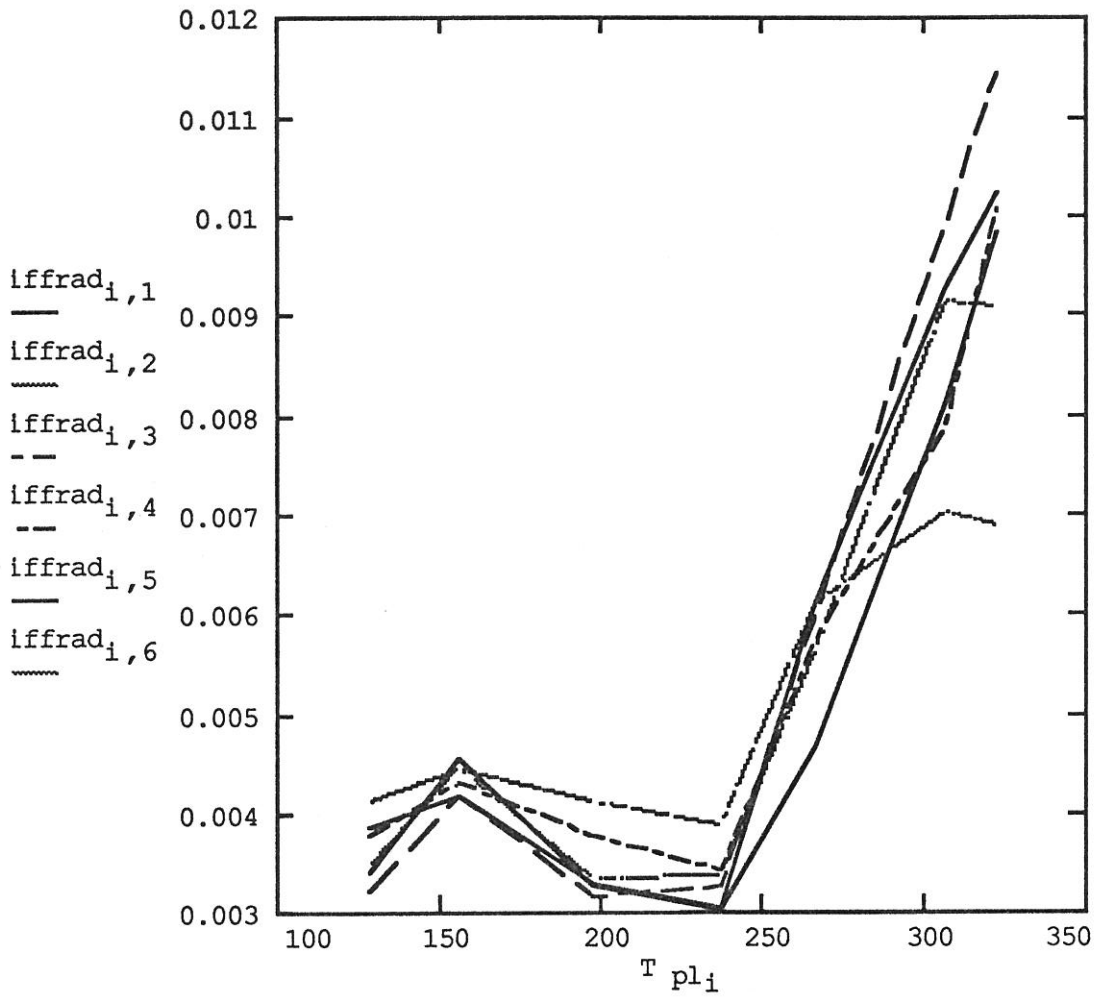

Figure 5-8. Ratio of Radiance Difference to the Radiance at 270K, for -20C Instrument Temperature

5.2 Signal-to-Noise Performance

At the time of the loss of Mars Observer, a detailed analysis of the thermal bolometer channel SNR performance had not been completed. This detailed study has not been performed. However, initial analysis was done to verify that the instrument met its functional requirements with a SNR of ~2000.

6.0 TIME HISTORY OF INSTRUMENT RESPONSE

Spectrometer instrument response variations were tracked throughout the TES integration, test, and flight phases. These tests included ambient, thermal vacuum, and space conditions. In some cases (e.g. thermal vacuum) both cold and hot targets were available. However, in many cases (e.g. bench ambient) only a hot target was available. For this reason, the instrument response has been computed using only a single target and assuming that the instrument temperature was equal to the spectrometer detector telemetry value. Table 4-1 summarizes the test conditions for the tests used in this time history summary.

Table 4-1

#	Test Condition	Test Name	Orbit	ICK Range	Detector Temp. (°C)	Target Temp. (°C)	.tdb vector
1	SBRC Post Vib. Bench	snrd6	1	538-547	25.6	45	1
2	SBRC TV N2	snre1	1	538-547	30.7	45(?)	7
3	SBRC vacuum - early	tvf8	2	37-46	-13.8	-140.8	13
4	SBRC vacuum - mid	tvn5	2	17-26	13.7	-190.	19
5	SBRC vacuum - mid	tkv33	2	17-26	7.38	-190.	25
6	SBRC vacuum - late	tvn38	2	37-46	25.0	49.1	31
7	Pre-ship Ambient	datab4					
8	GE Ambient	te_data1a8	1	18-25	22.3	45	43
9	GE TV	te_defa9	6	1467-1476	36.8	-38	49
10	GE pre-ship Ambient	te_data1a9	1	18-25	23.9	45	55
11	Cape Ambient	te_data1d1	1	18-25	24.3	45	61
12	First Space	te_inner1	0	15-?	15.2	-270	67
13	Second Space - C7	te_outer1	0	15-?	7.24	-270	73

14	Third Space - C12	te_c12_fov1	0	15-?	-1.1	-270	79

Data stored in file $CALIB/archive/inst_resp/resp_sng.tdb

Figure 4-1 gives the instrument response (in TN) in single-scan mode for all of the tests listed in Table 4-1. The large differences in response are due to the significant differences in detector temperature, as discussed in Section 3.2. Close inspection reveals subtle differences near 1000 and 680 cm-1. Figure 4-2a shows the results of all tests acquired to GE thermal vacuum chamber under vacuum. Figure 4-2b gives the results of all tests in GE thermal vacuum and later. Figure 4-3 gives the same before (4-3a) and during and after (4-3b) data at an expanded scale. It is apparent from these figures that a change occurred in the instrument response during vacuum conditions and that the instrument response did not revert to its earlier value after thermal vacuum. No changes were observed before and after thermal vacuum at SBRC, which lasted significantly longer (~30 days) than the GE test (~10 days). The cause of this change is unknown, but served to improve response. Importantly, no further changes were observed during transport to the Cape nor after launch.

FIGURE CAPTIONS

1-1) Cross-section of the TES internal reference surface

1-2) Location of the three thermisters in the reference surface. From SBRC drawing 400367, Sheet 3, Section C-C.

1-3a) Cross-section of the external calibration blackbodies showing dimensions and the location of the temperature sensors.

1-3b) Photograph of the finished external calibration blackbody.

1-3c) Photograph of the two external calibration blackbodies, along with the TES flight instrument, in the SBRC thermal vacuum chamber. Image was taken immediately prior to closing the chamber door for thermal vacuum calibration.

1-4) TES thermal vacuum timeline.

2-1) Pre-shipment Elevation field of view definition and alignment. (a) Detectors 1-3. (b) Detectors 4-6.

2-2) Pre-shipment Azimuth field of view definition and alignment. (a) Detectors 1-2. (b) Detectors 3-4. (c) Detectors 5-6.

2-3) Spatial location of half power points for spectrometer, bolometer, and albedo channels in elevation and azimuth

2-4) Detailed detector response mapping for detectors 2 and 5.

2-5) Intermediate out-of-field energty - Detector 1.

2-6) Illustration of smoothing algorithm described in text to estimate percent of energy contained versus distance from center of Albedo detector 2.

2-7) Percent of energy contained versus distance from center of: (a) Albedo detectors; (b) thermal bolometer detectors.

2-8) Schematic of method used to estimate out-of-field energy using line scan data.

2-9) Examples of far out-of-field results.

2-10) Altered versus unaltered thermal bolometer repsonse functions. See text for details.

2-11) Normalized slope response simulation.

3-1) Instrument response function. (a) Detector heaters off case. (b) Detector heaters on. Instrument response in units of TES Numbers (TN)/(W cm^{-2} str^{-1} cm^{-1}).

3-2) Instrument response versus detector temperature for detector heaters off. (a) First six selected wavenumbers. (b) Second six wavenumbers. (c) Third six wavenumbers. Instrument response in units of TES Numbers (TN)/(W cm^{-2} str^{-1} cm^{-1}).

3-3) V vs B. Example of (Vplanet - Vspace) versus (Bplanet - Bspace). V in units of TES Numbers (TN).

3-4) Y-axis offset for an unforced, linear fit to (Vplanet - Vspace) versus (Bplanet - Bspace). Data were not corrected for instrument temperature. (a) Instrument setpoint temp = -10 °C. (b) Instrument setpoint temp = 0 °C. (c) Instrument setpoint temp = +10 °C. (d) Instrument setpoint temp = +20 °C. V in units of TES Numbers (TN).

3-5) Y-axis offset for an unforced, linear fit to (Vplanet - Vspace) versus (Bplanet - Bspace). Data have been corrected for instrument temperature. (a) Instrument setpoint temp = -10 °C. (b) Instrument setpoint temp = 0 °C. (c) Instrument setpoint temp = +10 °C. (d) Instrument setpoint temp = +20 °C. V in units of TES Numbers (TN).

3-6) Y-axis offset converted to irradiance (W cm^{-2} str^{-1} cm^{-1}). (a) Instrument setpoint temp = -10 °C, detectors 2-5. (b) All instrument setpoint temperatures - detector 2.

3-7) Y residuals converted to irradiance (W cm^{-2} str^{-1} cm^{-1}). Unforced case: (a) Instrument setpoint temp = -10 °C. (b) Instrument setpoint temp = 0 °C. (c) Instrument setpoint temp = +10 °C. (d) Instrument setpoint temp = +20 °C. Forced case: (e) Instrument setpoint temp = -10 °C. (f) Instrument setpoint temp =

0 °C. (g) Instrument setpoint temp = +10 °C. (h) Instrument setpoint temp = +20 °C.

3-8) Schematic of the best-fit lines and residuals calculated for (Bplanet - Bspace) vs (Vplanet - Vspace).

3-9) Y-axis offset (radiance W cm^{-2} str^{-1} cm^{-1}). (a) Space_before only case. (b) Space before_mini case. V in units of TES Numbers (TN).

3-10) X-axis residuals (radiance W cm^{-2} str^{-1} cm^{-1}). Data for detector 2, all seven blackbody temperatures for instrument setpoint temperature of 0 °C.

3-11) Schematic showing the comparison of x- and y-axis residuals discuss in text.

3-12) Comparison of x-axis (irradinace W cm^{-2} cm^{-1}) residual for the 130 K planet blackbody with the difference between blackbodies at -146 and -143.5 °C.

3-13) Raw spectral data for detector 2 for all seven blackbody temperatures for instrument setpoint temperature of 0 °C. Spectral data in units of TES Numbers (TN).

3-14) Reference surface emissivity. (a) Single scan, all five good detectors with average for tvk22 - ICKs 199-214 (imc off set). (b) Single scan, all five good detectors with average - ICKs 703-718 (imc on set). (c) Double scan, all five good detectors with average for tvk22 - ICKs 435-465 (imc off set). (d) Double scan, all five good detectors with average - ICKs 873-903 (imc on set).

3-15) Derived emissivity of the space blackbody. Derivation method described in text.

3-16) Reference surface emissivity calculated using different reference surface temperatures for instrument setpoint temperature 0 °C. (a) Average of all three reference surface temperatures. (b) Reference surface temperature using thermister 1. (c) Reference surface temperature using thermister 2. (d) Reference surface temperature using thermister 3.

3-17) Reference surface emissivity calculated using different reference surface temperatures for instrument setpoint temperature -10 °C. (a) Average of all three

reference surface temperatures. (b) Reference surface temperature using thermister 1. (c) Reference surface temperature using thermister 2. (d) Reference surface temperature using thermister 3.

3-18) Difference between calcuated and Planck radiance (W cm^{-2} str^{-1} cm^{-1}) for all detectors. T_{inst} = 0 °C, T_{BB} = 270 K, heaters off (test set tvk22).

3-19) Difference between calcuated and Planck radiance (W cm^{-2} str^{-1} cm^{-1}) for detector 2 for all blackbody temperatures for T_{inst} = 0 °C. (a) Summary of all blackbody temperatures. (b-h) Comparison of a "best-fit" fraction of the radiance from a blackbody at the appropriate temperature.

3-20) Brightness temperature (K) derived for each planet blackbody case for T_{inst} = 0°C, detector heaters off.

3-21) Brightness temperature (K) derived for each planet blackbody case for T_{inst} = 0°C, detector heaters on.

3-22) Sigma values (TN) computed for the T_{inst} = 0°C case with spectrometer detector heater off. (a) space target (space1 & 2), (b) reference target (ref1); (c) planet target with imc off; (d) planet target with inc on.

3-23) Sigma values (TN) computed for the T_{inst} = 0°C case with spectrometer detector heater on. (a) space target (space1 & 2), (b) reference target (ref1); (c) planet target with imc off; (d) planet target with inc on.

3-24) Spectrometer gain values. Comparison of the signals from the external planet blackbody at the four gain settings. The instrument setpoint temperature was +30°C, heaters were off, and the planet blackbody temperature was 310 K (test tvn27). Nominal gains of 1, 2.5, 4, and 8 were used in flight software to scale the signal in TN transmitted from the instrument.

3-25) Ratio of gain 2/gain 1, 3/1, and 4/1 for the signals from the reference surface at a temperature of 22.3 °C.

3-26) Illustration of characteristic spectral shape observed in derived reference surface emissivity.

3-27) Time variation in the raw data for wavenumbers 1503.5 and 1608.6 for test tvl22, spectrometer detector heaters on.

3-28) 10-ICK time averages of spectral data for wavenumbers 1503.5 and 1608.6 for test tvl22, spectrometer heaters on.

3-29) Ratio of spectra from ICK 42 and 52 for test tvl22, spectrometer heaters on.

3-30) 10-ICK averages of the time variation in the spectral data for wavenumbers 1503.5 and 1608.6 for test tvk22, spectrometer detector heaters off.

3-31) Ratio of the raw spectral data for ICKs 62, 102, 122, and 152 relative to ICK 42 for test tvk22, spectrometer detector heaters off.

3-32) Comparison of the 10 ICK averages for wavenumber 1503 for test tvl22, heaters on. (a) detectors 2 and 3; (b) detectors 2 and 5.

4-1) Time history of instrument response. Calculated assuming instrument temperature equal to detector temperature. Tests are listed in Table 4-1.

4-2 Instrument response (TN/W cm^{-2} str^{-1} cm^{-1}). (a) All tests prior to GE thermal vacuum. (b) All tests during and after GE thermal vacuum.

4-3 Instrument response (TN/W cm^{-2} str^{-1} cm^{-1}). (a) All tests prior to GE thermal vacuum. (b) All tests during and after GE thermal vacuum.

5-1) Temperature Dependence of Bolometer Channel Responsivities

5-2) Ratio of Radiance Error at Each Planet Temperature

5-3) Ratio of Radiance Difference to the Radiance at 270K, for +30C Instrument Temperature

5-4) Ratio of Radiance Difference to the Radiance at 270K, for +20C Instrument Temperature

5-5) Ratio of Radiance Difference to the Radiance at 270K, for +10C Instrument Temperature

5-6) Ratio of Radiance Difference to the Radiance at 270K, for +0C Instrument Temperature

5-7) Ratio of Radiance Difference to the Radiance at 270K, for -10C Instrument Temperature

5-8) Ratio of Radiance Difference to the Radiance at 270K, for -20C Instrument Temperature

Drawing 6647

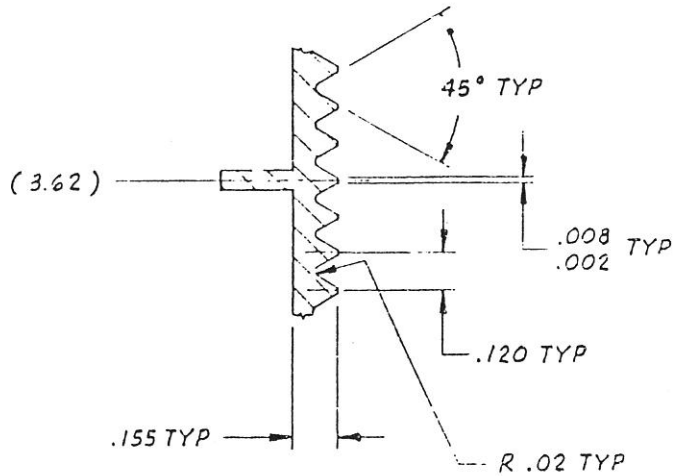

SECTION E-E
SCALE: 4/1

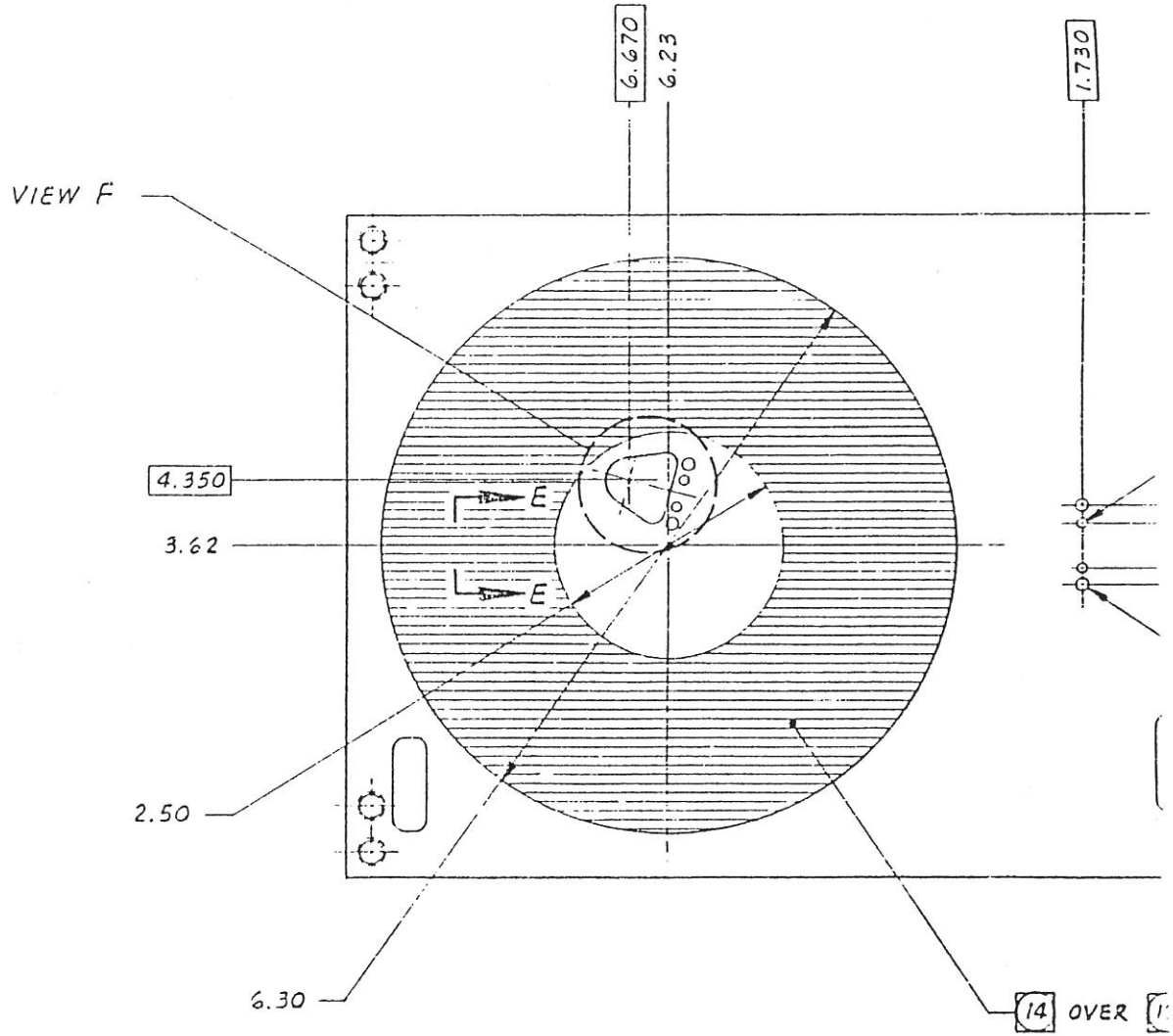

Fig. 11

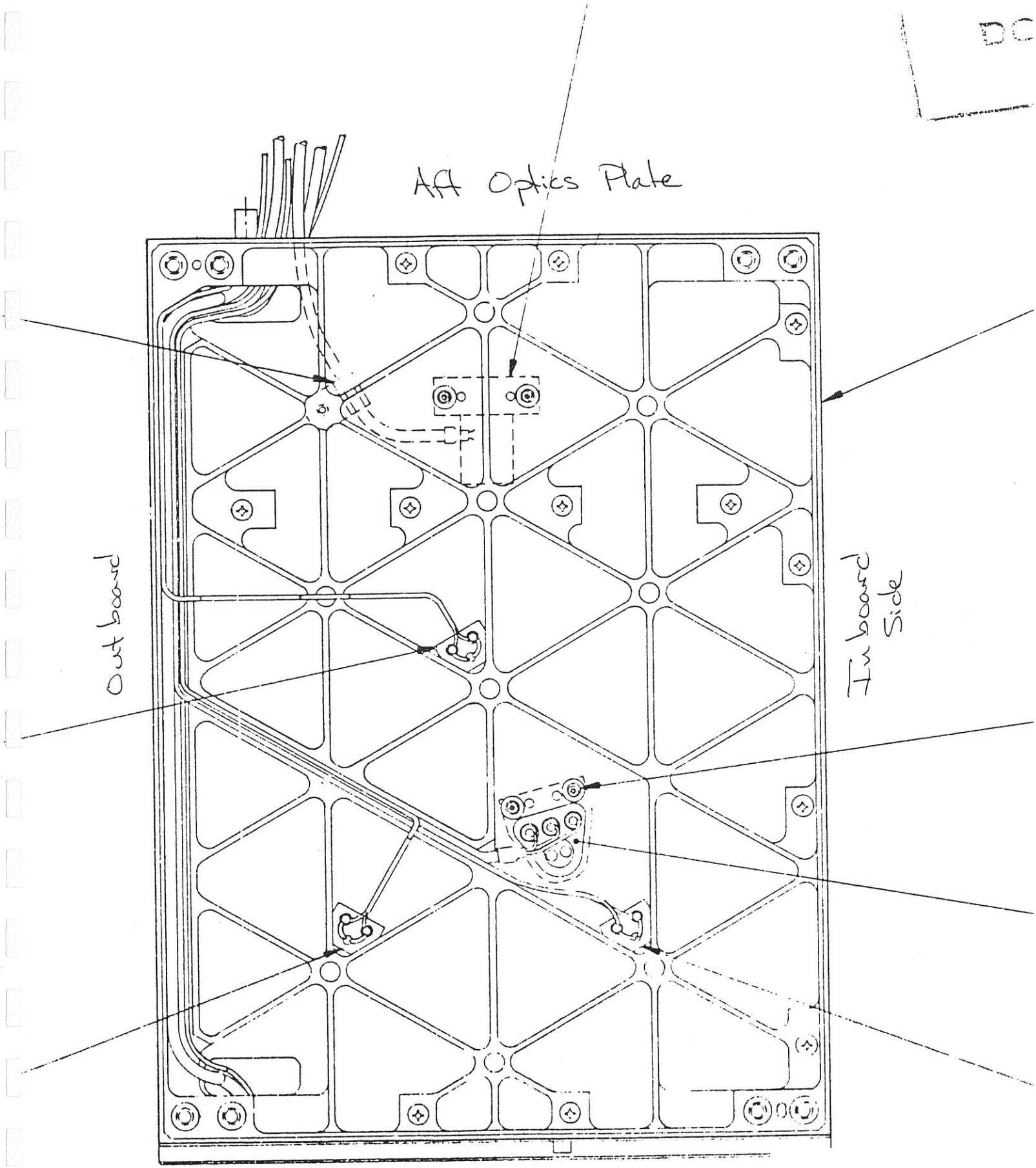

Fig. 1-2

SBRC
Drawing 400367

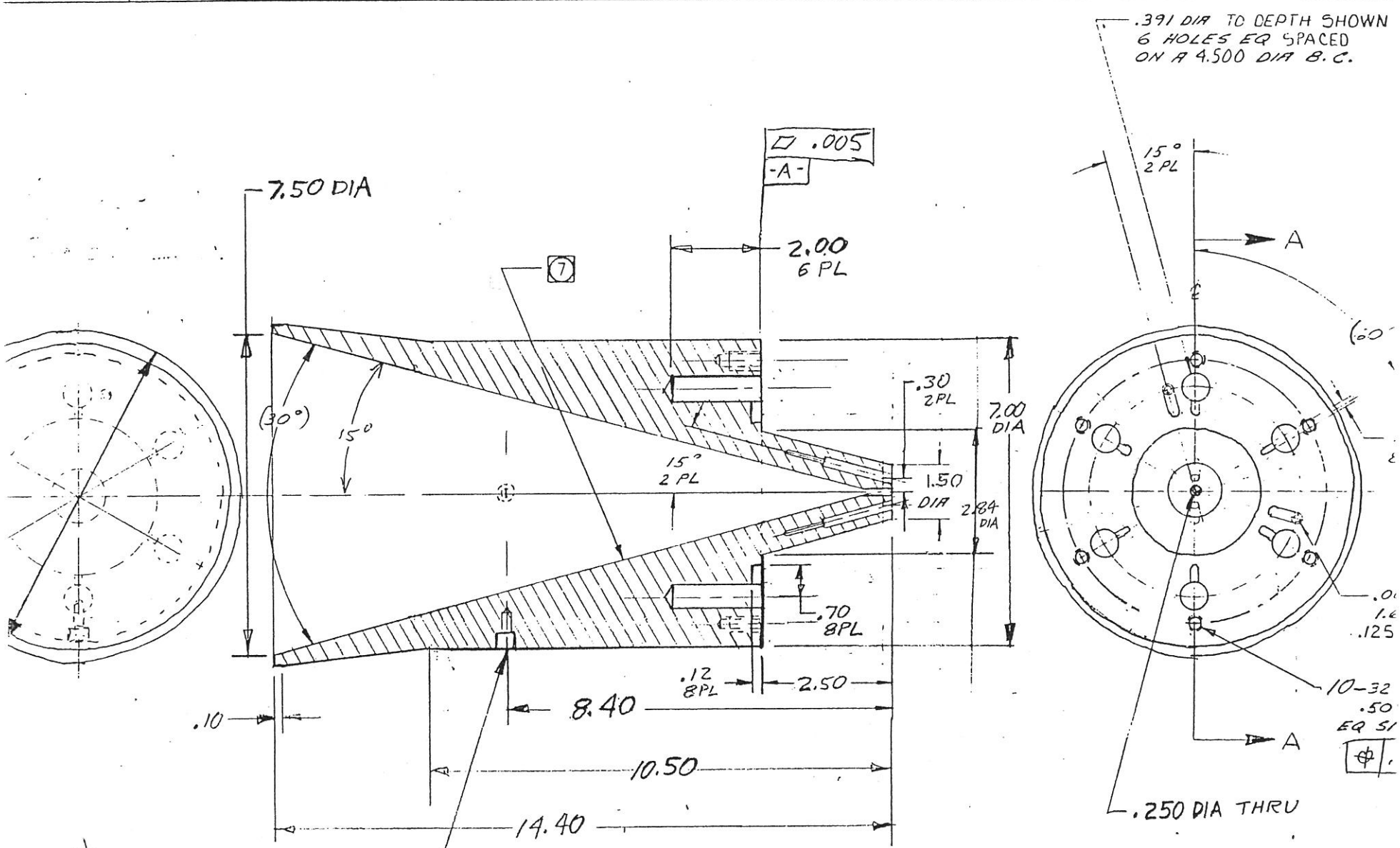

Fig. 1-3a

PRELIMINARY

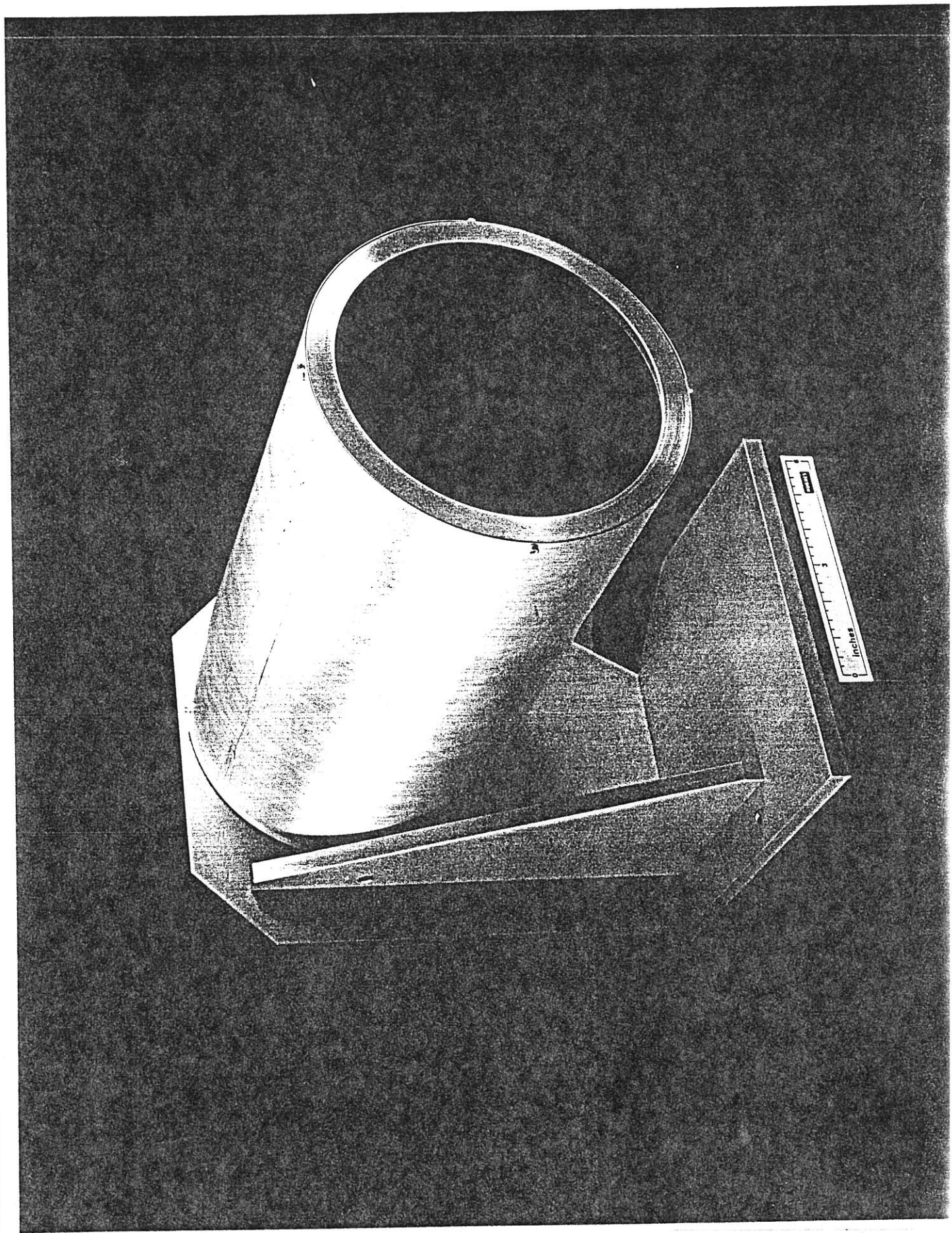

Fig. 1-3b

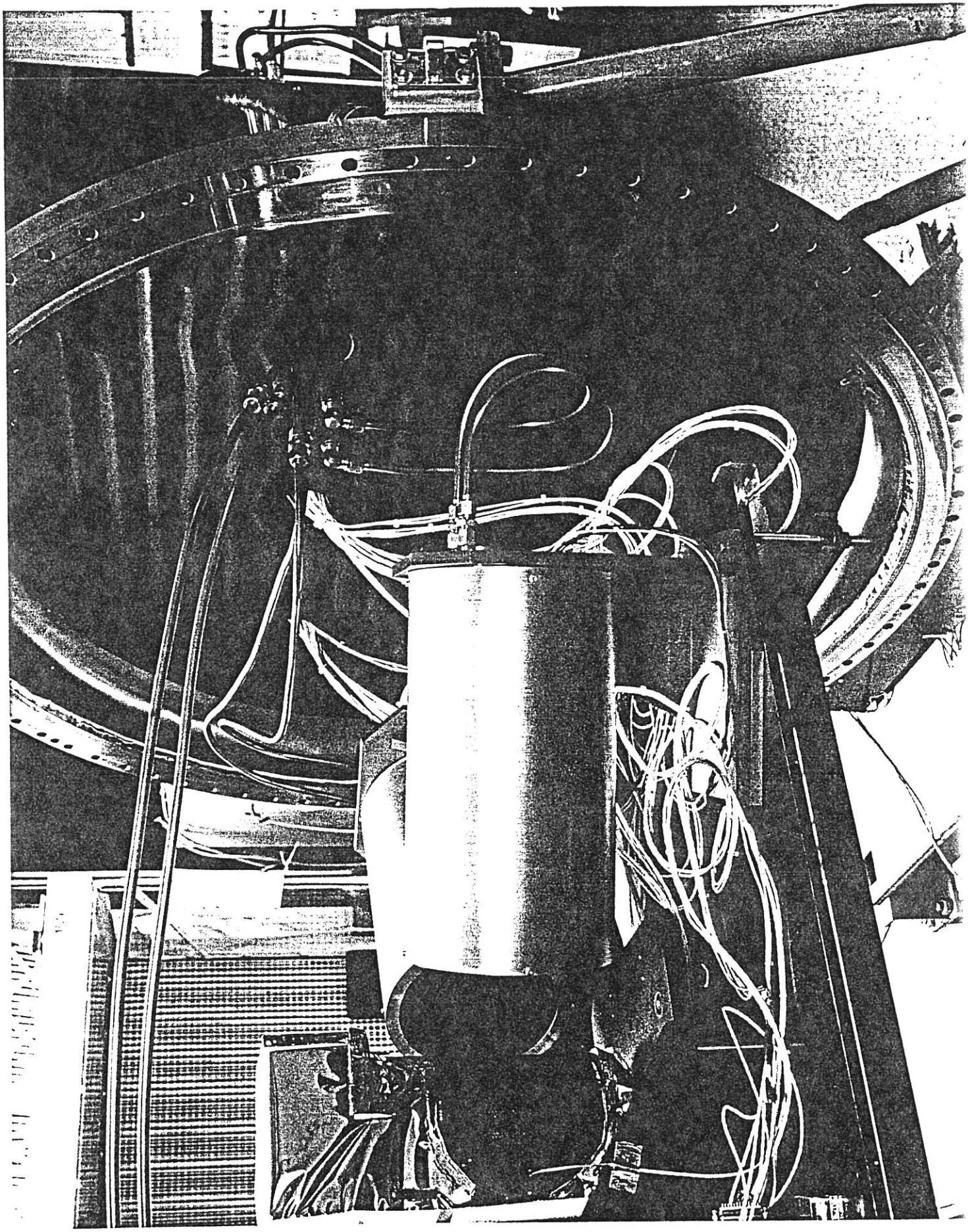

Fig. 1-3c

9/17/92

TES T/V Test Profile (Actual)
Instrument Temperature (°C)
40
30
20
10
0
-10
-20
Elapsed Time From 9/13/91 (Days)
9/13/91 23:04
10/13/91 23:04
0.00
1.00
2.00
3.00
4.00
5.00
6.00
7.00
8.00
9.00
10.00
11.00
12.00
13.00
14.00
15.00
16.00
17.00
18.00
19.00
20.00
21.00
22.00
23.00
24.00
25.00
26.00
27.00
28.00
29.00
30.00
Ambient
Heaters OFF
ICE Problem
Heaters OFF
Ambient
Heaters ON
Heater Debug
Heaters ON
Heaters ON
Heaters ON
Heaters ON
Heaters ON
Heaters ON
Heaters ON
Heaters OFF
Heaters ON
Heaters OFF
Heaters OFF
Thermal Balance Test
Heaters OFF
Heaters OFF
Heaters OFF
Heaters ON
Heater Debug
Thermal Balance Test
Heater Debug
Heaters OFF
Heaters ON
Heaters OFF

Fig. 1-4

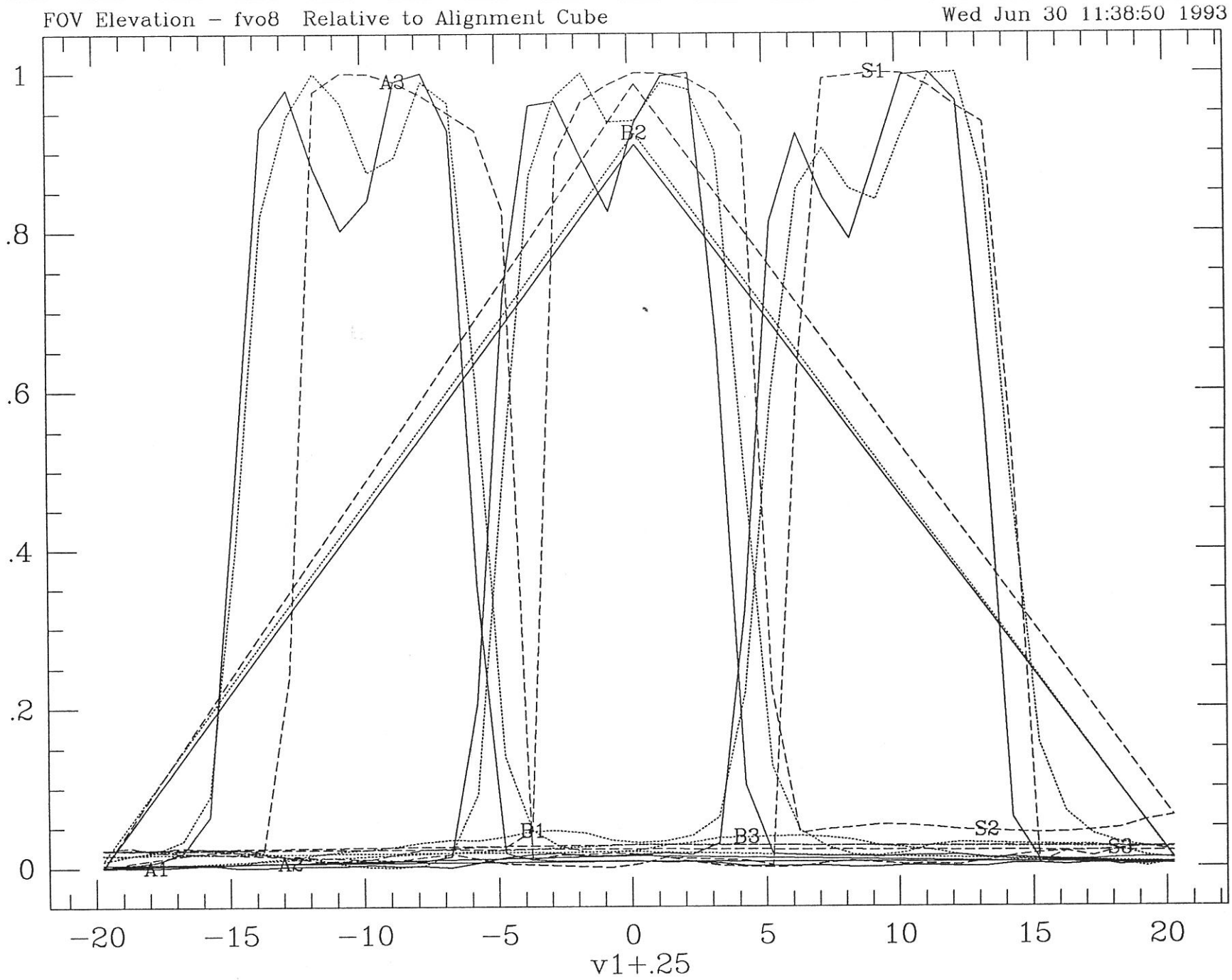
FOV Elevation – fvo8 Relative to Alignment Cube
Wed Jun 30 11:38:50 1993
1
.8
.6
.4
.2
0
A3
S1
B2
B1
B3
S2
S3
A1
A2
−20
−15
−10
−5
0
5
10
15
20
v1+.25

Fig. 2-1A

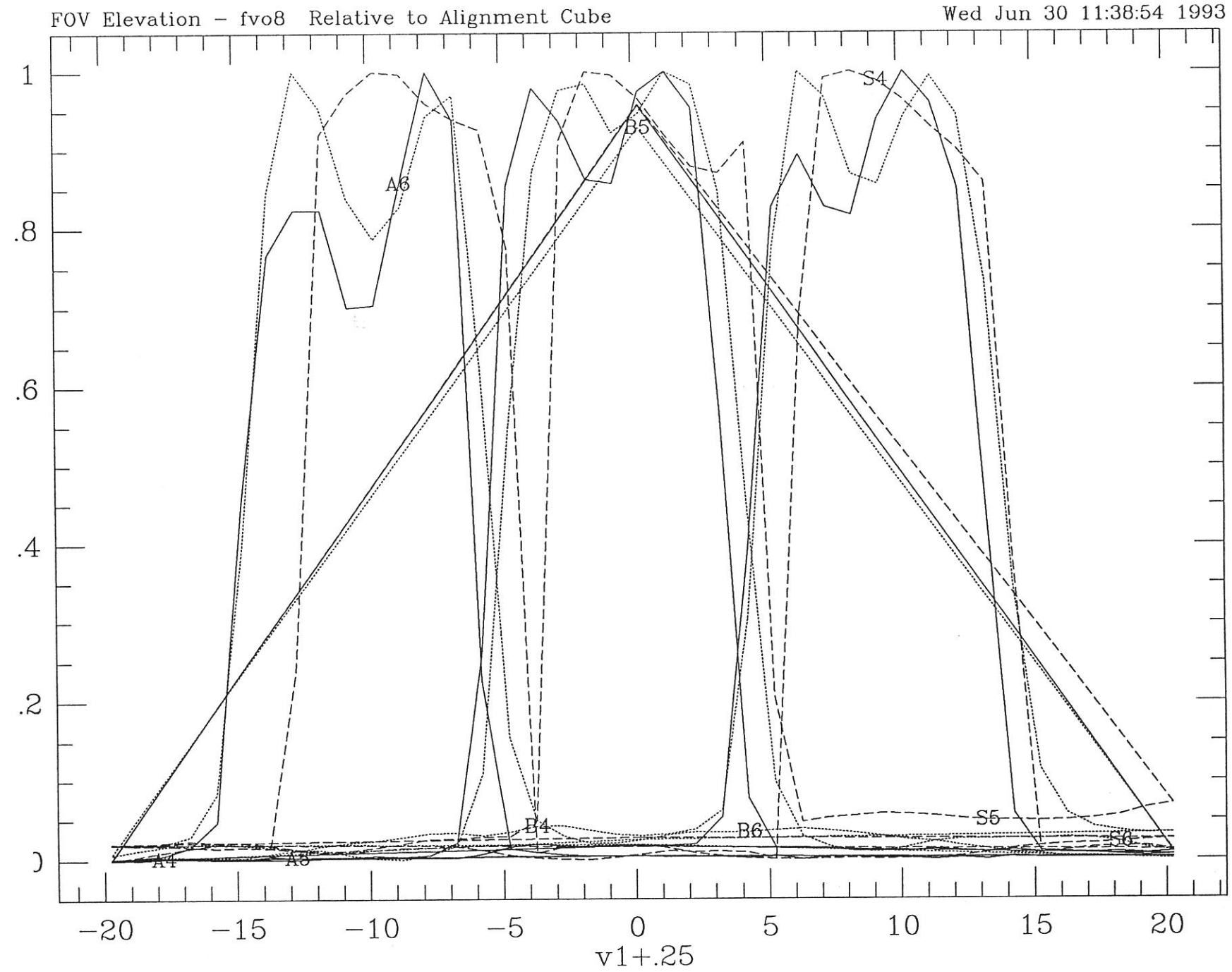
FOV Elevation – fvo8 Relative to Alignment Cube
Wed Jun 30 11:38:54 1993
1
.8
.6
.4
.2
0
A6
B5
S4
S5
S6
B4
B6
A4
A5
−20
−15
−10
−5
0
5
10
15
20
v1+.25

Fig. 2-6

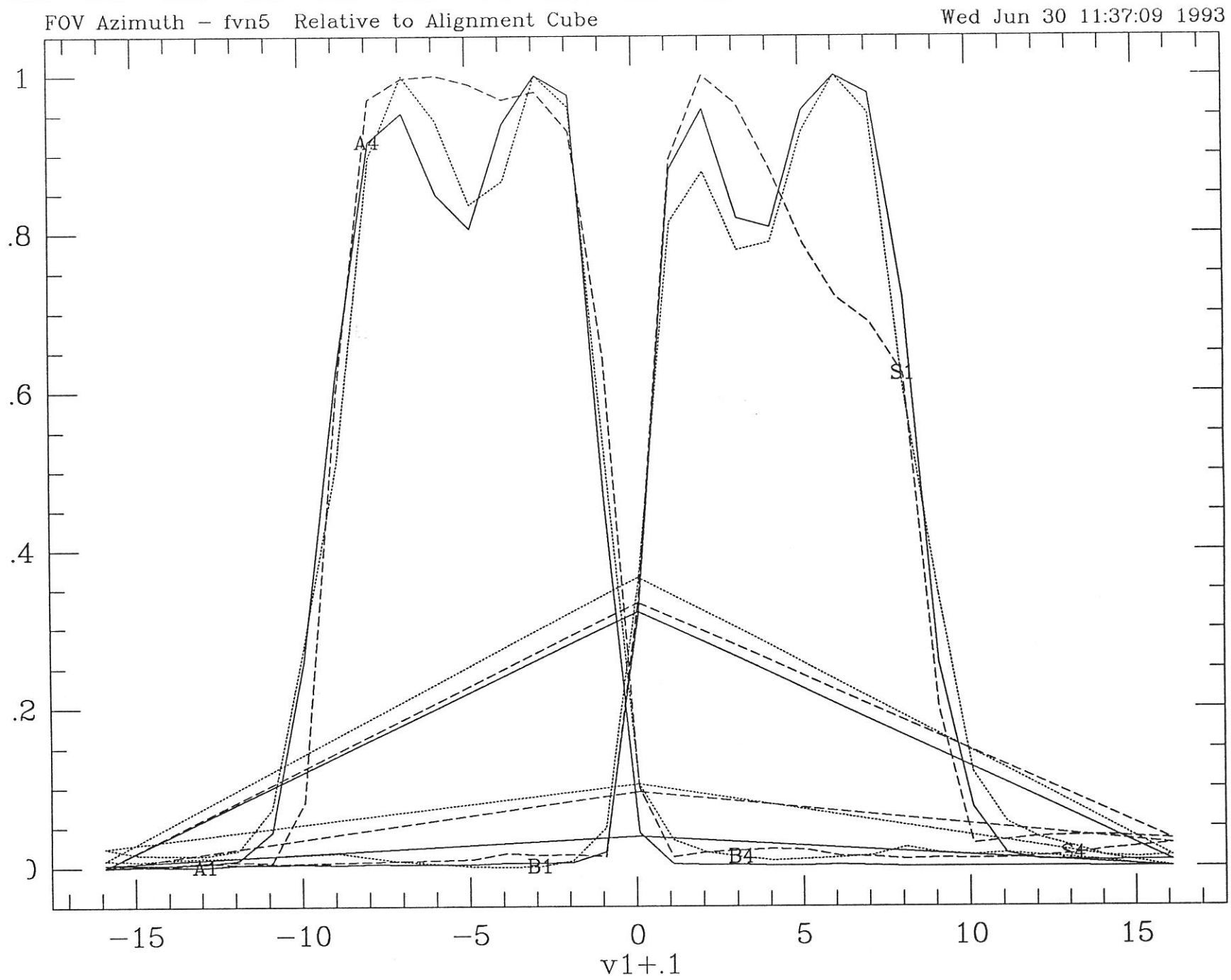
FOV Azimuth – fvn5 Relative to Alignment Cube
Wed Jun 30 11:37:09 1993
1
.8
.6
.4
.2
0
A4
S1
A1
B1
B4
S4
−15
−10
−5
0
5
10
15
v1+.1

Fig. 2-29

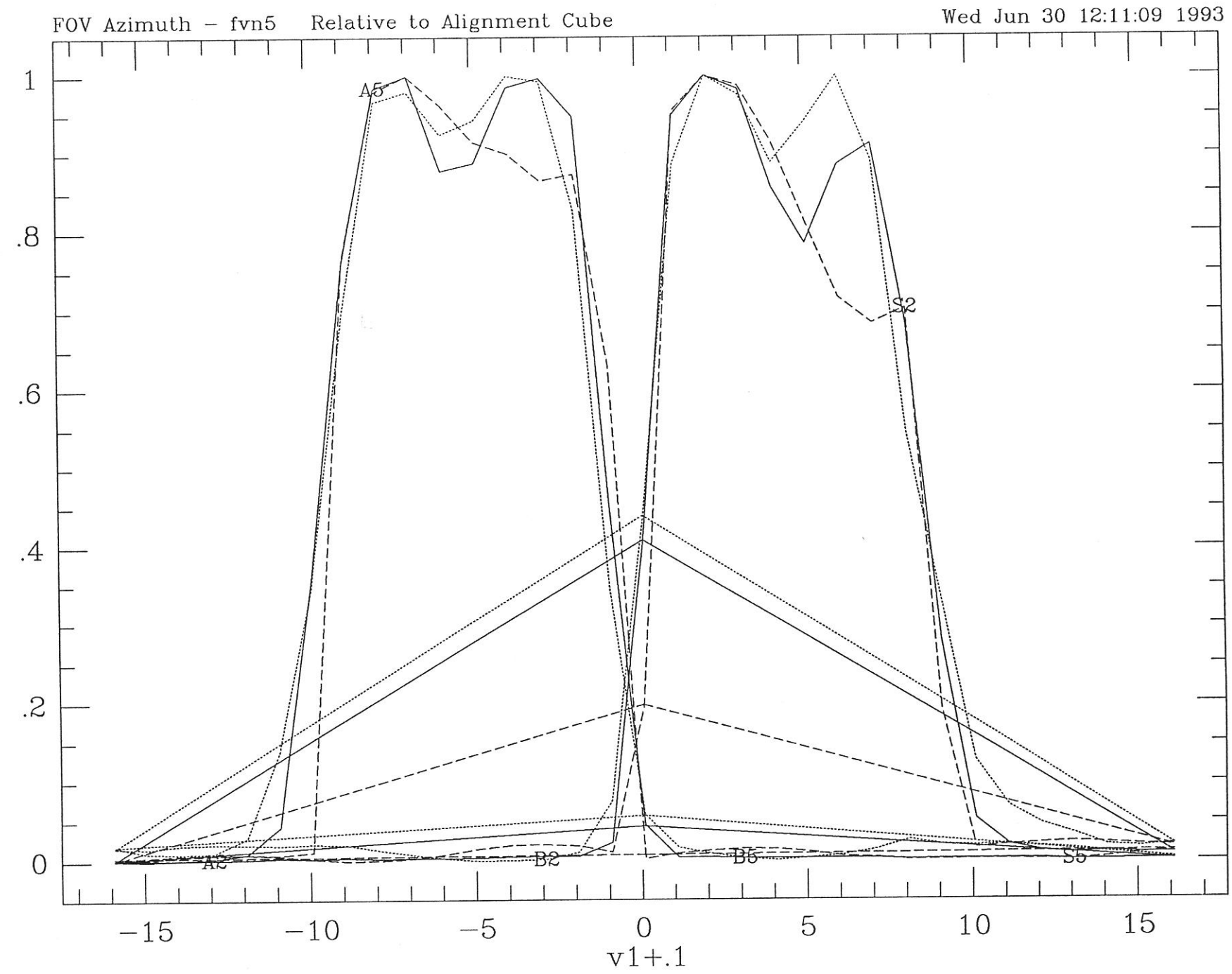
FOV Azimuth – fvn5 Relative to Alignment Cube
Wed Jun 30 12:11:09 1993
1
.8
.6
.4
.2
0
A5
S2
A2
B2
B5
S5
−15
−10
−5
0
5
10
15
v1+.1

Fig. 2-26

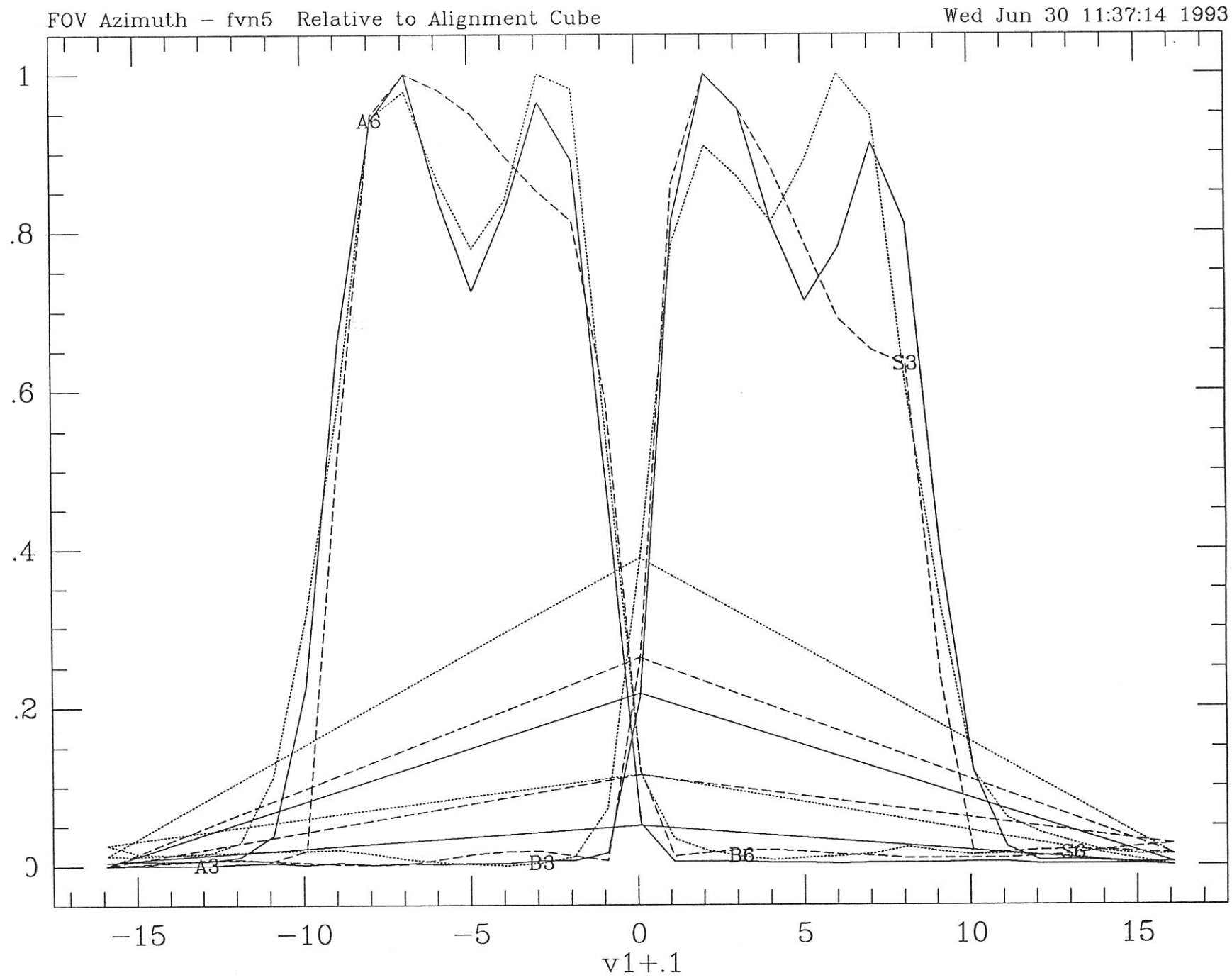
FOV Azimuth – fvn5 Relative to Alignment Cube
Wed Jun 30 11:37:14 1993
1
.8
.6
.4
.2
0
A6
S3
A3
B3
B6
S6
−15
−10
−5
0
5
10
15
v1+.1

Fig. 2-2c

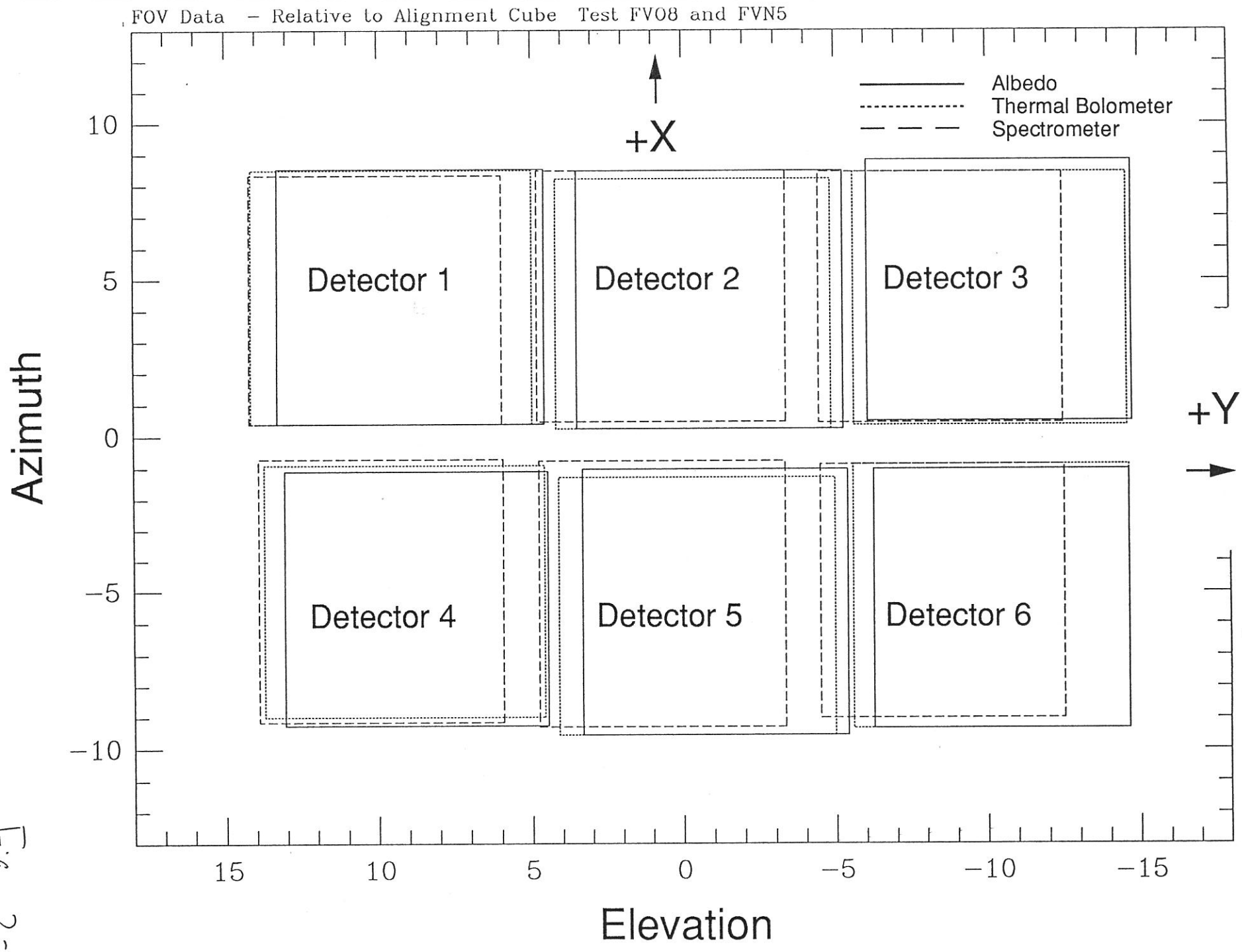
FOV Data – Relative to Alignment Cube Test FV08 and FVN5
Albedo
Thermal Bolometer
Spectrometer
+X
+Y
Detector 1
Detector 2
Detector 3
Detector 4
Detector 5
Detector 6
Azimuth
Elevation
10
5
0
−5
−10
15
10
5
0
−5
−10
−15

Fig. 2-3

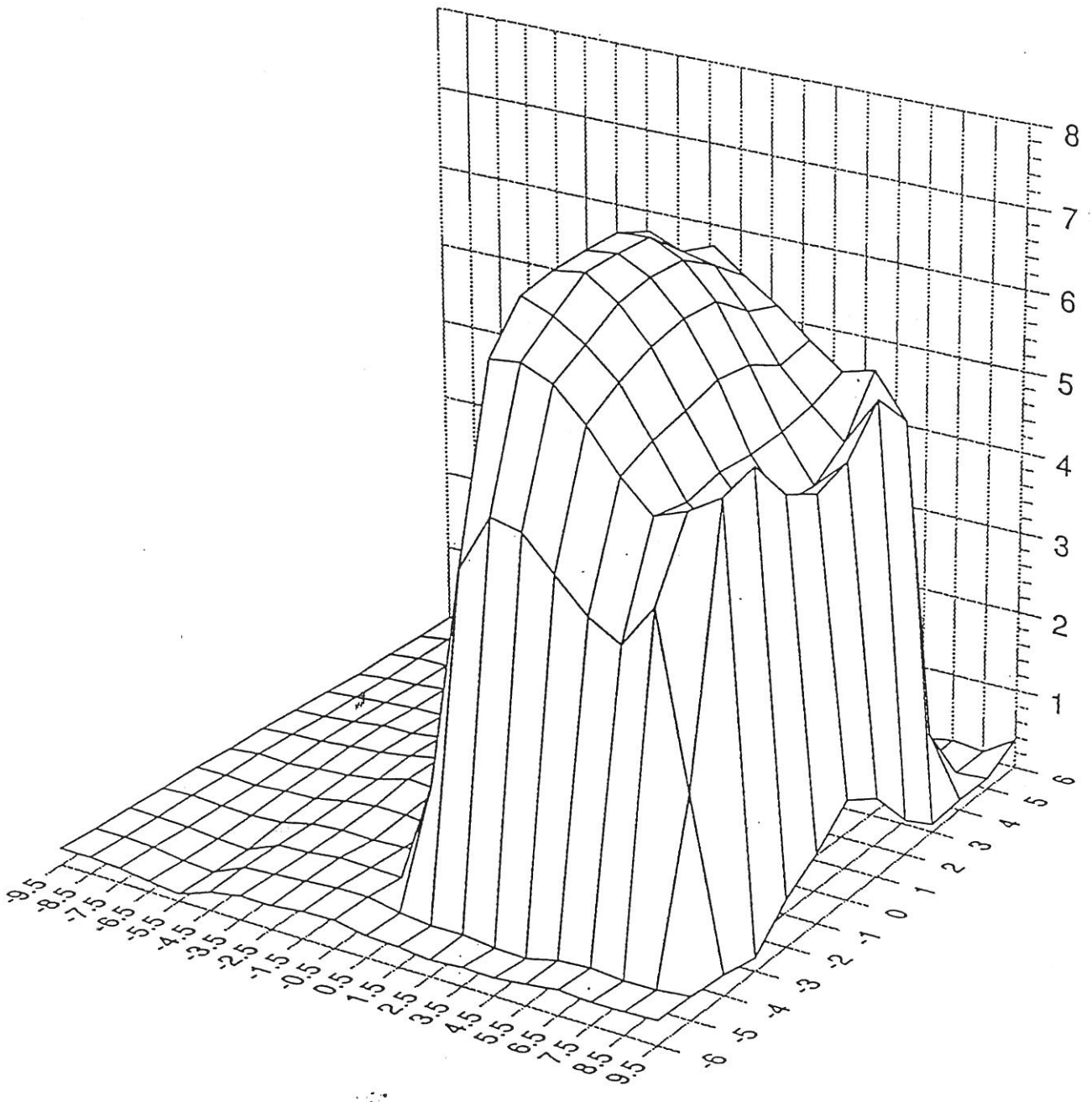
8
7
6
5
4
3
2
1
-9.5 -8.5 -7.5 -6.5 -5.5 -4.5 -3.5 -2.5 -1.5 -0.5 0.5 1.5 2.5 3.5 4.5 5.5 6.5 7.5 8.5 9.5
-6 -5 -4 -3 -2 -1 0 1 2 3 4 5 6

DET#2

Fig. 2-4a

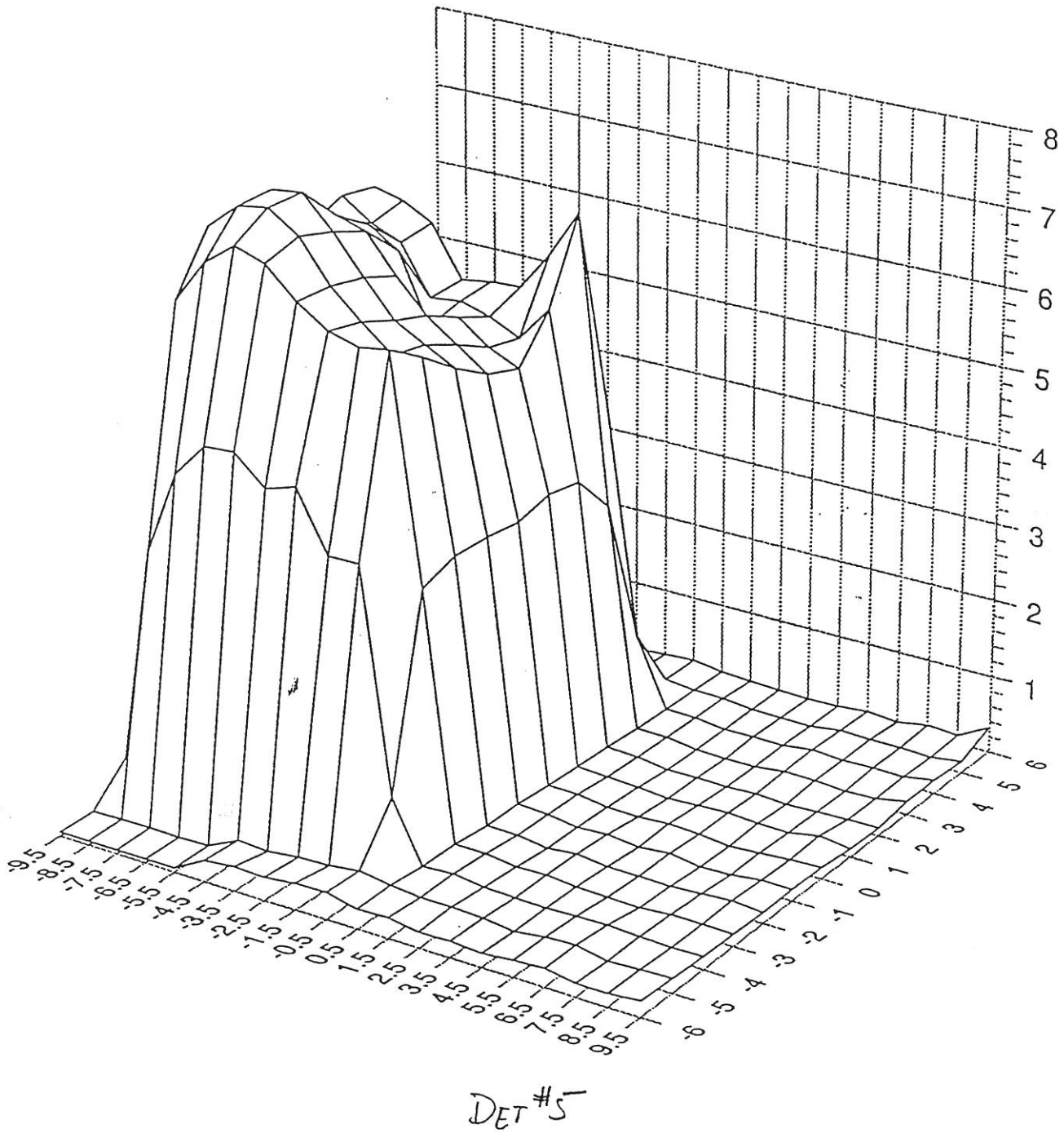
8
7
6
5
4
3
2
1
-9.5 -8.5 -7.5 -6.5 -5.5 -4.5 -3.5 -2.5 -1.5 -0.5 0.5 1.5 2.5 3.5 4.5 5.5 6.5 7.5 8.5 9.5
-6 -5 -4 -3 -2 -1 0 1 2 3 4 5 6

DET #5

Fig. 2-46

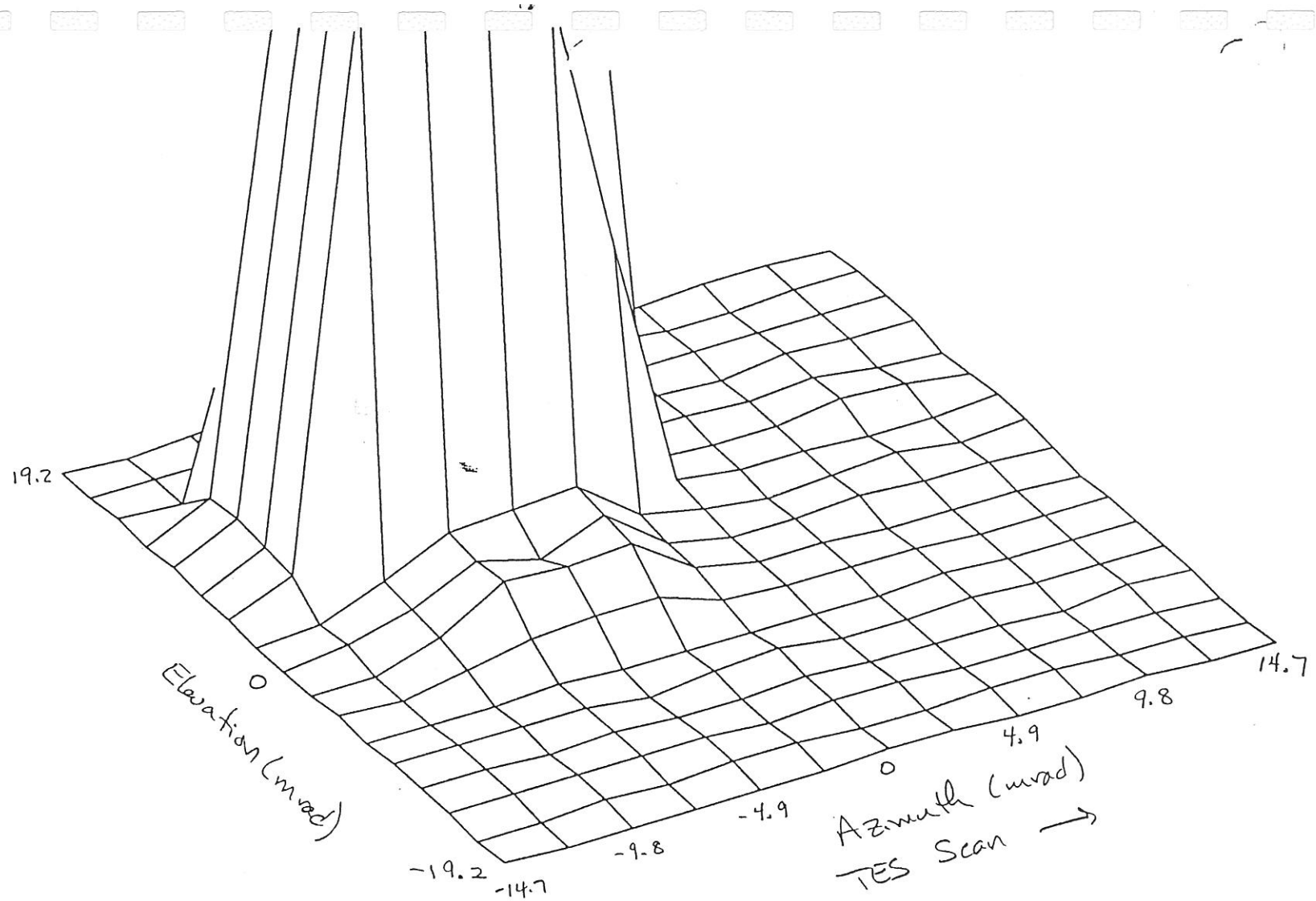

fva: detector 1, alb channel, difference
zscale = 0.05 (plotted 6/3/91)

Fig. 2-5p

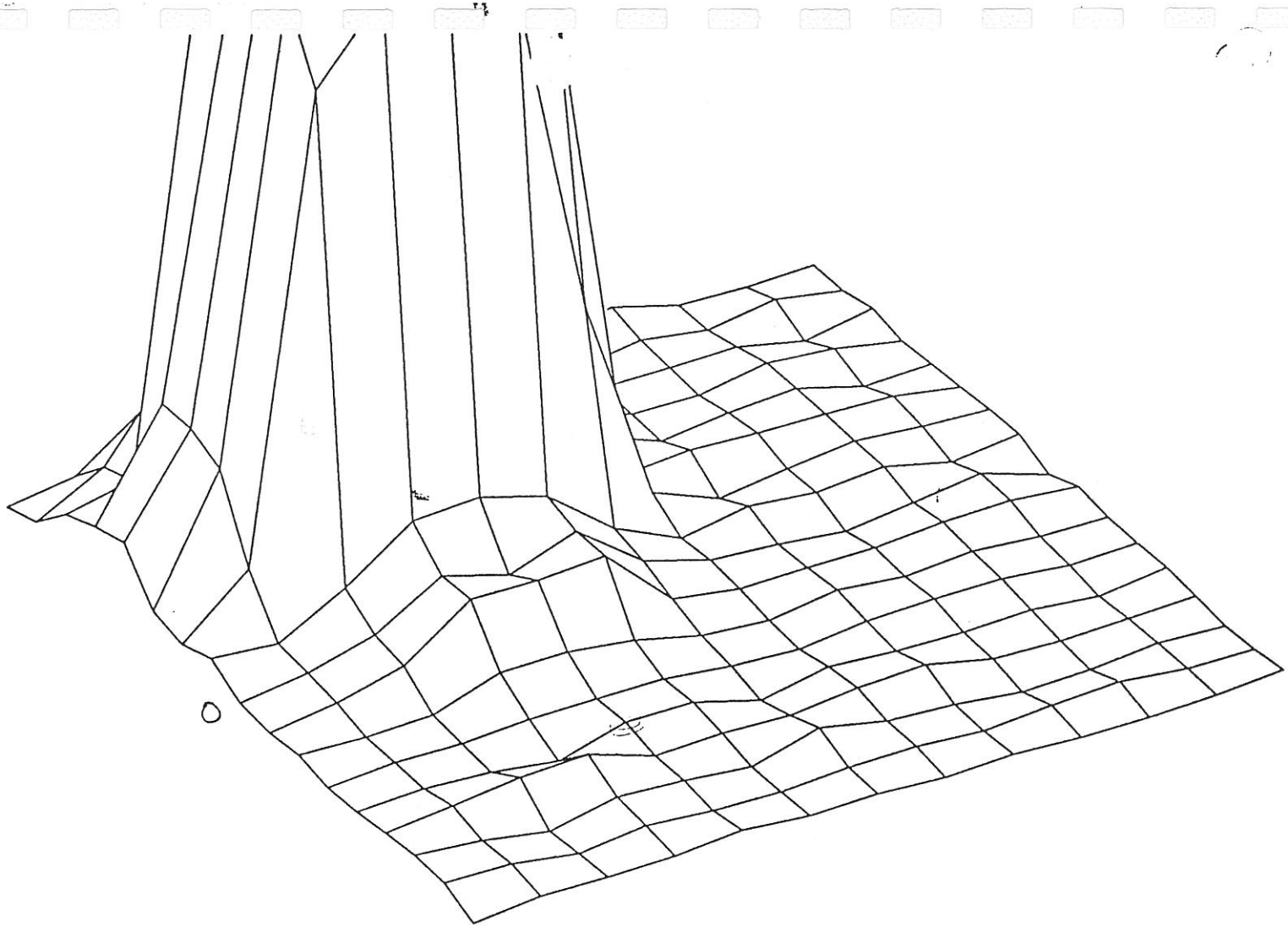

fva: detector 1, bol channel, difference
zscale = 0.2 (plotted 6/3/91)

Fig. 2-50

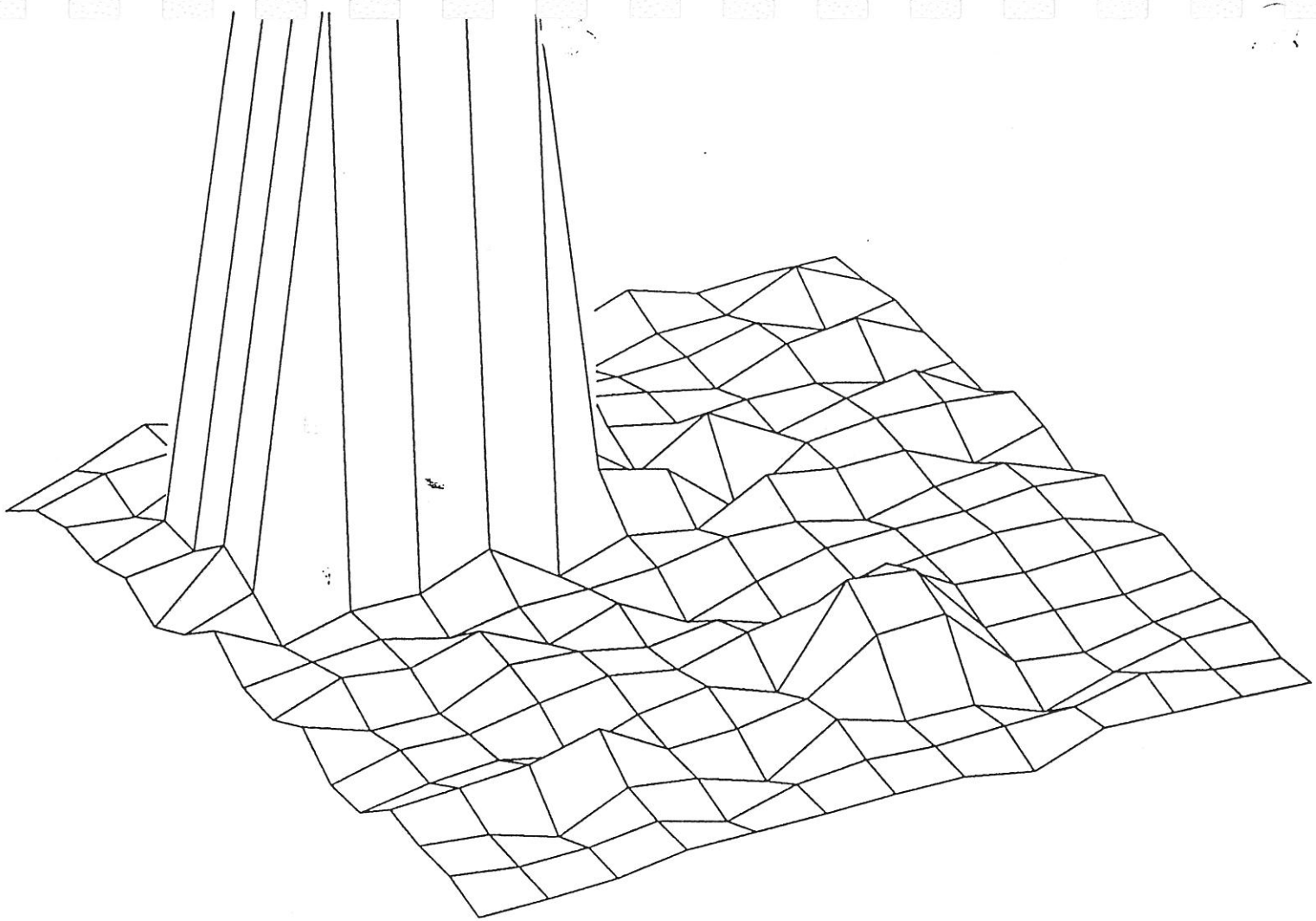

fva: detector 1, pp channel, difference
zscale = .5 (plotted 6/3/91)

Fig. 2-5c

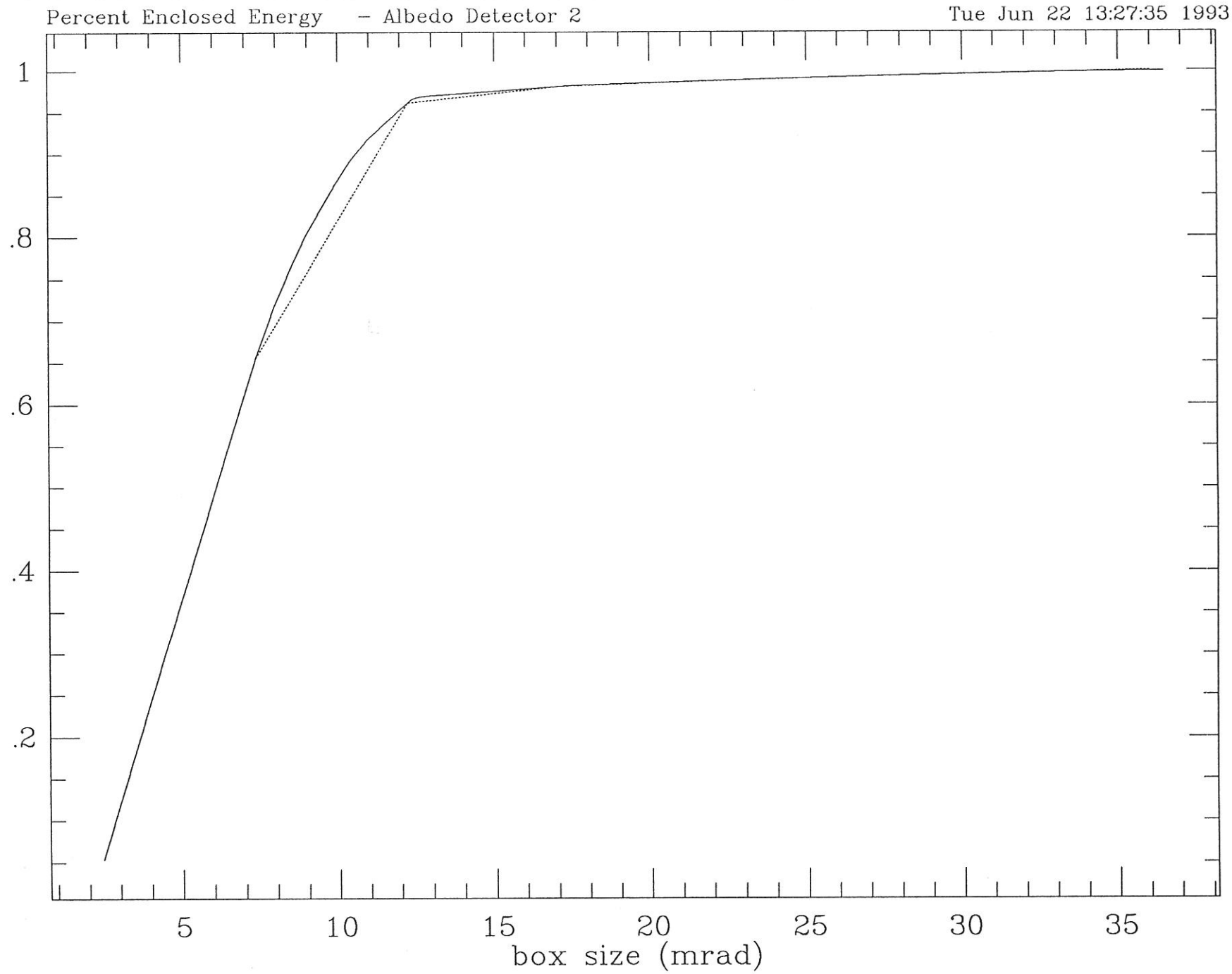
Percent Enclosed Energy - Albedo Detector 2
Tue Jun 22 13:27:35 1993
1
.8
.6
.4
.2
5
10
15
20
25
30
35
box size (mrad)

Fig 3-9

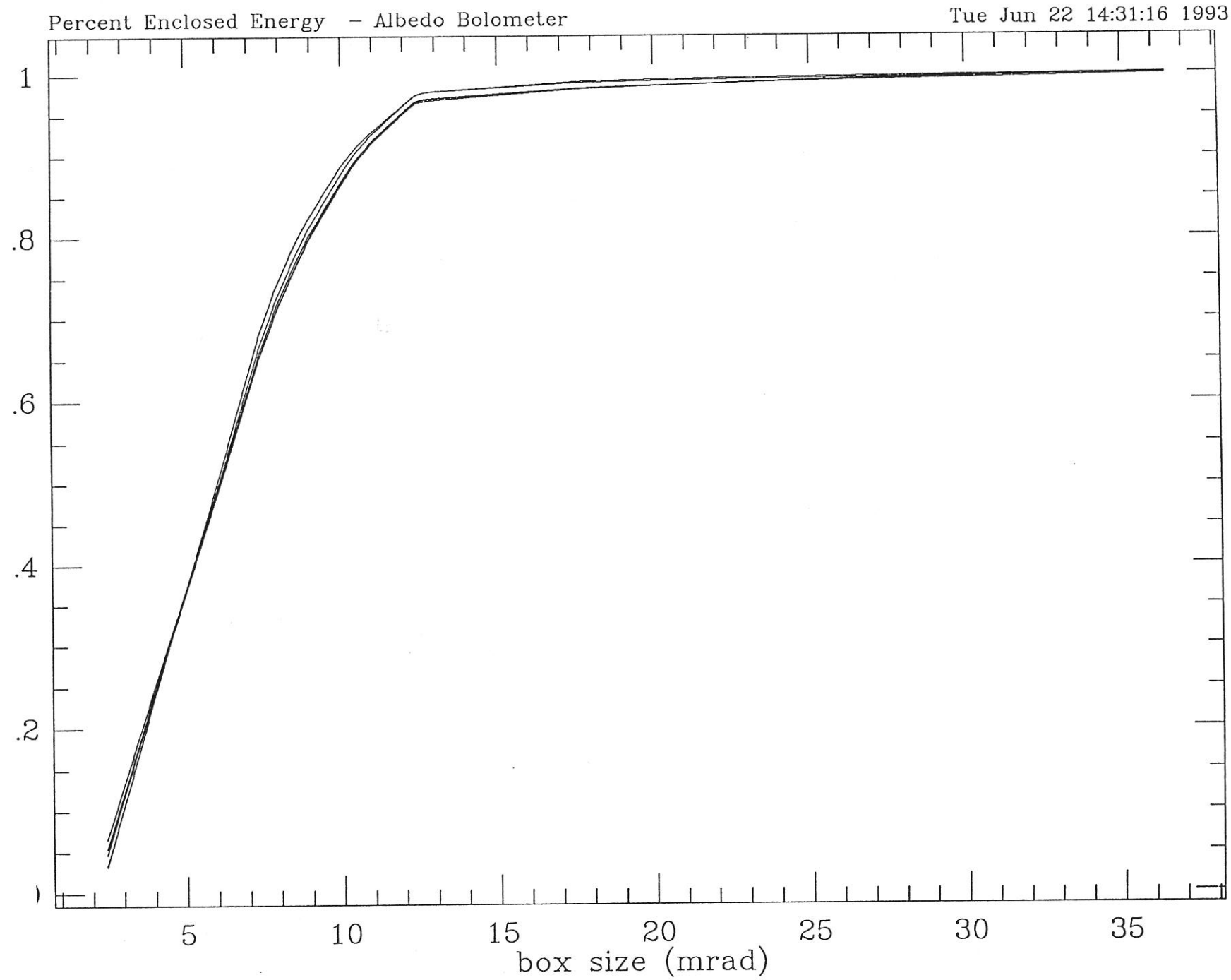
Percent Enclosed Energy – Albedo Bolometer
Tue Jun 22 14:31:16 1993
1
.8
.6
.4
.2
0
5
10
15
20
25
30
35
box size (mrad)

Fig 2-12

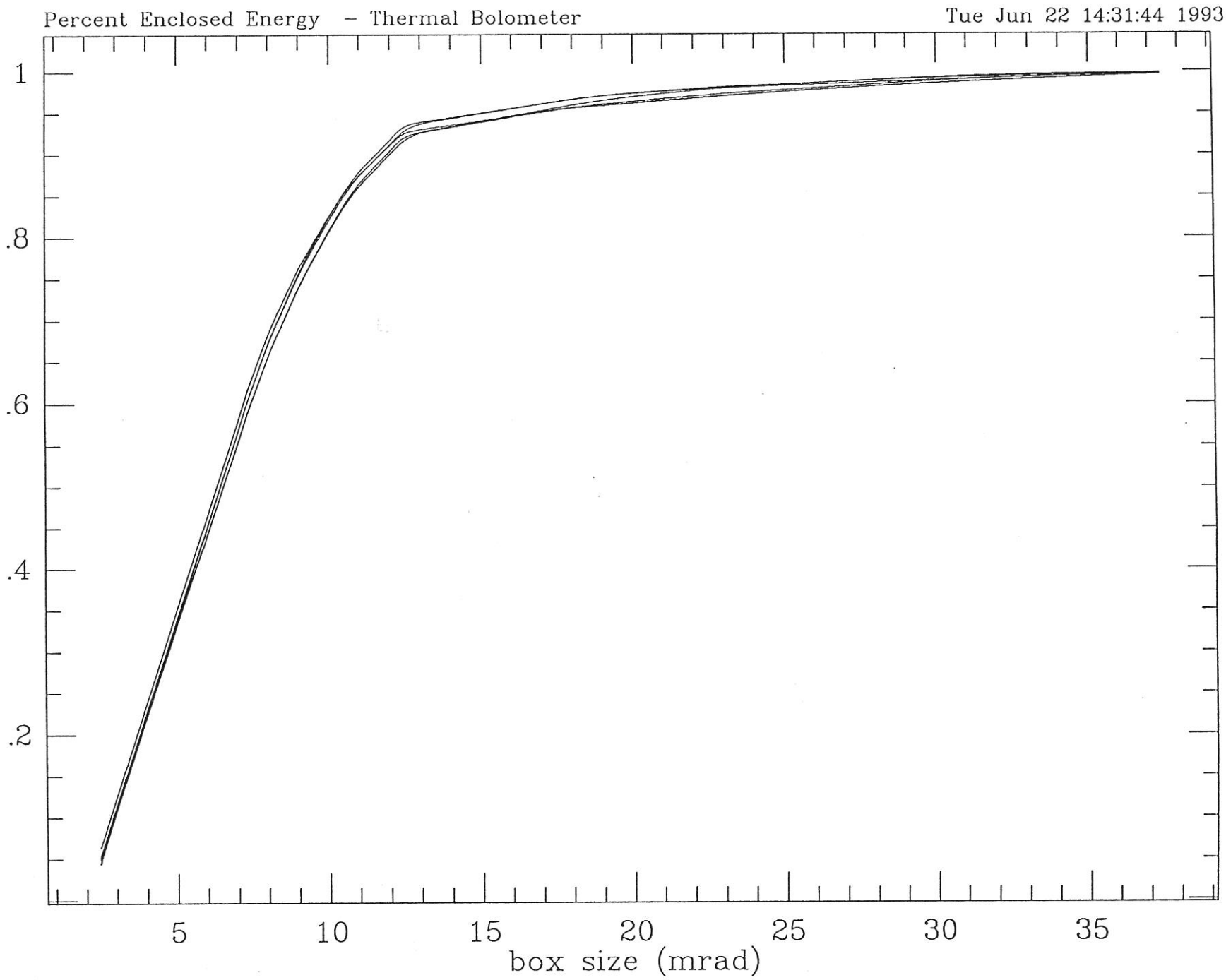
Percent Enclosed Energy – Thermal Bolometer
Tue Jun 22 14:31:44 1993
1
.8
.6
.4
.2
5
10
15
20
25
30
35
box size (mrad)

Fig. 3-16

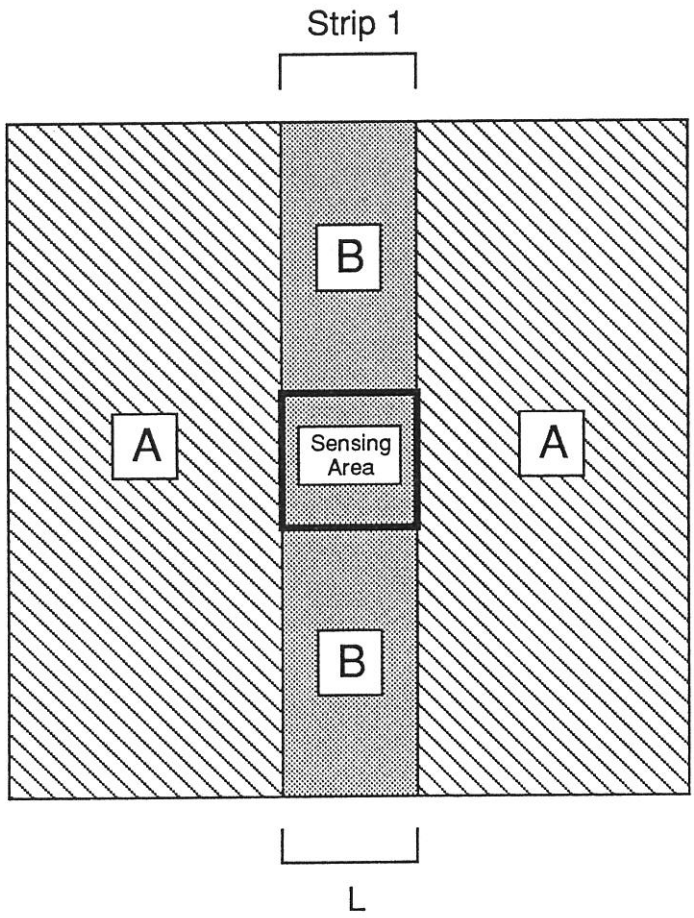
Strip 1
B
A
Sensing Area
A
B
L

(a)

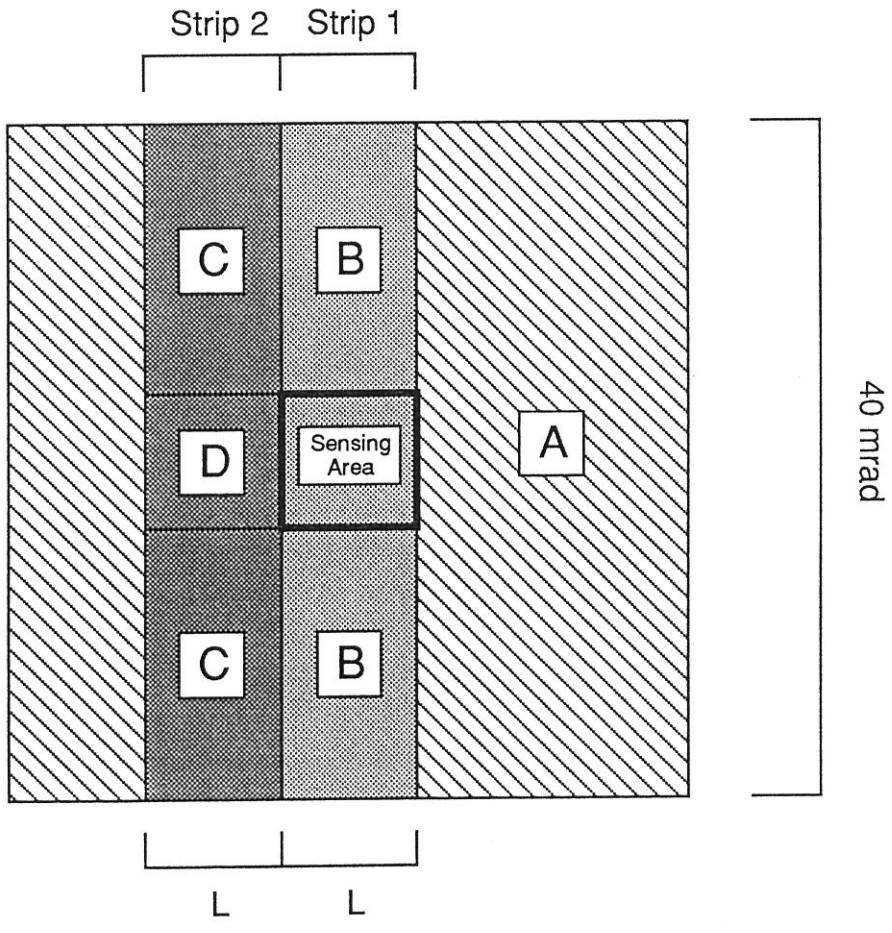
Strip 2
Strip 1
C
B
D
Sensing Area
A
C
B
40 mrad
L
L

(b)

Fig. 2-8

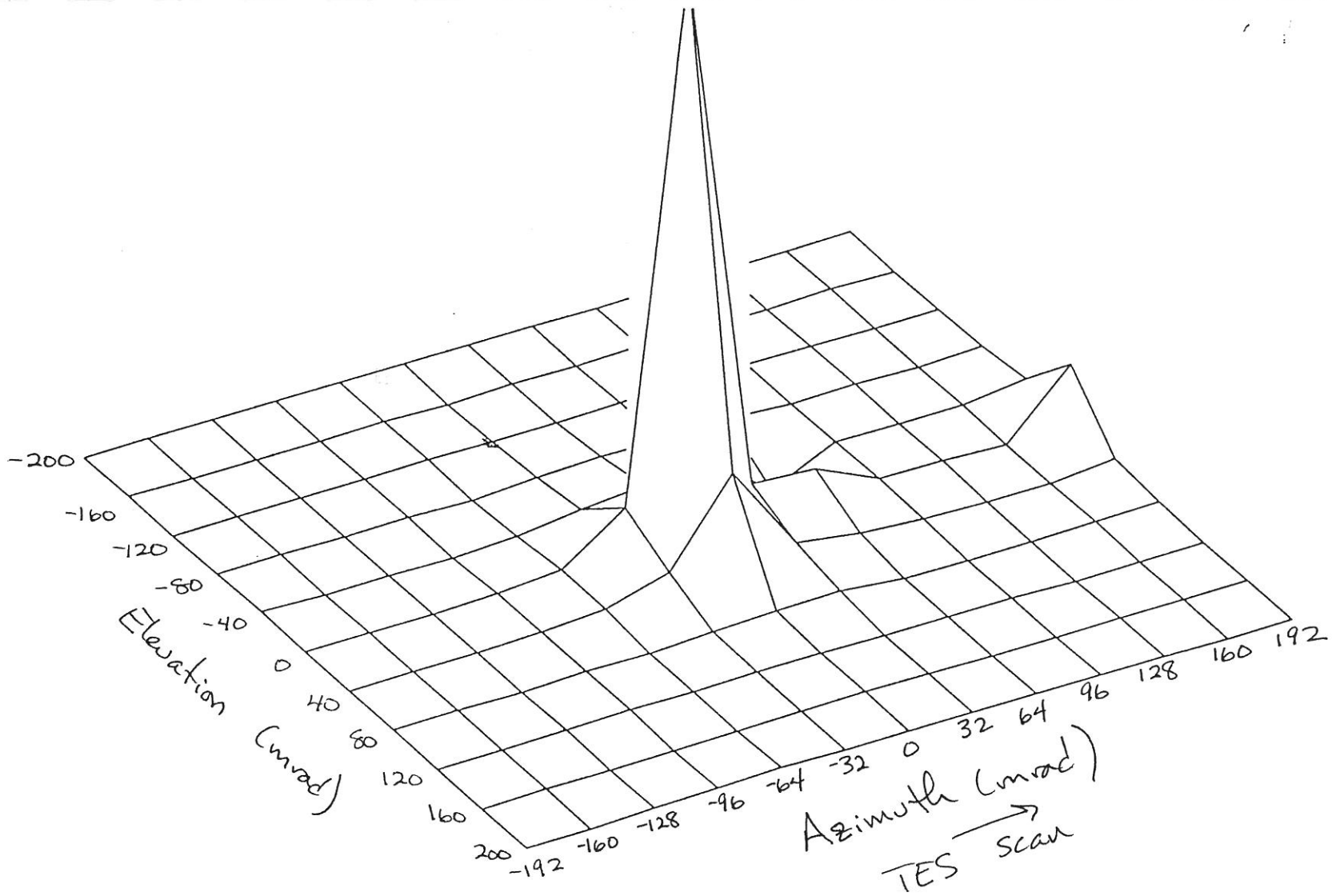

Fig 2-9a

detector 1, alb channel, difference

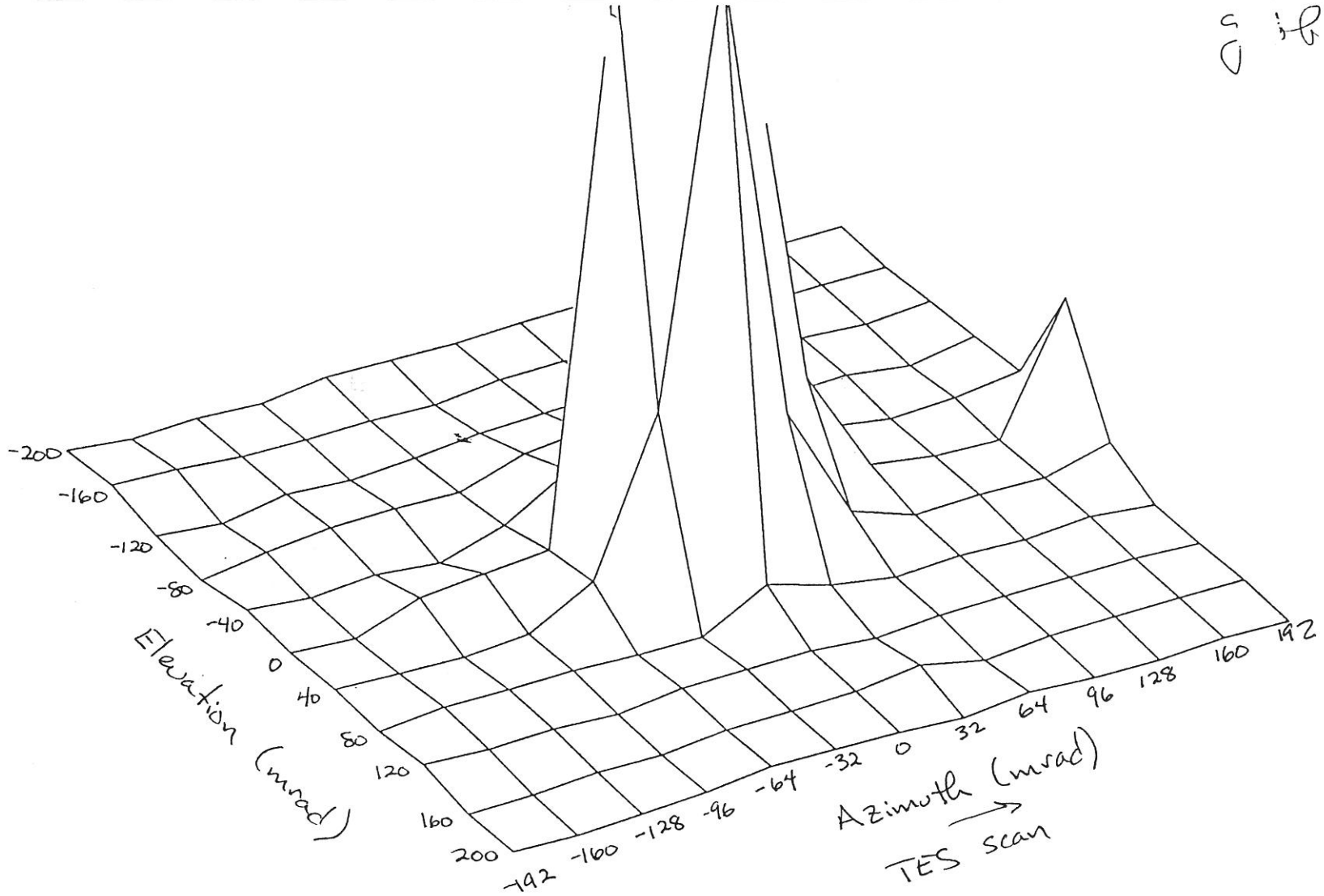

detector 1, bol channel, difference

Fig. 2-9b

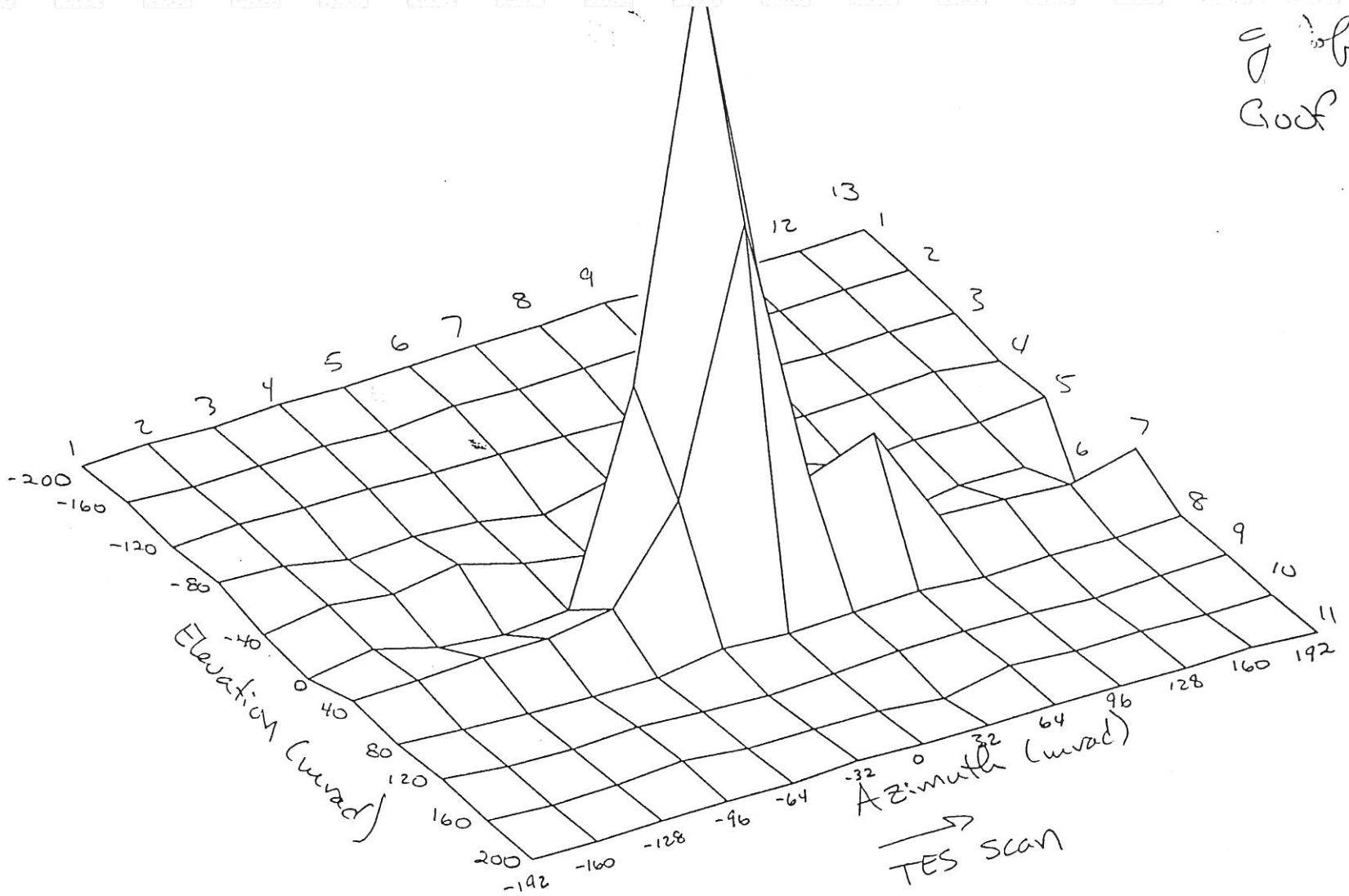

detector 1, spc channel, difference

$R(\lambda) = -8.377 \times 10^{-3} \lambda + 1.0377$

TES.bolo.cal.Exc Chart 5

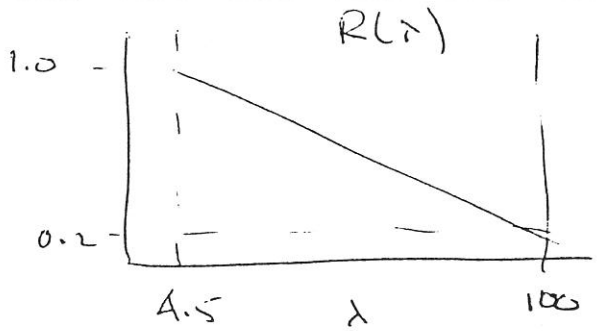

Slope Response Simulation

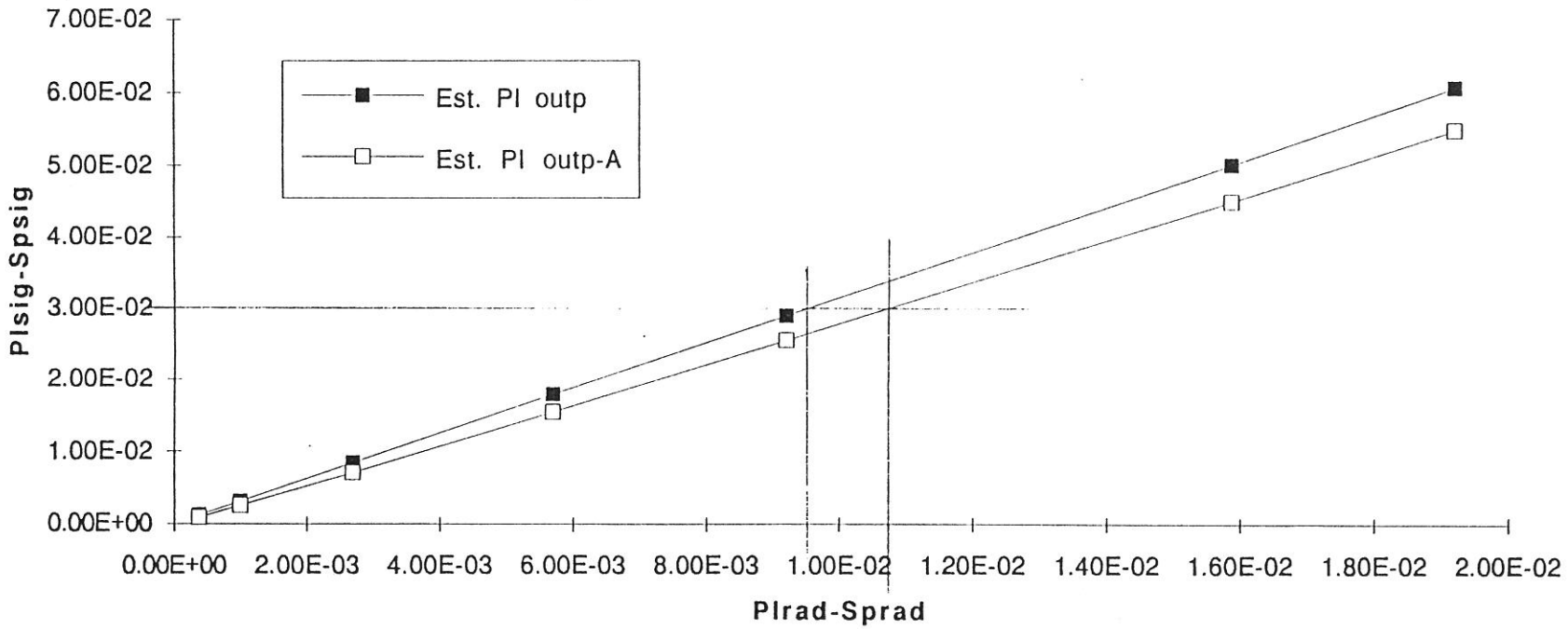

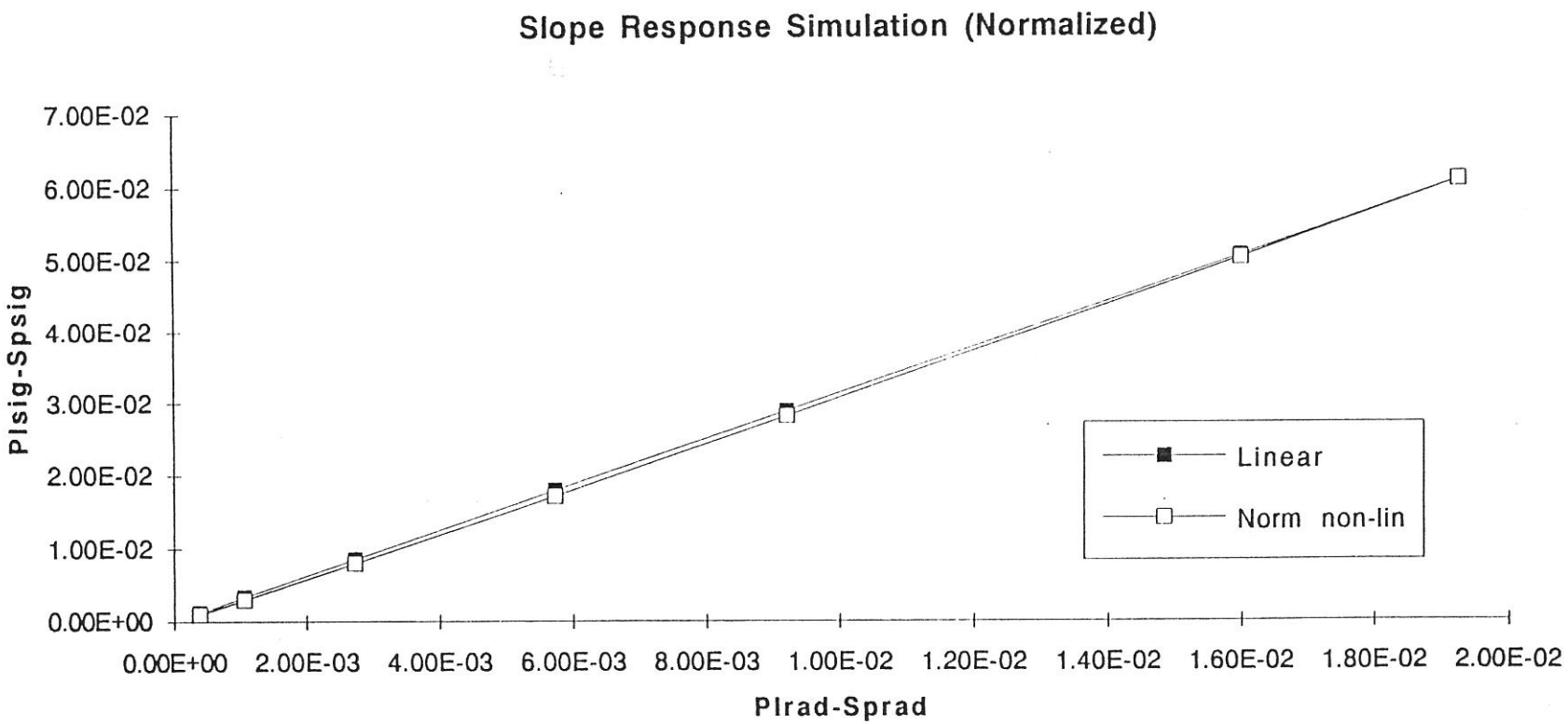
Slope Response Simulation (Normalized)
7.00E-02
6.00E-02
5.00E-02
4.00E-02
3.00E-02
2.00E-02
1.00E-02
0.00E+00
Plsig-Spsig
0.00E+00
2.00E-03
4.00E-03
6.00E-03
8.00E-03
1.00E-02
1.20E-02
1.40E-02
1.60E-02
1.80E-02
2.00E-02
Plrad-Sprad
Linear
Norm non-lin

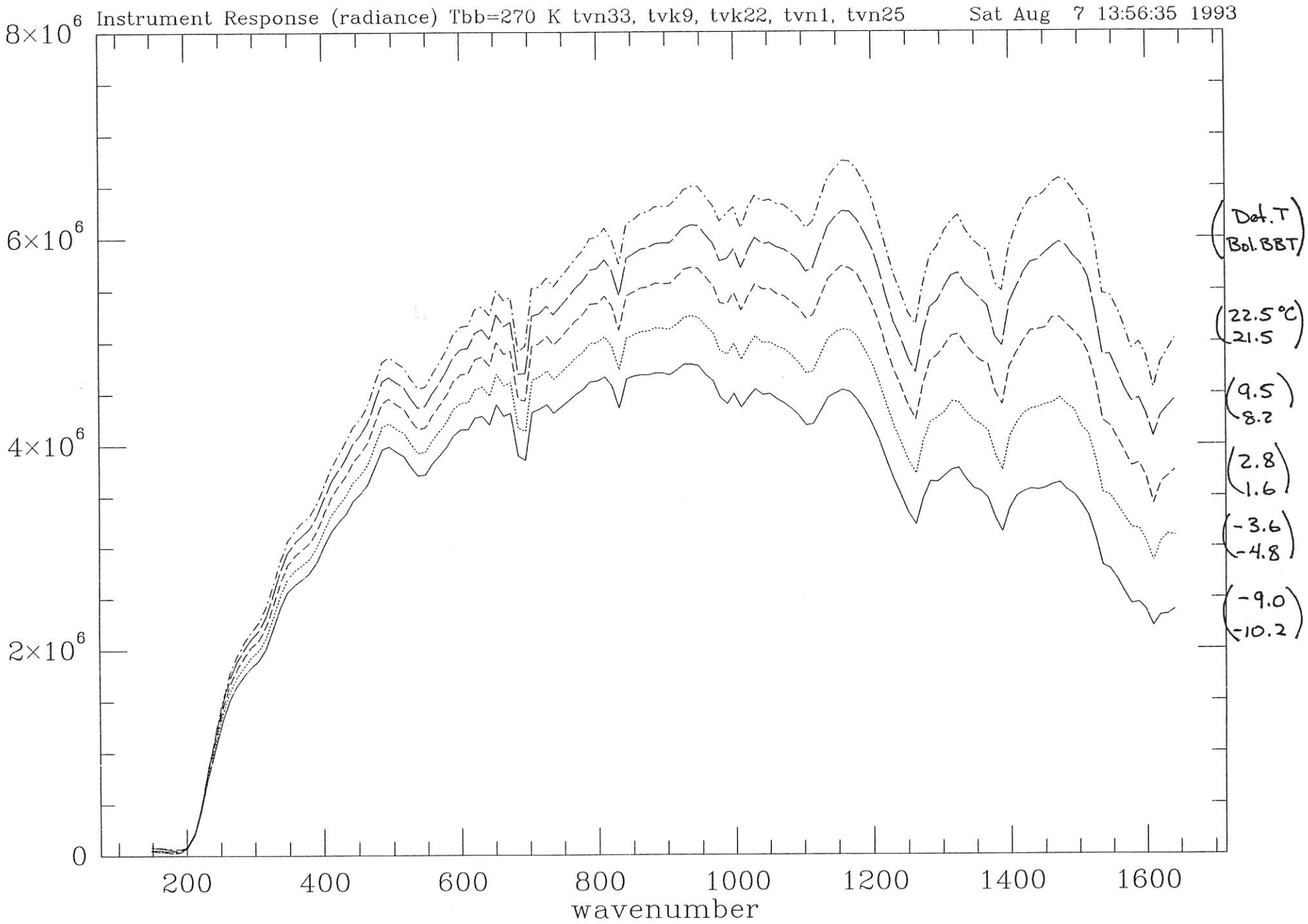
Instrument Response (radiance) Tbb=270 K tvn33, tvk9, tvk22, tvn1, tvn25
Sat Aug 7 13:56:35 1993
8×10^6
6×10^6
4×10^6
2×10^6
0
200
400
600
800
1000
1200
1400
1600
wavenumber
Det.T
Bol.BBT
22.5°C
21.5
9.5
8.2
2.8
1.6
-3.6
-4.8
-9.0
-10.2

Fig 3-12

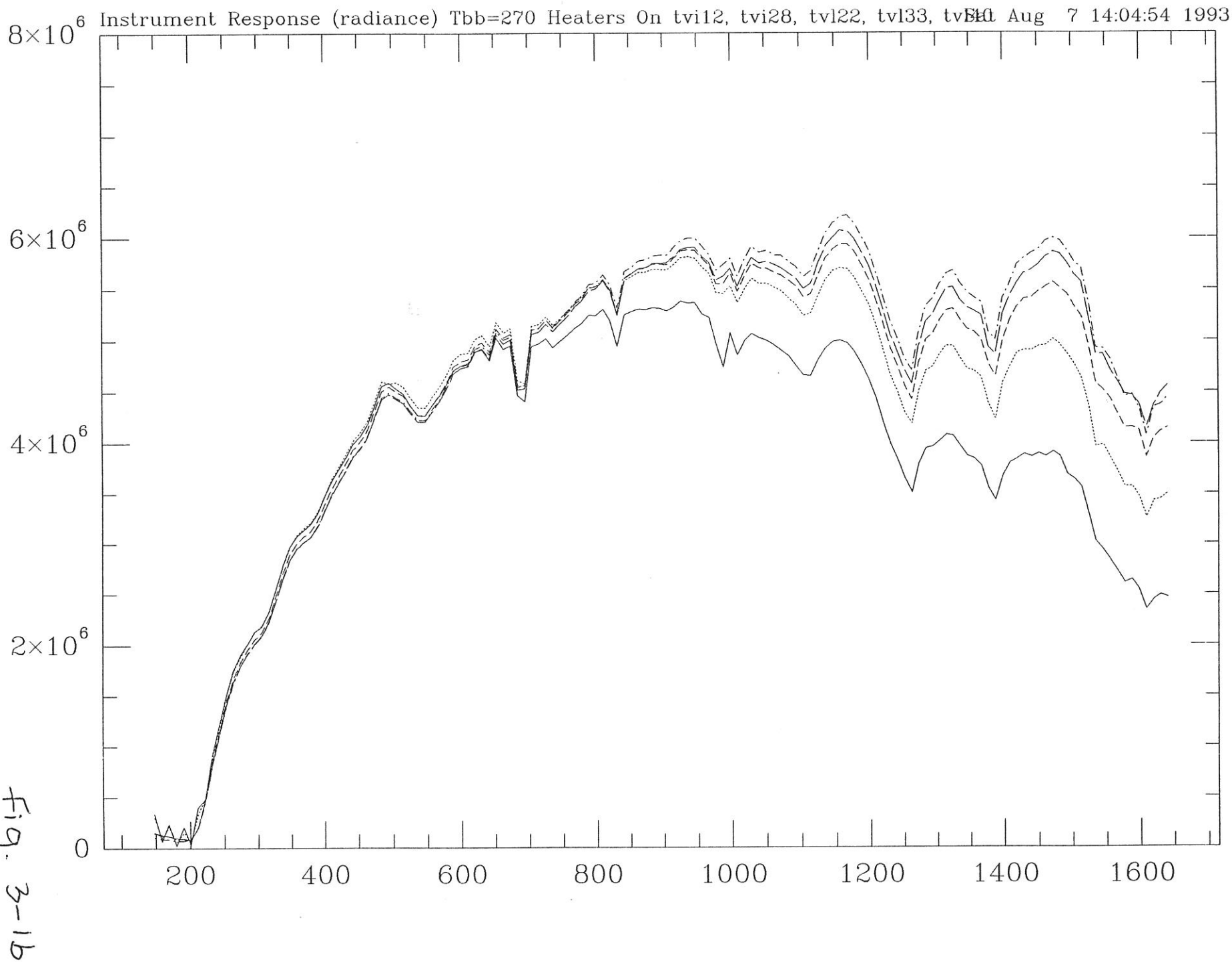
Instrument Response (radiance) Tbb=270 Heaters On tvi12, tvi28, tvl22, tvl33, tvl41
Sat Aug 7 14:04:54 1993
8×10^6
6×10^6
4×10^6
2×10^6
0
200
400
600
800
1000
1200
1400
1600

Fig. 3-16

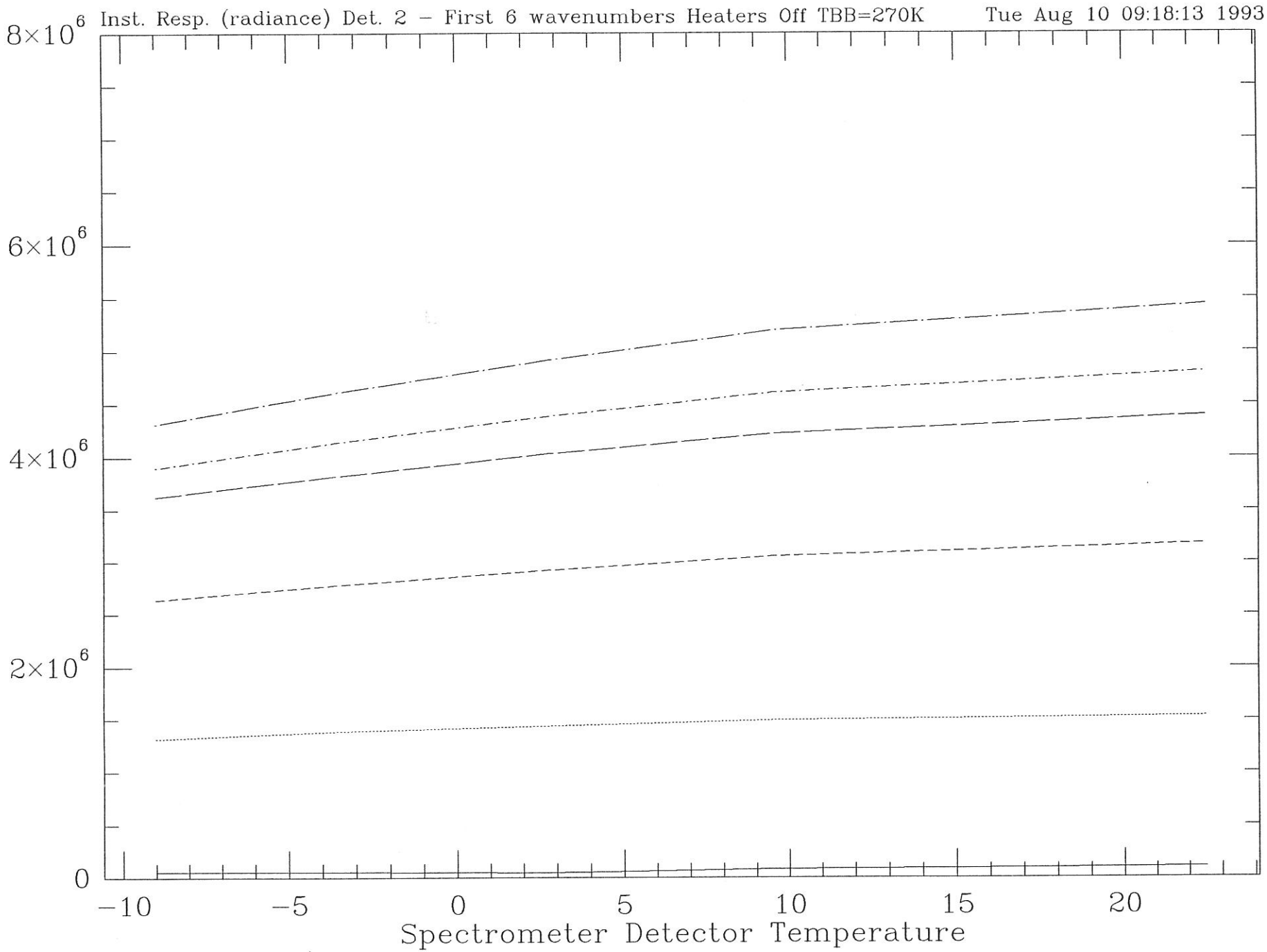
Inst. Resp. (radiance) Det. 2 – First 6 wavenumbers Heaters Off TBB=270K
Tue Aug 10 09:18:13 1993
8×10^6
6×10^6
4×10^6
2×10^6
0
−10
−5
0
5
10
15
20
Spectrometer Detector Temperature

Fig. 3-22

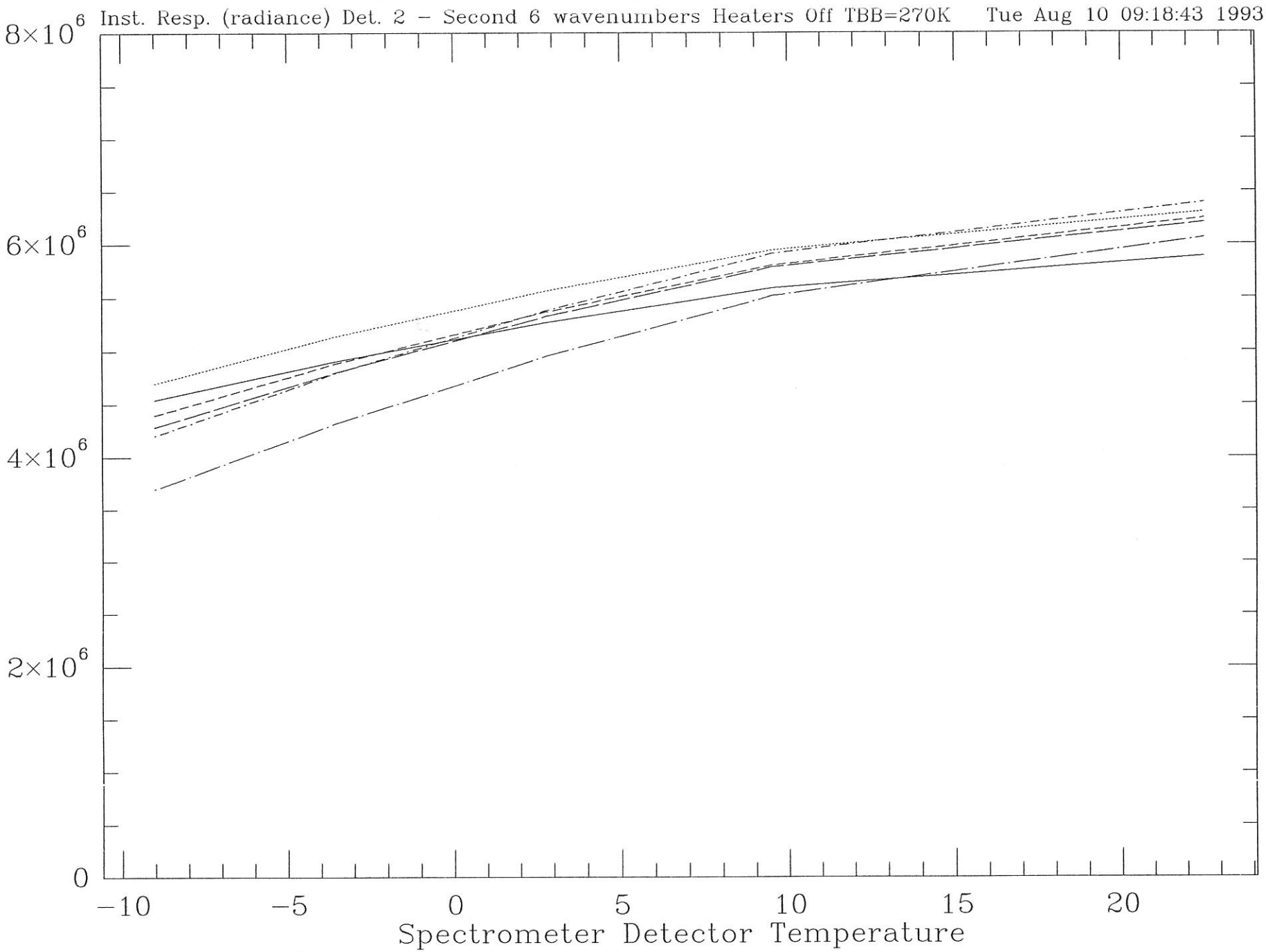
Inst. Resp. (radiance) Det. 2 – Second 6 wavenumbers Heaters Off TBB=270K Tue Aug 10 09:18:43 1993
8×10^6
6×10^6
4×10^6
2×10^6
0
−10
−5
0
5
10
15
20
Spectrometer Detector Temperature

Fig. 3-26

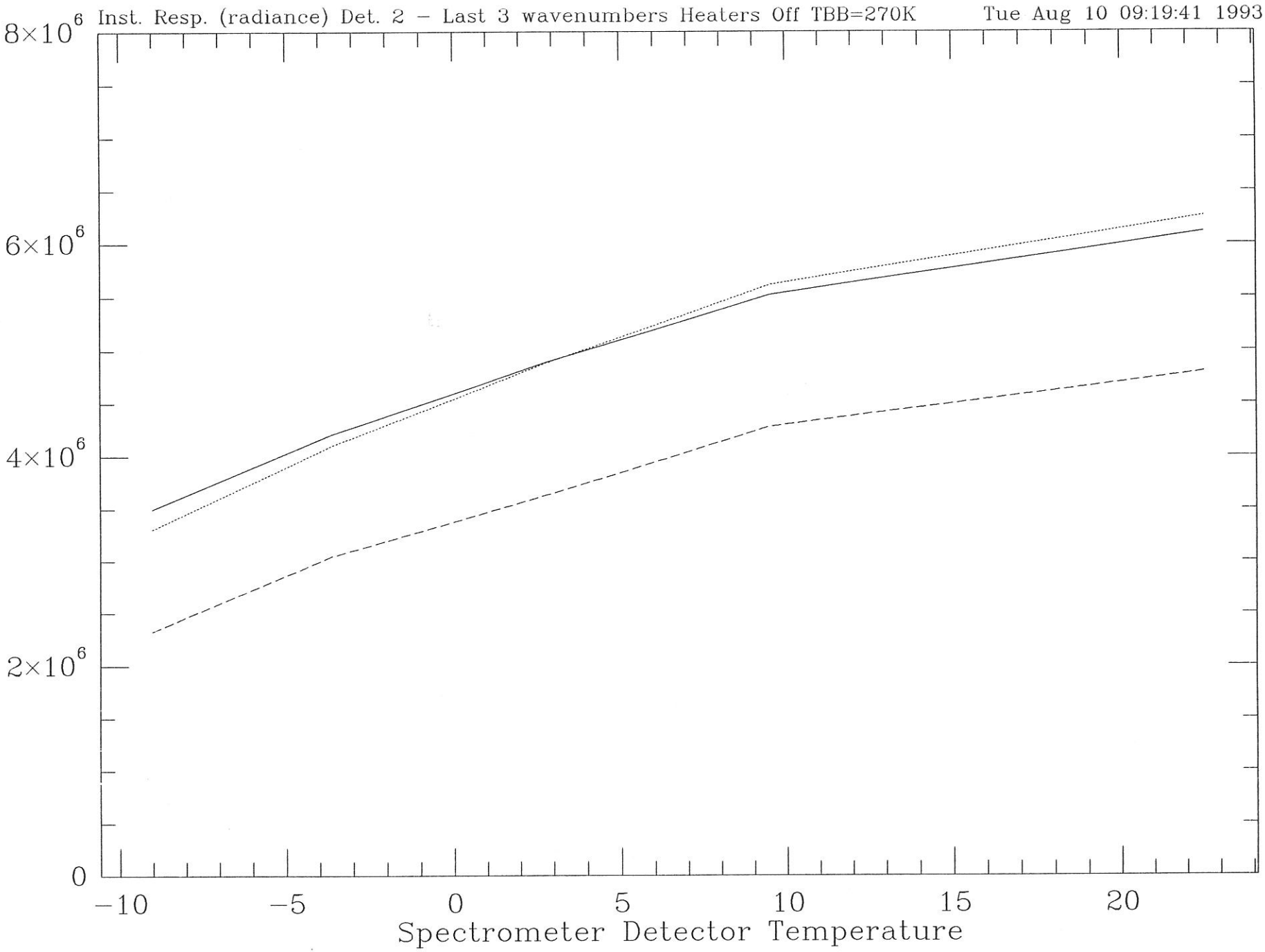
Inst. Resp. (radiance) Det. 2 – Last 3 wavenumbers Heaters Off TBB=270K
Tue Aug 10 09:19:41 1993
8×10^6
6×10^6
4×10^6
2×10^6
0
−10
−5
0
5
10
15
20
Spectrometer Detector Temperature

Fig. 3-2c

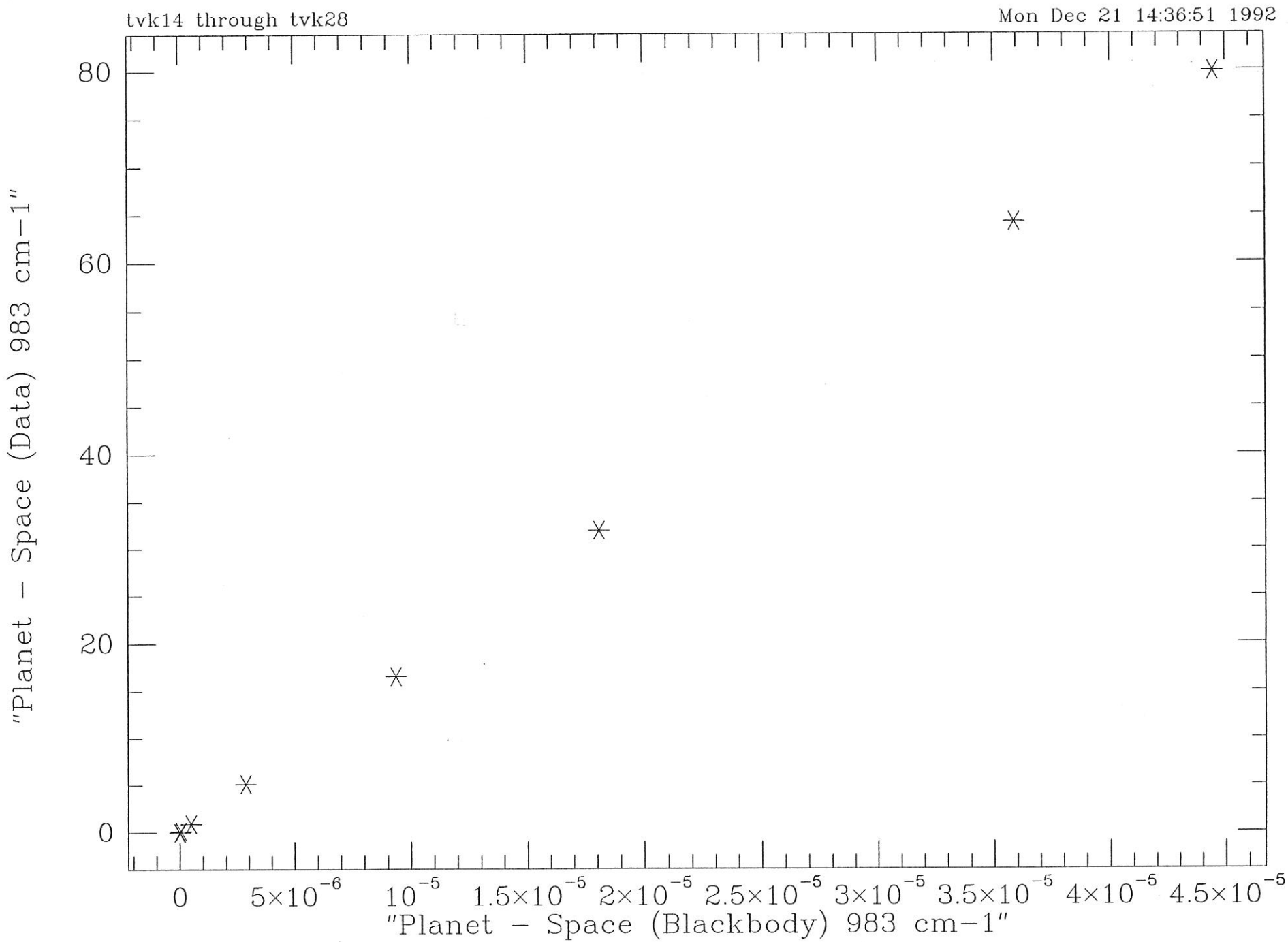
tvk14 through tvk28
Mon Dec 21 14:36:51 1992
"Planet - Space (Data) 983 cm-1"
80
60
40
20
0
0
5×10^-6
10^-5
1.5×10^-5
2×10^-5
2.5×10^-5
3×10^-5
3.5×10^-5
4×10^-5
4.5×10^-5
"Planet - Space (Blackbody) 983 cm-1"

Fig 3-3

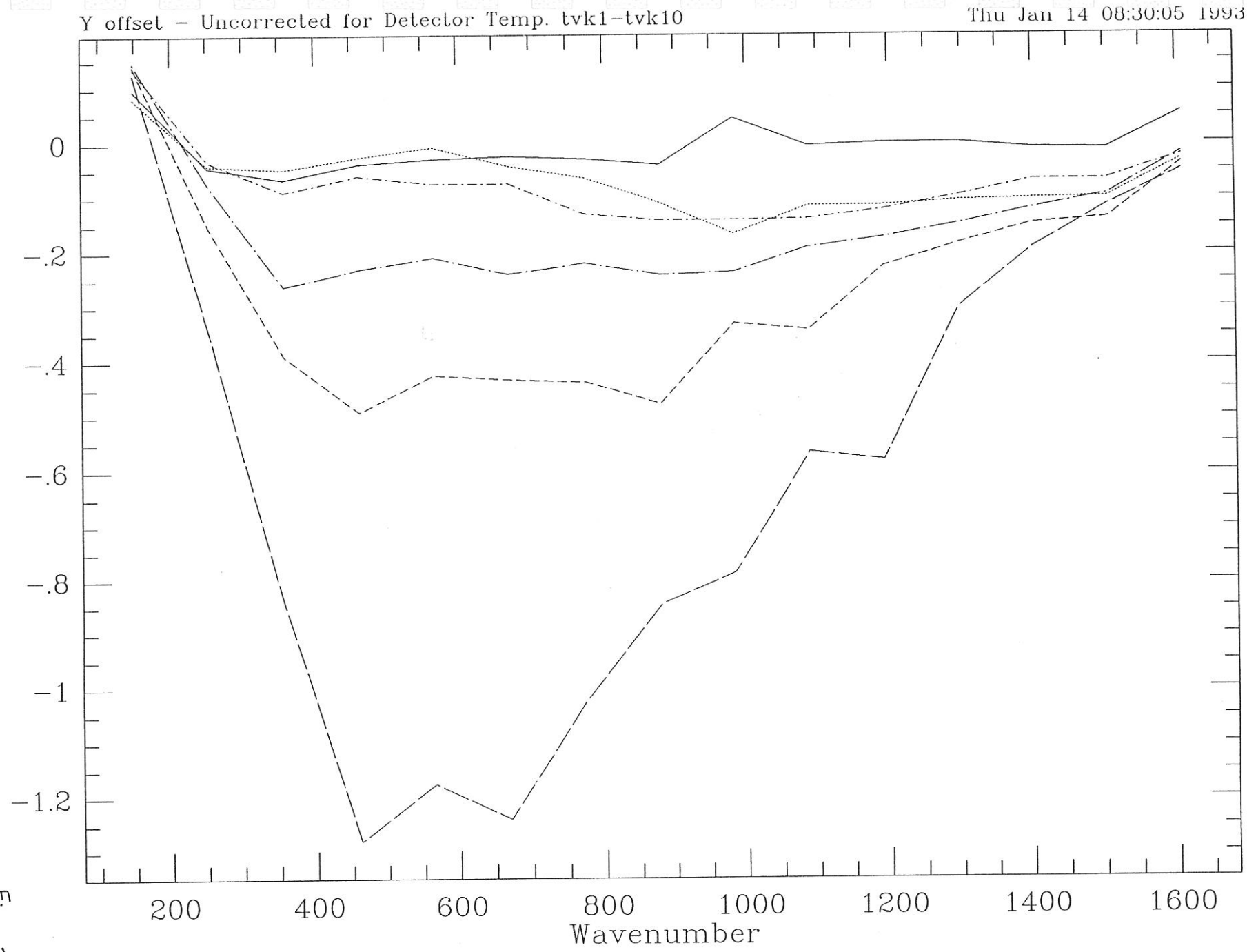
Y offset - Uncorrected for Detector Temp. tvk1-tvk10
Thu Jan 14 08:30:05 1993
0
-.2
-.4
-.6
-.8
-1
-1.2
200
400
600
800
1000
1200
1400
1600
Wavenumber

Fig. 3-4e

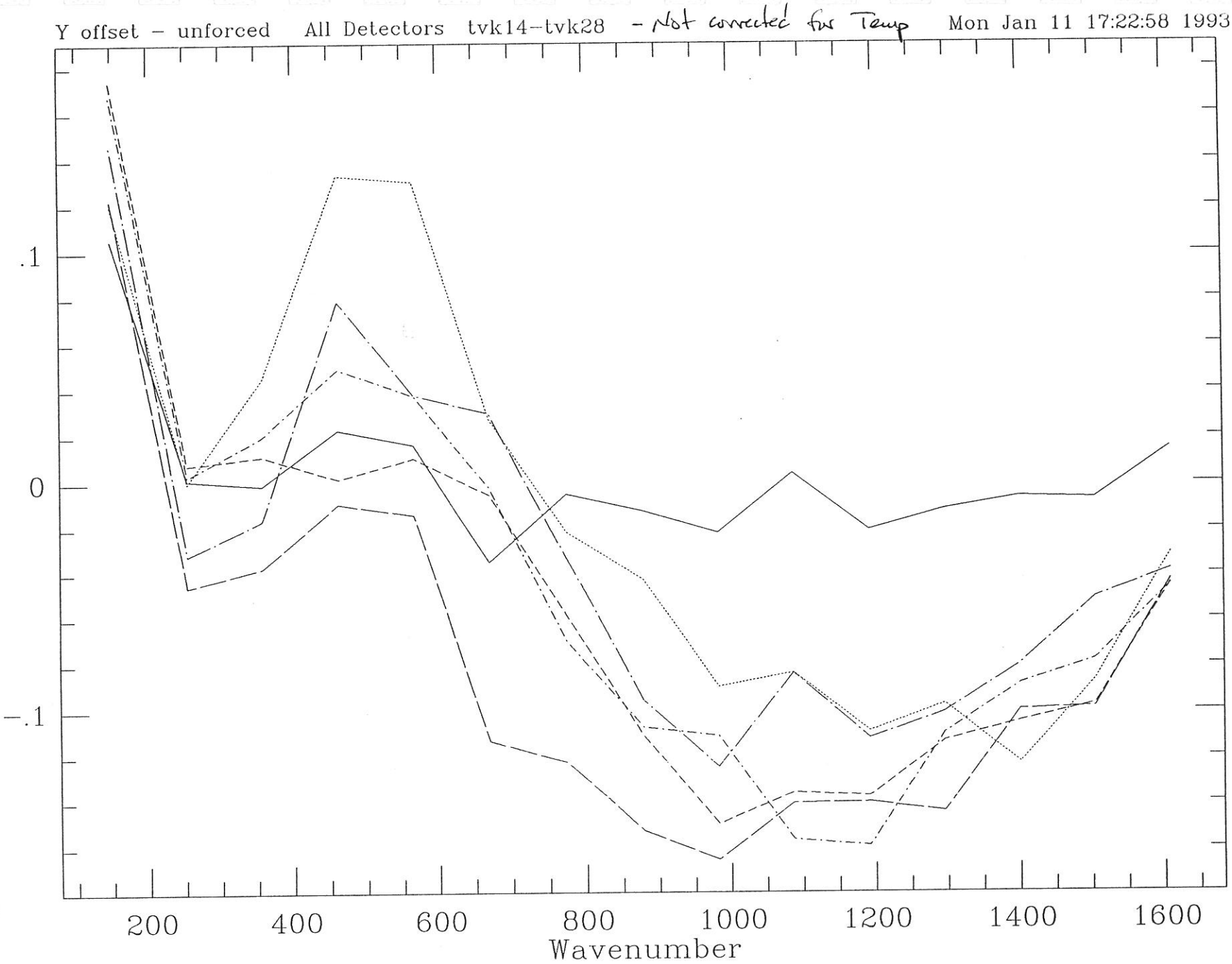
Y offset – unforced All Detectors tvk14–tvk28 – Not corrected for Temp Mon Jan 11 17:22:58 1993
.1
0
–.1
200
400
600
800
1000
1200
1400
1600
Wavenumber

Fig 3-46

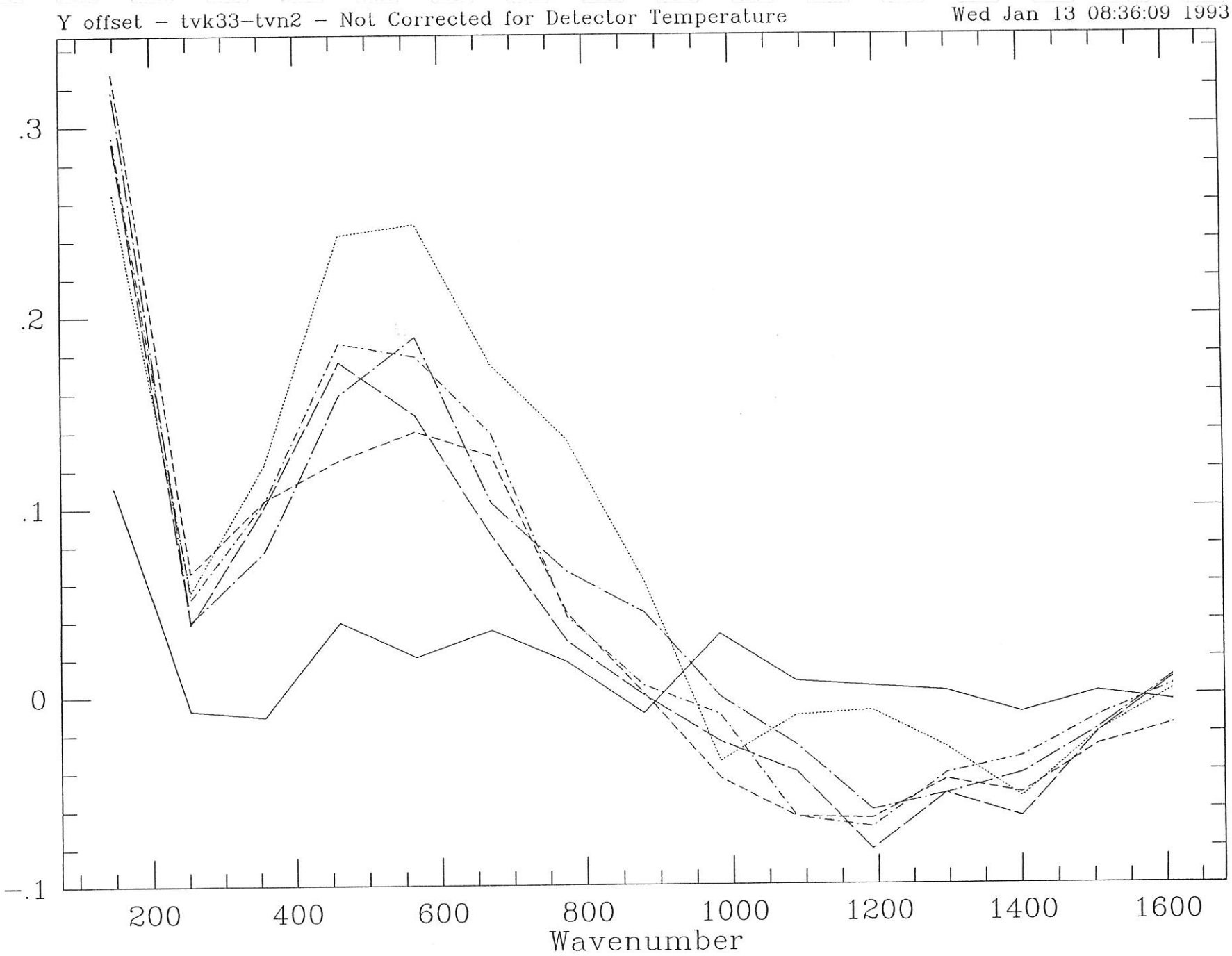
Y offset - tvk33-tvn2 - Not Corrected for Detector Temperature
Wed Jan 13 08:36:09 1993
.3
.2
.1
0
-.1
200
400
600
800
1000
1200
1400
1600
Wavenumber

Fig. 3-4c

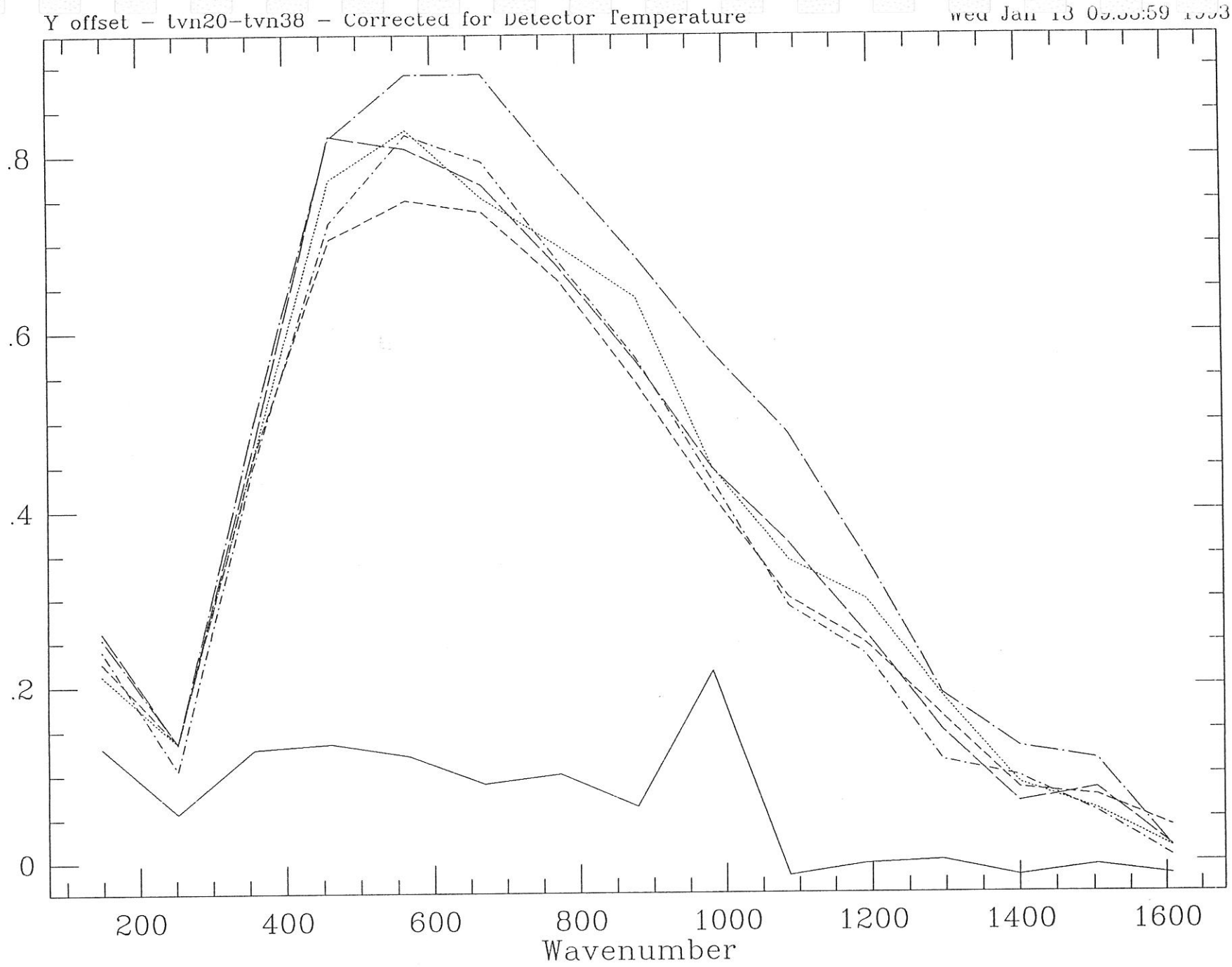
Y offset - tvn20-tvn38 - Corrected for Detector Temperature
Wed Jan 13 09:55:59 1993
.8
.6
.4
.2
0
200
400
600
800
1000
1200
1400
1600
Wavenumber

Fig 3-44

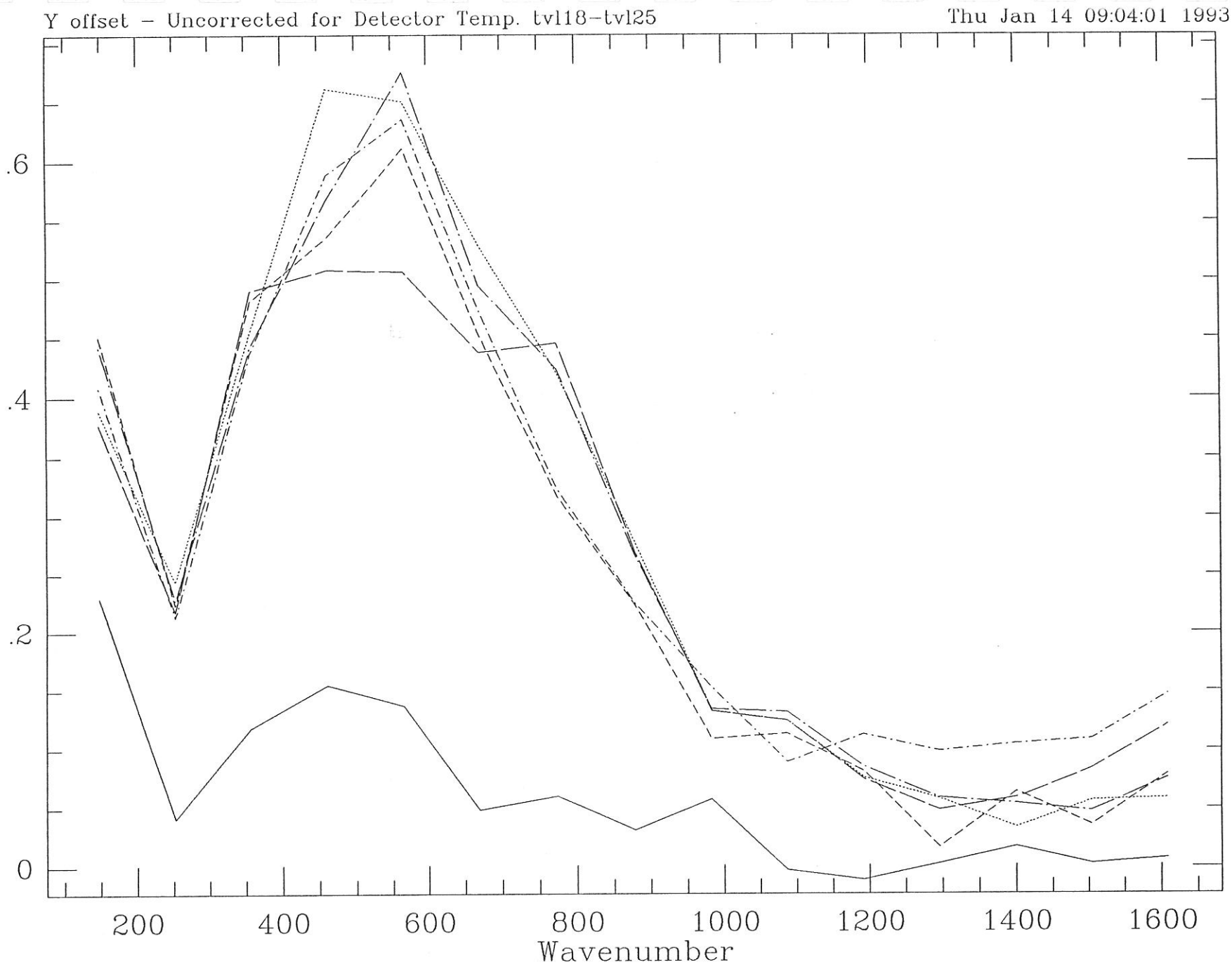
Y offset – Uncorrected for Detector Temp. tvl18–tvl25
Thu Jan 14 09:04:01 1993
.6
.4
.2
0
200
400
600
800
1000
1200
1400
1600
Wavenumber

Fig. 3-4e

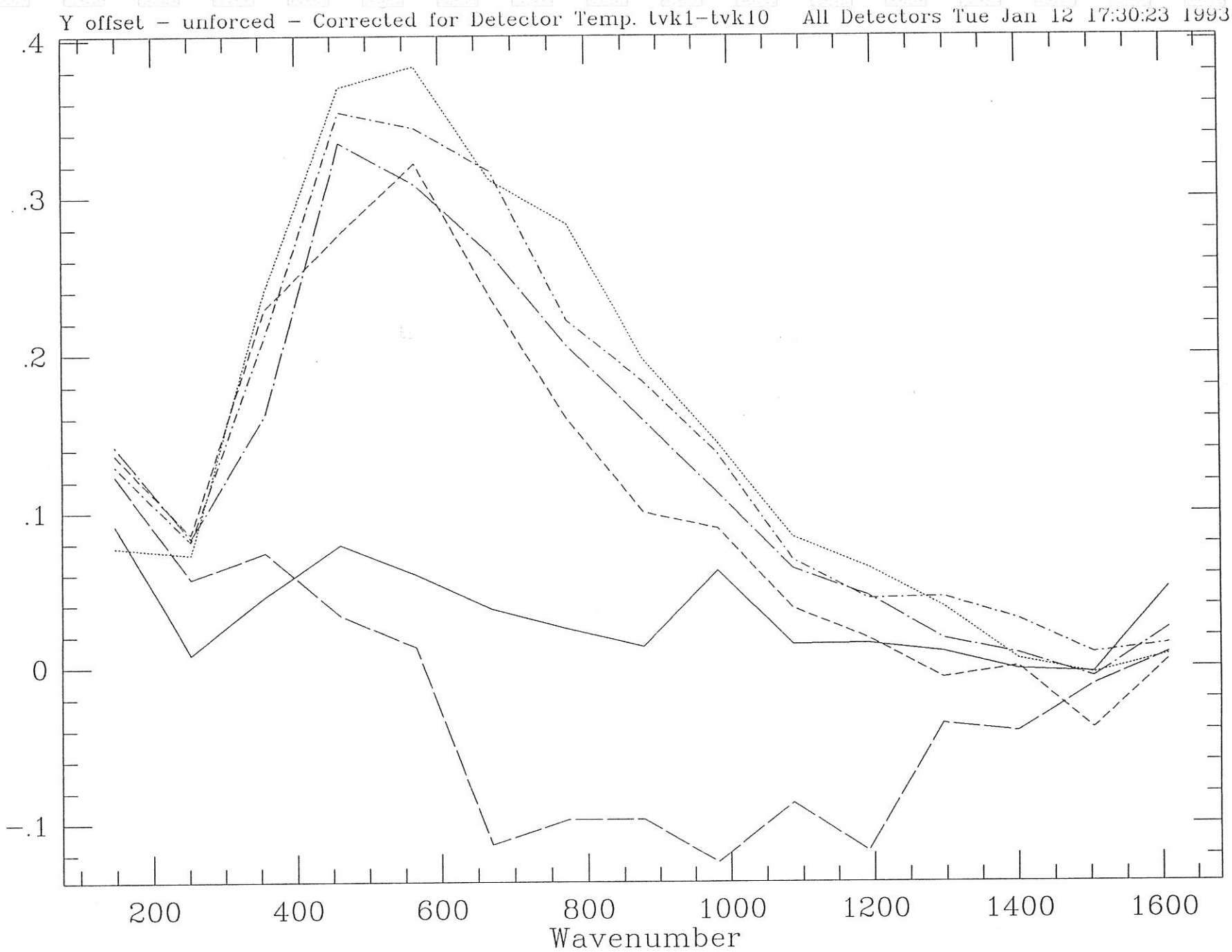
Y offset - unforced - Corrected for Detector Temp. tvk1-tvk10 All Detectors Tue Jan 12 17:30:23 1993
.4
.3
.2
.1
0
-.1
200
400
600
800
1000
1200
1400
1600
Wavenumber

Fig. 3-5a

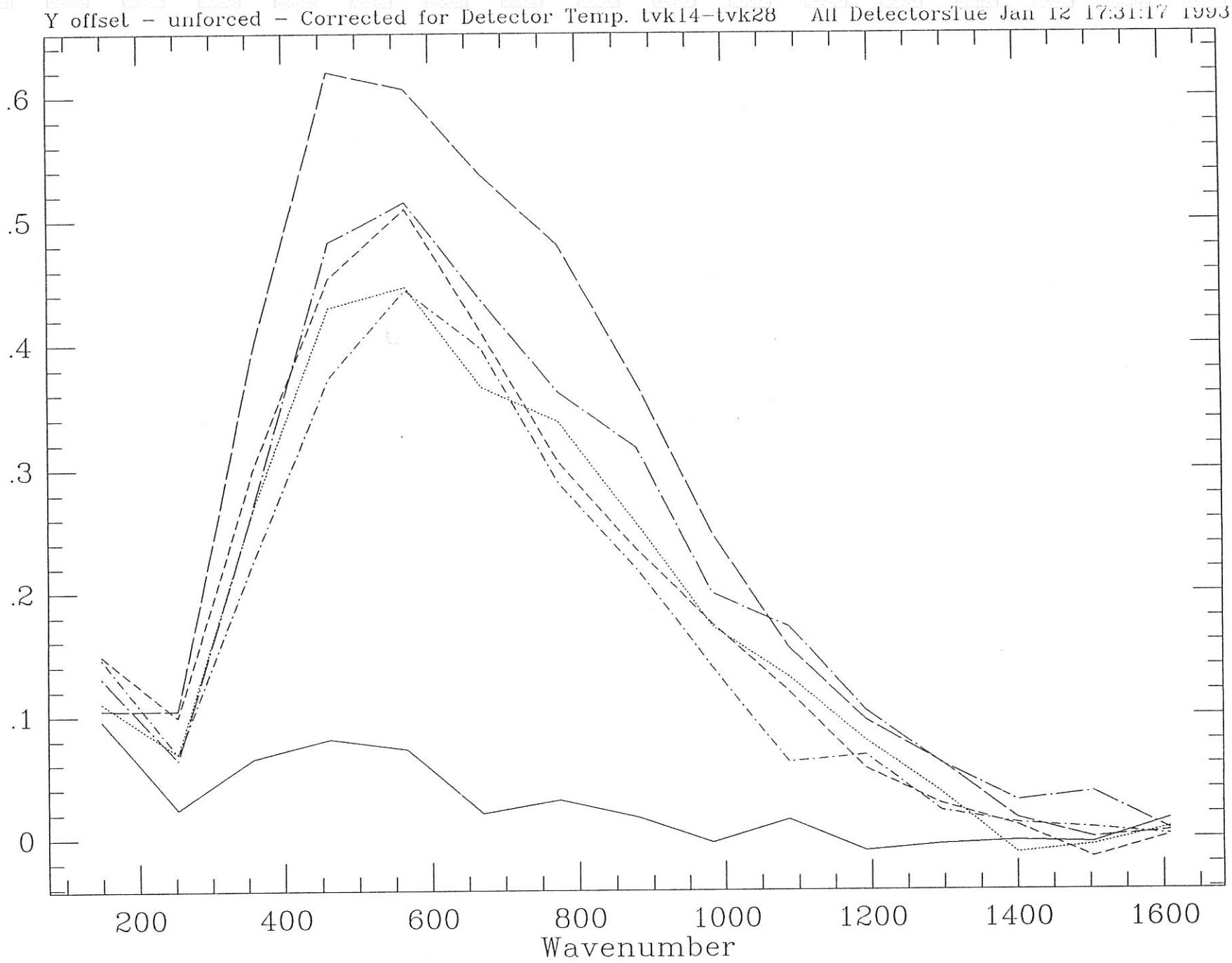
Y offset - unforced - Corrected for Detector Temp. tvk14-tvk28 All DetectorsTue Jan 12 17:31:17 1993
.6
.5
.4
.3
.2
.1
0
200
400
600
800
1000
1200
1400
1600
Wavenumber

Fig. 3-59

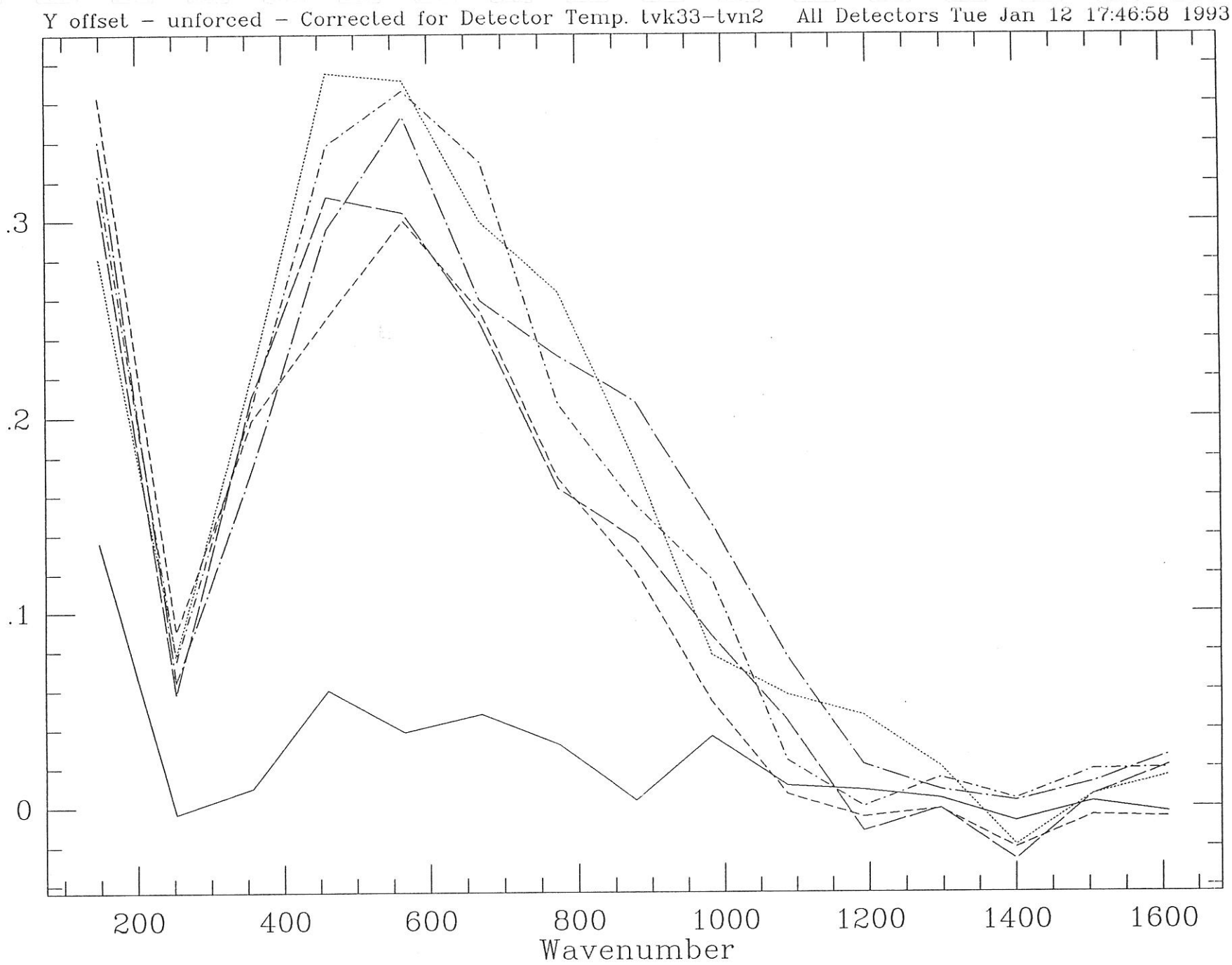
Y offset - unforced - Corrected for Detector Temp. tvk33-tvn2 All Detectors Tue Jan 12 17:46:58 1993
.3
.2
.1
0
200
400
600
800
1000
1200
1400
1600
Wavenumber

Fig. 3-5c

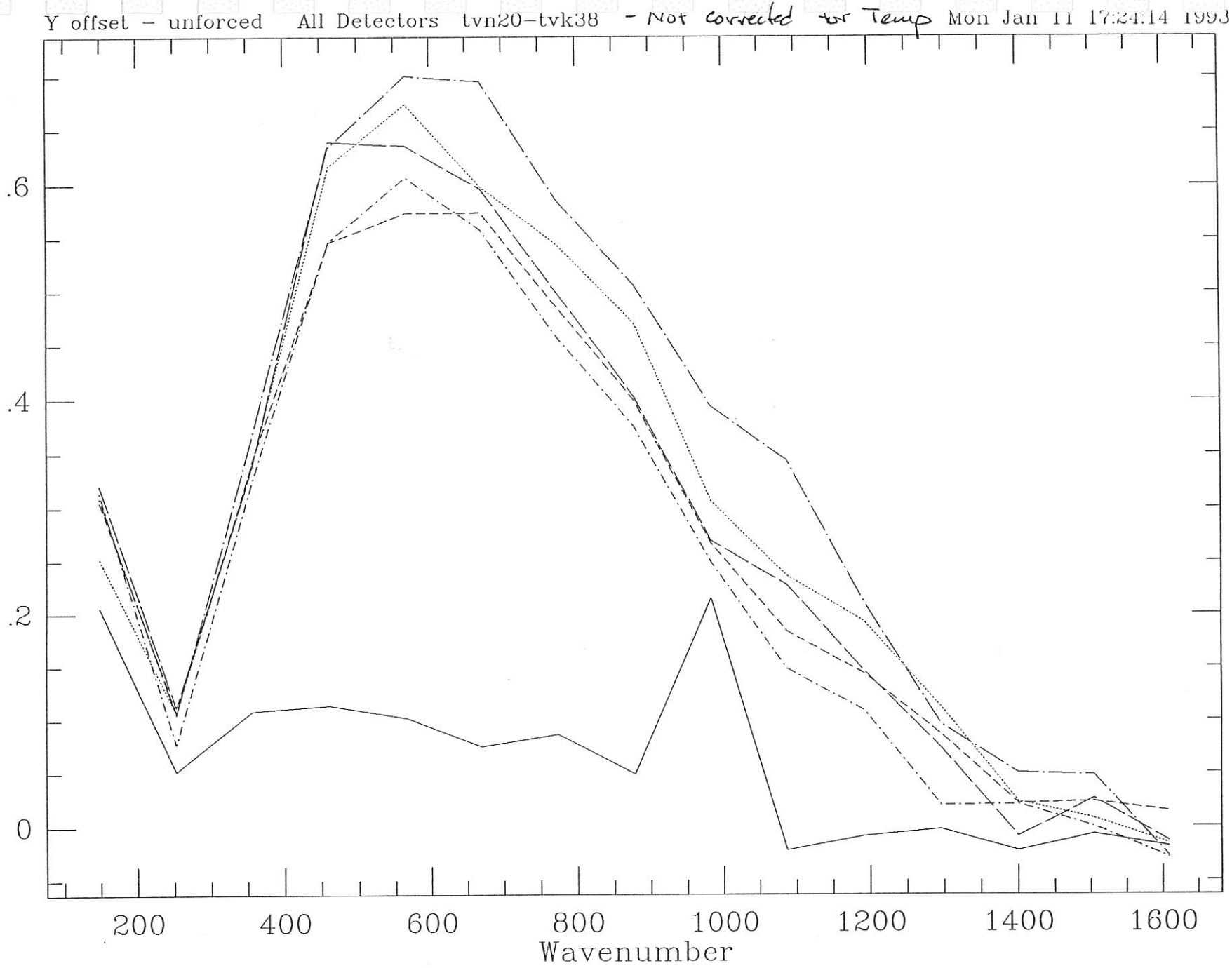
Y offset – unforced All Detectors tvn20–tvk38 – Not corrected for Temp Mon Jan 11 17:24:14 1993
.6
.4
.2
0
200
400
600
800
1000
1200
1400
1600
Wavenumber

Fig. 3-5d

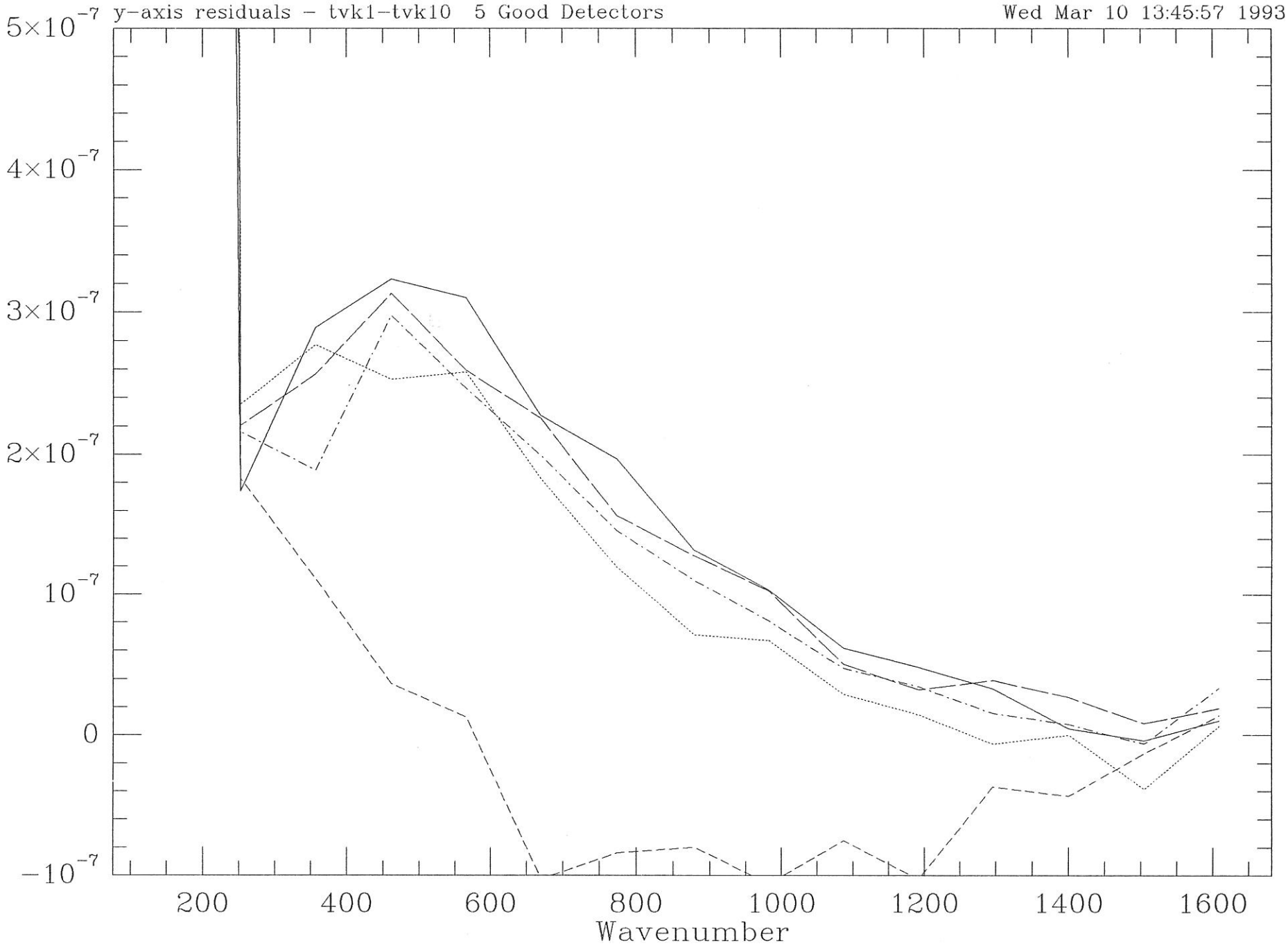
y-axis residuals - tvk1-tvk10 5 Good Detectors
Wed Mar 10 13:45:57 1993
5×10^-7
4×10^-7
3×10^-7
2×10^-7
10^-7
0
-10^-7
200
400
600
800
1000
1200
1400
1600
Wavenumber

Fig. 3-6a

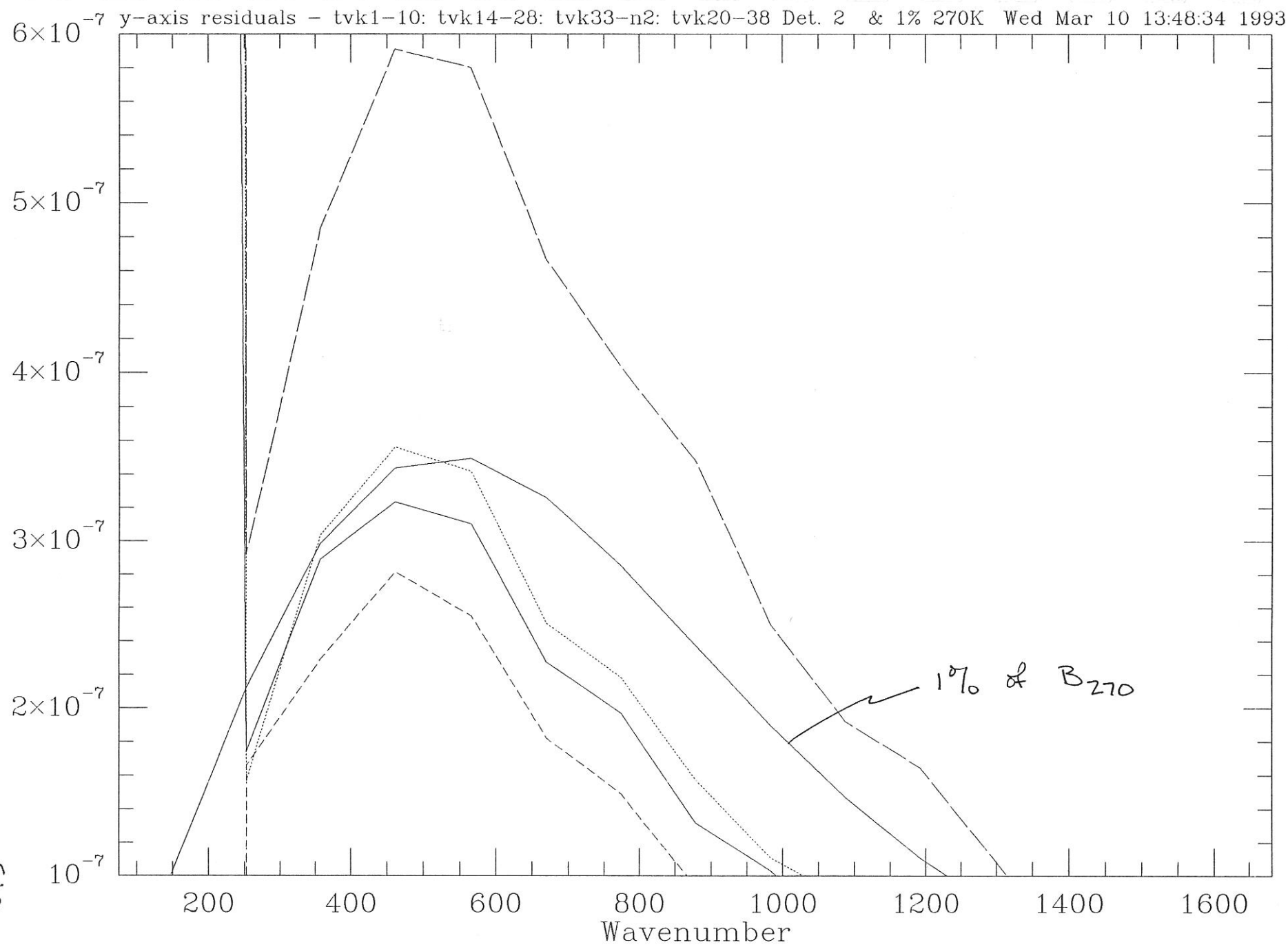
y-axis residuals - tvk1-10: tvk14-28: tvk33-n2: tvk20-38 Det. 2 & 1% 270K Wed Mar 10 13:48:34 1993
6×10^-7
5×10^-7
4×10^-7
3×10^-7
2×10^-7
10^-7
200
400
600
800
1000
1200
1400
1600
Wavenumber
1% of B270

fig. 3-66

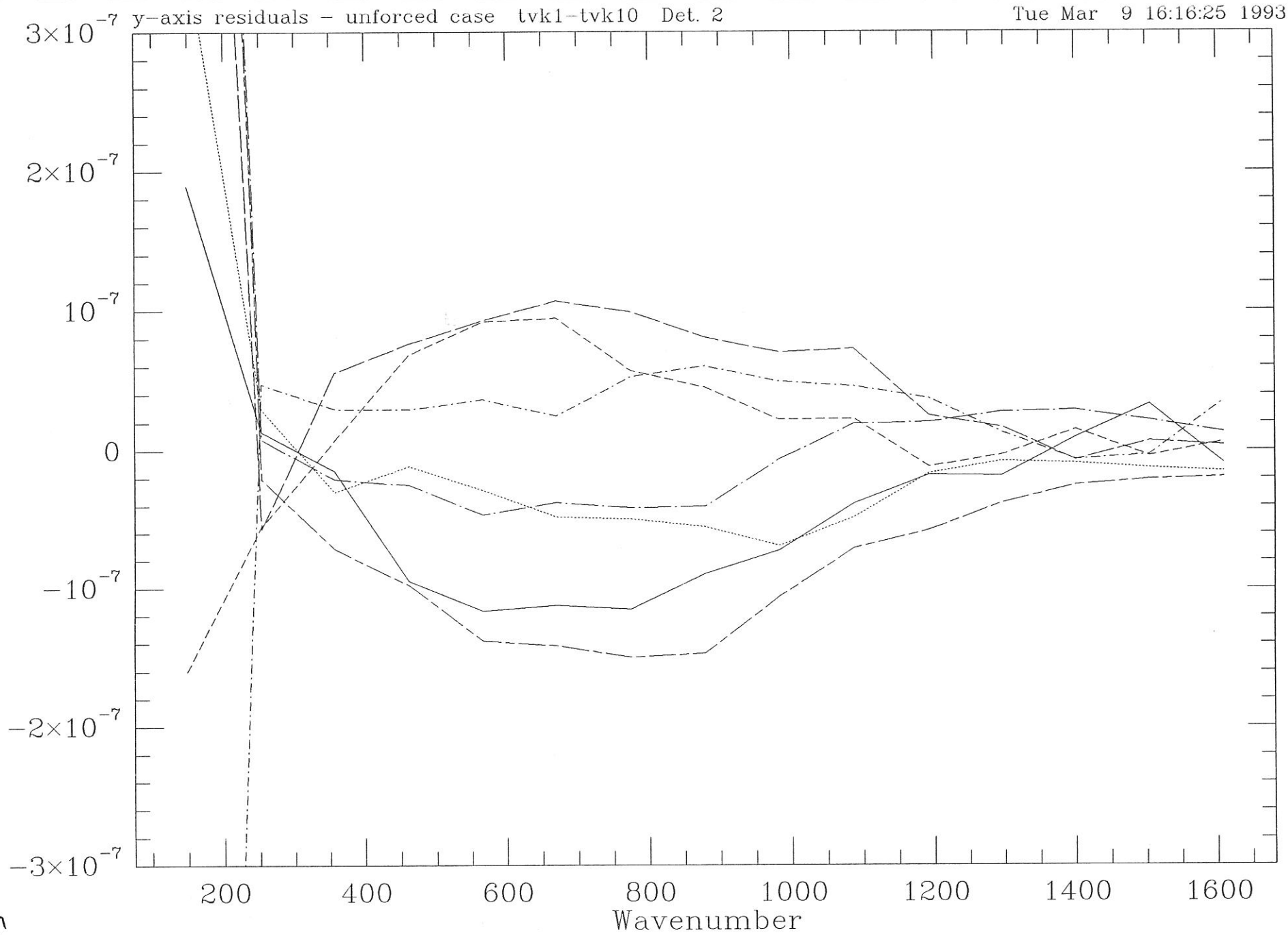
y-axis residuals - unforced case tvk1-tvk10 Det. 2
Tue Mar 9 16:16:25 1993
3×10^-7
2×10^-7
10^-7
0
-10^-7
-2×10^-7
-3×10^-7
200
400
600
800
1000
1200
1400
1600
Wavenumber

Fig 3-7c

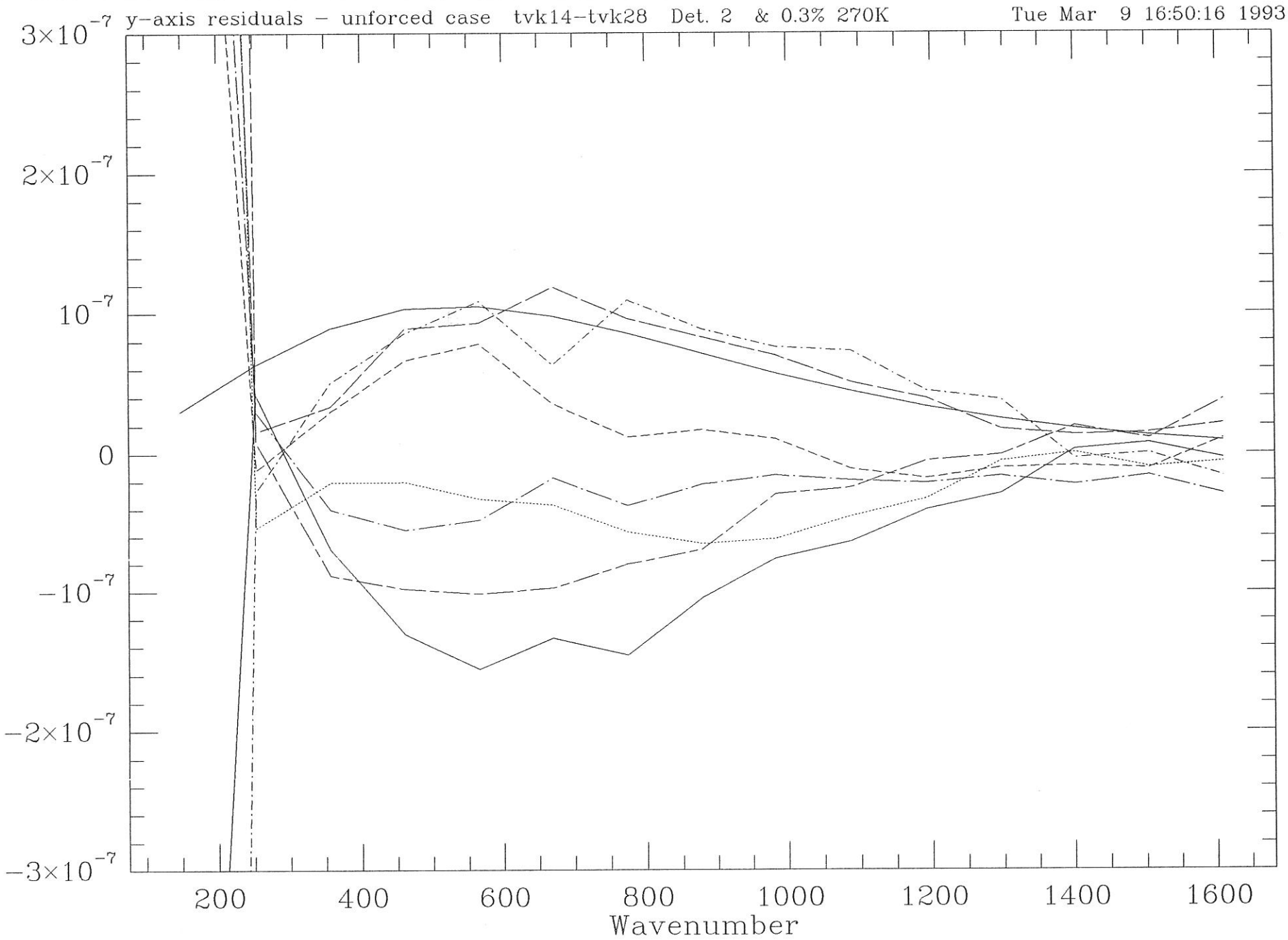
y-axis residuals – unforced case tvk14–tvk28 Det. 2 & 0.3% 270K
Tue Mar 9 16:50:16 1993
3×10^-7
2×10^-7
10^-7
0
-10^-7
-2×10^-7
-3×10^-7
200
400
600
800
1000
1200
1400
1600
Wavenumber

Fig. 3-76

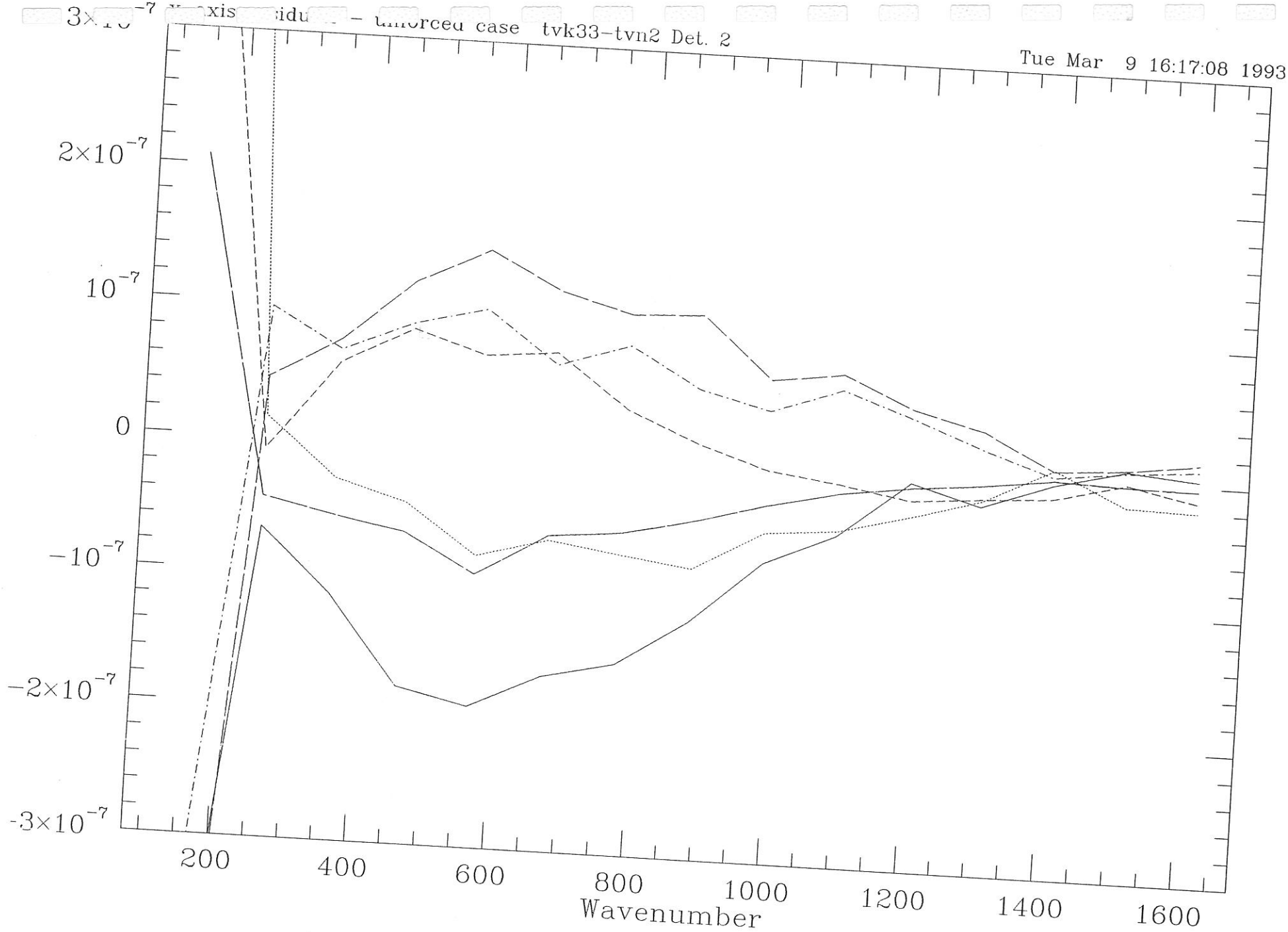
– unforced case tvk33-tvn2 Det. 2
Tue Mar 9 16:17:08 1993
2×10⁻⁷
10⁻⁷
0
−10⁻⁷
−2×10⁻⁷
-3×10⁻⁷
200
400
600
800
1000
1200
1400
1600
Wavenumber

Fig. 3-7c

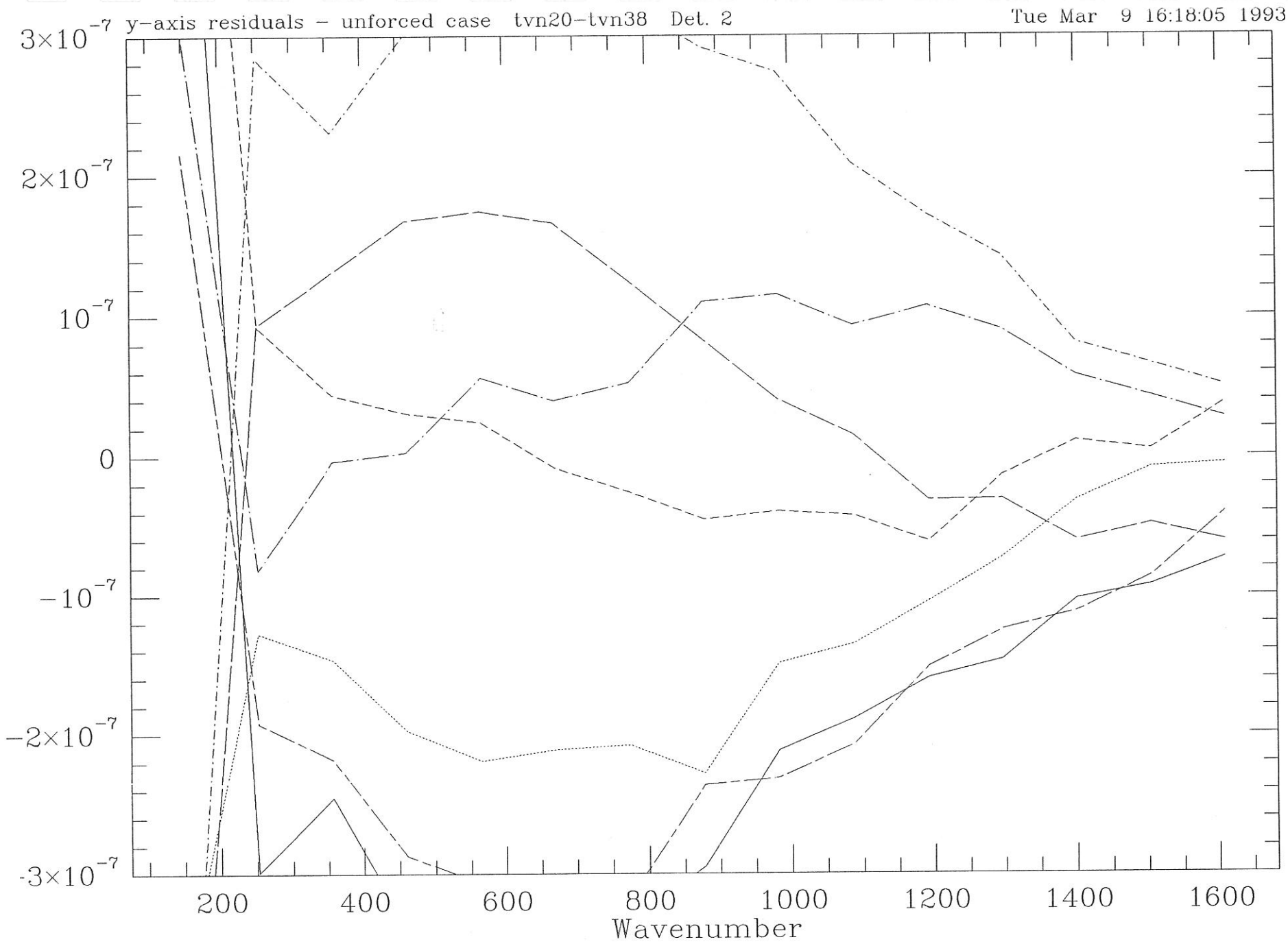
y-axis residuals - unforced case tvn20-tvn38 Det. 2
Tue Mar 9 16:18:05 1993
3×10^-7
2×10^-7
10^-7
0
-10^-7
-2×10^-7
-3×10^-7
200
400
600
800
1000
1200
1400
1600
Wavenumber

fig. 3-7a

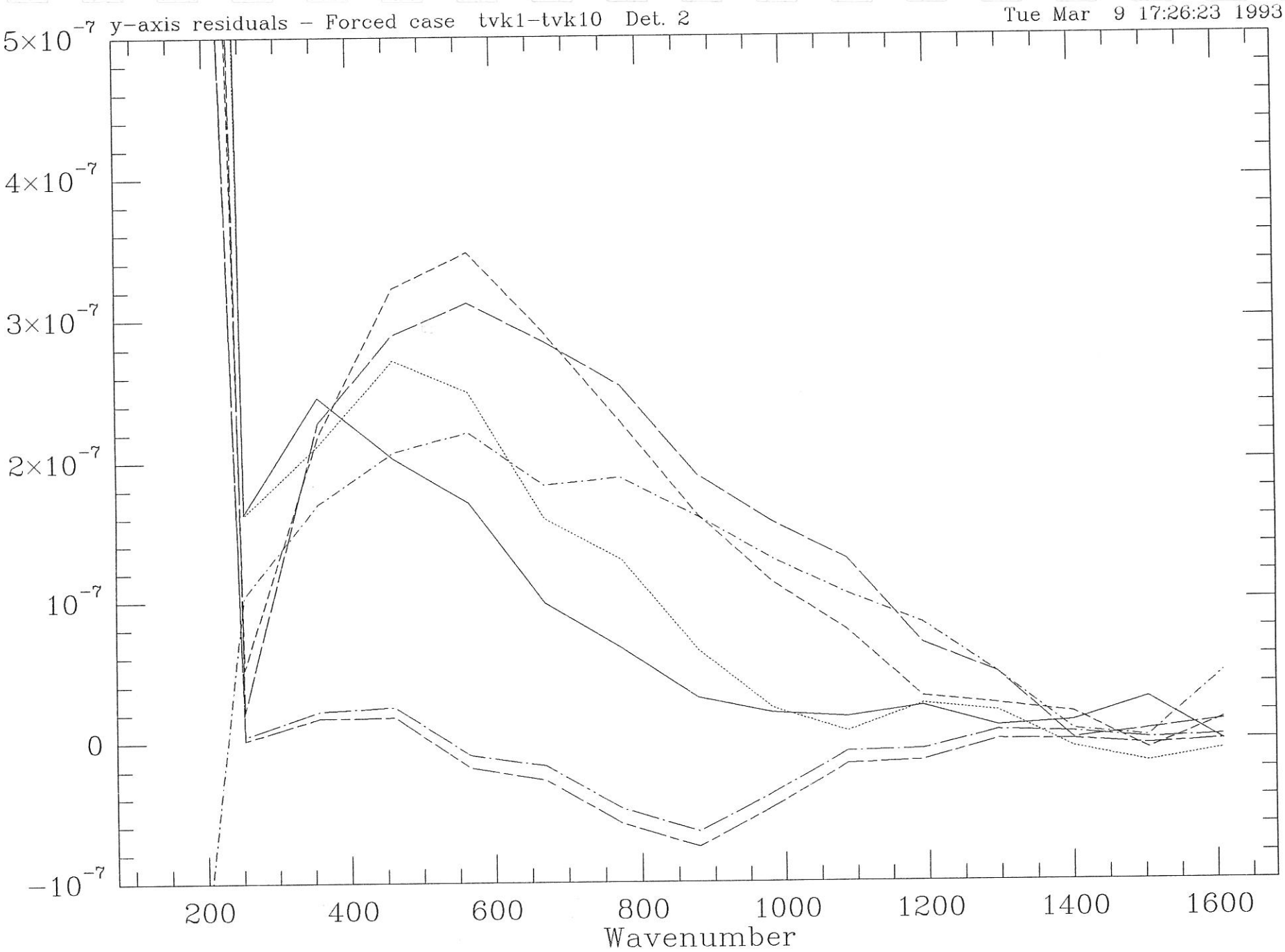
y-axis residuals - Forced case tvk1-tvk10 Det. 2
Tue Mar 9 17:26:23 1993
5×10^-7
4×10^-7
3×10^-7
2×10^-7
10^-7
0
-10^-7
200
400
600
800
1000
1200
1400
1600
Wavenumber

fig. 3-7e

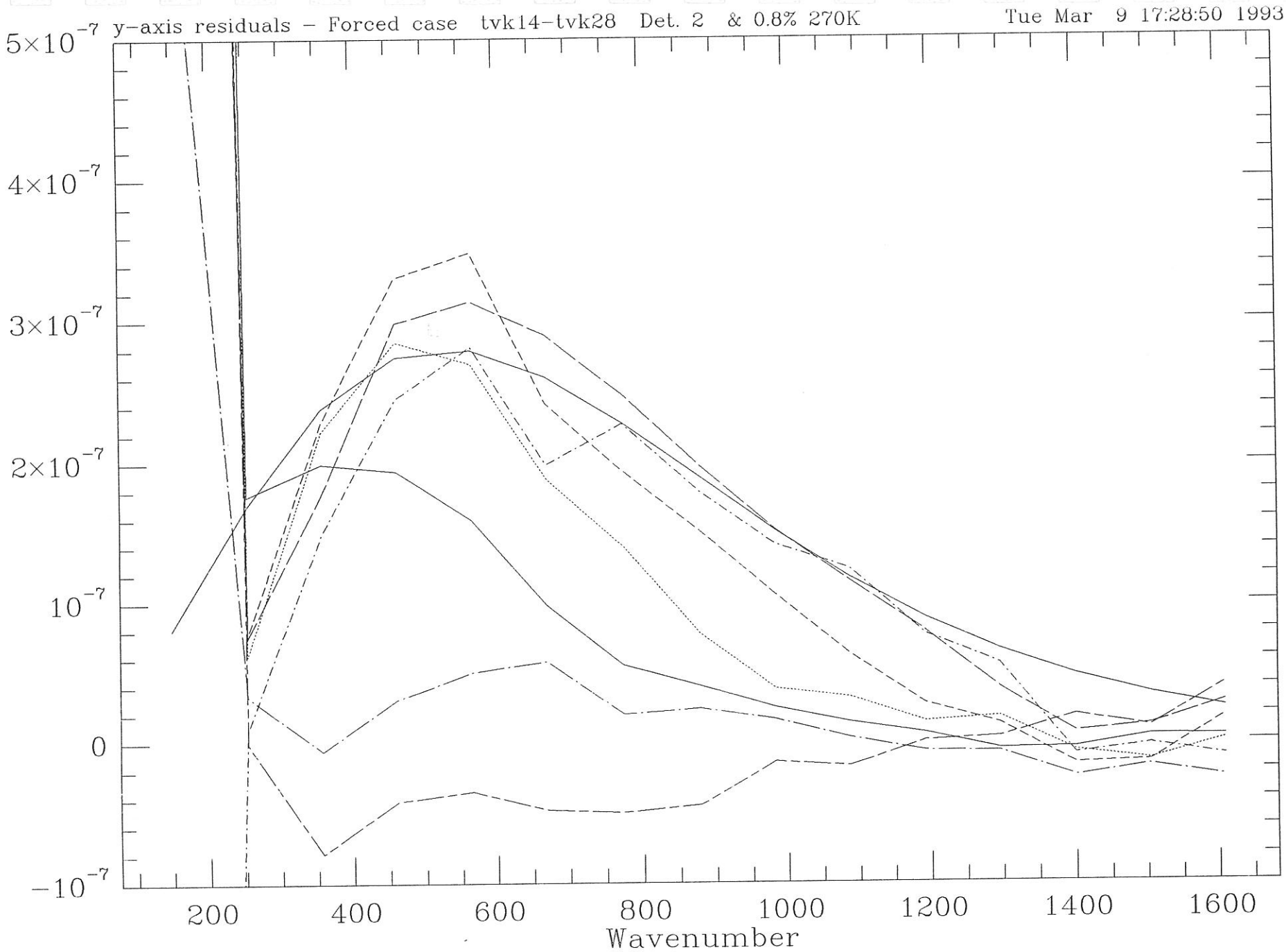
y-axis residuals – Forced case tvk14–tvk28 Det. 2 & 0.8% 270K
Tue Mar 9 17:28:50 1993
5×10^-7
4×10^-7
3×10^-7
2×10^-7
10^-7
0
-10^-7
200
400
600
800
1000
1200
1400
1600
Wavenumber

fig. 3-14

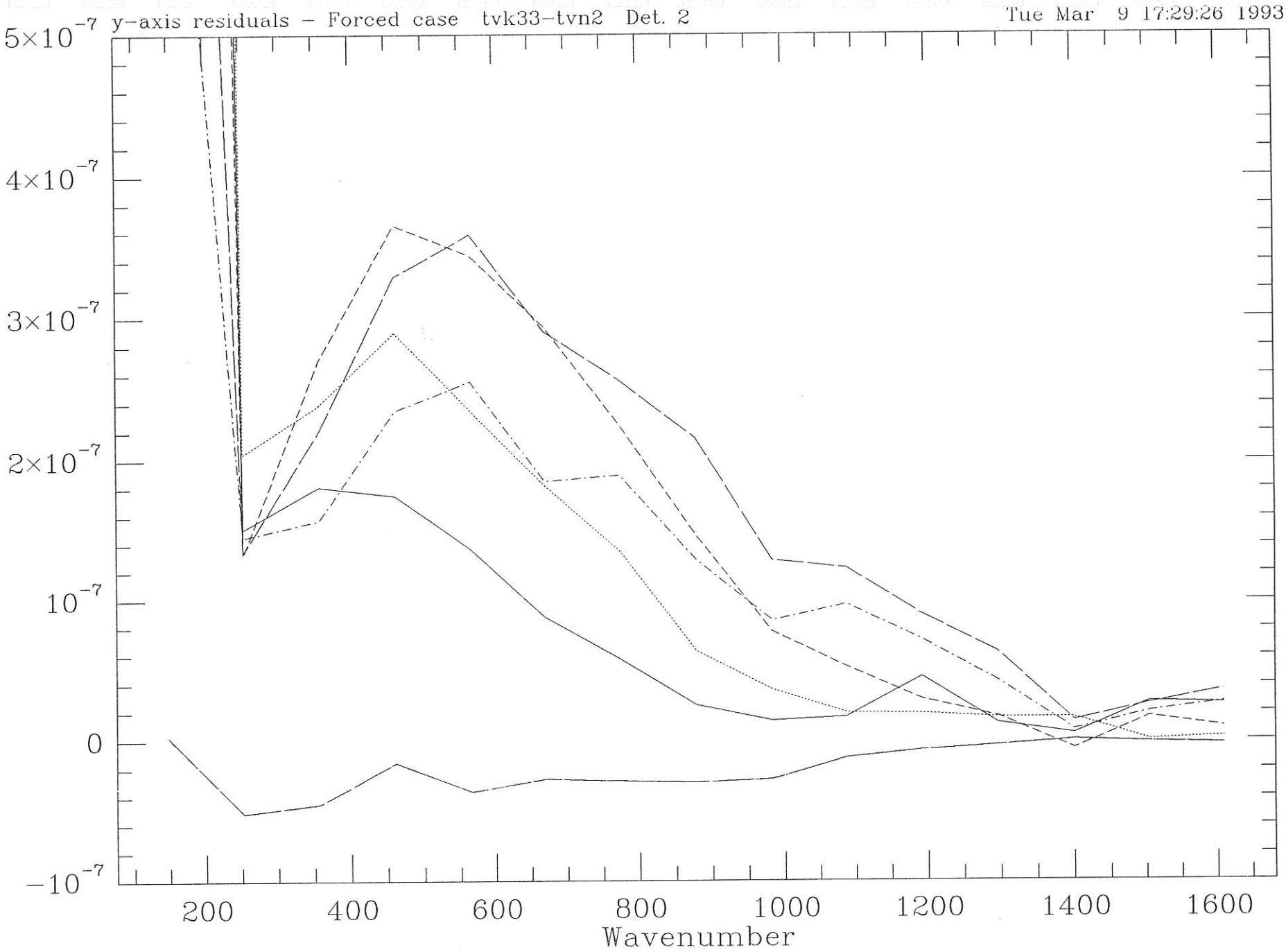
y-axis residuals – Forced case tvk33–tvn2 Det. 2
Tue Mar 9 17:29:26 1993
5×10^-7
4×10^-7
3×10^-7
2×10^-7
10^-7
0
-10^-7
200
400
600
800
1000
1200
1400
1600
Wavenumber

Fig. 3-79

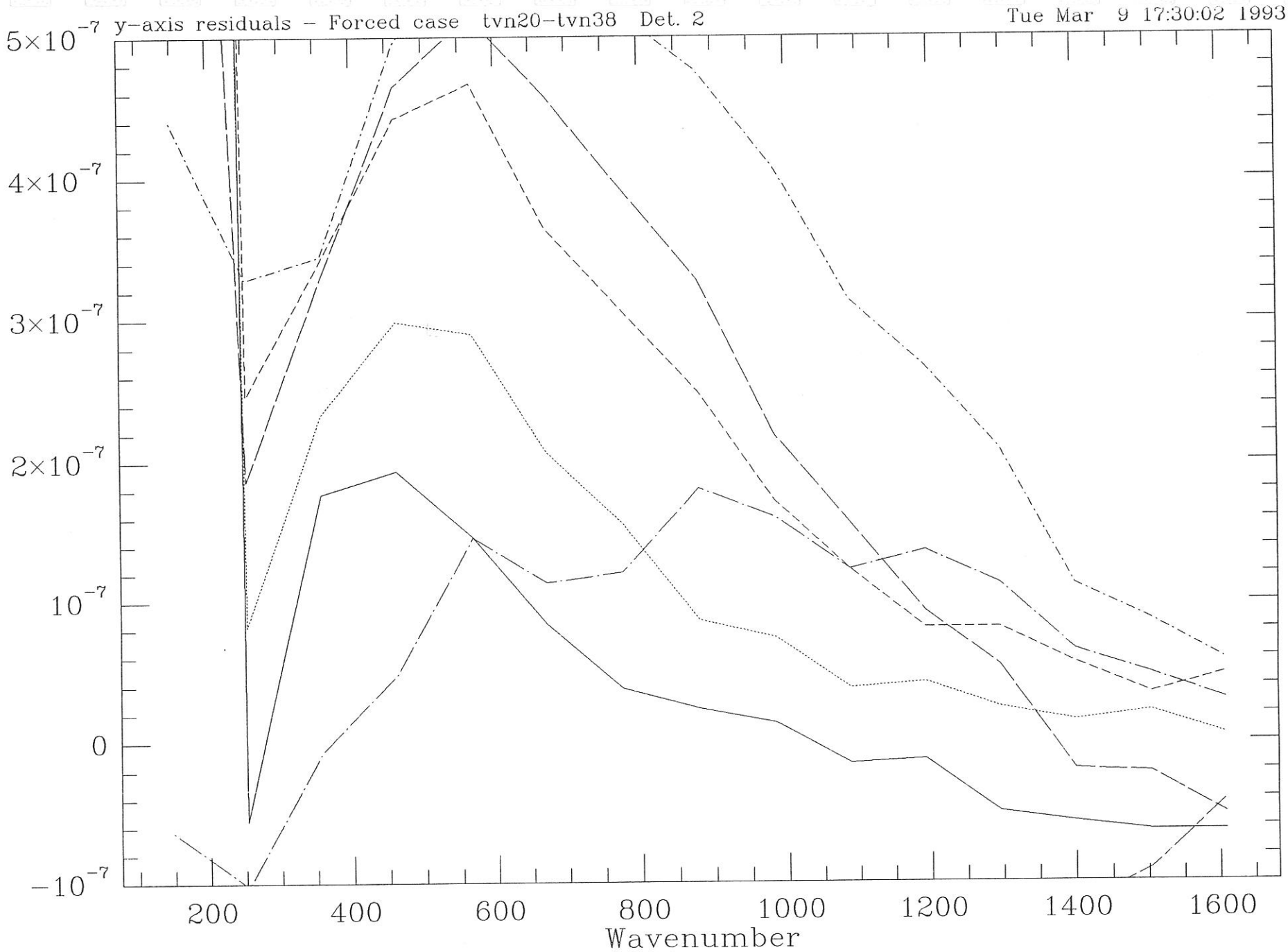
y-axis residuals - Forced case tvn20-tvn38 Det. 2
Tue Mar 9 17:30:02 1993
5×10^-7
4×10^-7
3×10^-7
2×10^-7
10^-7
0
-10^-7
200
400
600
800
1000
1200
1400
1600
Wavenumber

fig. 3-74

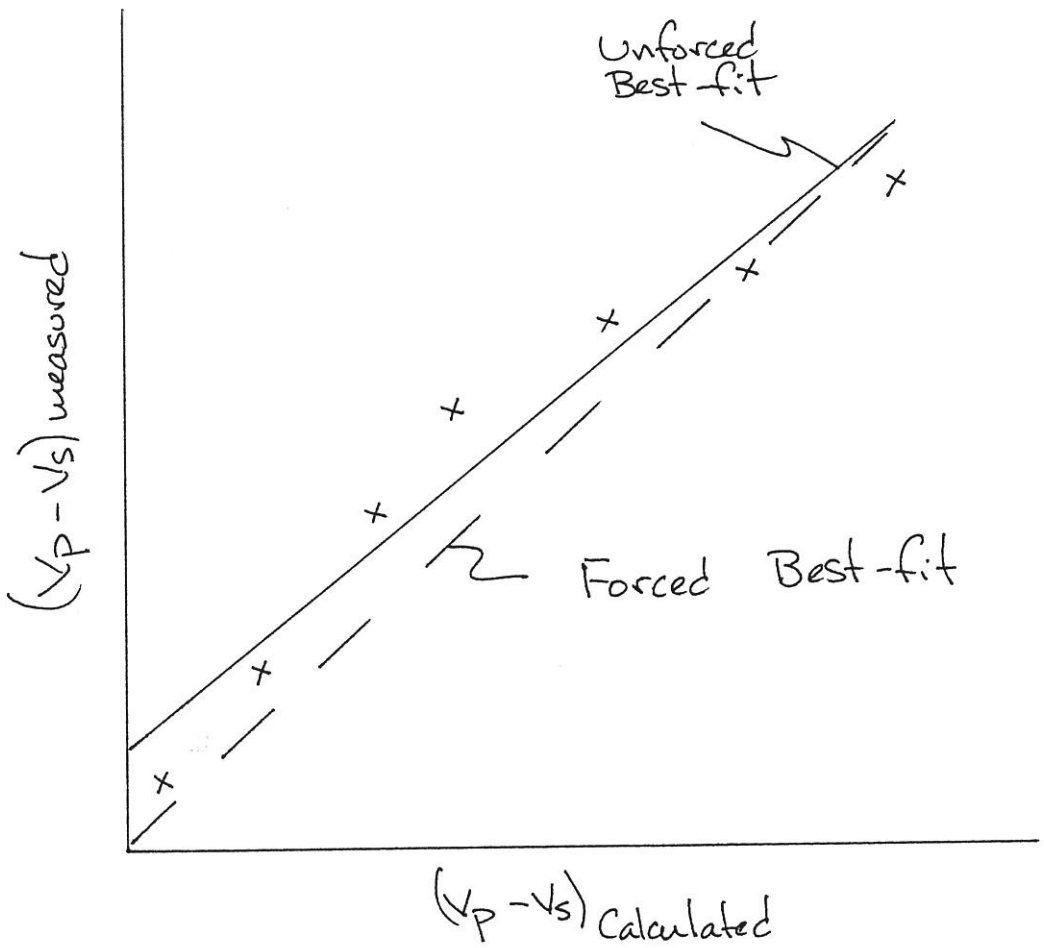
Unforced
Best-fit
Forced Best-fit
$(V_P - V_S)$ measured
$(V_P - V_S)$ Calculated

Fig. 3-8

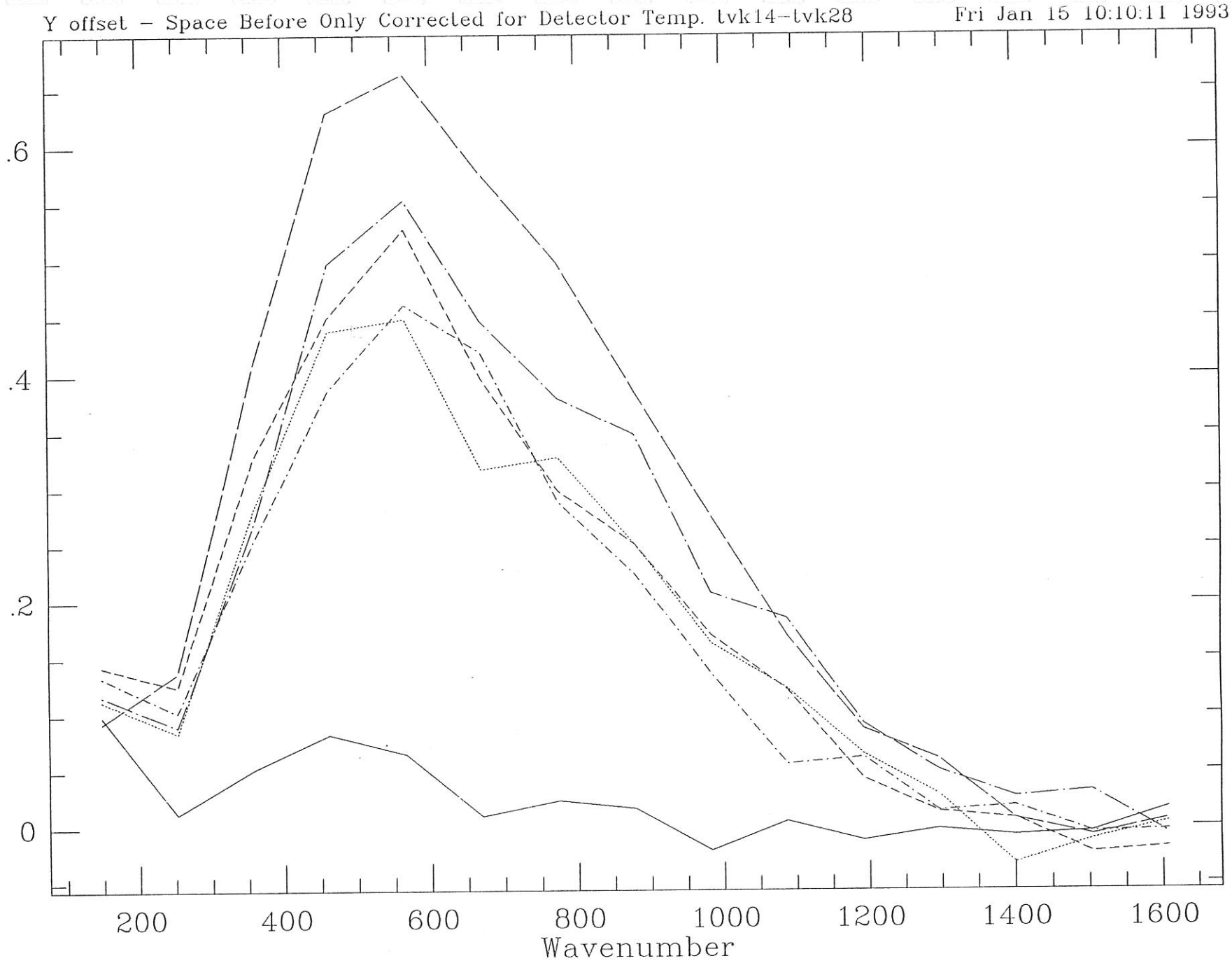
Y offset – Space Before Only Corrected for Detector Temp. tvk14–tvk28
Fri Jan 15 10:10:11 1993
.6
.4
.2
0
200
400
600
800
1000
1200
1400
1600
Wavenumber

Fig. 3-9a

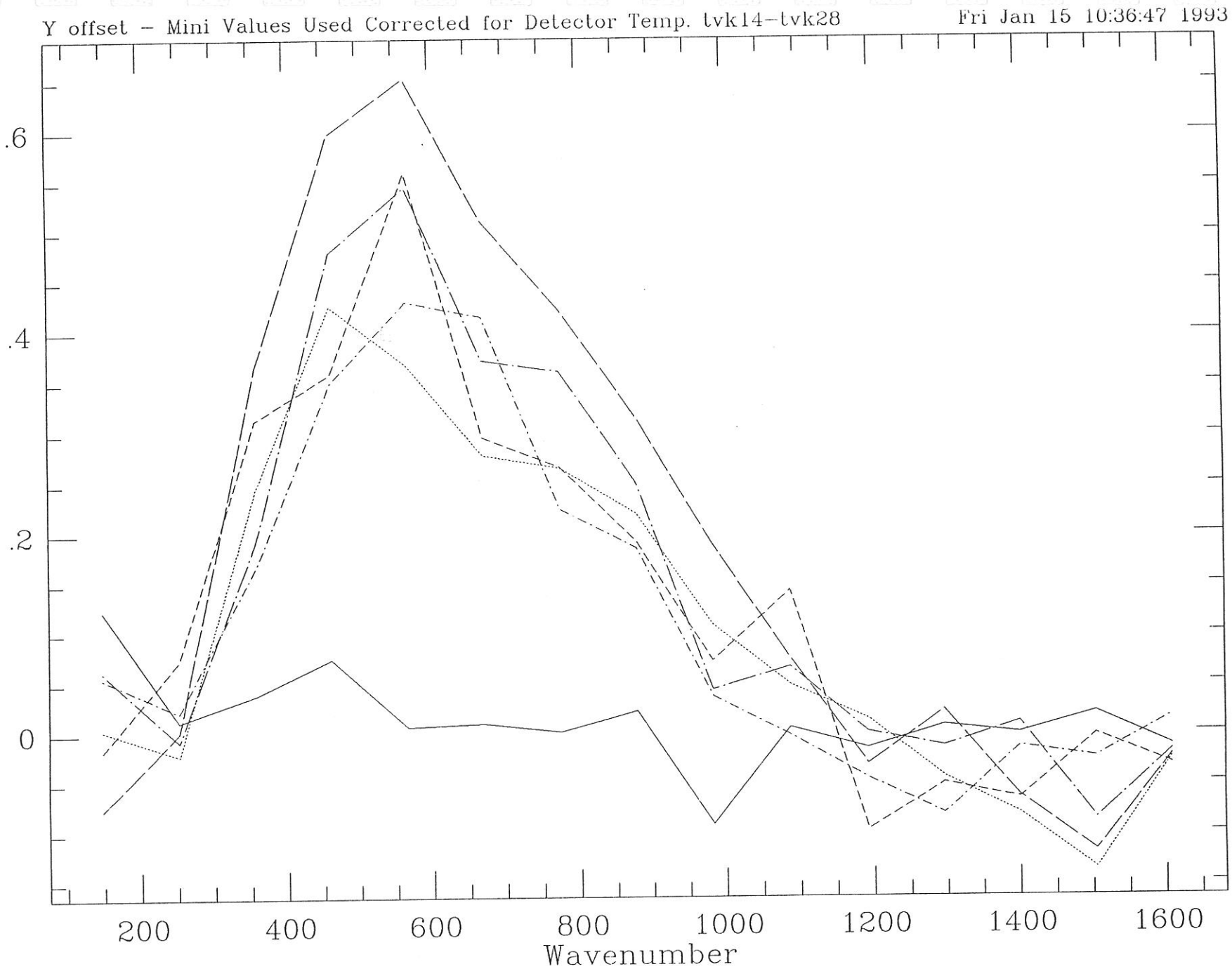
Y offset – Mini Values Used Corrected for Detector Temp. tvk14–tvk28
Fri Jan 15 10:36:47 1993
.6
.4
.2
0
200
400
600
800
1000
1200
1400
1600
Wavenumber

Fig. 3-96

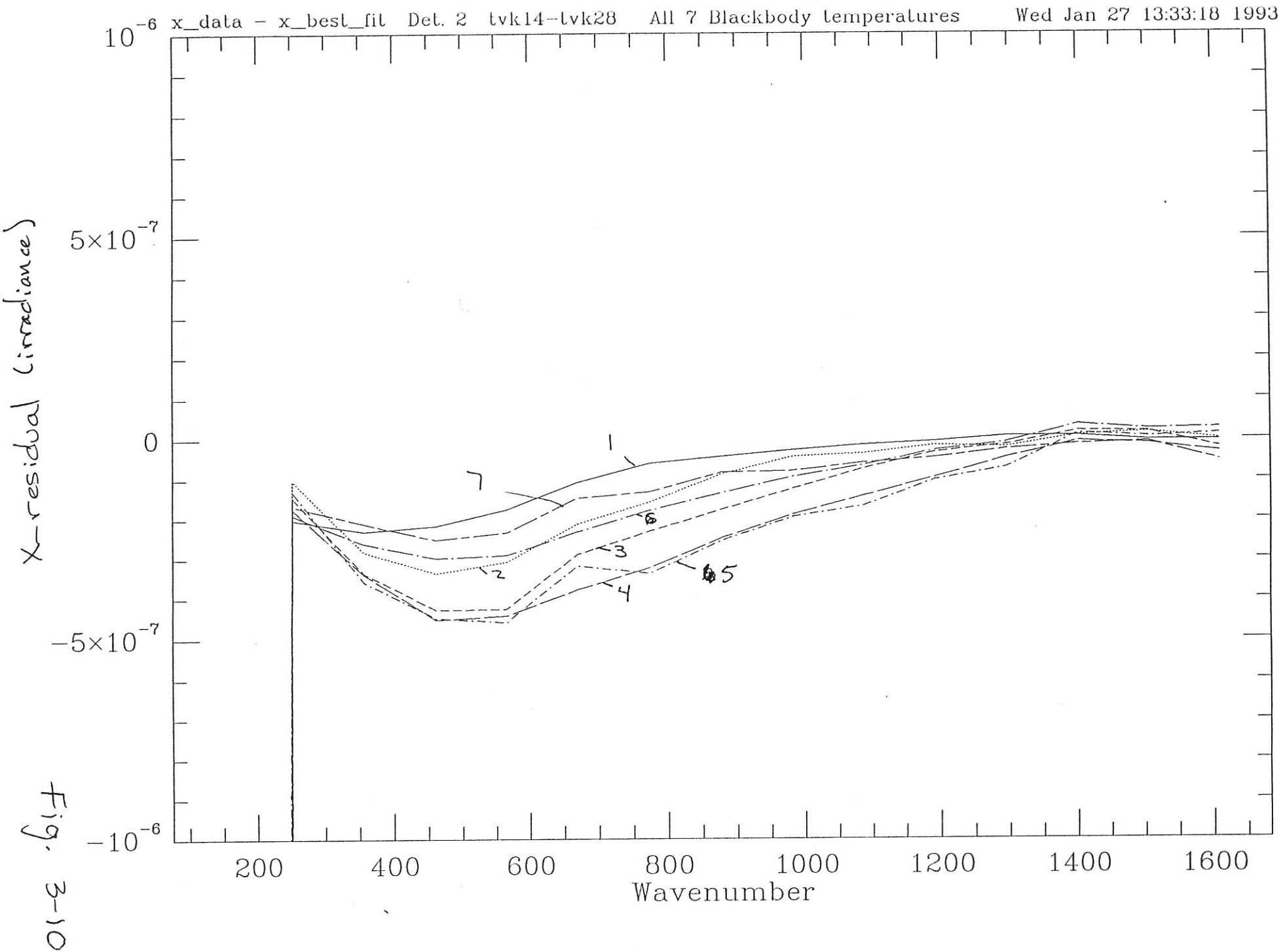
10^-6 x_data - x_best_fit Det. 2 tvk14-tvk28 All 7 Blackbody temperatures Wed Jan 27 13:33:18 1993
X_residual (irradiance)
5×10^-7
0
-5×10^-7
-10^-6
200
400
600
800
1000
1200
1400
1600
Wavenumber
1
2
3
4
5
6
7
8

Fig. 3-10

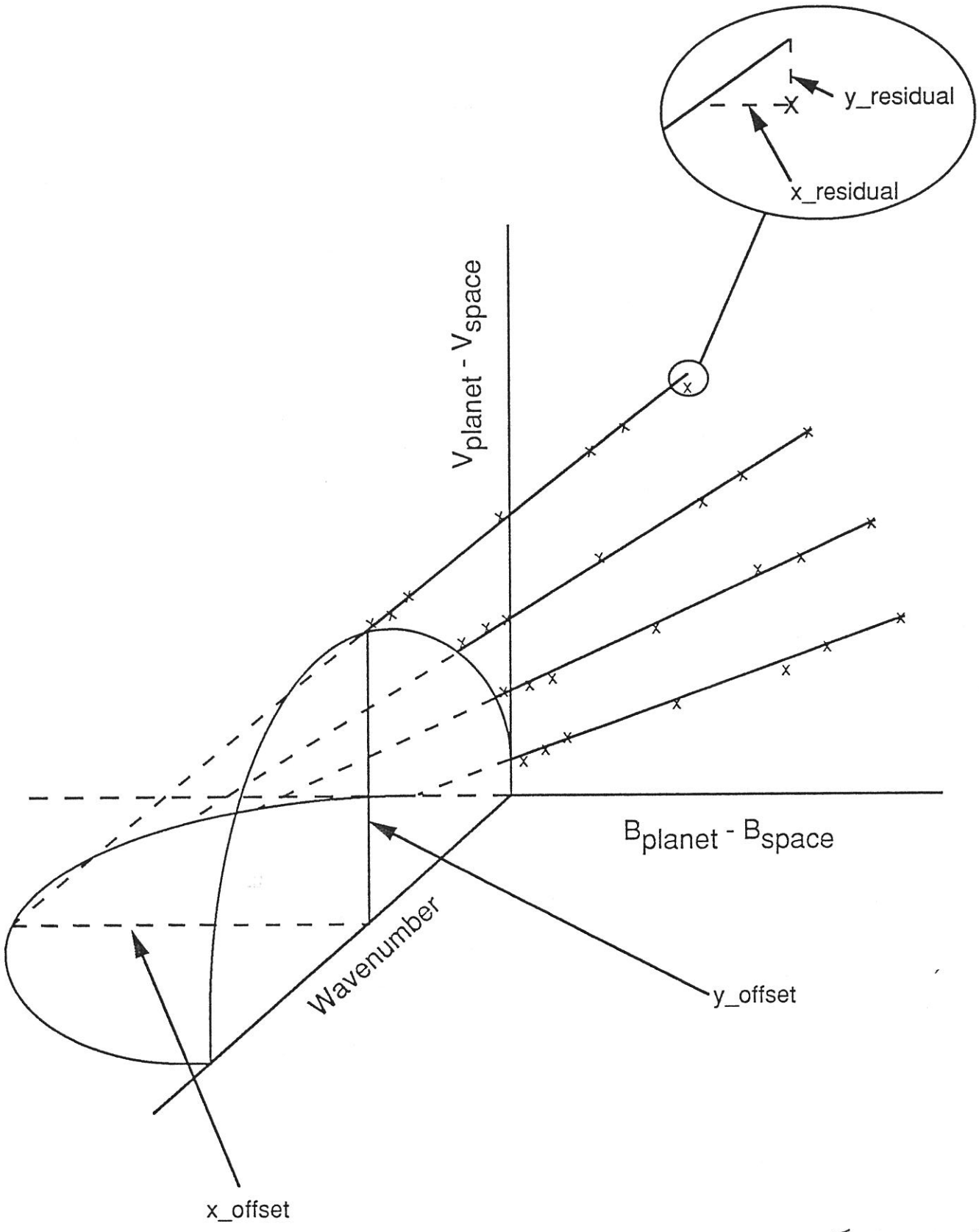
y_residual
x_residual
$V_{planet} - V_{space}$
$B_{planet} - B_{space}$
Wavenumber
y_offset
x_offset

Fig. 3-11

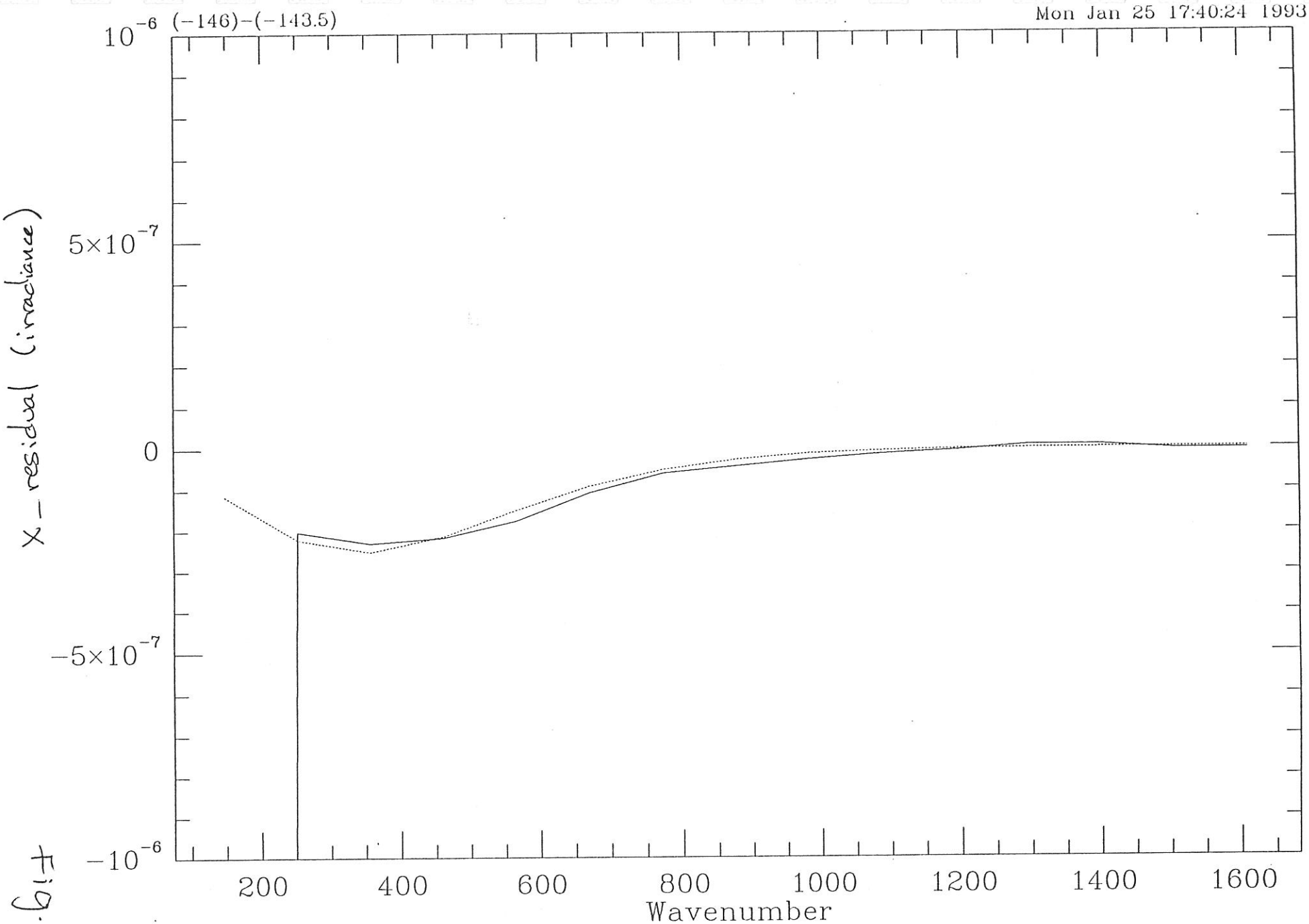
Mon Jan 25 17:40:24 1993
(-146)-(-143.5)
10^{-6}
5×10^{-7}
0
-5×10^{-7}
-10^{-6}
X - residual (radiance)
200
400
600
800
1000
1200
1400
1600
Wavenumber

Fig. 3-12

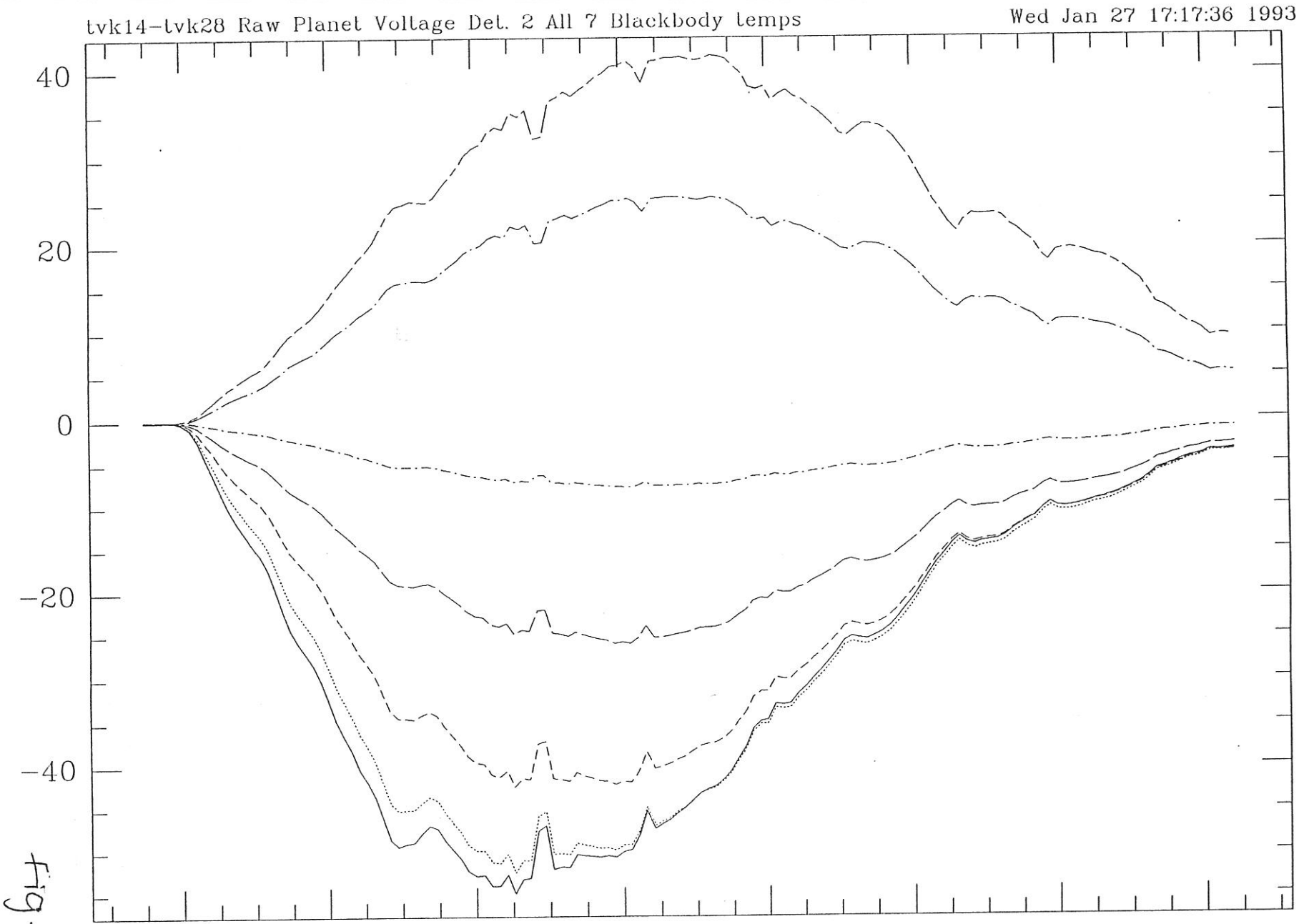
tvk14-tvk28 Raw Planet Voltage Det. 2 All 7 Blackbody temps
Wed Jan 27 17:17:36 1993
40
20
0
-20
-40
200
400
600
800
1000
1200
1400
1600
wavenumber

Fig. 3-13

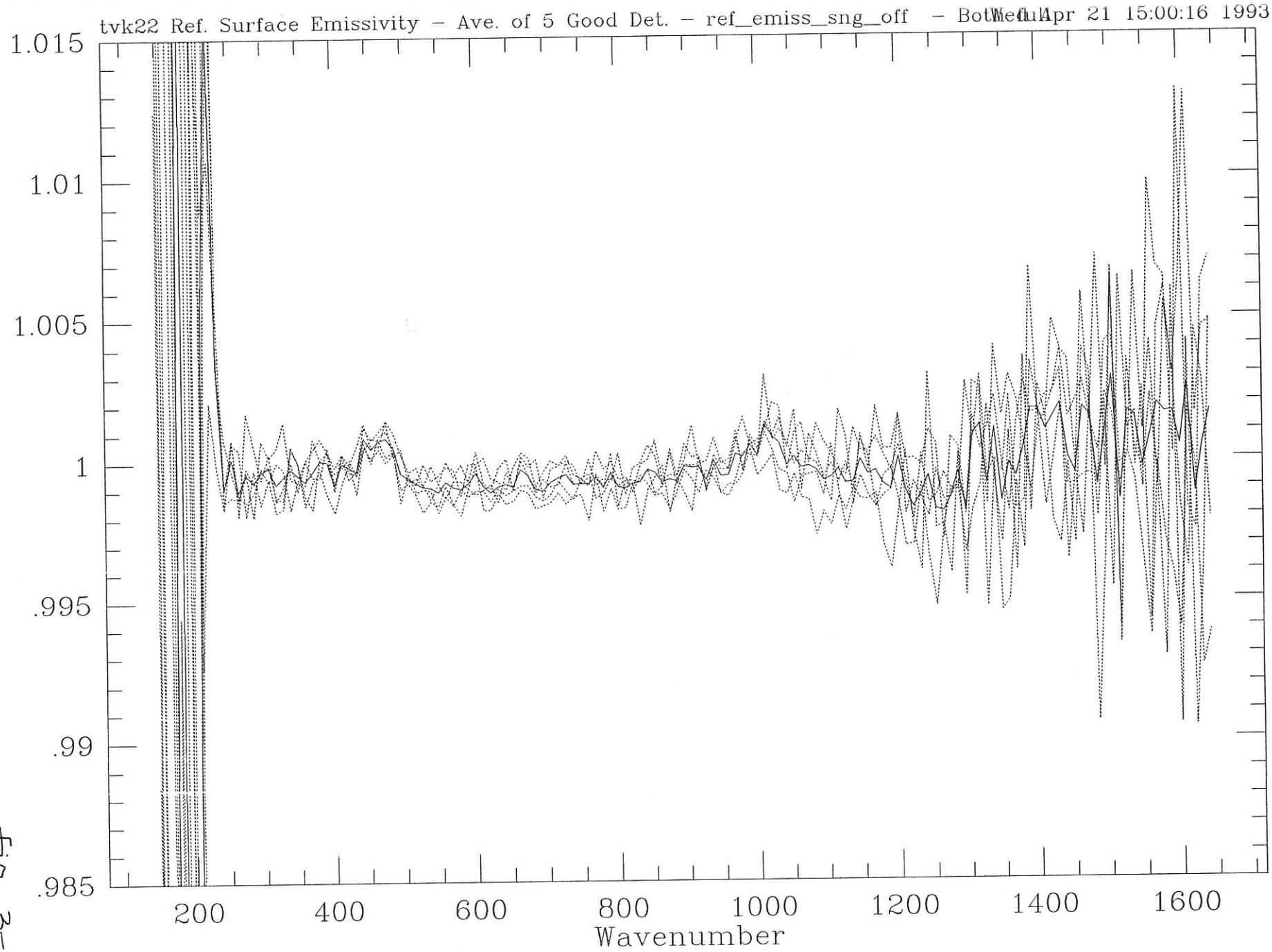
tvk22 Ref. Surface Emissivity - Ave. of 5 Good Det. - ref_emiss_sng_off - Bot
Wed Apr 21 15:00:16 1993
1.015
1.01
1.005
1
.995
.99
.985
200
400
600
800
1000
1200
1400
1600
Wavenumber

fig. 3-14a

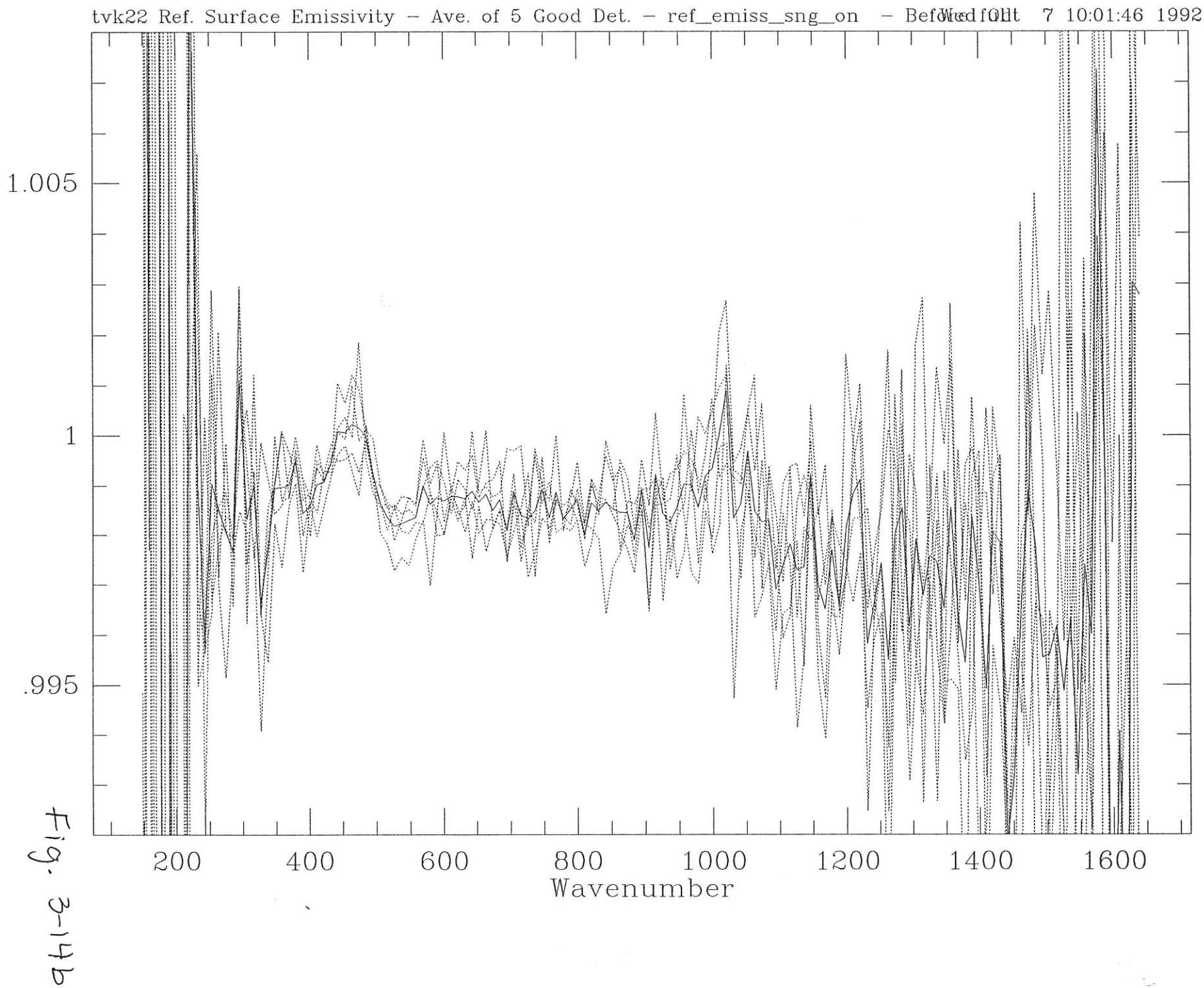
tvk22 Ref. Surface Emissivity - Ave. of 5 Good Det. - ref_emiss_sng_on - Before Test
Wed Oct 7 10:01:46 1992
1.005
1
.995
200
400
600
800
1000
1200
1400
1600
Wavenumber

Fig. 3-14b

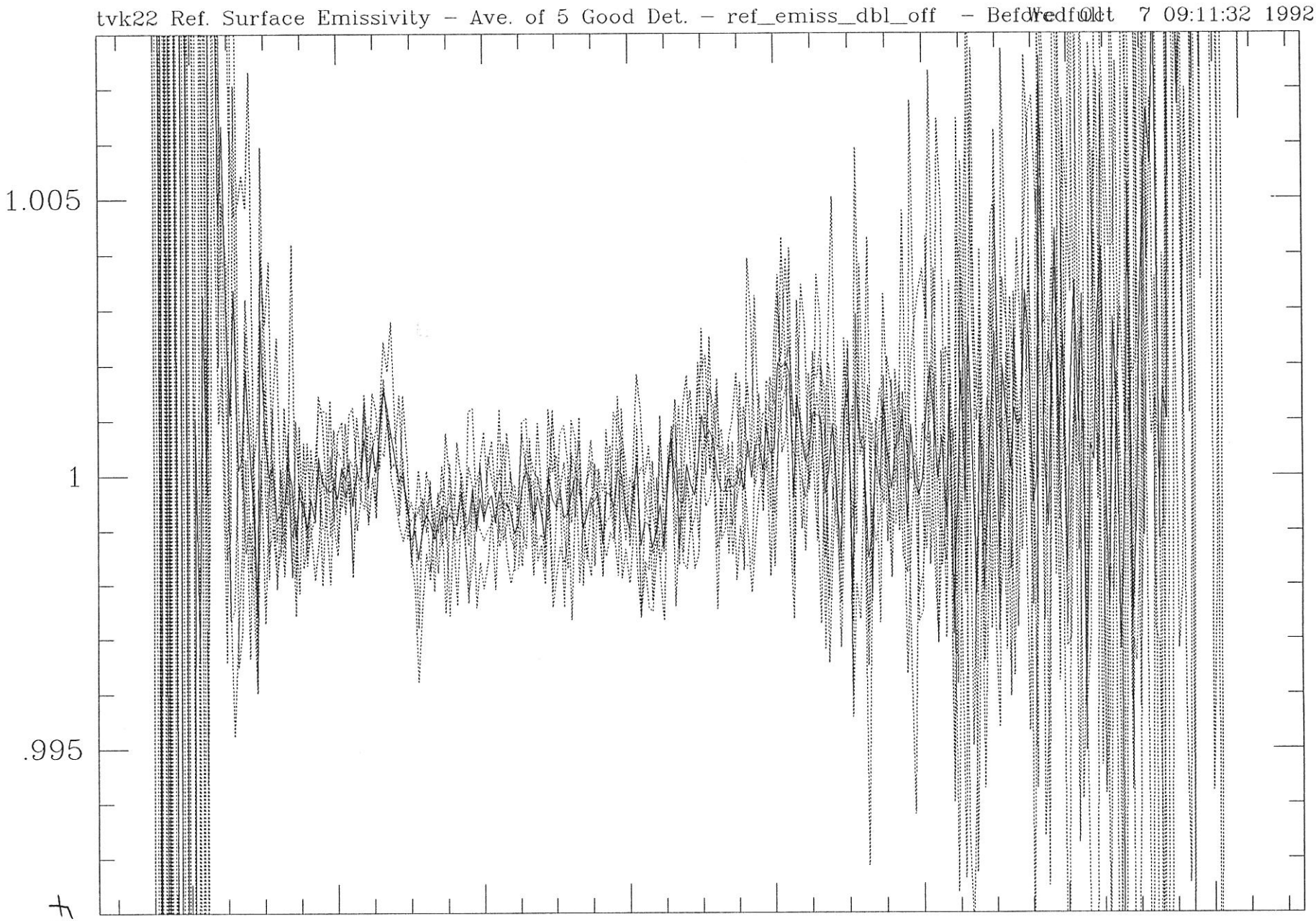
tvk22 Ref. Surface Emissivity - Ave. of 5 Good Det. - ref_emiss_dbl_off - Before Wed Oct 7 09:11:32 1992
1.005
1
.995
200
400
600
800
1000
1200
1400
1600
Wavenumber

fig. 3-14c

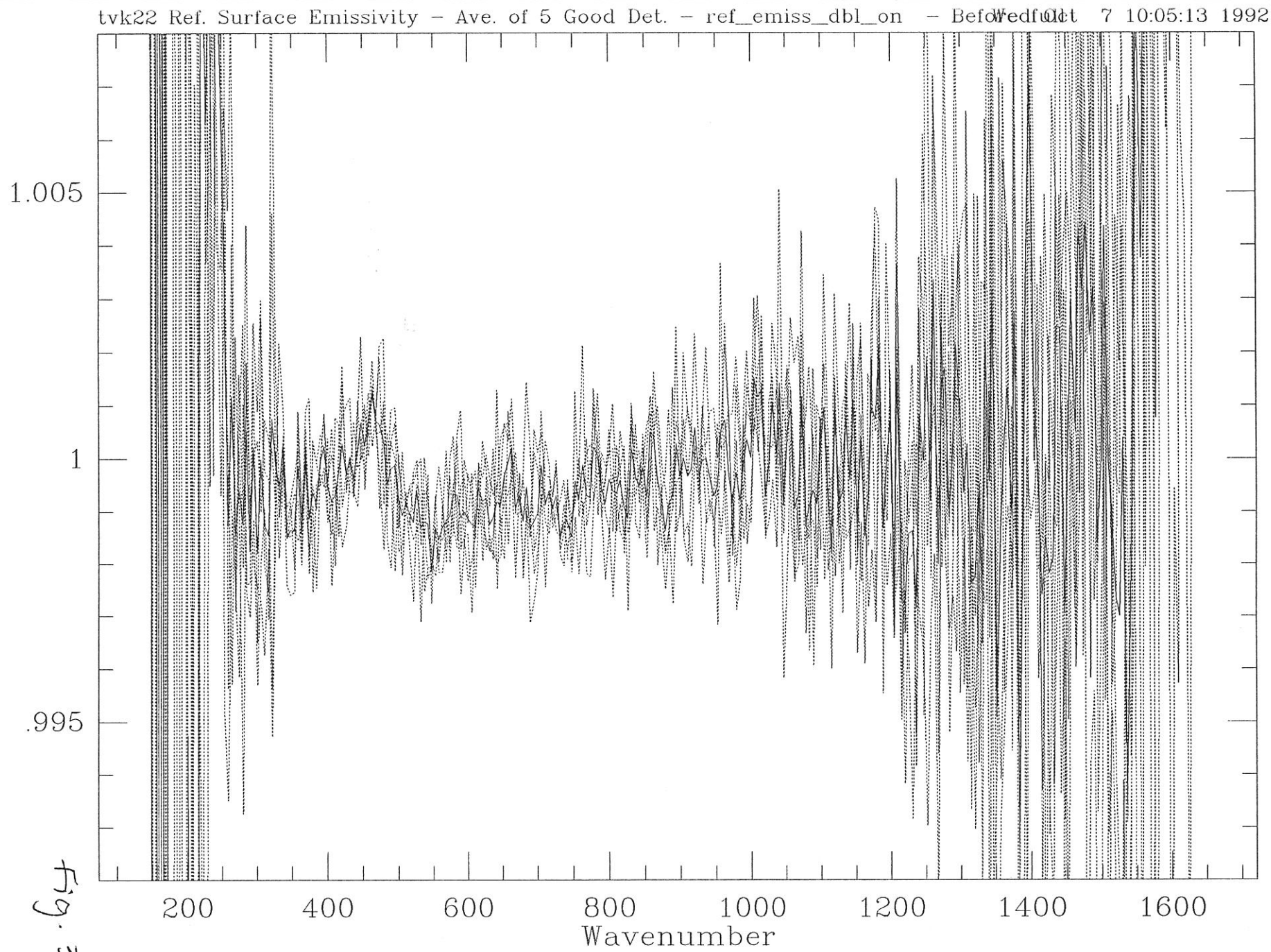
tvk22 Ref. Surface Emissivity - Ave. of 5 Good Det. - ref_emiss_dbl_on - Before Wed Oct 7 10:05:13 1992
1.005
1
.995
200
400
600
800
1000
1200
1400
1600
Wavenumber

Fig. 3-14d

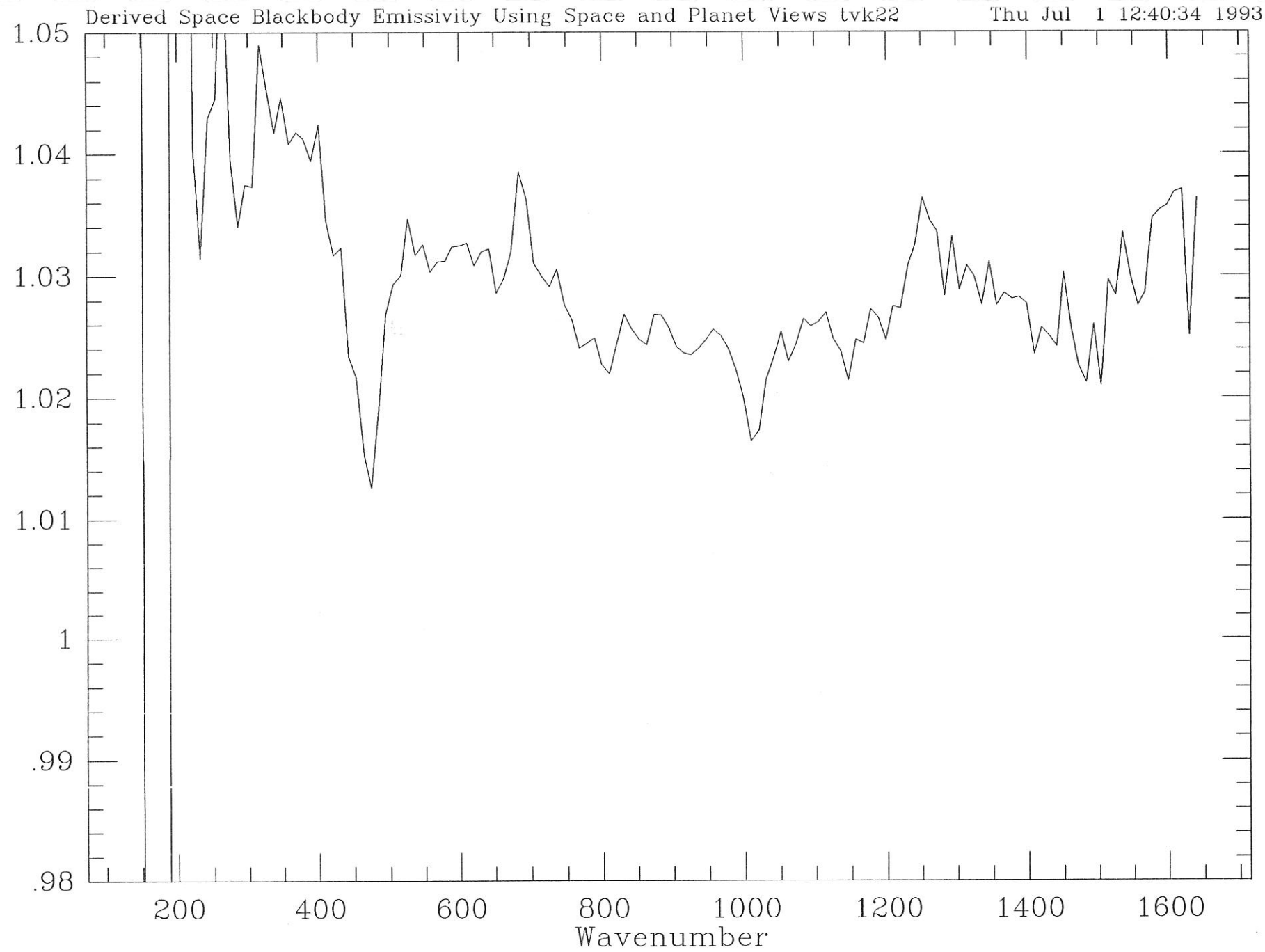
Derived Space Blackbody Emissivity Using Space and Planet Views tvk22
Thu Jul 1 12:40:34 1993
1.05
1.04
1.03
1.02
1.01
1
.99
.98
200
400
600
800
1000
1200
1400
1600
Wavenumber

Fig. 3-15

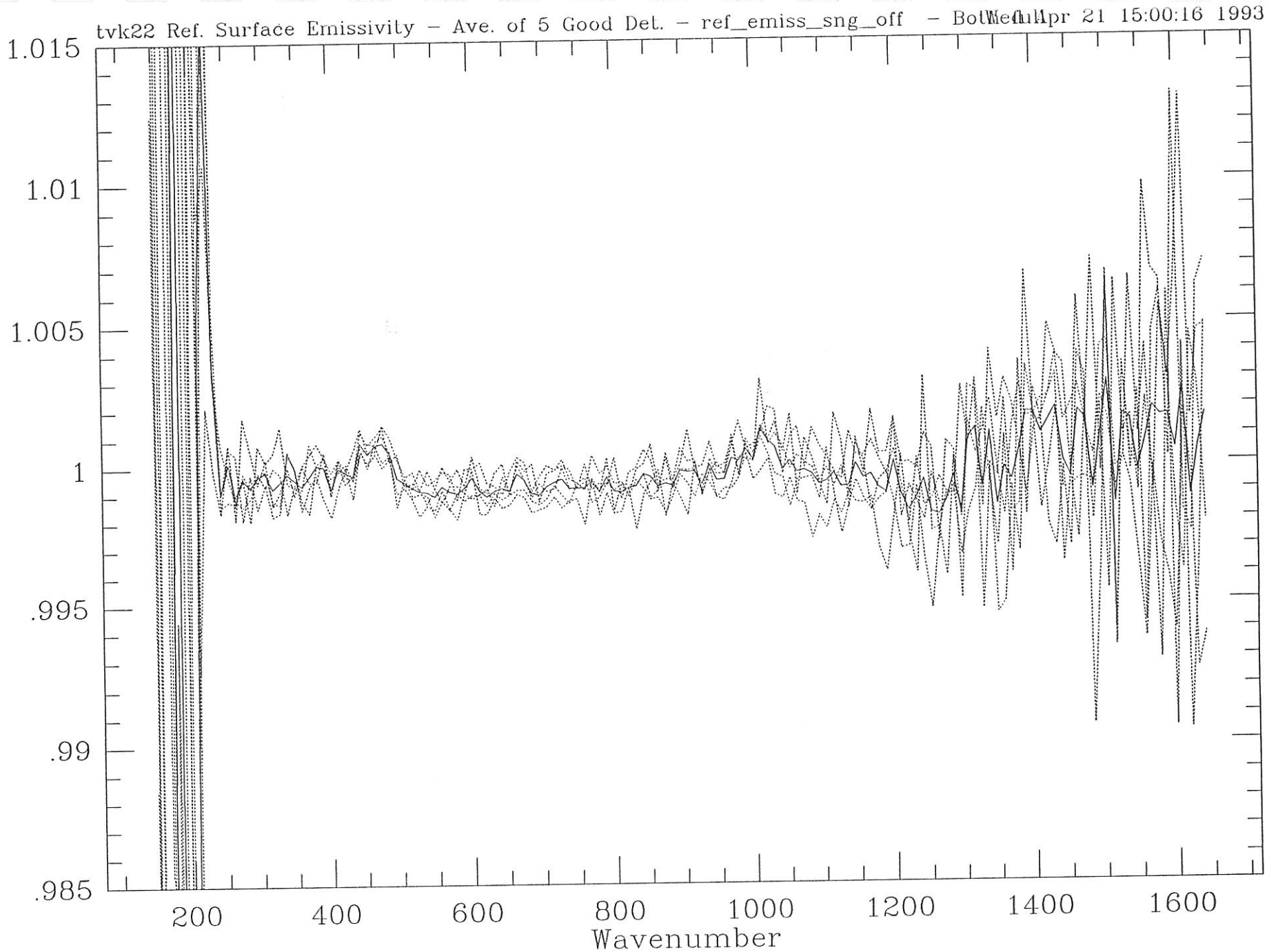
tvk22 Ref. Surface Emissivity - Ave. of 5 Good Det. - ref_emiss_sng_off - Bot Wed Apr 21 15:00:16 1993
1.015
1.01
1.005
1
.995
.99
.985
200
400
600
800
1000
1200
1400
1600
Wavenumber

Fig. 3-16e

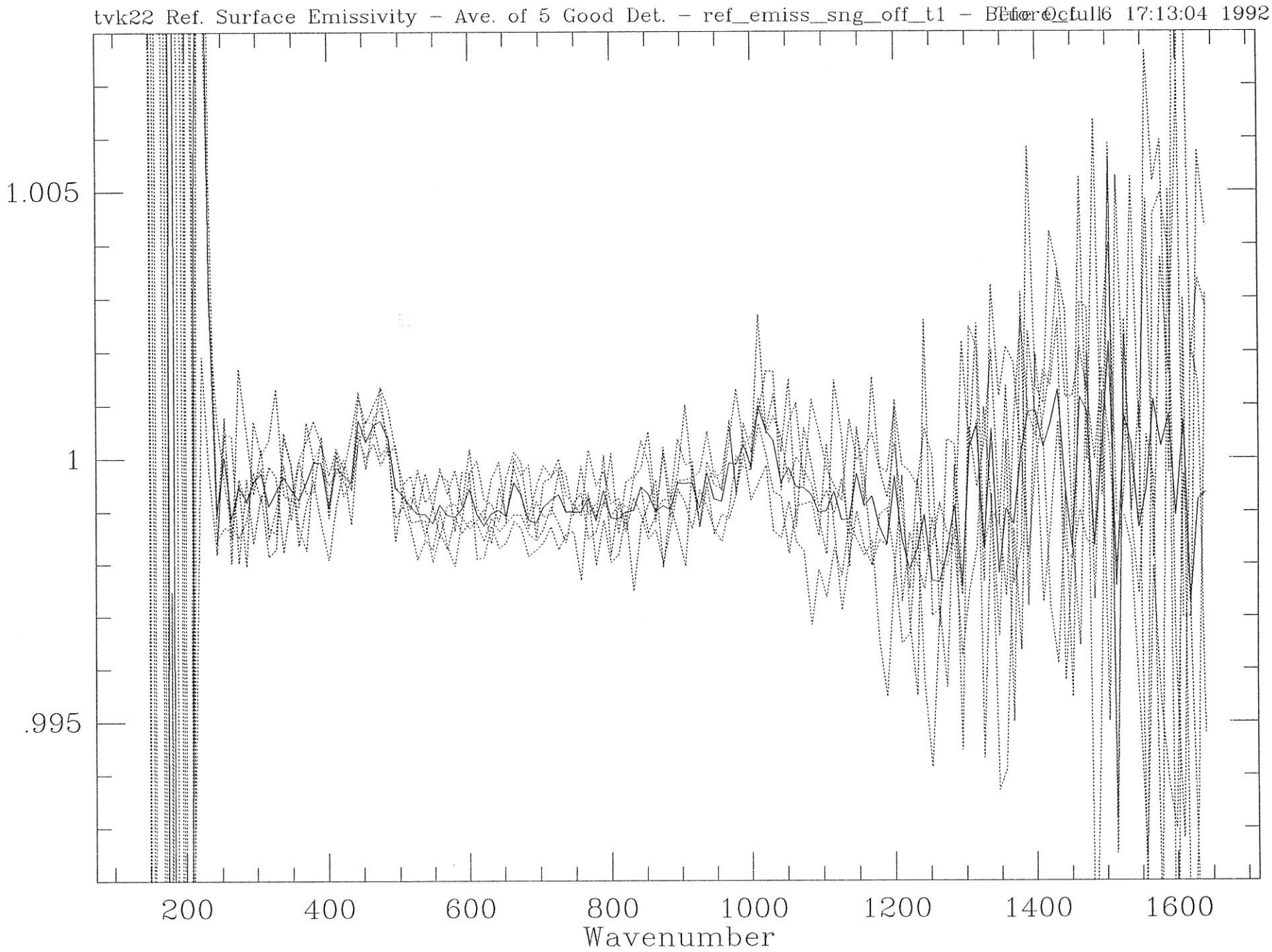
tvk22 Ref. Surface Emissivity - Ave. of 5 Good Det. - ref_emiss_sng_off_t1 - Before Cal
Oct 16 17:13:04 1992
1.005
1
.995
200
400
600
800
1000
1200
1400
1600
Wavenumber

Fig. 3-16b

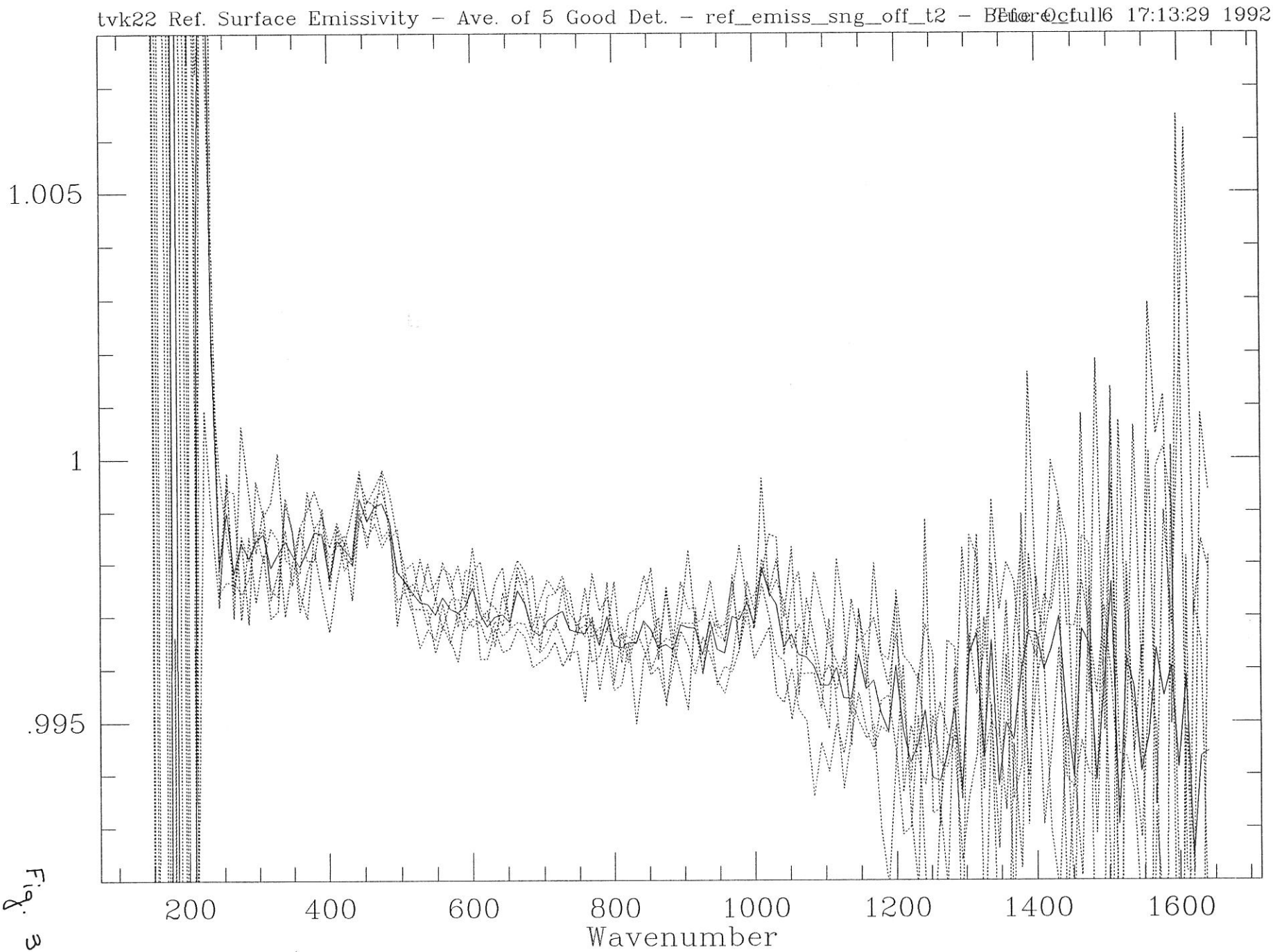
tvk22 Ref. Surface Emissivity - Ave. of 5 Good Det. - ref_emiss_sng_off_t2 - Before cal
Oct 16 17:13:29 1992
1.005
1
.995
200
400
600
800
1000
1200
1400
1600
Wavenumber

Fig. 3-16c

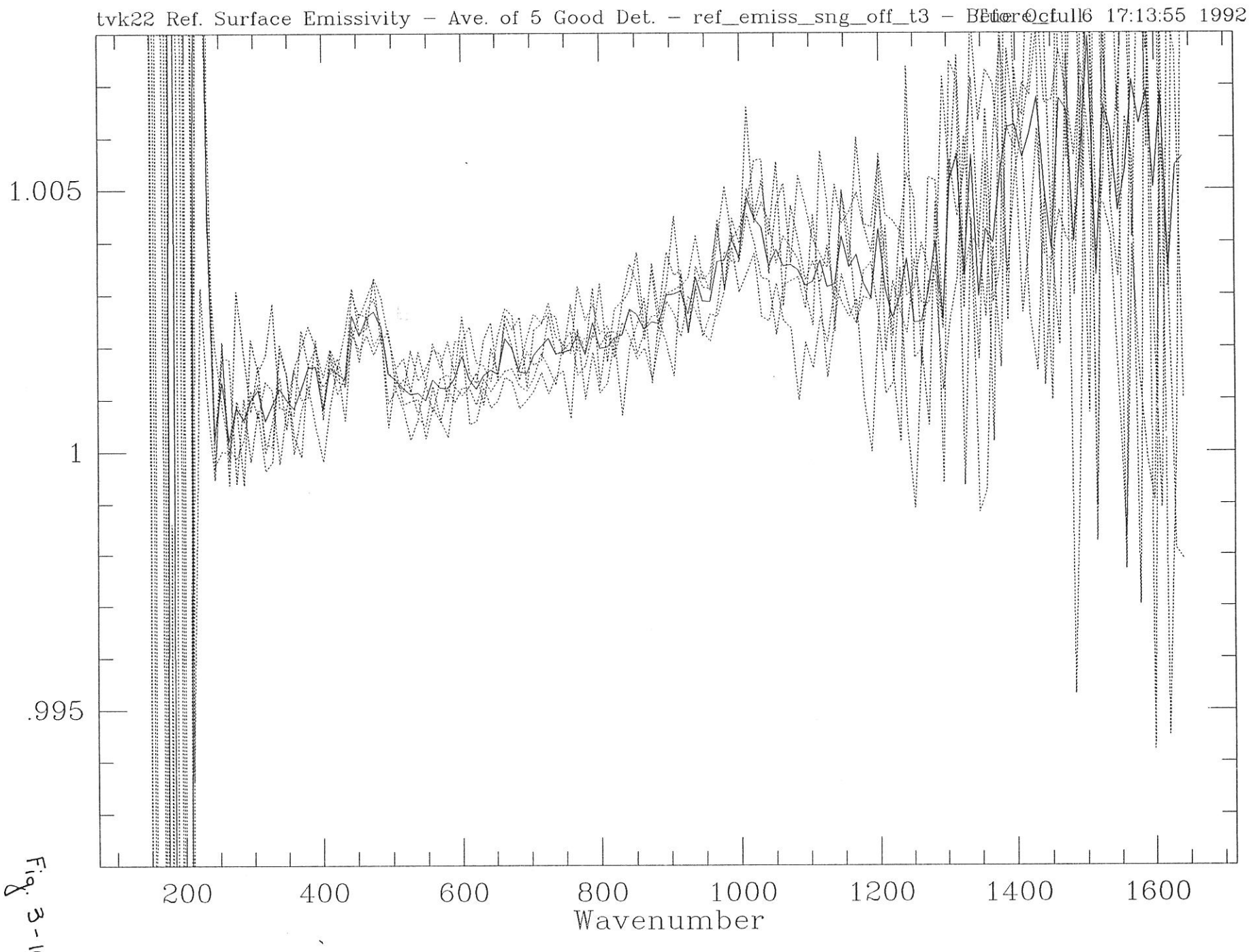
tvk22 Ref. Surface Emissivity – Ave. of 5 Good Det. – ref_emiss_sng_off_t3 – Before Oct 6 17:13:55 1992
1.005
1
.995
200
400
600
800
1000
1200
1400
1600
Wavenumber

Fig. 3-16d

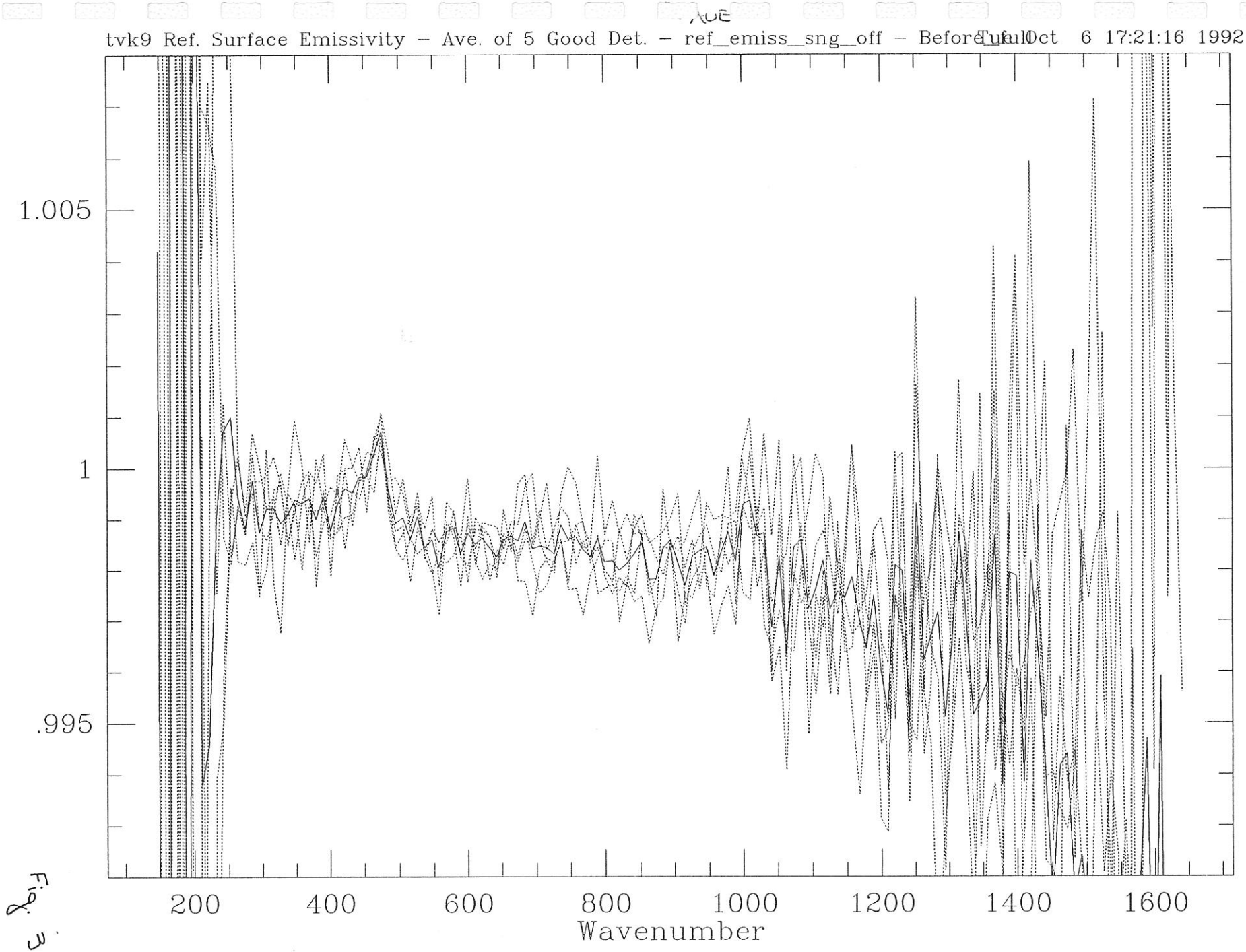
tvk9 Ref. Surface Emissivity - Ave. of 5 Good Det. - ref_emiss_sng_off - Before_ful
Tue Oct 6 17:21:16 1992
1.005
1
.995
200
400
600
800
1000
1200
1400
1600
Wavenumber

Fig. 3-17e

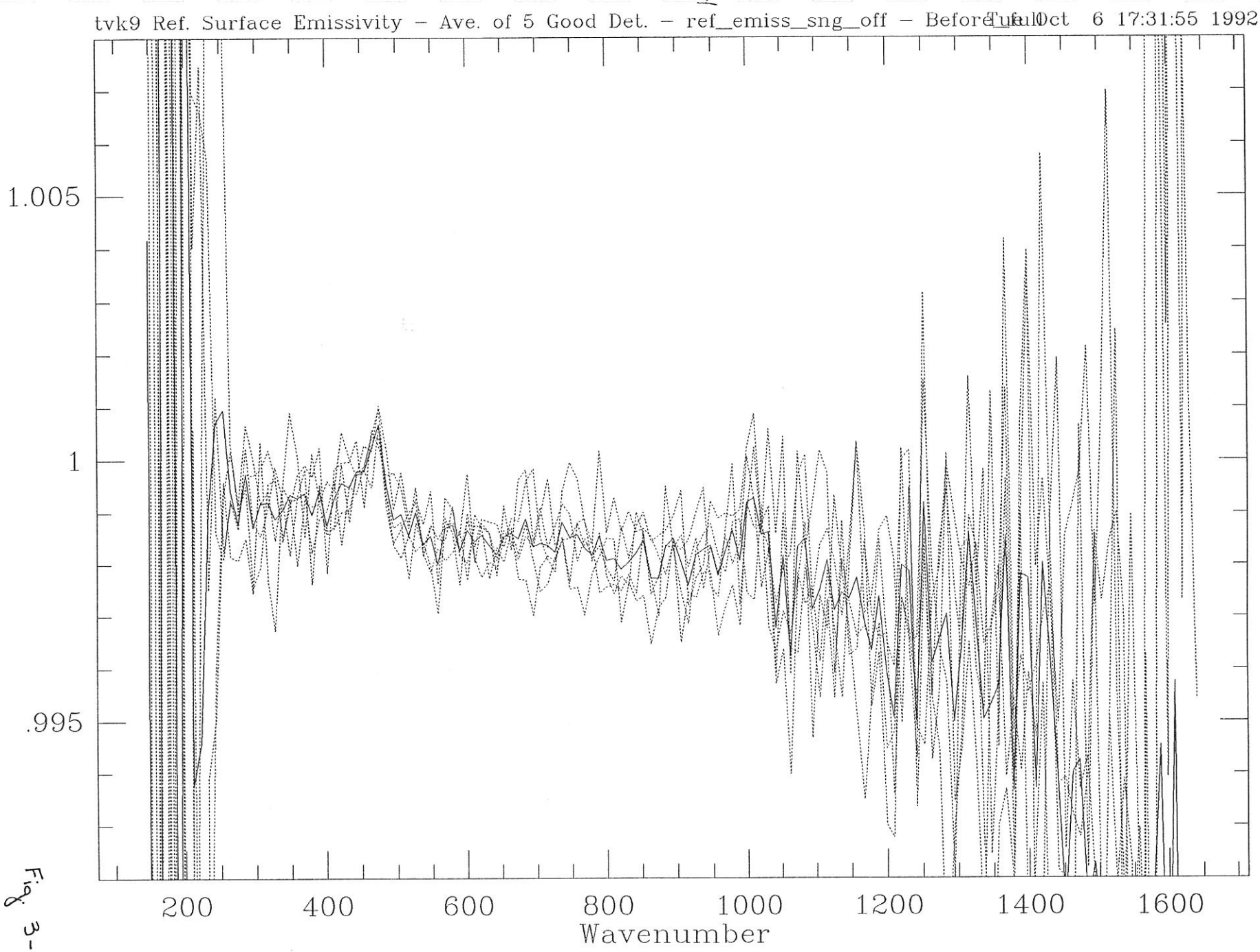
tvk9 Ref. Surface Emissivity - Ave. of 5 Good Det. - ref_emiss_sng_off - Before Tue Oct 6 17:31:55 1992
1.005
1
.995
200
400
600
800
1000
1200
1400
1600
Wavenumber

Fig. 3-17b

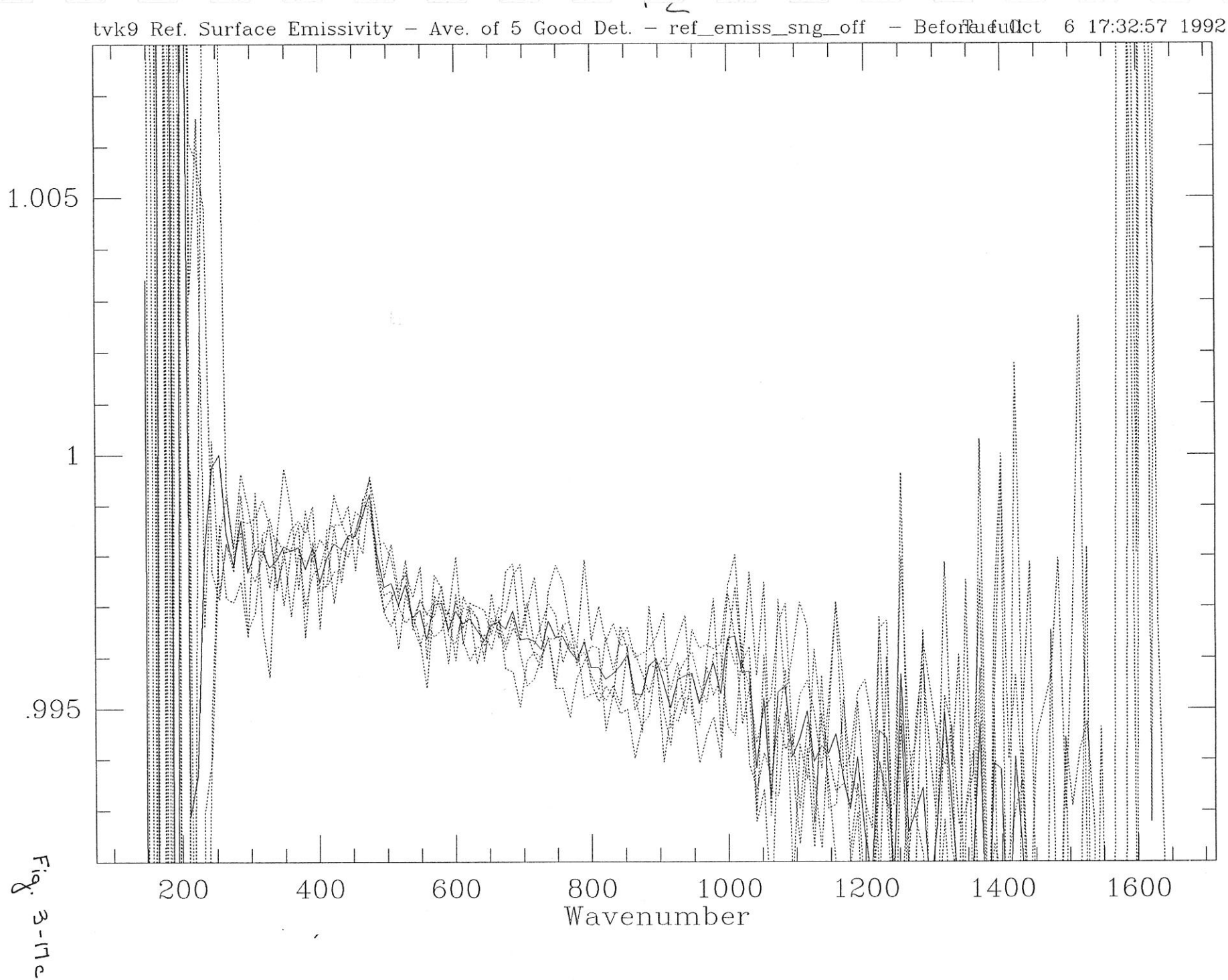
tvk9 Ref. Surface Emissivity - Ave. of 5 Good Det. - ref_emiss_sng_off - Before cal Tue Oct 6 17:32:57 1992
1.005
1
.995
200
400
600
800
1000
1200
1400
1600
Wavenumber

Fig. 3-17c

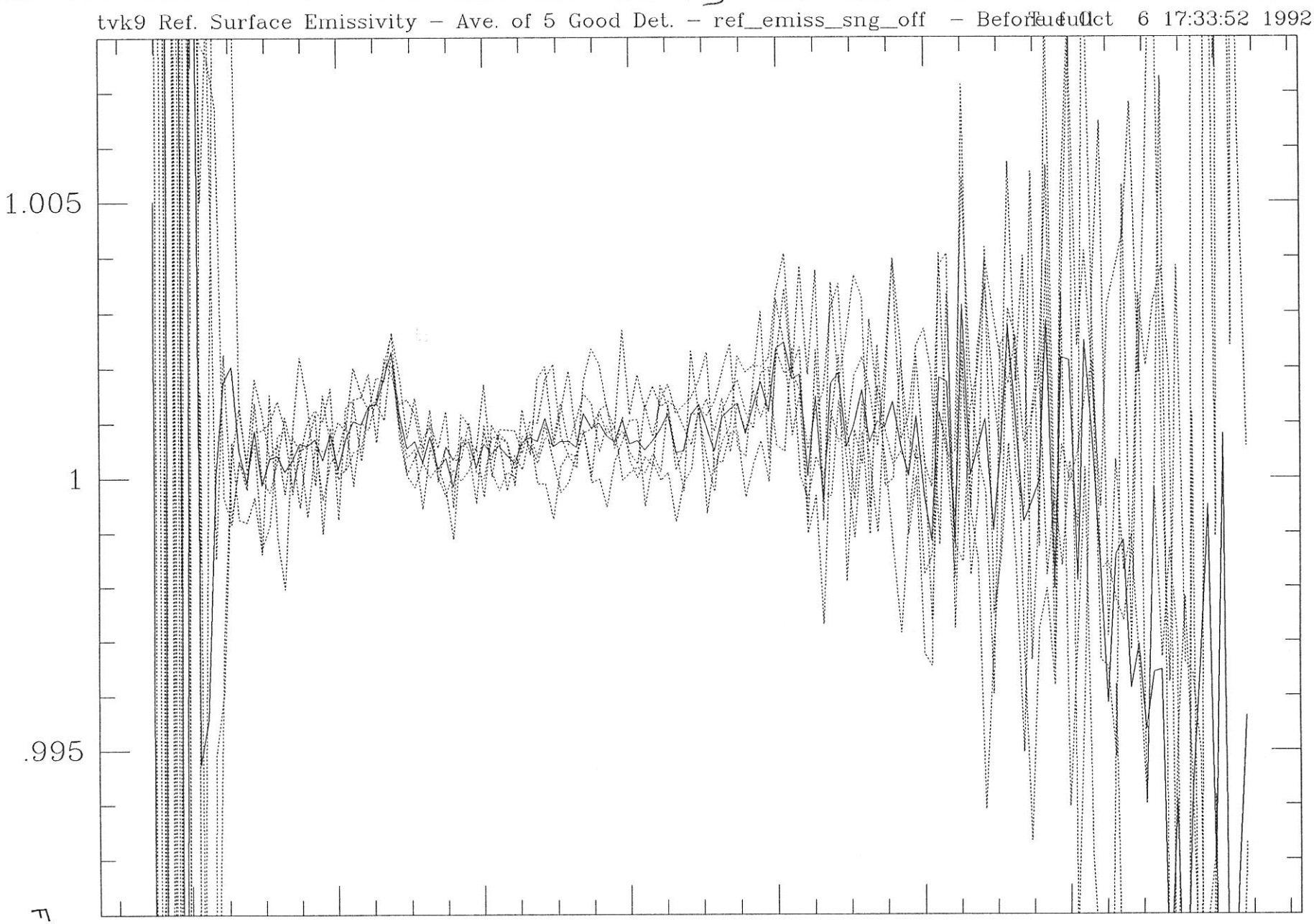
tvk9 Ref. Surface Emissivity - Ave. of 5 Good Det. - ref_emiss_sng_off - Before cal Tue Oct 6 17:33:52 1992
1.005
1
.995
200
400
600
800
1000
1200
1400
1600
Wavenumber

Fig. 3-17d

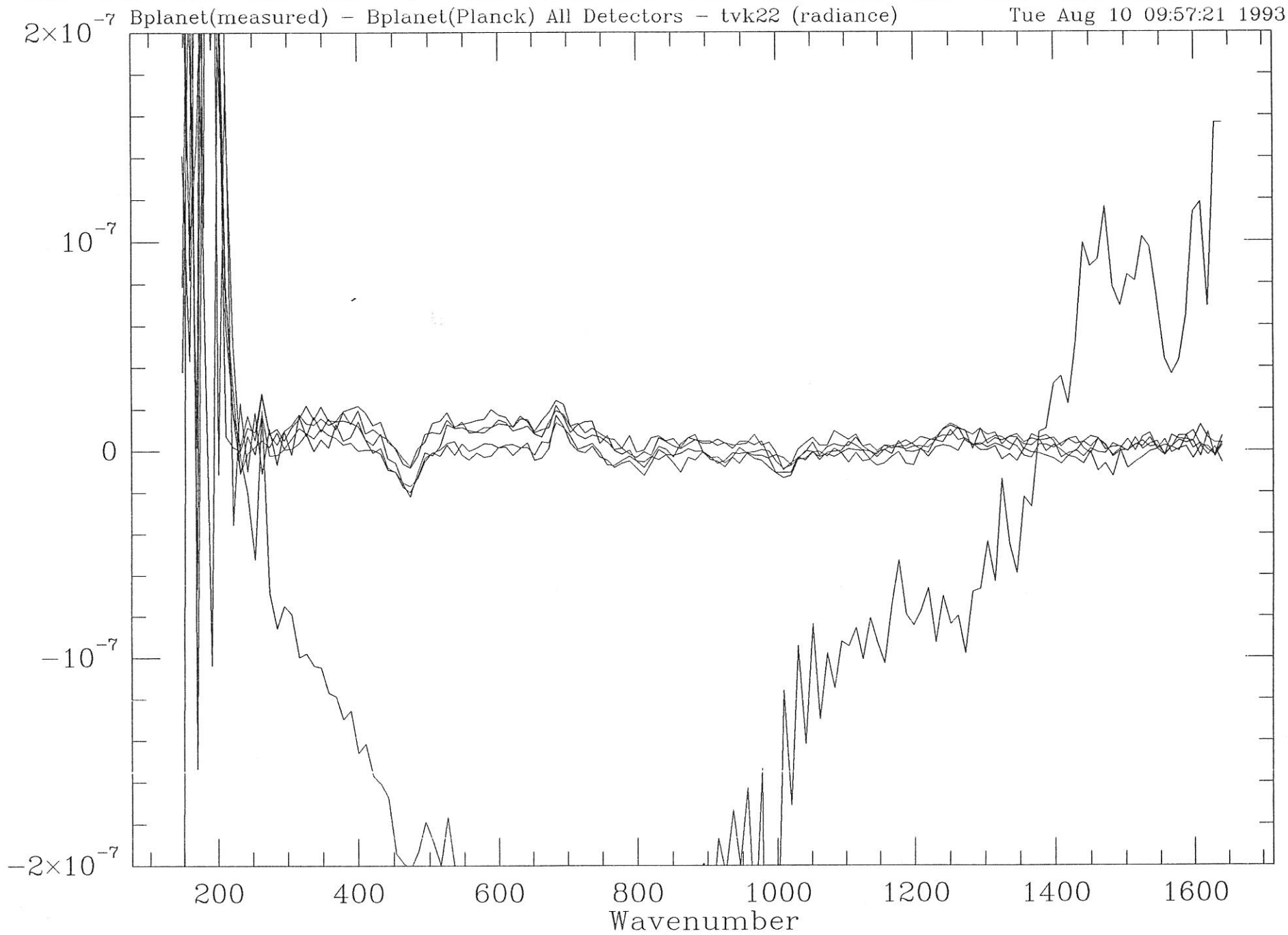
Bplanet(measured) − Bplanet(Planck) All Detectors − tvk22 (radiance)
Tue Aug 10 09:57:21 1993
2×10^-7
10^-7
0
−10^-7
−2×10^-7
200
400
600
800
1000
1200
1400
1600
Wavenumber

Fig. 3-18

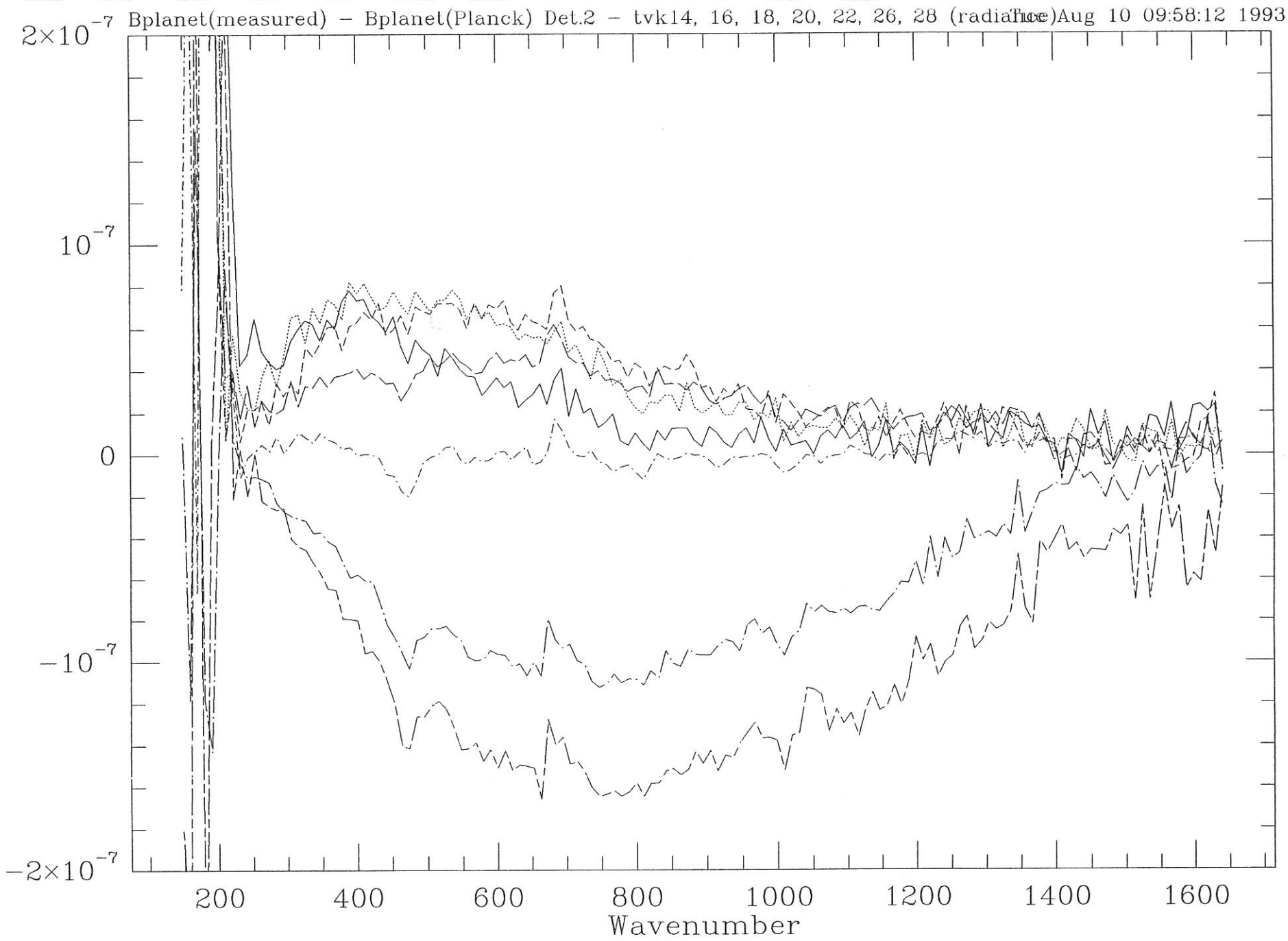
Bplanet(measured) − Bplanet(Planck) Det.2 − tvk14, 16, 18, 20, 22, 26, 28 (radiance)
Tue Aug 10 09:58:12 1993
2×10⁻⁷
10⁻⁷
0
−10⁻⁷
−2×10⁻⁷
200
400
600
800
1000
1200
1400
1600
Wavenumber

fig. 3-19a

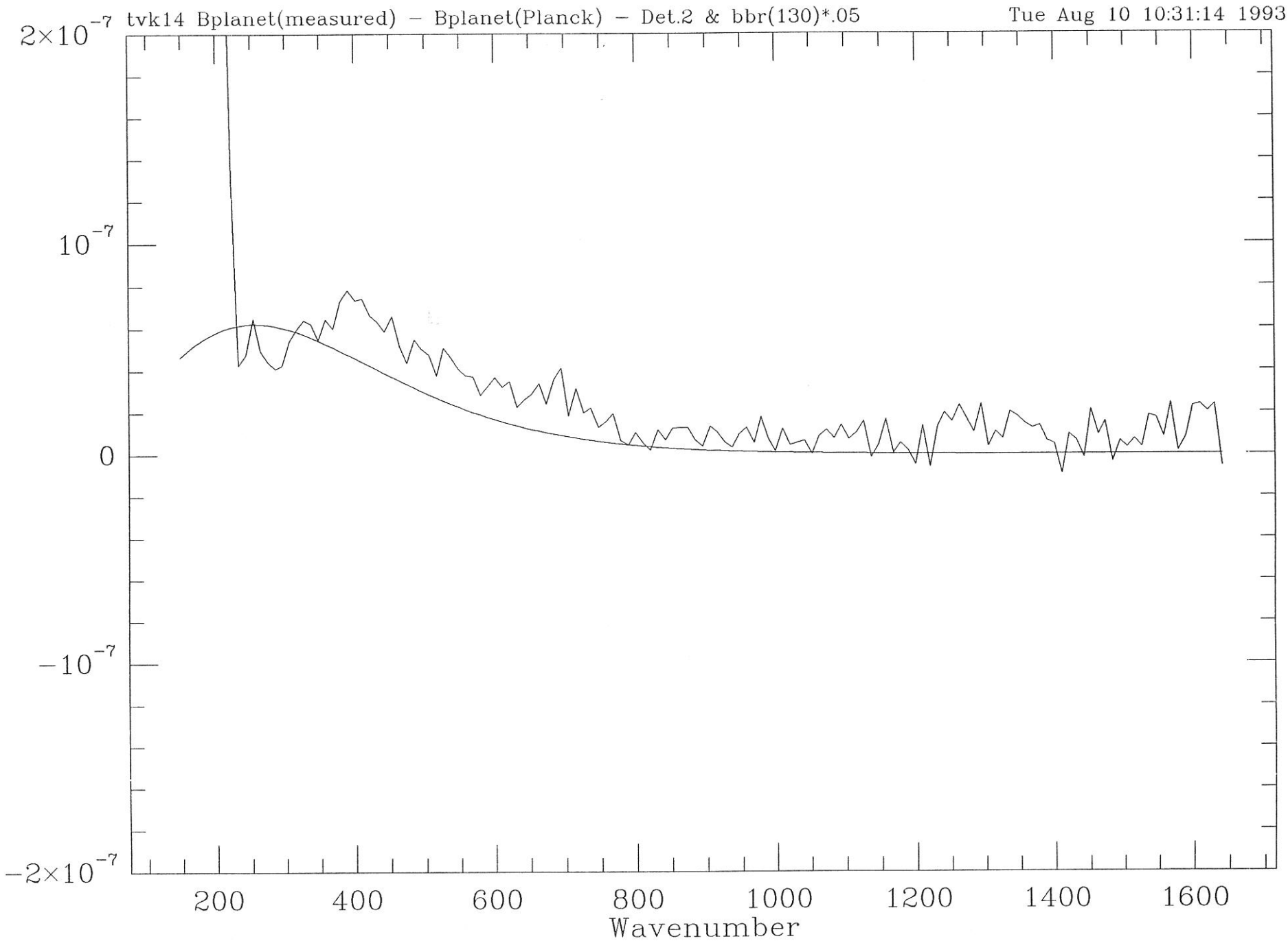
tvk14 Bplanet(measured) − Bplanet(Planck) − Det.2 & bbr(130)*.05
Tue Aug 10 10:31:14 1993
2×10^-7
10^-7
0
−10^-7
−2×10^-7
200
400
600
800
1000
1200
1400
1600
Wavenumber

fig. 3-19

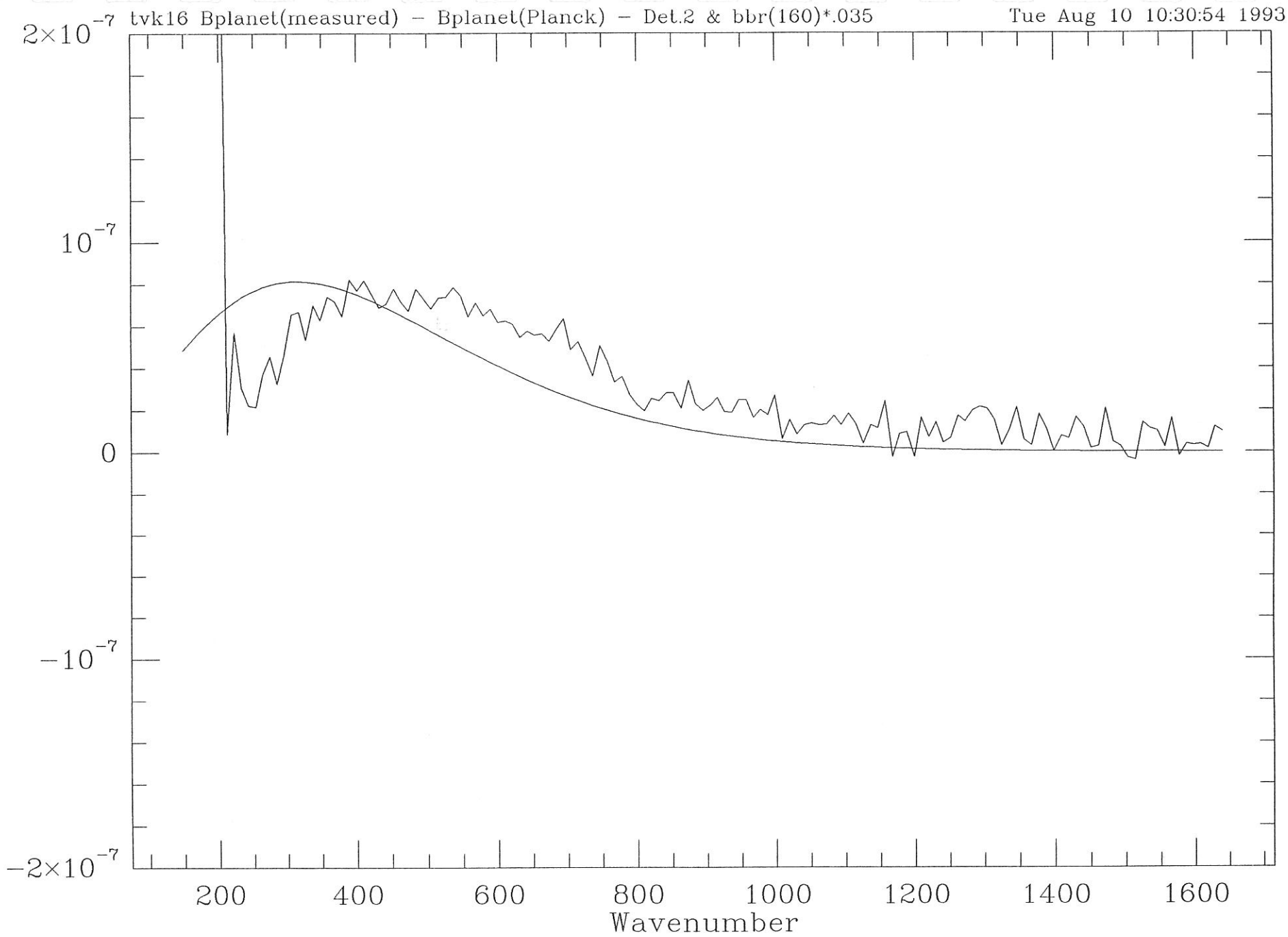
tvk16 Bplanet(measured) − Bplanet(Planck) − Det.2 & bbr(160)*.035
Tue Aug 10 10:30:54 1993
2×10^-7
10^-7
0
−10^-7
−2×10^-7
200
400
600
800
1000
1200
1400
1600
Wavenumber

Fig. 3-19c

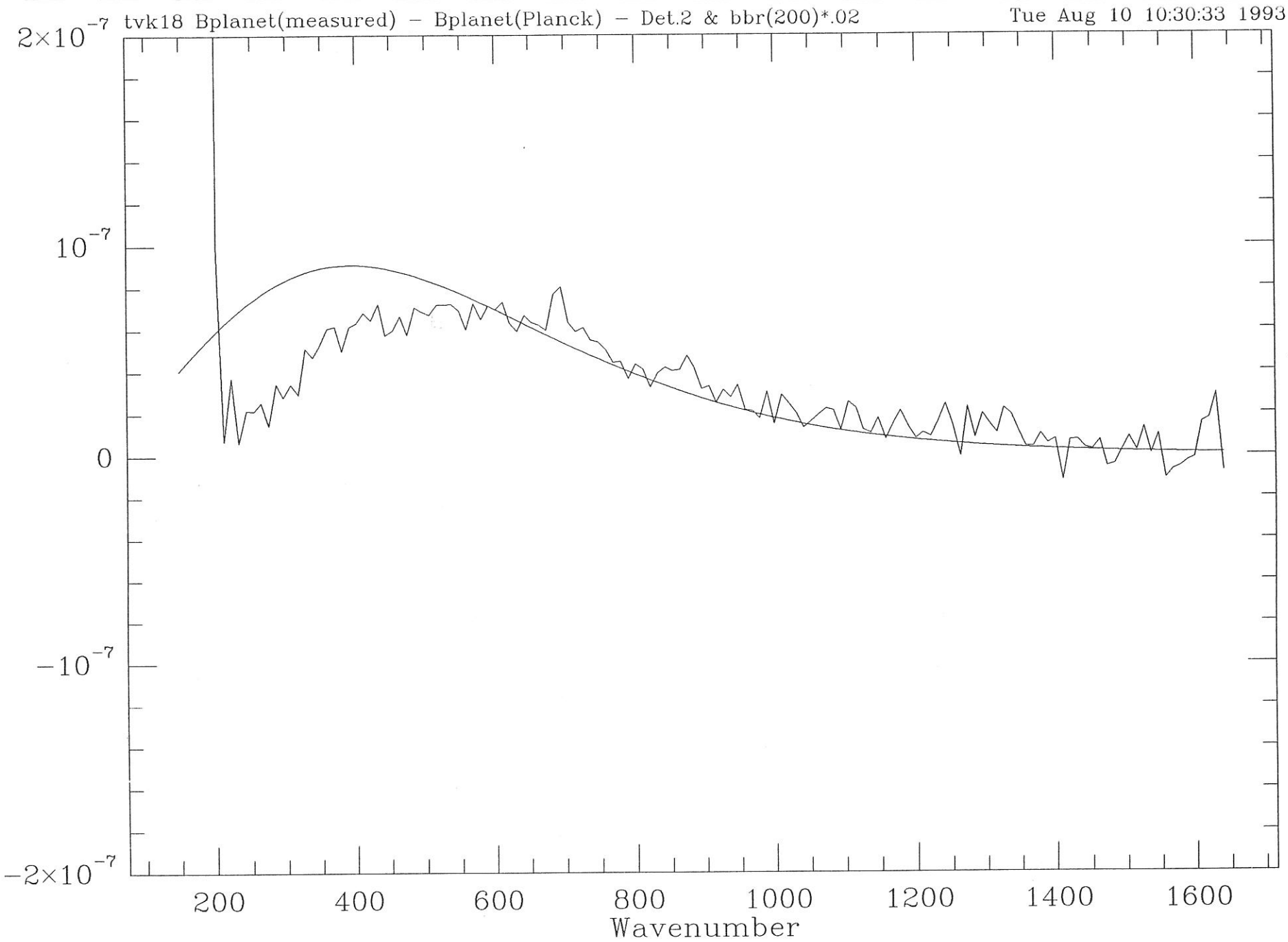
tvk18 Bplanet(measured) − Bplanet(Planck) − Det.2 & bbr(200)*.02
Tue Aug 10 10:30:33 1993
2×10^-7
10^-7
0
−10^-7
−2×10^-7
200
400
600
800
1000
1200
1400
1600
Wavenumber

Fig. 3-19d

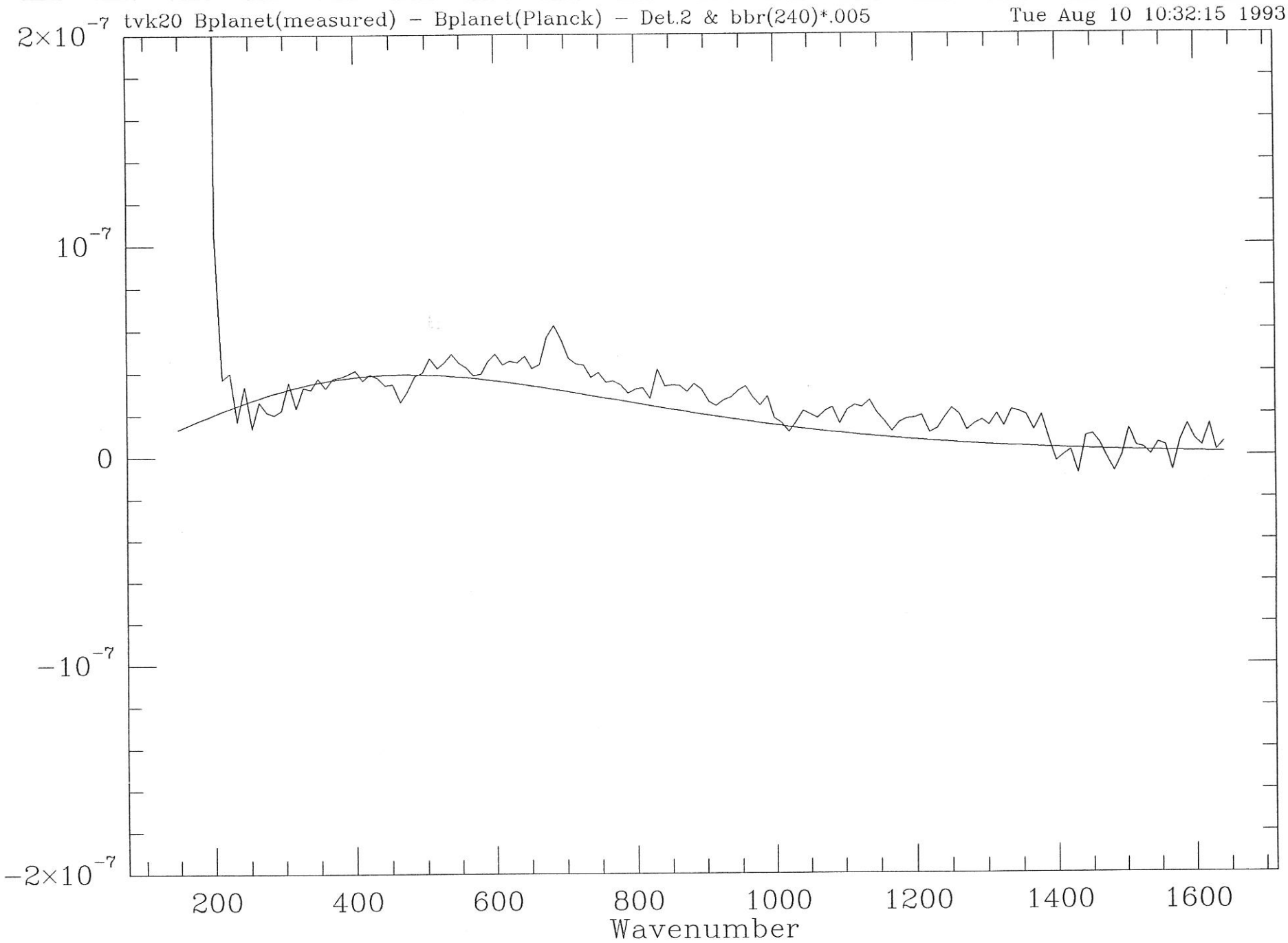
2×10^-7 tvk20 Bplanet(measured) − Bplanet(Planck) − Det.2 & bbr(240)*.005
Tue Aug 10 10:32:15 1993
10^-7
0
−10^-7
−2×10^-7
200
400
600
800
1000
1200
1400
1600
Wavenumber

Fig. 3-19e

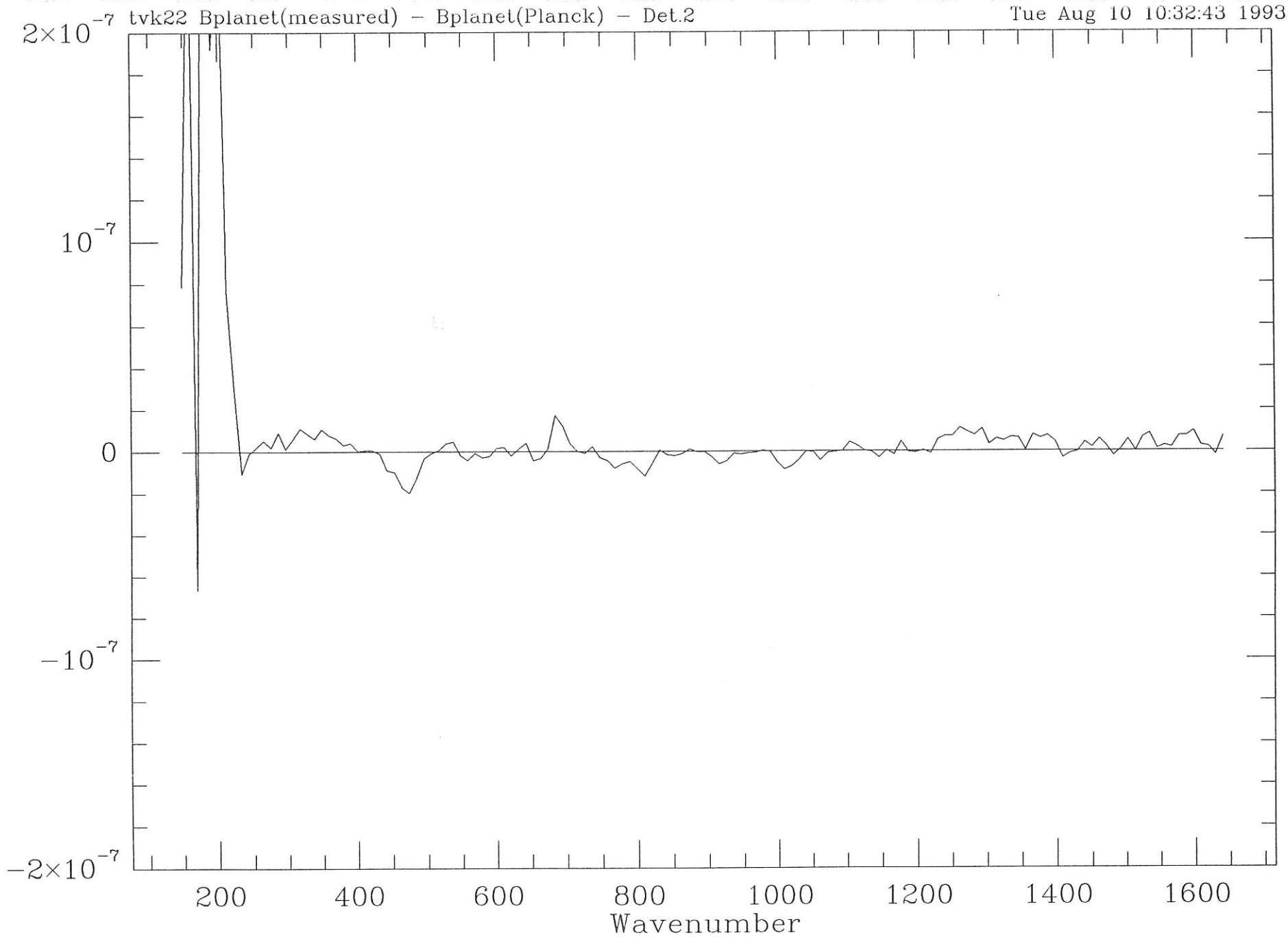
2×10^-7 tvk22 Bplanet(measured) − Bplanet(Planck) − Det.2
Tue Aug 10 10:32:43 1993
10^-7
0
−10^-7
−2×10^-7
200
400
600
800
1000
1200
1400
1600
Wavenumber

fig. 3-19f

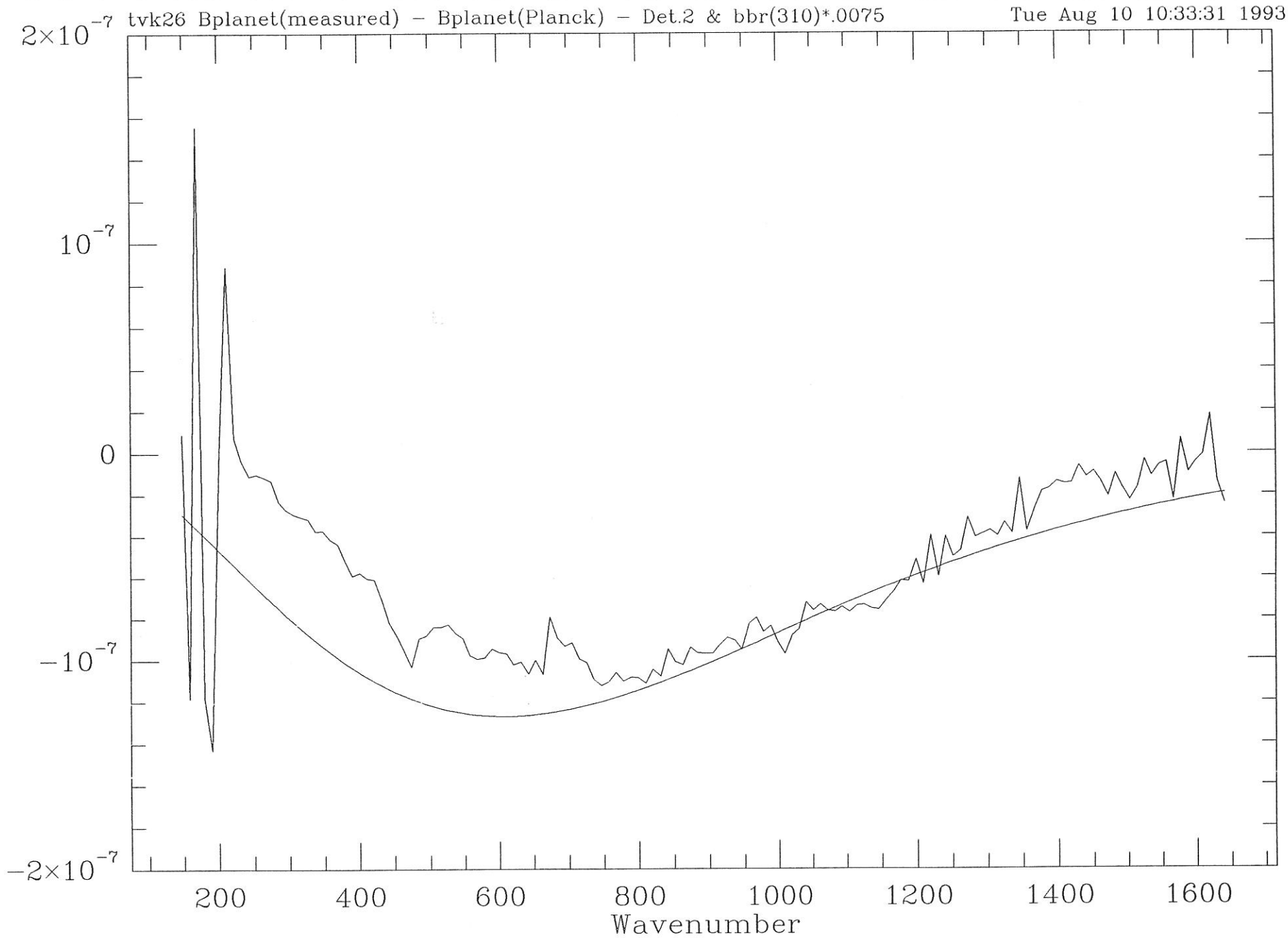
2×10^-7 tvk26 Bplanet(measured) − Bplanet(Planck) − Det.2 & bbr(310)*.0075
Tue Aug 10 10:33:31 1993
10^-7
0
−10^-7
−2×10^-7
200
400
600
800
1000
1200
1400
1600
Wavenumber

Fig. 3-199

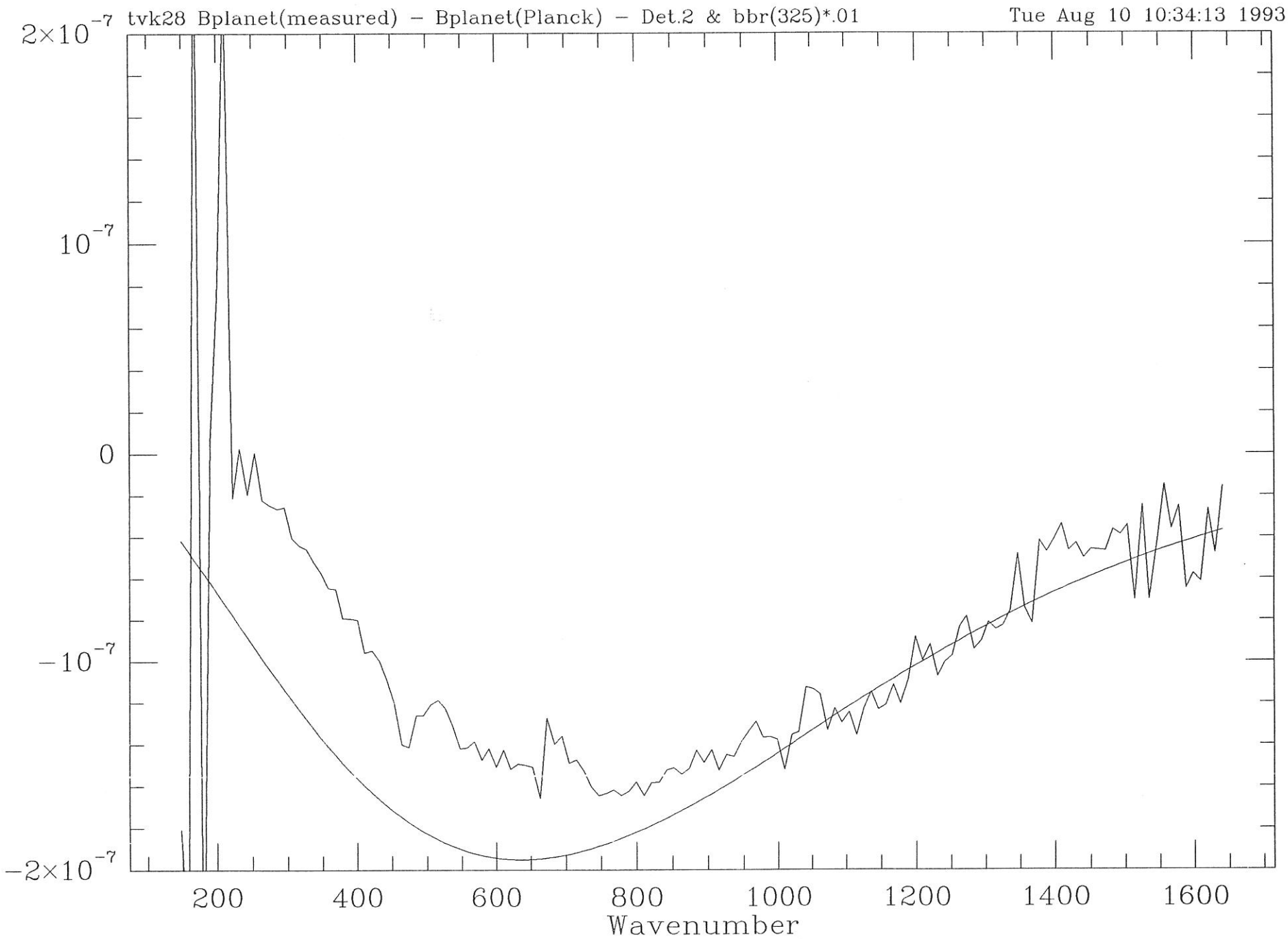
2×10^-7 tvk28 Bplanet(measured) − Bplanet(Planck) − Det.2 & bbr(325)*.01
Tue Aug 10 10:34:13 1993
10^-7
0
−10^-7
−2×10^-7
200
400
600
800
1000
1200
1400
1600
Wavenumber

Fig. 3-19

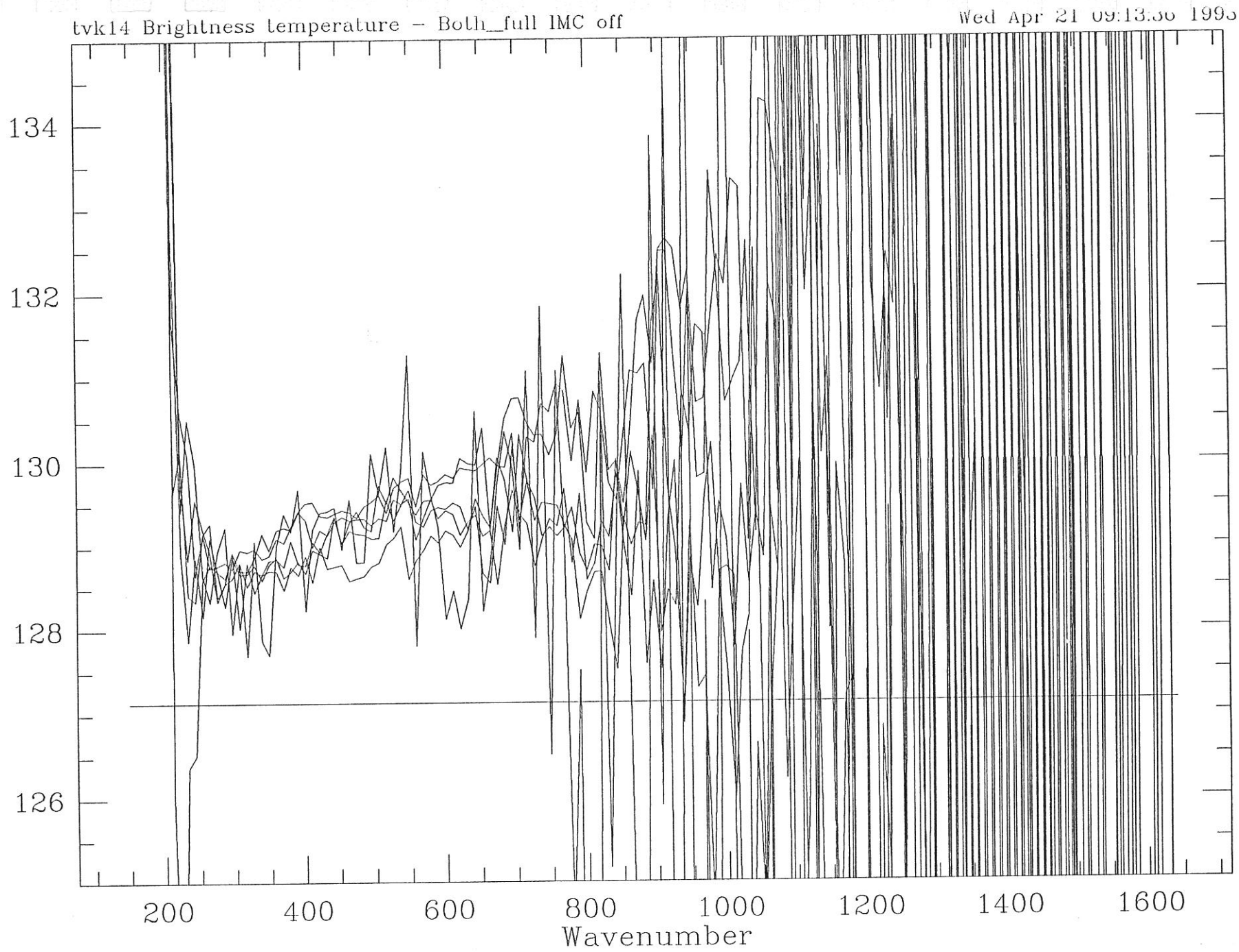
tvk14 Brightness temperature – Both_full IMC off
Wed Apr 21 09:13:36 1993
134
132
130
128
126
200
400
600
800
1000
1200
1400
1600
Wavenumber

fig. 3-20a

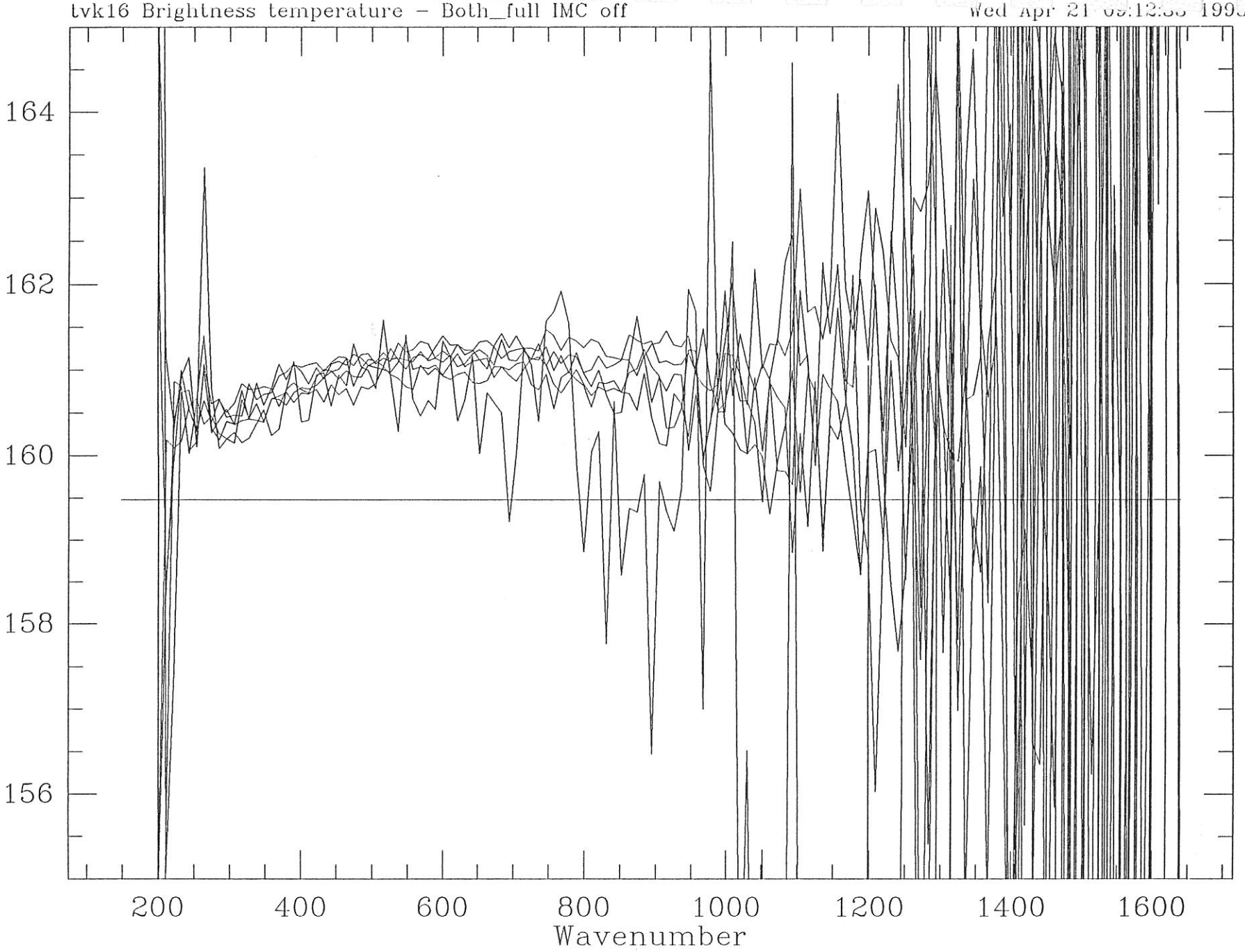
tvk16 Brightness temperature - Both_full IMC off
Wed Apr 21
164
162
160
158
156
200
400
600
800
1000
1200
1400
1600
Wavenumber

fig. 3-20b

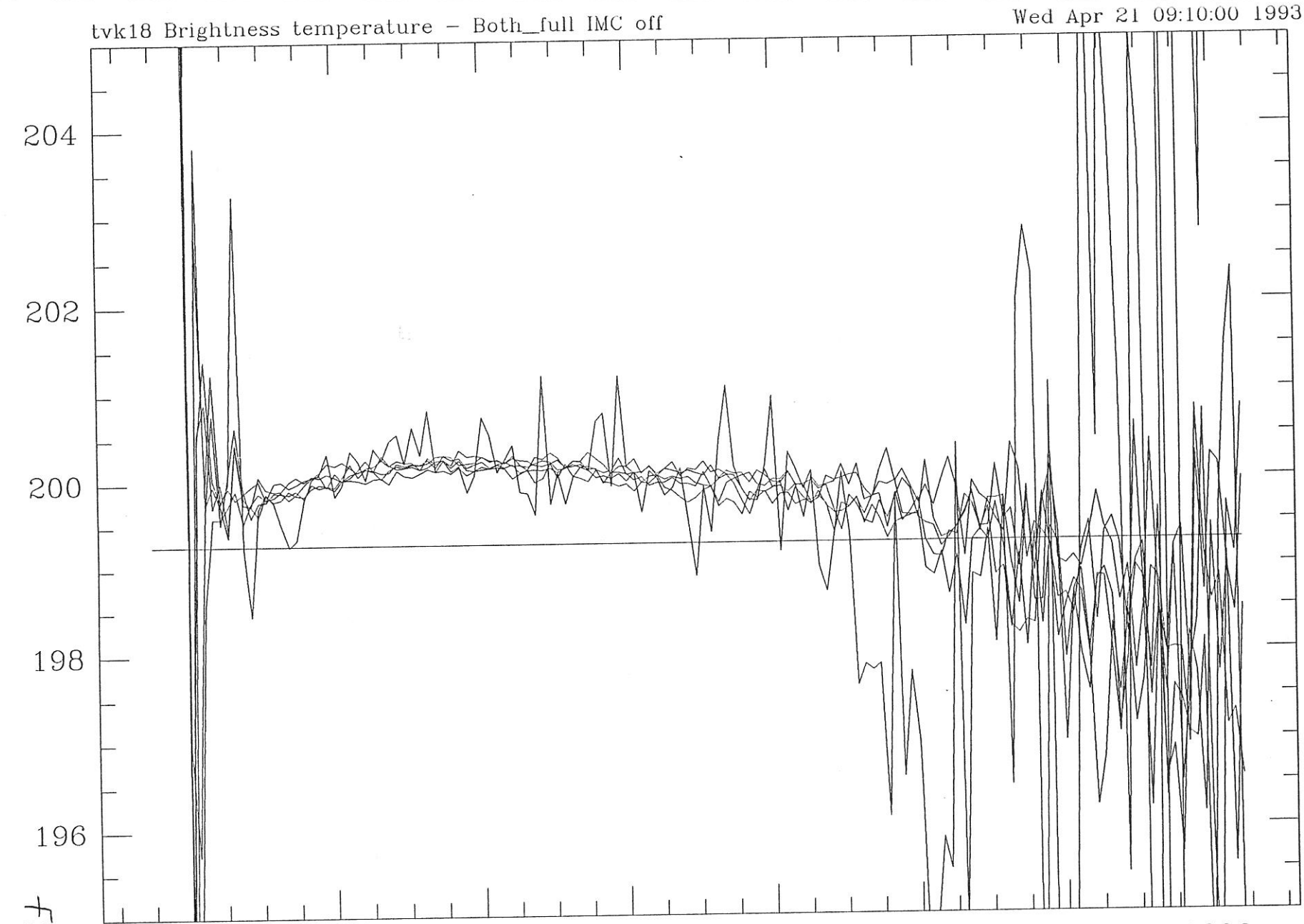
tvk18 Brightness temperature – Both_full IMC off
Wed Apr 21 09:10:00 1993
204
202
200
198
196
200
400
600
800
1000
1200
1400
1600
Wavenumber

fig. 3-20c

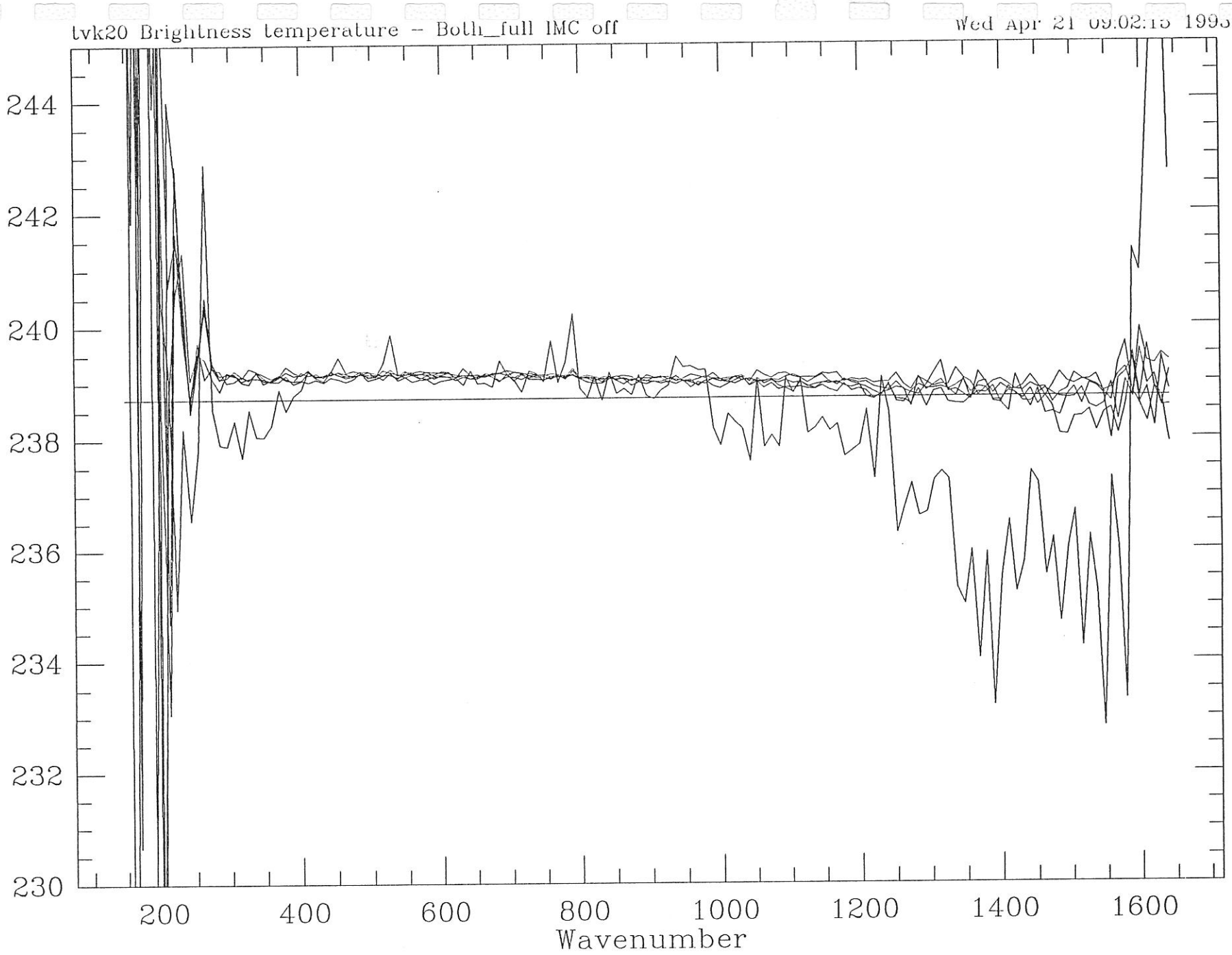
tvk20 Brightness temperature - Both_full IMC off
Wed Apr 21 09:02:15 1993
244
242
240
238
236
234
232
230
200
400
600
800
1000
1200
1400
1600
Wavenumber

fig. 3-20d

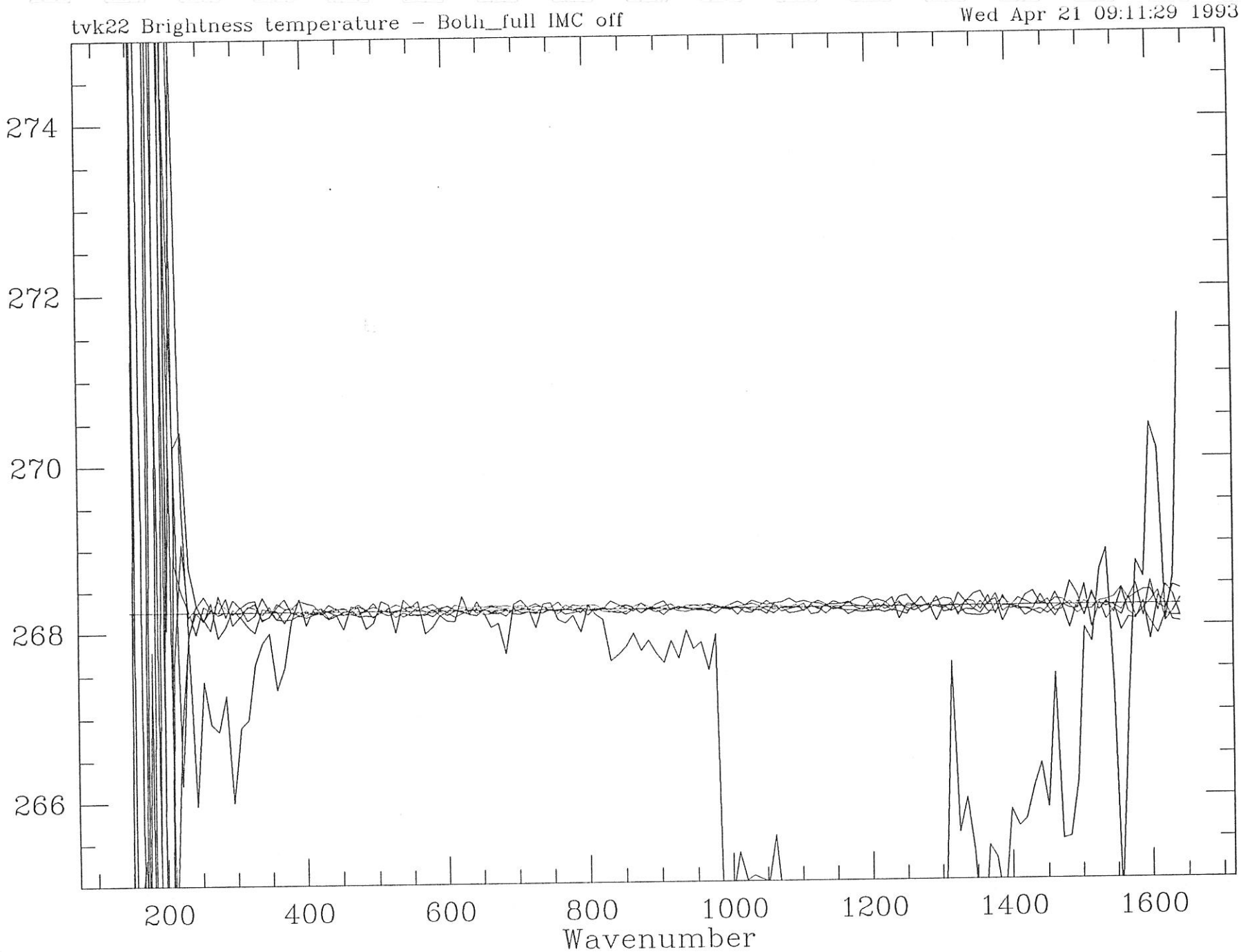
tvk22 Brightness temperature - Both_full IMC off
Wed Apr 21 09:11:29 1993
274
272
270
268
266
200
400
600
800
1000
1200
1400
1600
Wavenumber

fig. 3-20e

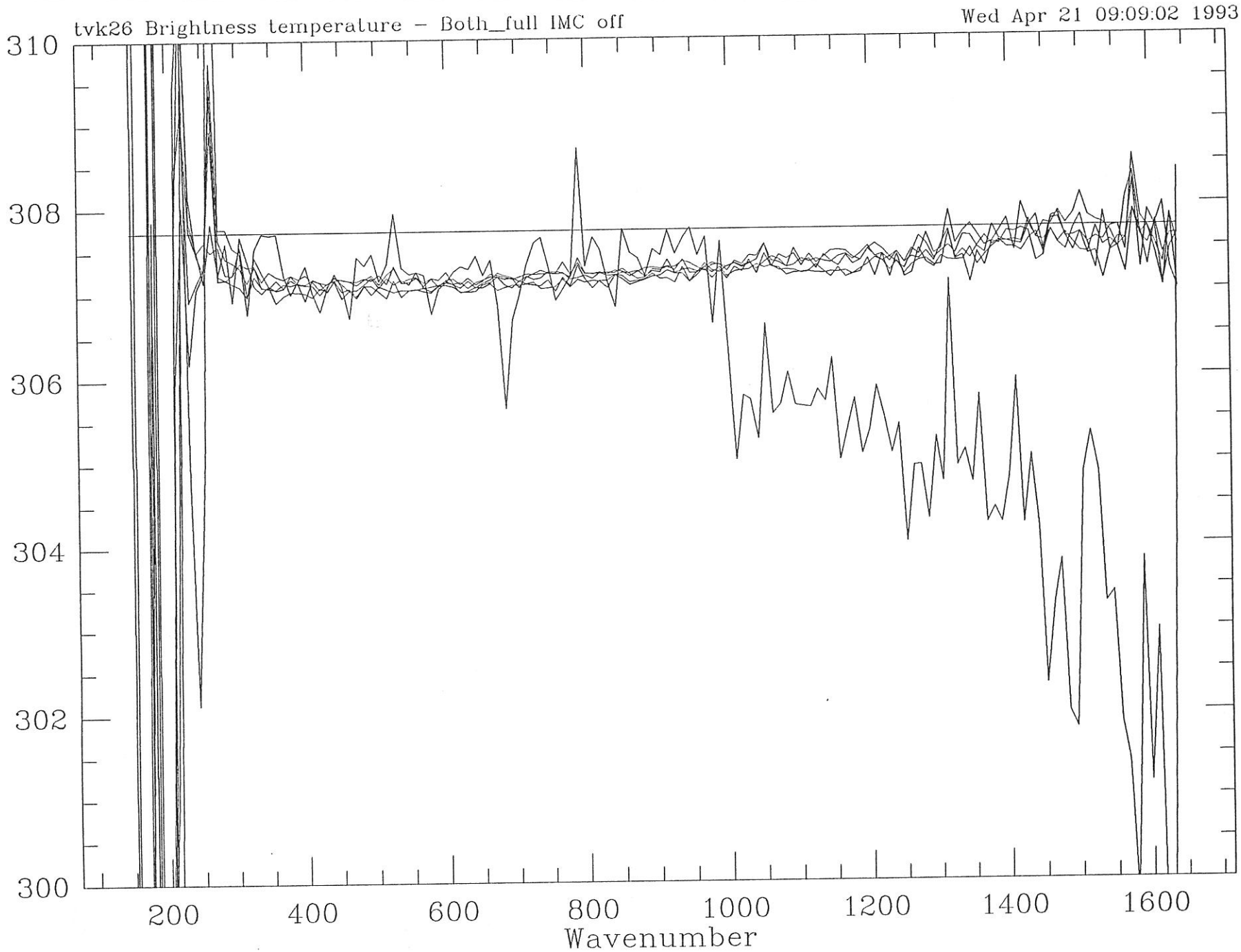
tvk26 Brightness temperature – Both_full IMC off
Wed Apr 21 09:09:02 1993
310
308
306
304
302
300
200
400
600
800
1000
1200
1400
1600
Wavenumber

fig. 3-20f

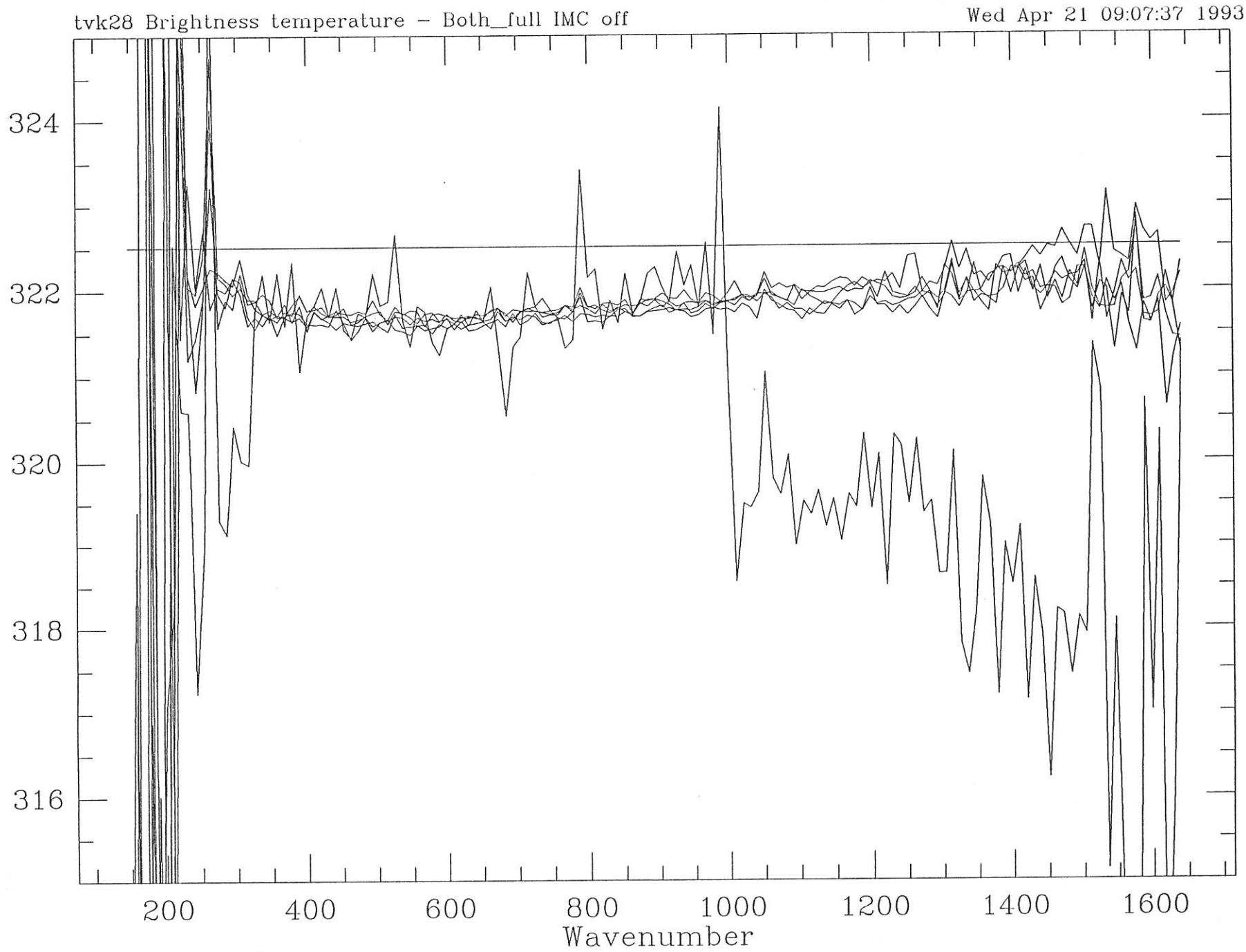
tvk28 Brightness temperature – Both_full IMC off
Wed Apr 21 09:07:37 1993
324
322
320
318
316
200
400
600
800
1000
1200
1400
1600
Wavenumber

Fig. 3-209

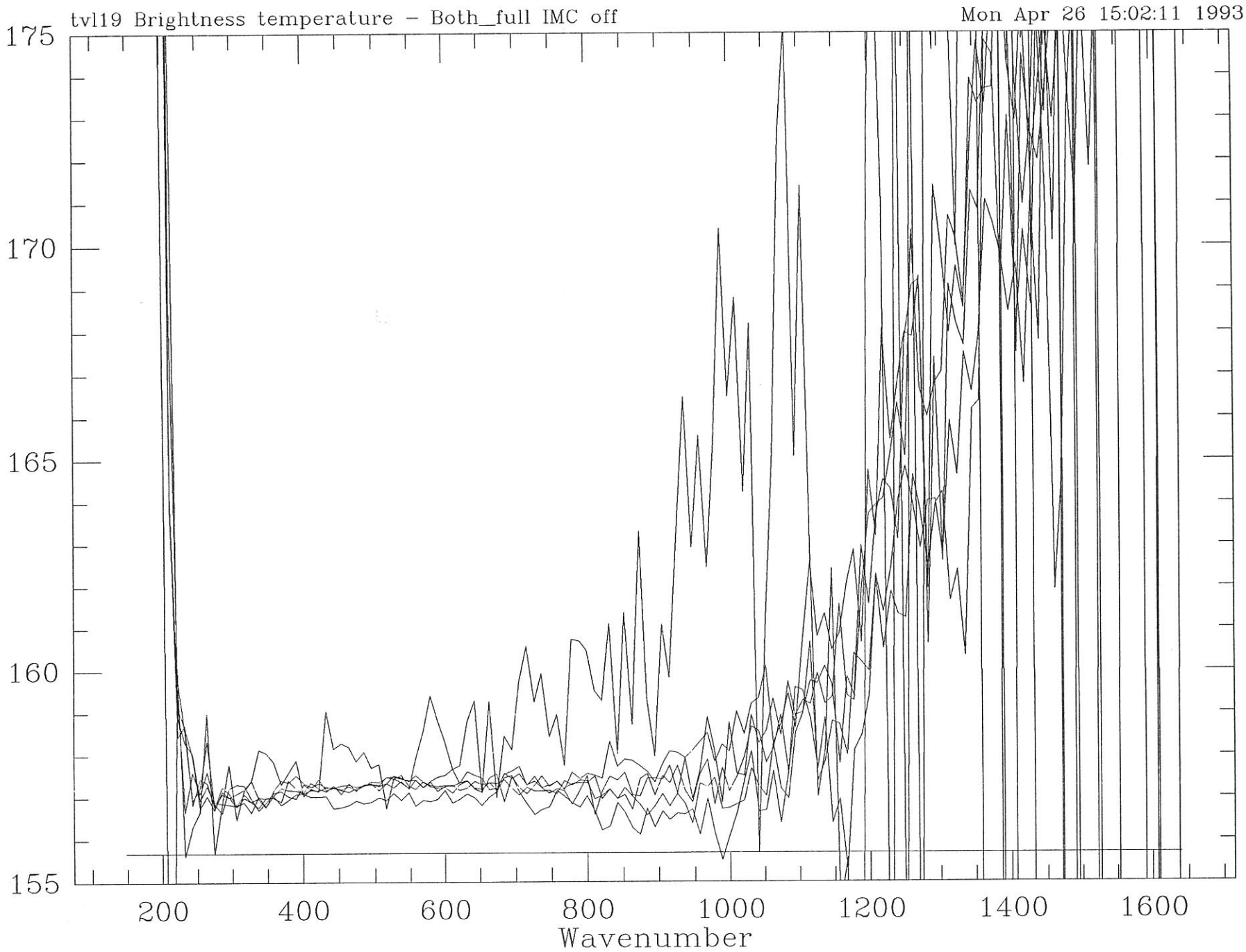
tvl19 Brightness temperature – Both_full IMC off
Mon Apr 26 15:02:11 1993
175
170
165
160
155
200
400
600
800
1000
1200
1400
1600
Wavenumber

Fig. 3-21a

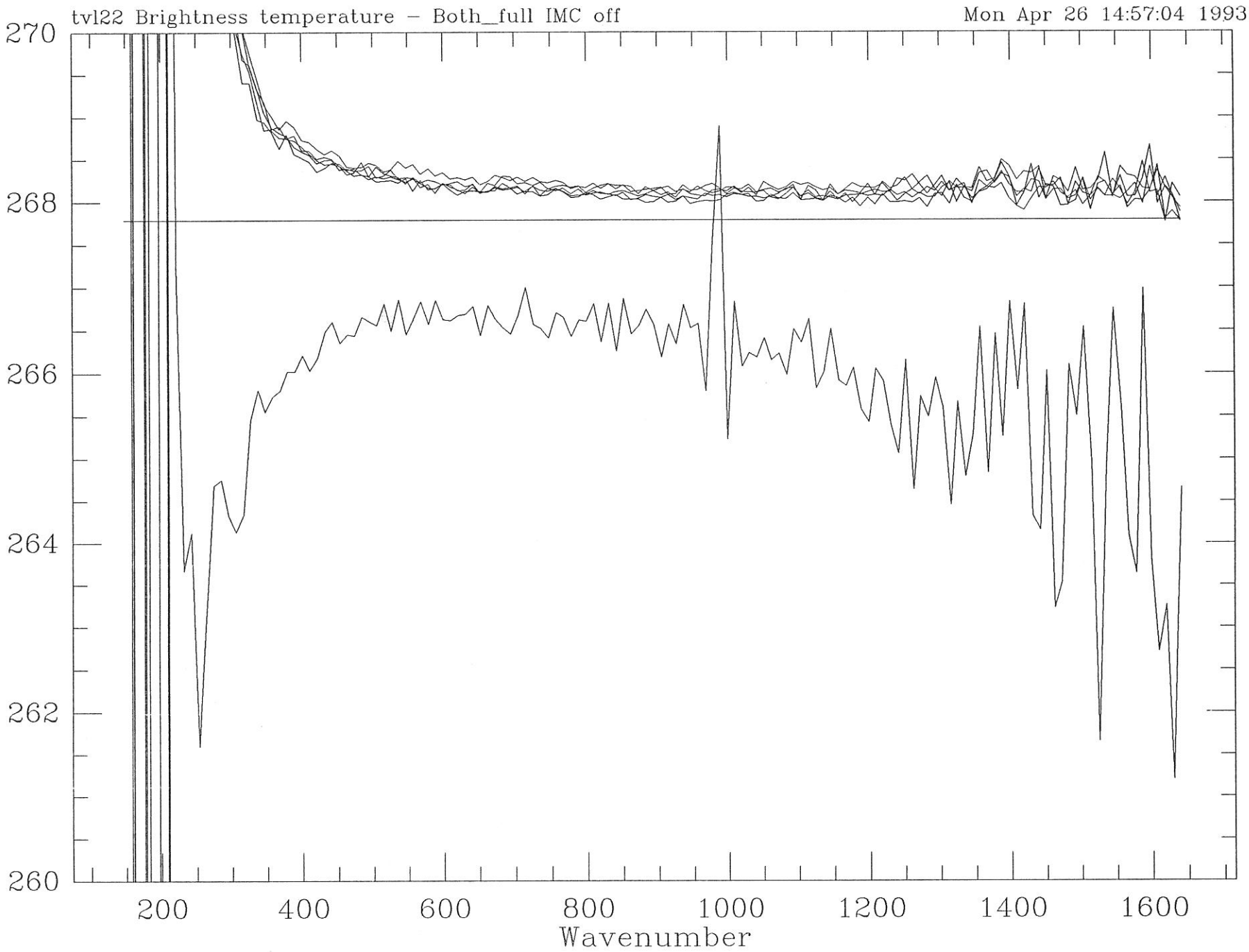
tvl22 Brightness temperature – Both_full IMC off
Mon Apr 26 14:57:04 1993
270
268
266
264
262
260
200
400
600
800
1000
1200
1400
1600
Wavenumber

fig. 3-21b

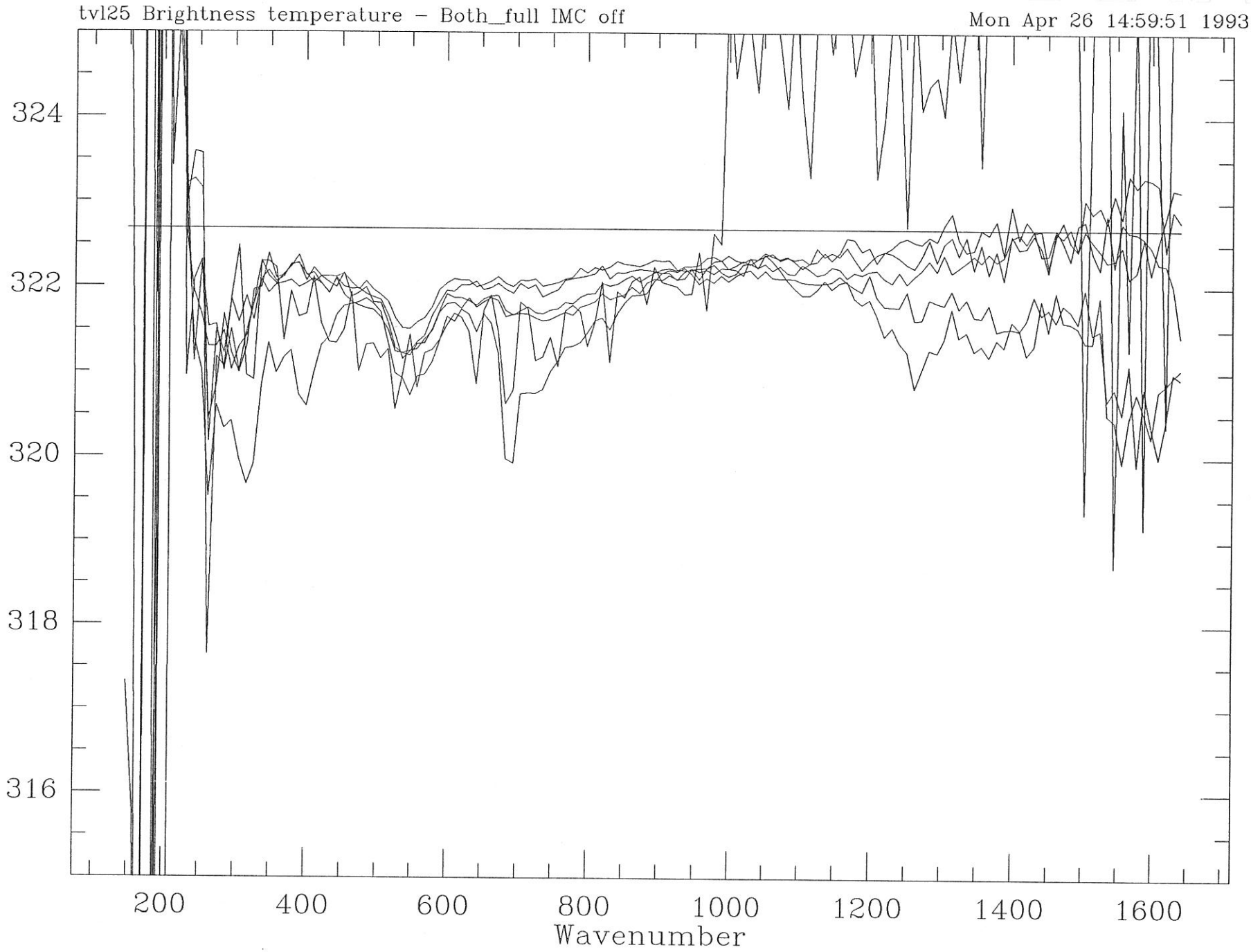
tvl25 Brightness temperature – Both_full IMC off
Mon Apr 26 14:59:51 1993
324
322
320
318
316
200
400
600
800
1000
1200
1400
1600
Wavenumber

fig. 3-21c

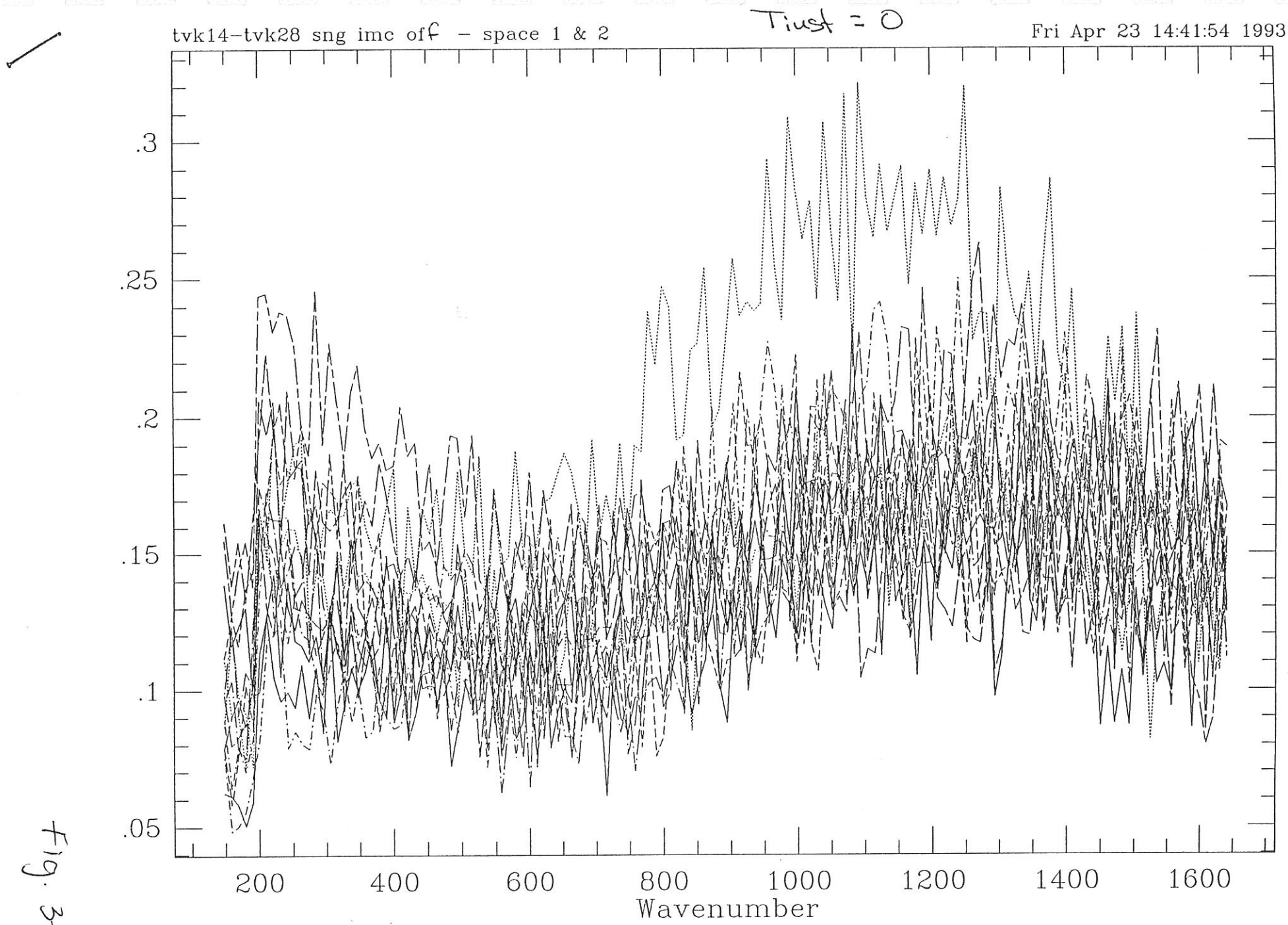
tvk14-tvk28 sng imc off - space 1 & 2
Tinst = 0
Fri Apr 23 14:41:54 1993
.3
.25
.2
.15
.1
.05
200
400
600
800
1000
1200
1400
1600
Wavenumber

fig. 3-22a

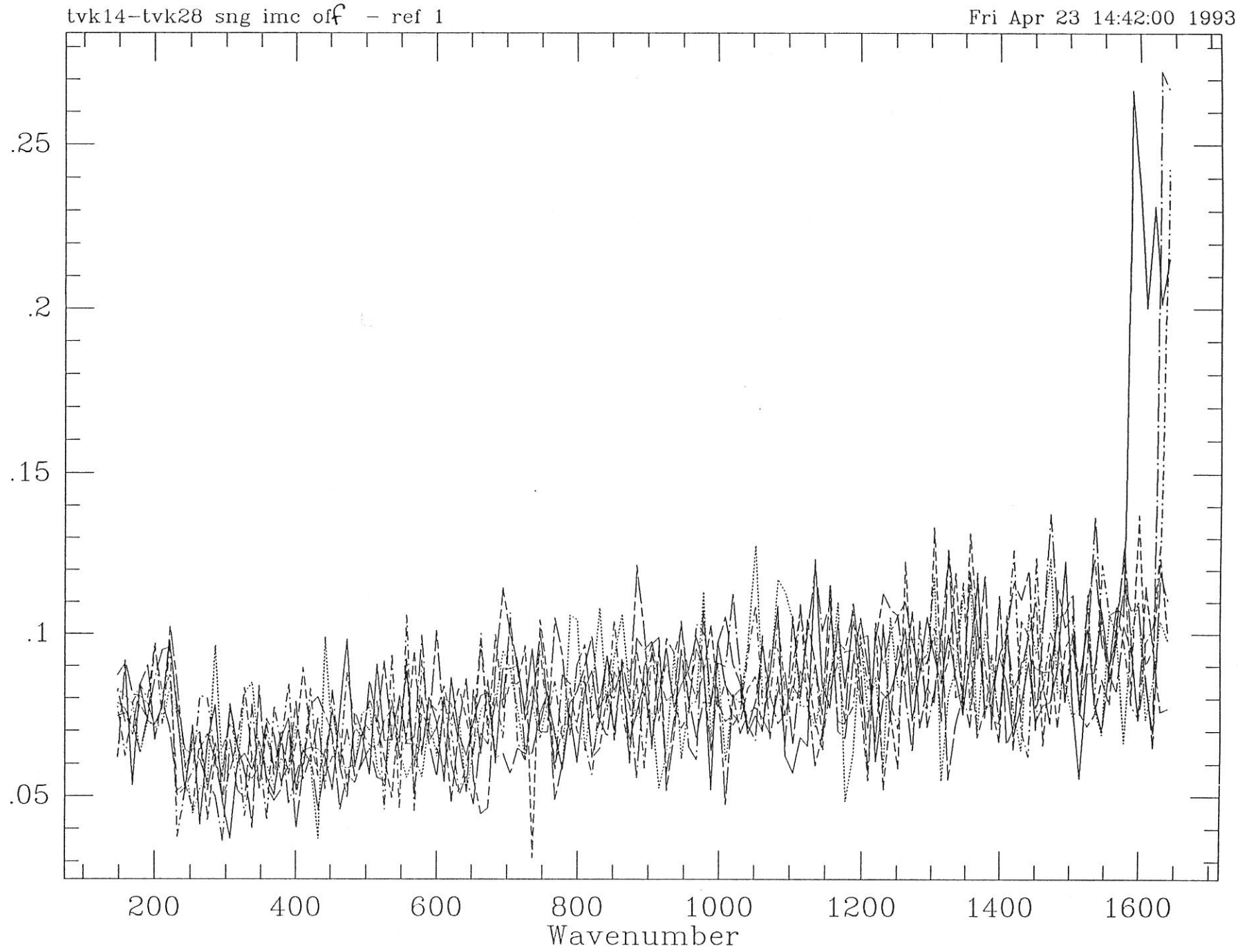
tvk14-tvk28 sng imc off - ref 1
Fri Apr 23 14:42:00 1993
.25
.2
.15
.1
.05
200
400
600
800
1000
1200
1400
1600
Wavenumber

fig. 3-22b

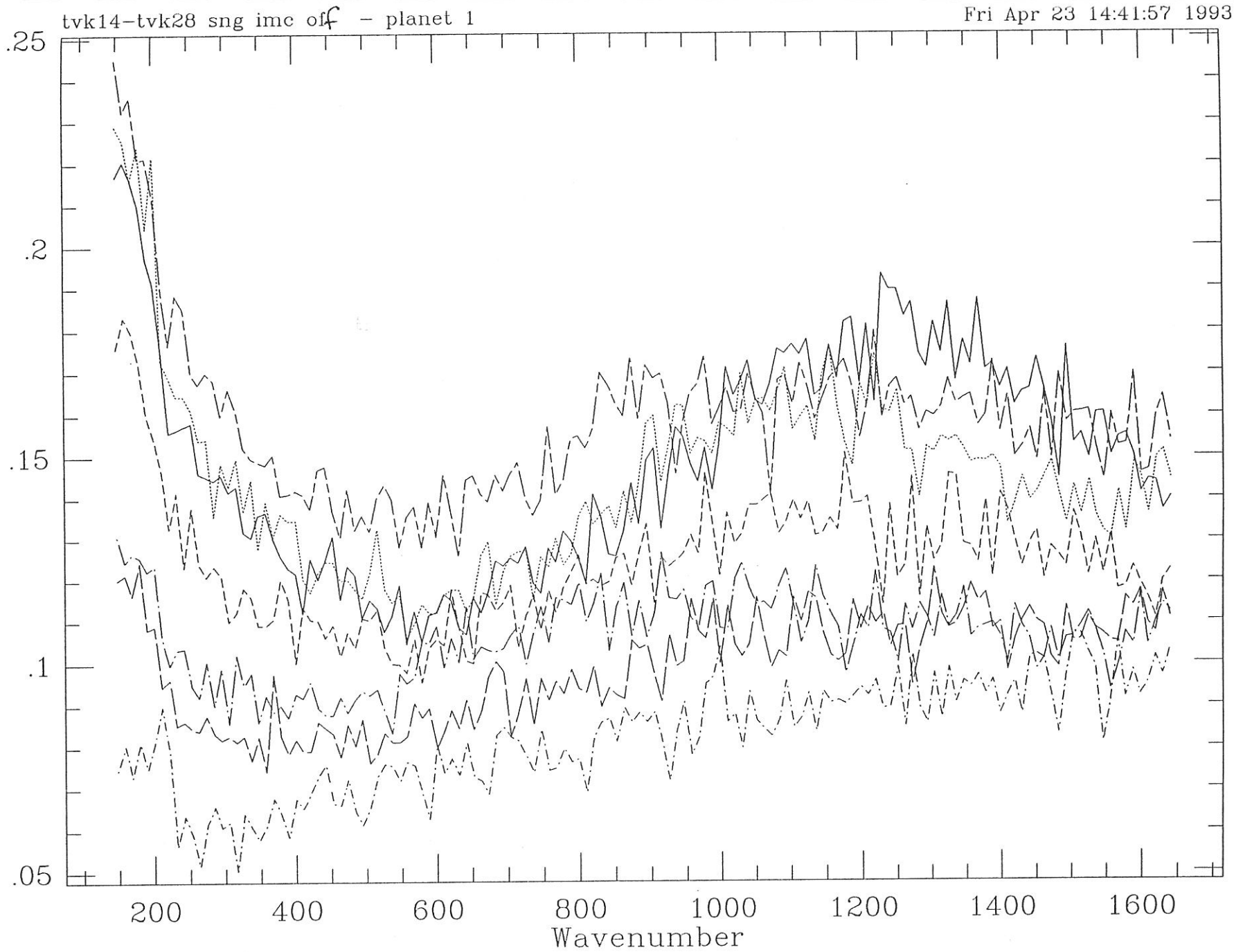
tvk14-tvk28 sng imc off - planet 1
Fri Apr 23 14:41:57 1993
.25
.2
.15
.1
.05
200
400
600
800
1000
1200
1400
1600
Wavenumber

fig. 3-22c

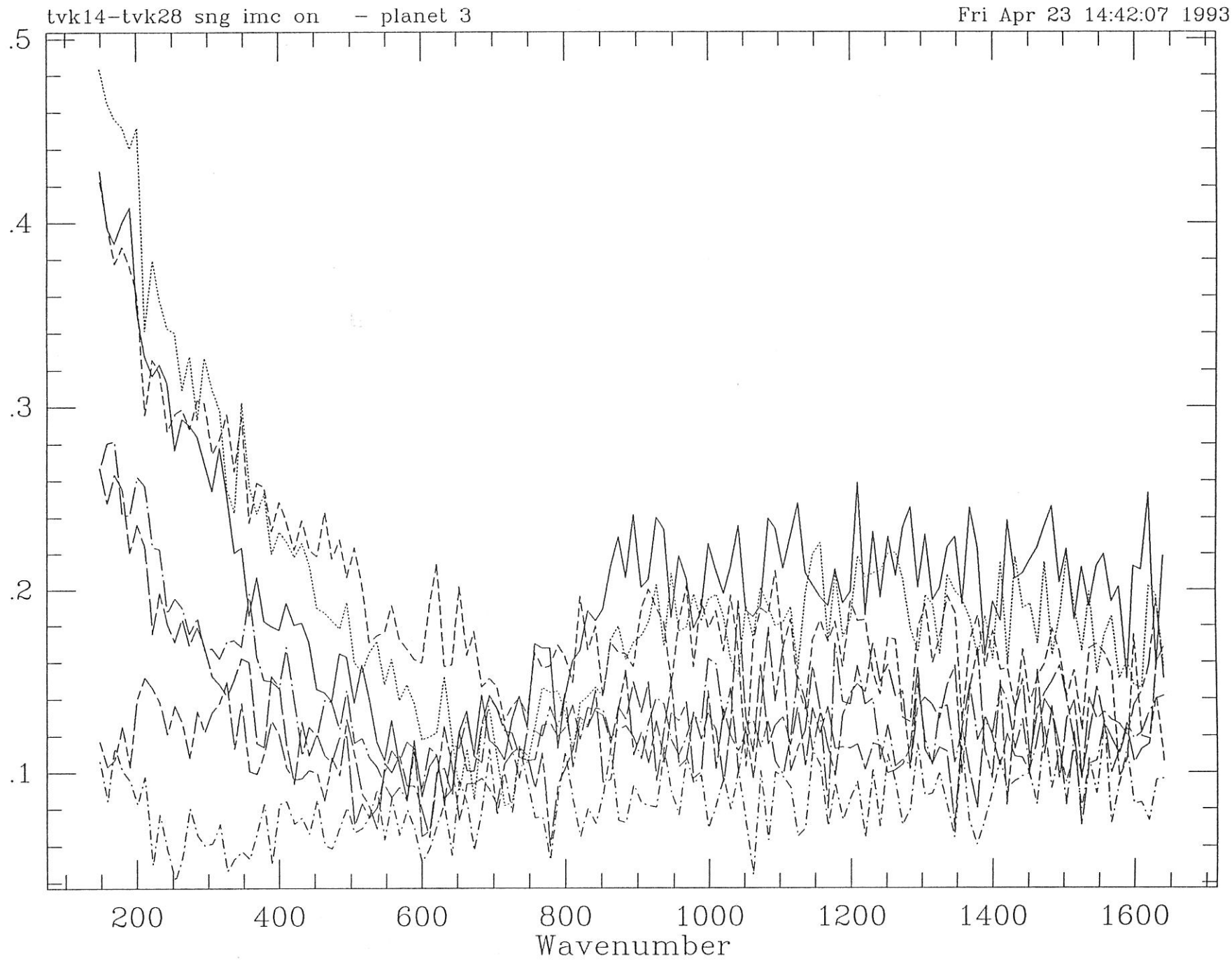
tvk14-tvk28 sng imc on - planet 3
Fri Apr 23 14:42:07 1993
.5
.4
.3
.2
.1
200
400
600
800
1000
1200
1400
1600
Wavenumber

Fig 3-22 pg

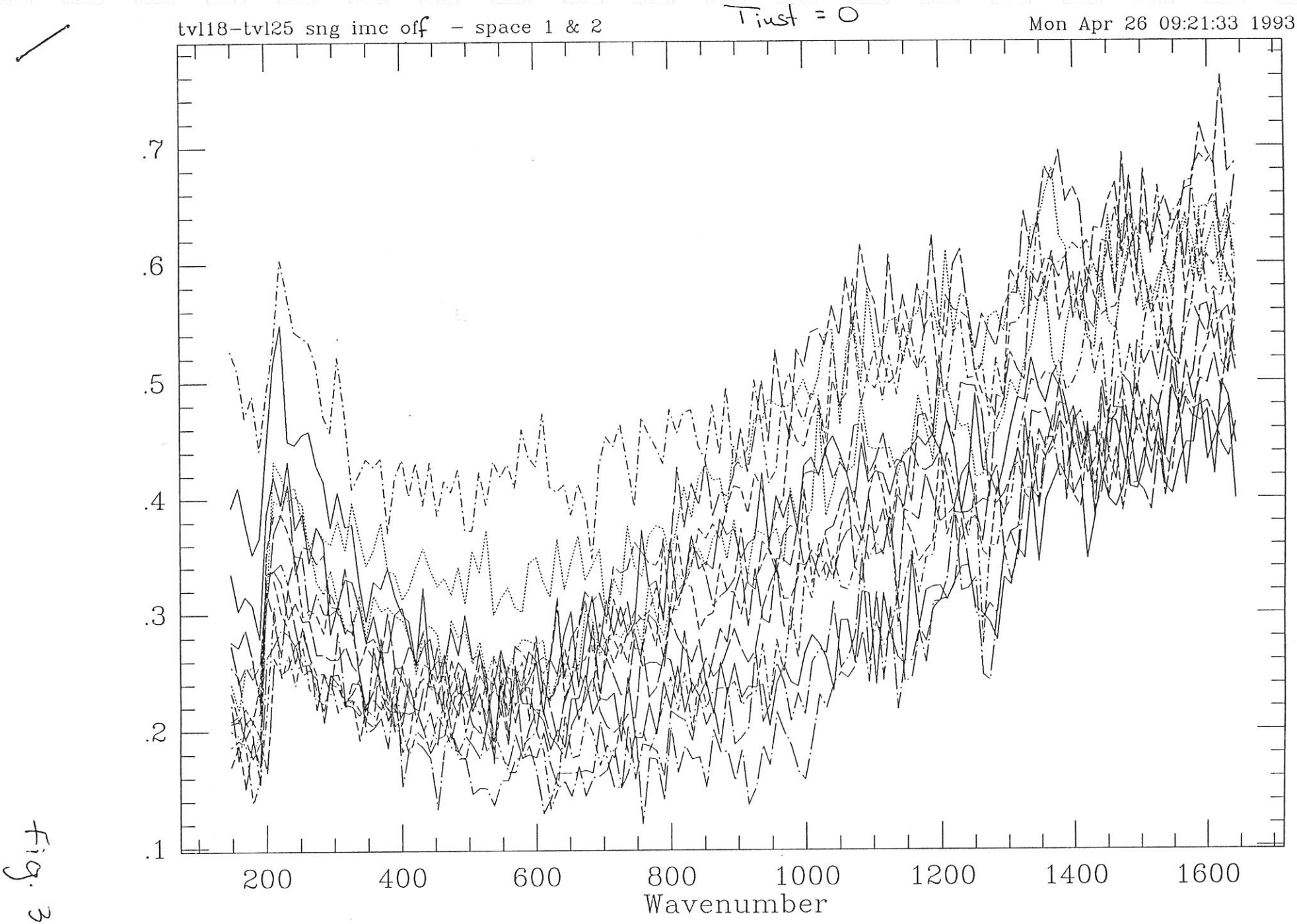
tvl18-tvl25 sng imc off - space 1 & 2
Tinst = 0
Mon Apr 26 09:21:33 1993
.7
.6
.5
.4
.3
.2
.1
200
400
600
800
1000
1200
1400
1600
Wavenumber

fig. 3-23a

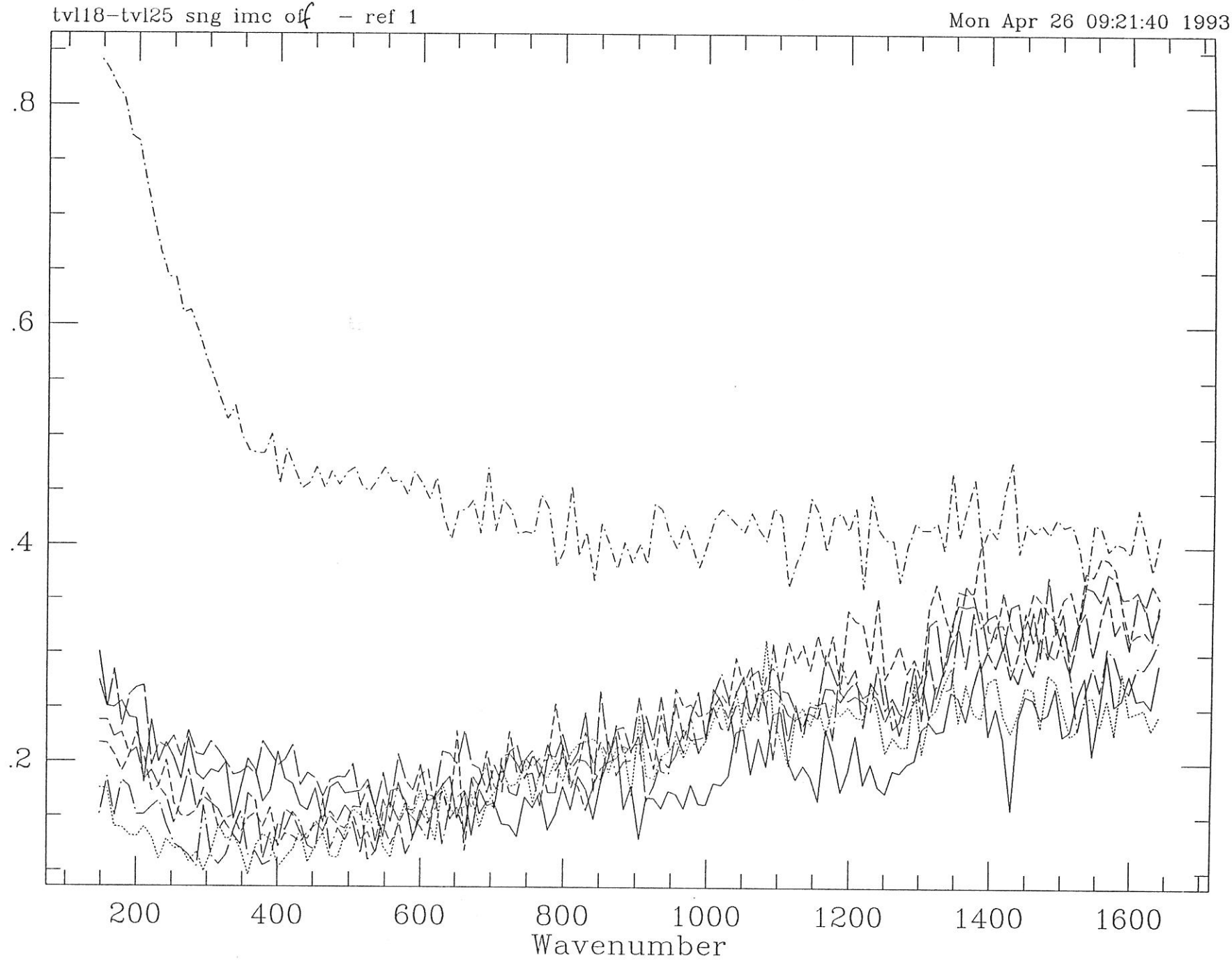
tvl18-tvl25 sng imc off - ref 1
Mon Apr 26 09:21:40 1993
.8
.6
.4
.2
200
400
600
800
1000
1200
1400
1600
Wavenumber

fig. 3-23b

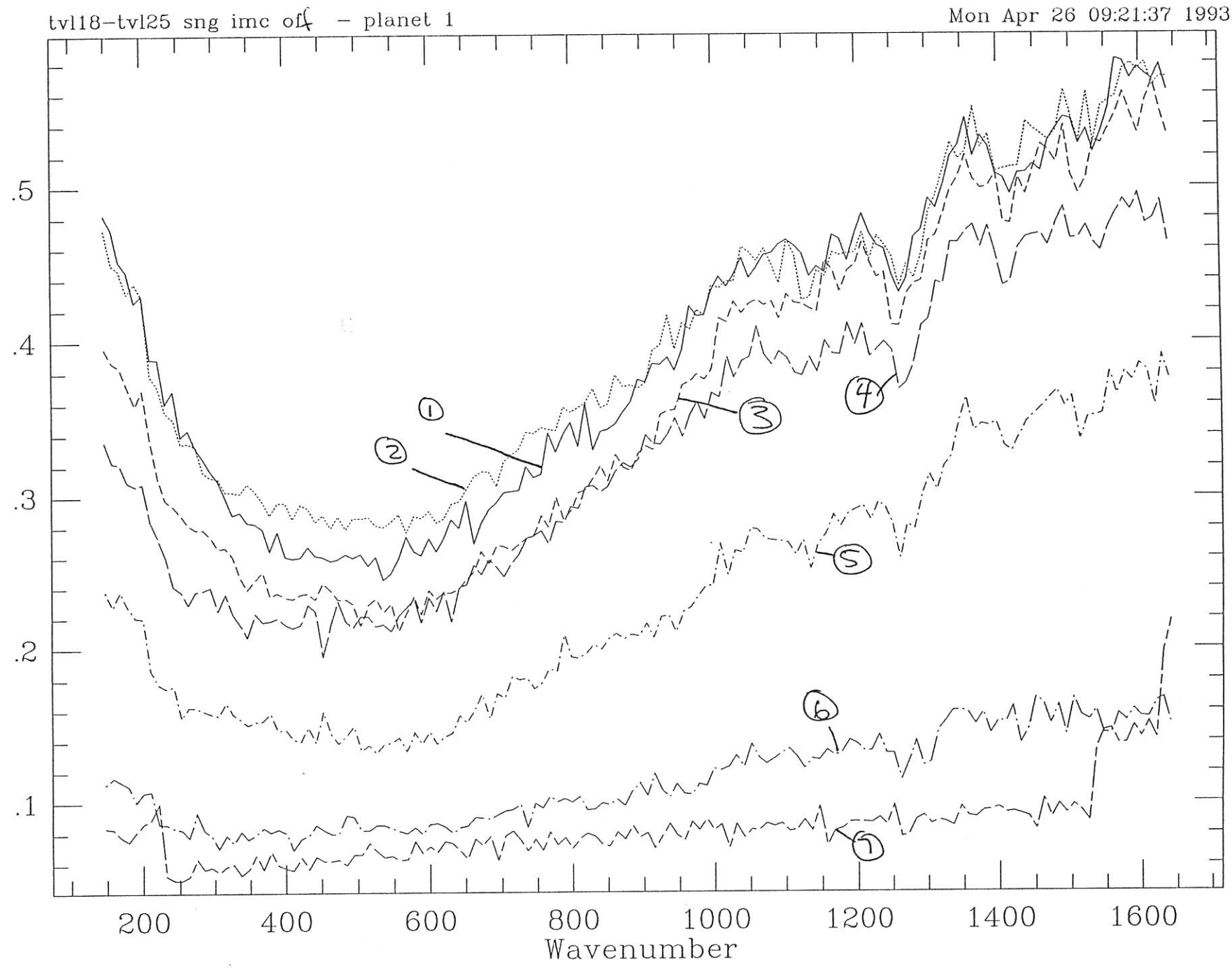
tvl18-tvl25 sng imc off - planet 1
Mon Apr 26 09:21:37 1993
.5
.4
.3
.2
.1
200
400
600
800
1000
1200
1400
1600
Wavenumber
1
2
3
4
5
6
7

fig. 3-23c

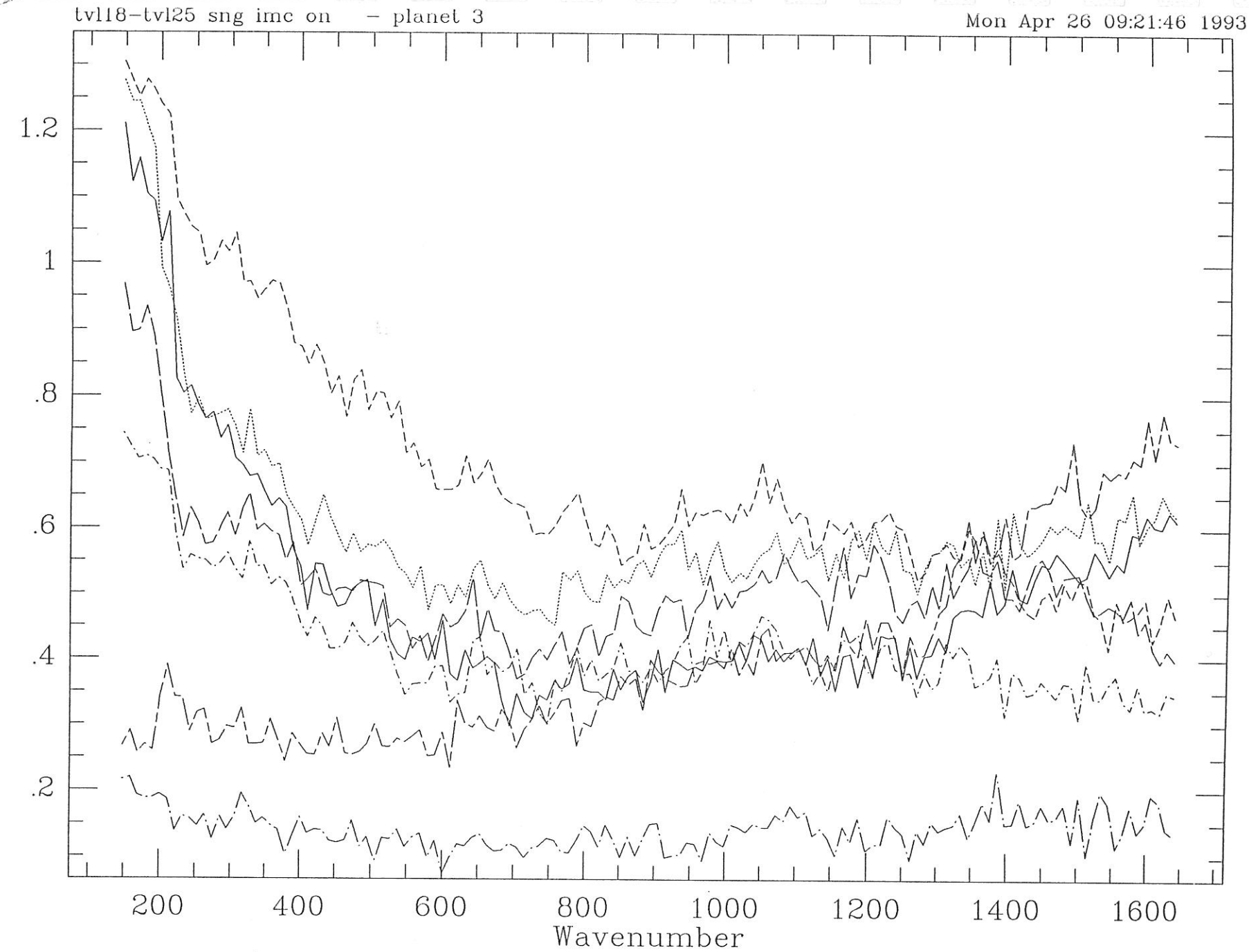
tvl18-tvl25 sng imc on - planet 3
Mon Apr 26 09:21:46 1993
1.2
1
.8
.6
.4
.2
200
400
600
800
1000
1200
1400
1600
Wavenumber

fig. 3-23d

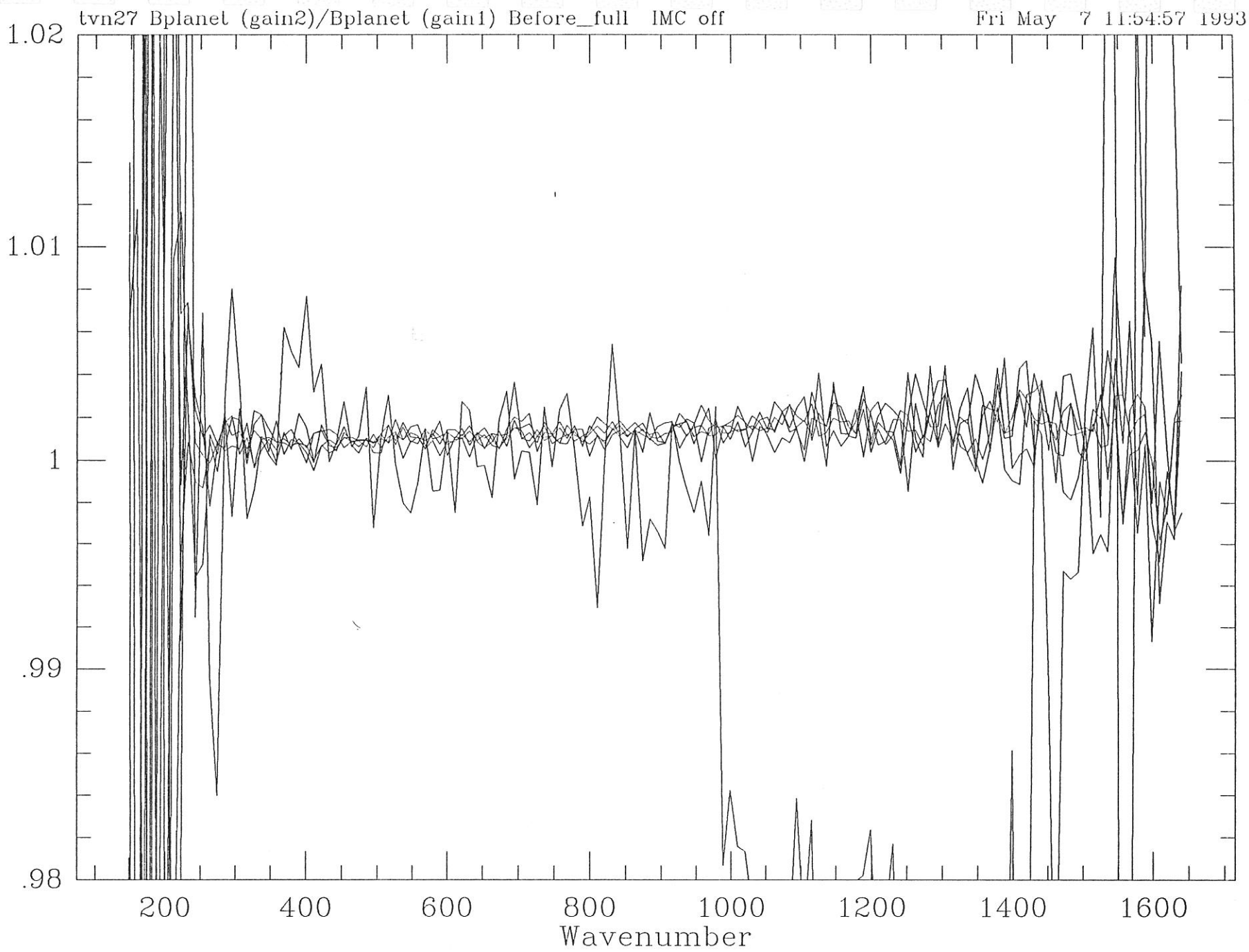
tvn27 Bplanet (gain2)/Bplanet (gain1) Before_full IMC off
Fri May 7 11:54:57 1993
1.02
1.01
1
.99
.98
200
400
600
800
1000
1200
1400
1600
Wavenumber

Fig. 3-24a

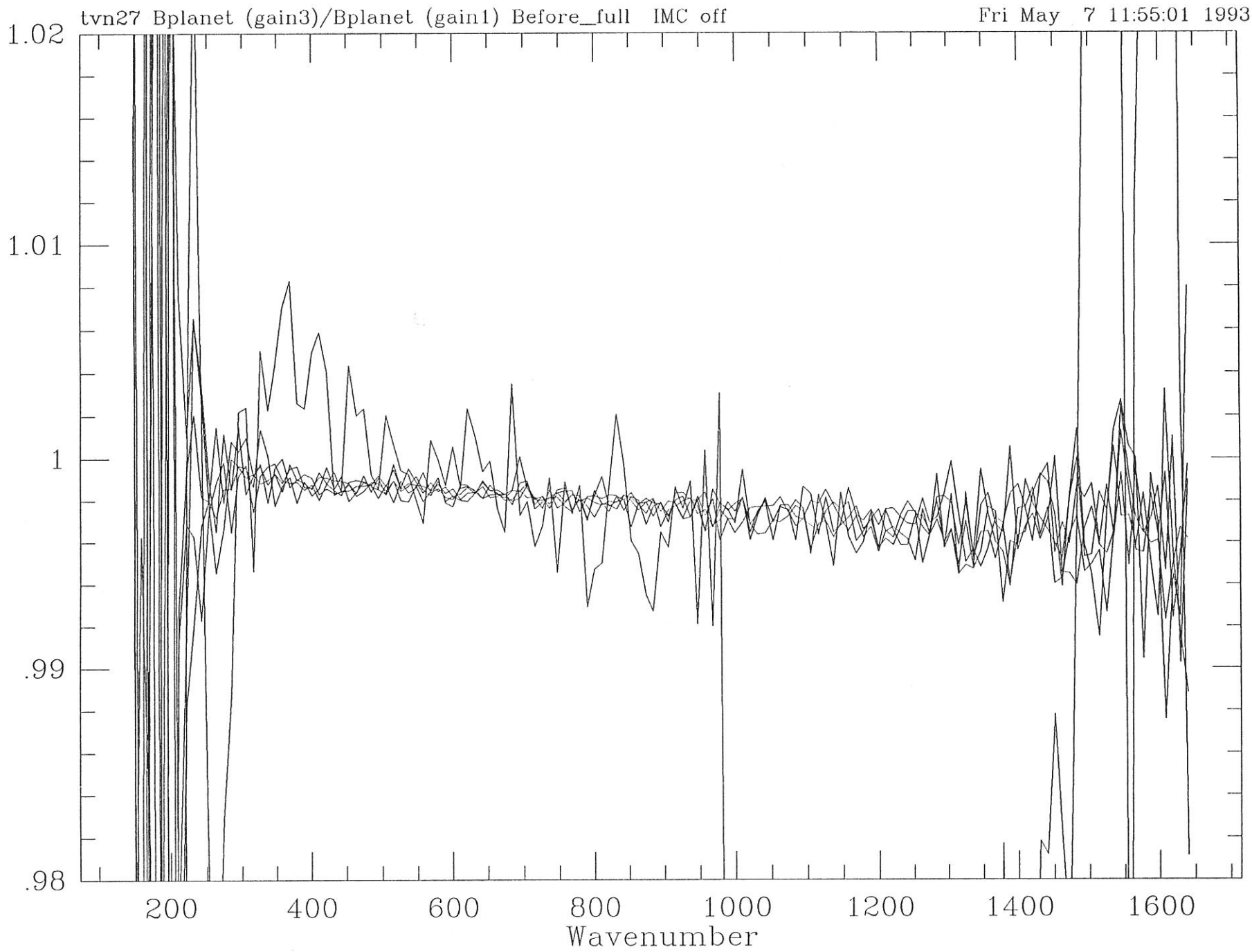
tvn27 Bplanet (gain3)/Bplanet (gain1) Before_full IMC off
Fri May 7 11:55:01 1993
1.02
1.01
1
.99
.98
200
400
600
800
1000
1200
1400
1600
Wavenumber

Fig. 3-24b

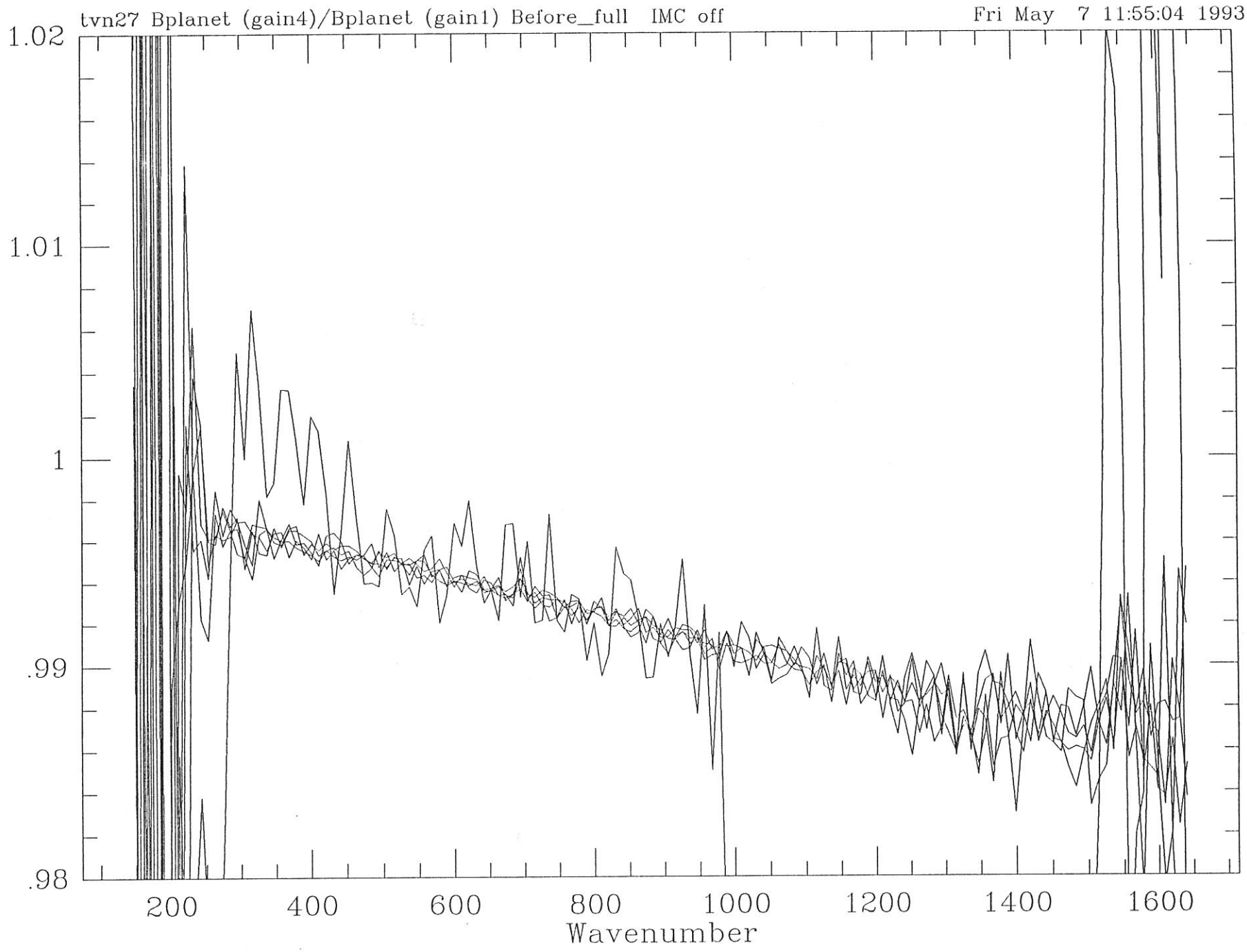
tvn27 Bplanet (gain4)/Bplanet (gain1) Before_full IMC off
Fri May 7 11:55:04 1993
1.02
1.01
1
.99
.98
200
400
600
800
1000
1200
1400
1600
Wavenumber

Fig 3-24c

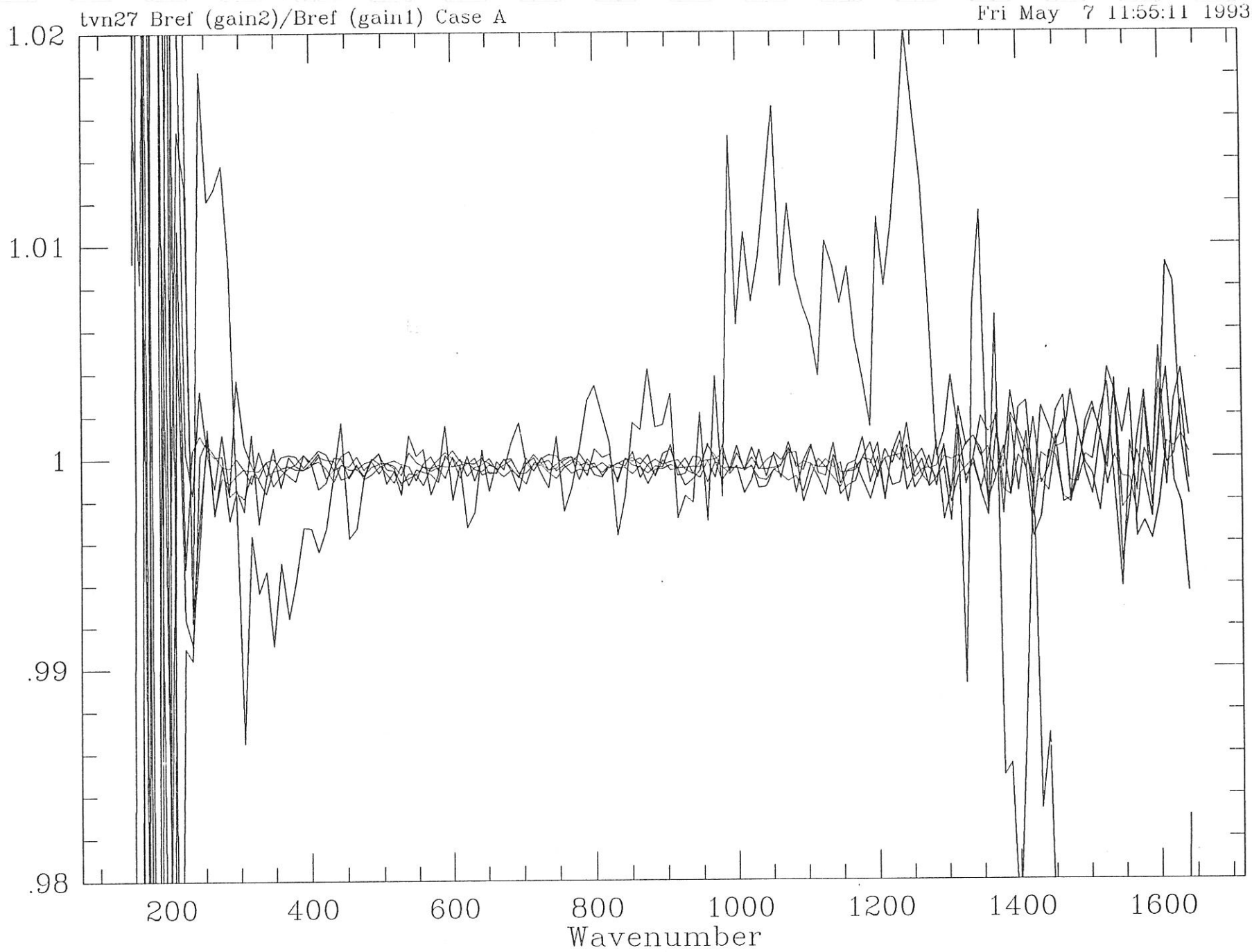
tvn27 Bref (gain2)/Bref (gain1) Case A
Fri May 7 11:55:11 1993
1.02
1.01
1
.99
.98
200
400
600
800
1000
1200
1400
1600
Wavenumber

Fig. 3-25e

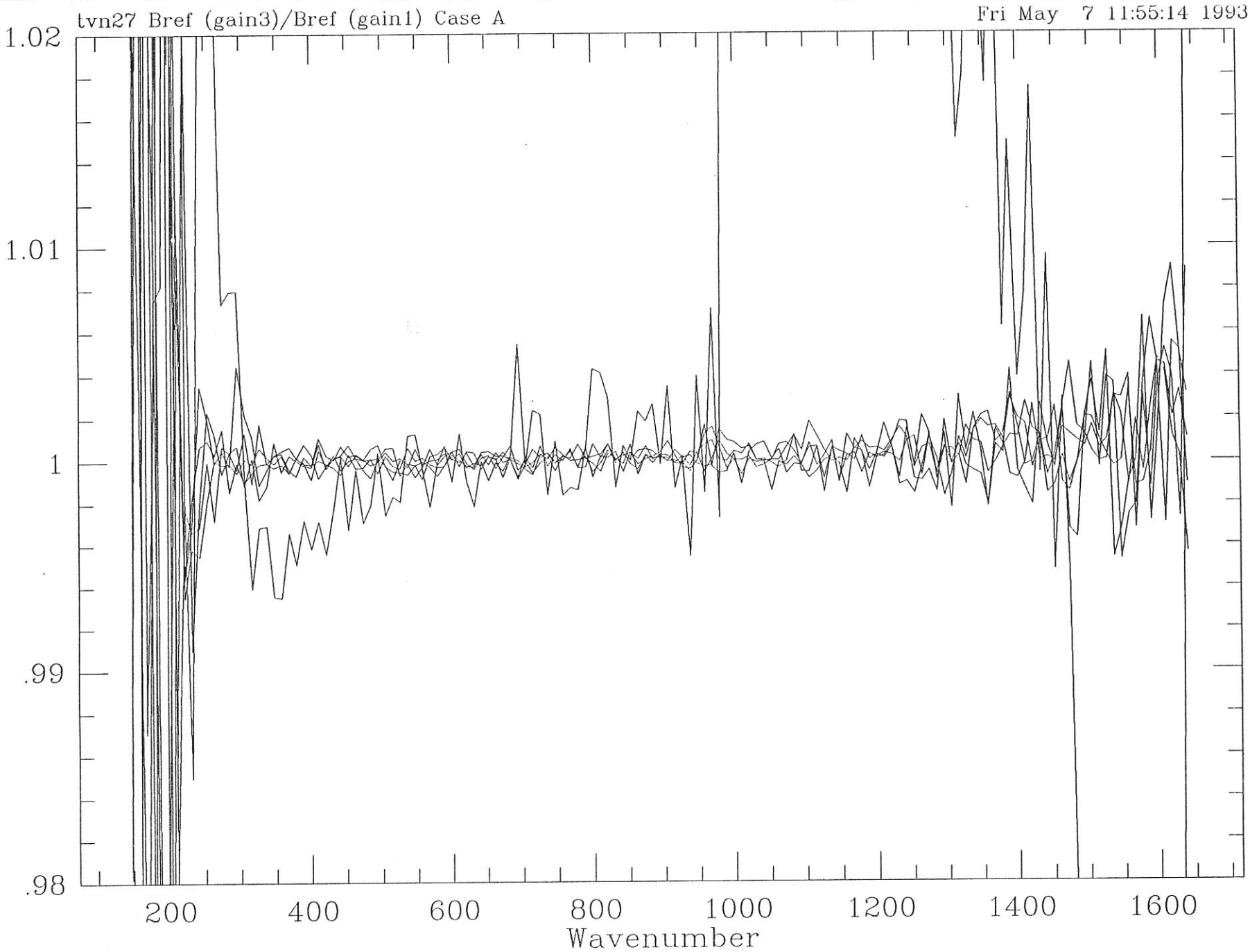
tvn27 Bref (gain3)/Bref (gain1) Case A
Fri May 7 11:55:14 1993
1.02
1.01
1
.99
.98
200
400
600
800
1000
1200
1400
1600
Wavenumber

Fig. 3-25b

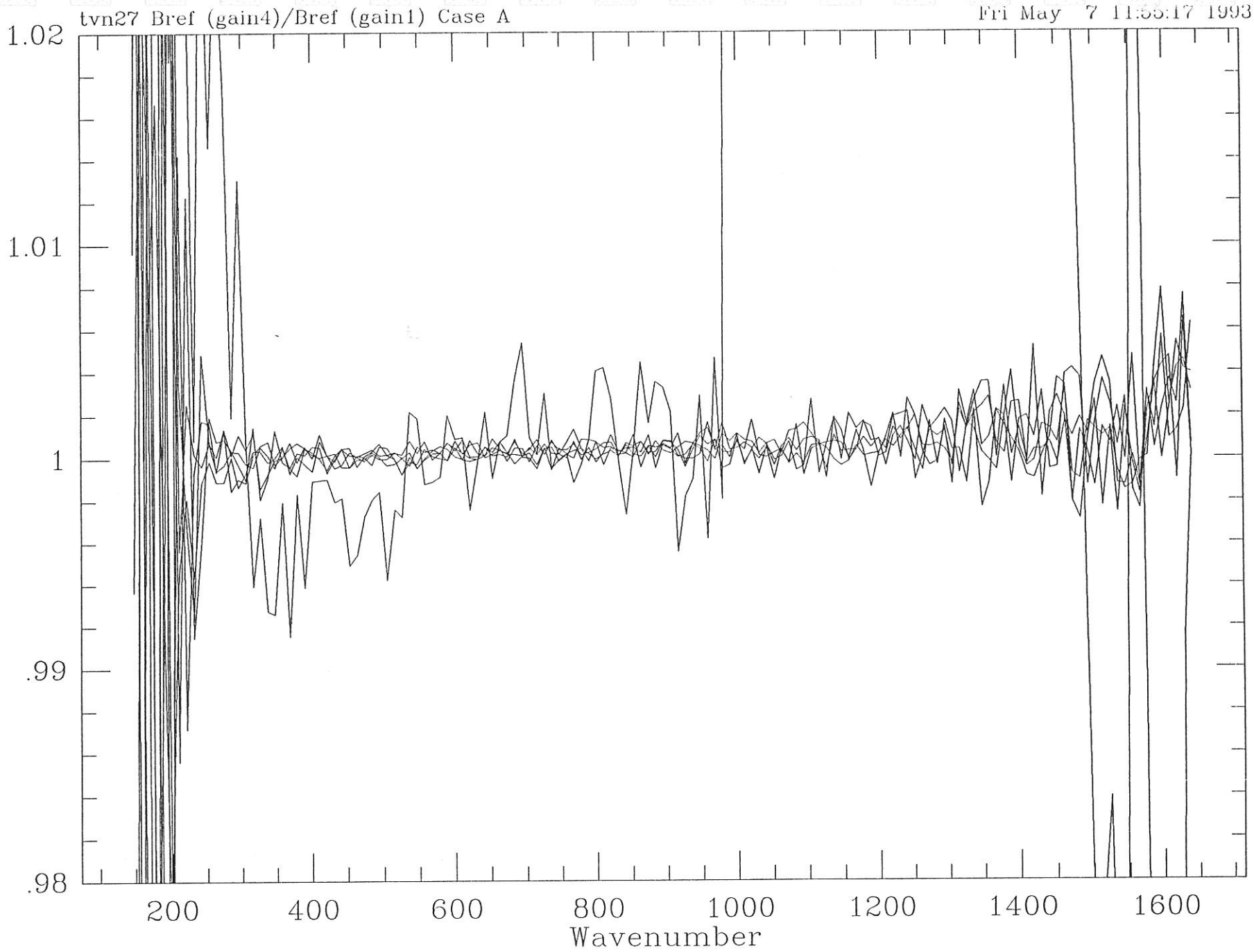
tvn27 Bref (gain4)/Bref (gain1) Case A
Fri May 7 11:55:17 1993
1.02
1.01
1
.99
.98
200
400
600
800
1000
1200
1400
1600
Wavenumber

Fig. 3-25c

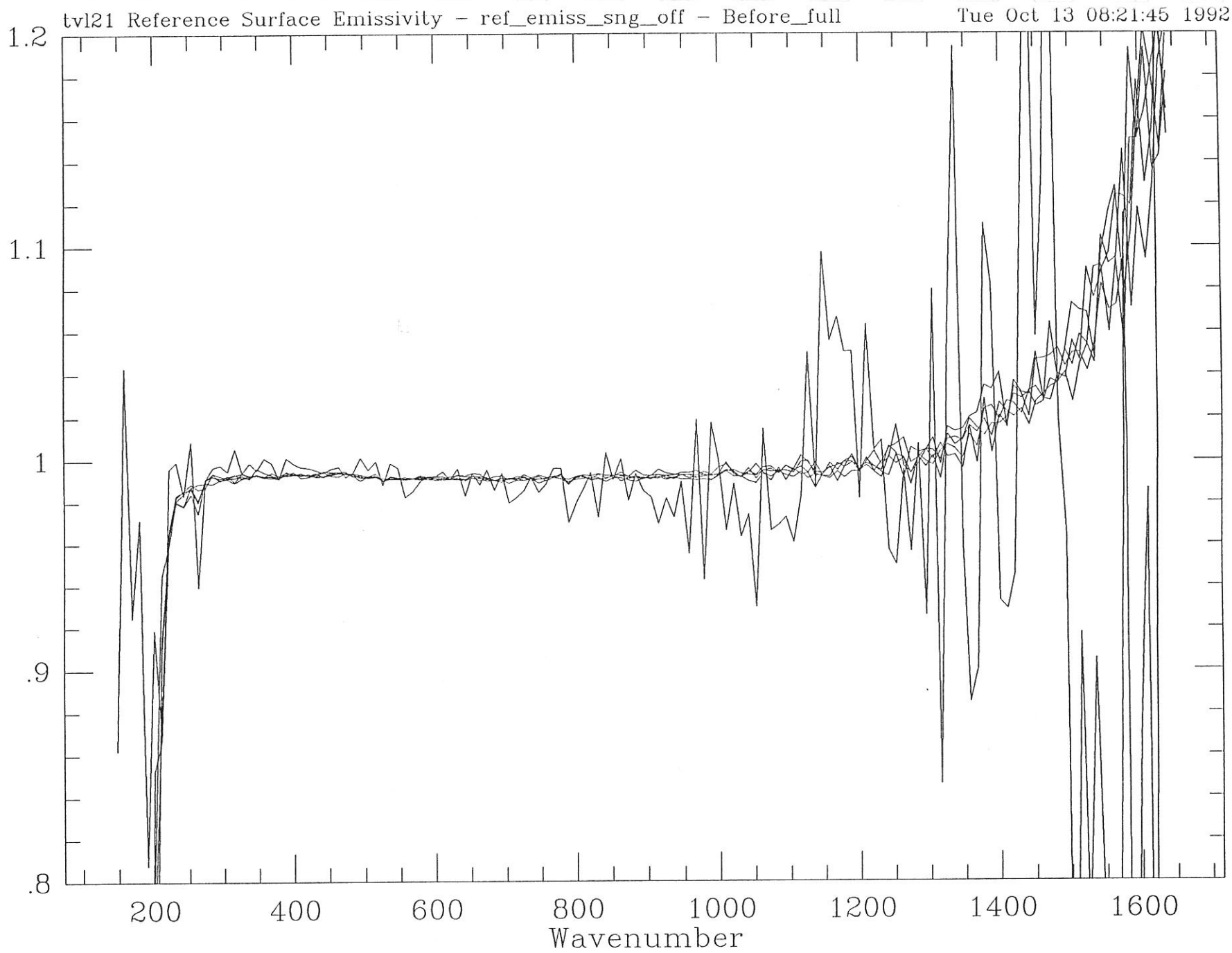
tvl21 Reference Surface Emissivity - ref_emiss_sng_off - Before_full
Tue Oct 13 08:21:45 1992
1.2
1.1
1
.9
.8
200
400
600
800
1000
1200
1400
1600
Wavenumber

Fig. 3-26

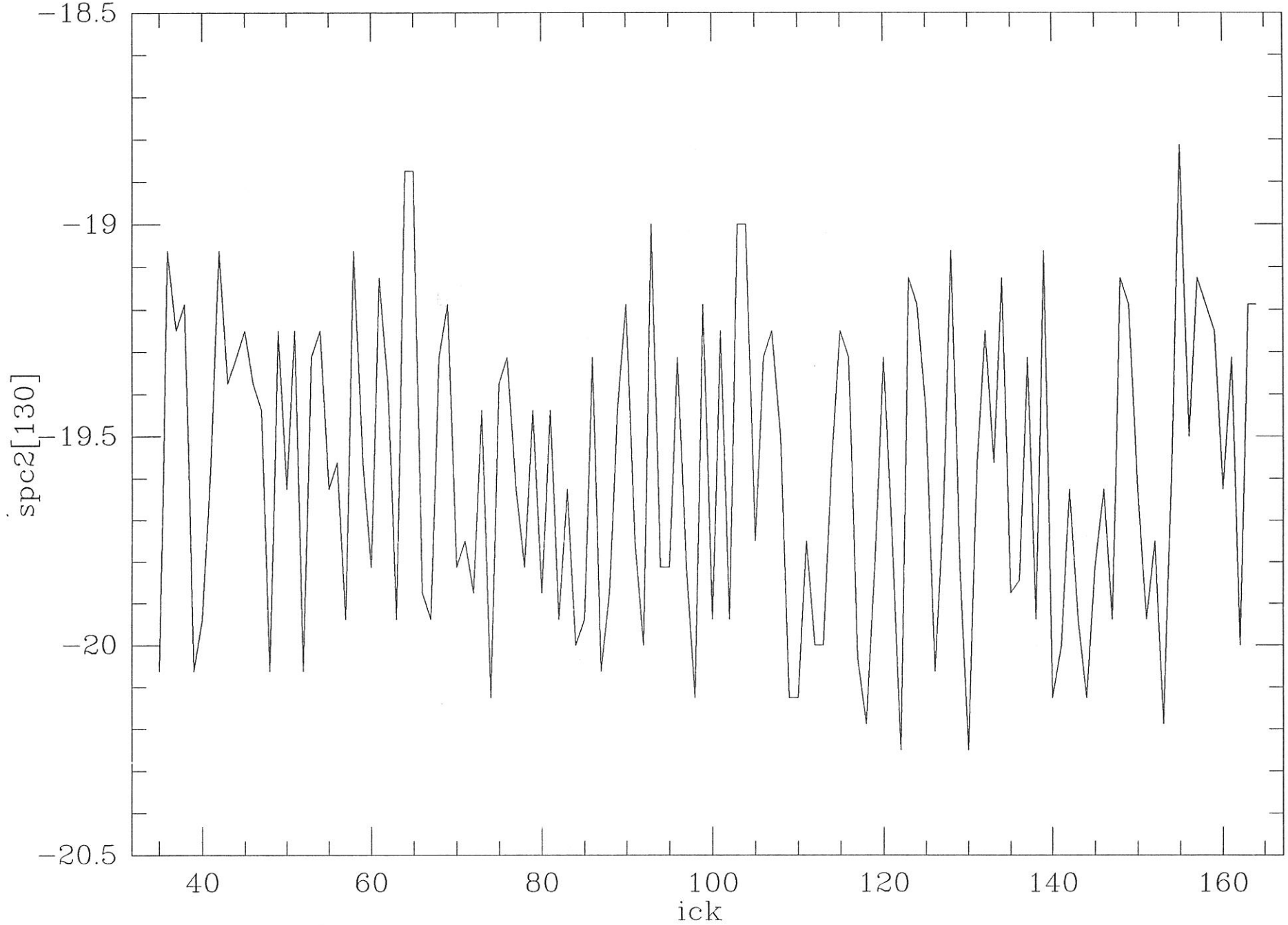

Fig. 3-21a

Mon May 3 11:30:22 1993 Database: /tes/steph/data/tvl22

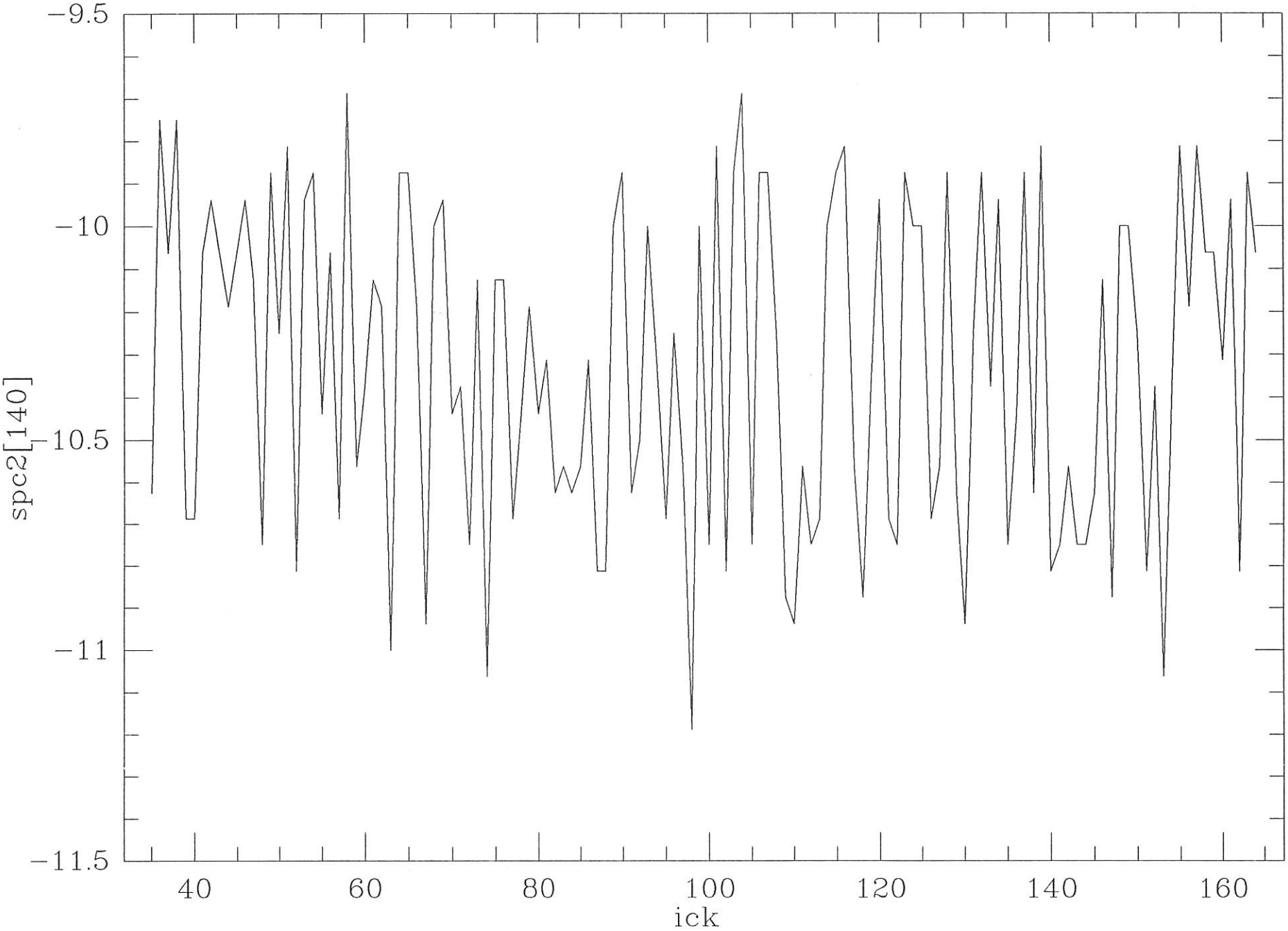

Fig 3-376

Mon May 3 11:29:33 1993 Database: /tes/steph/data/tvl22

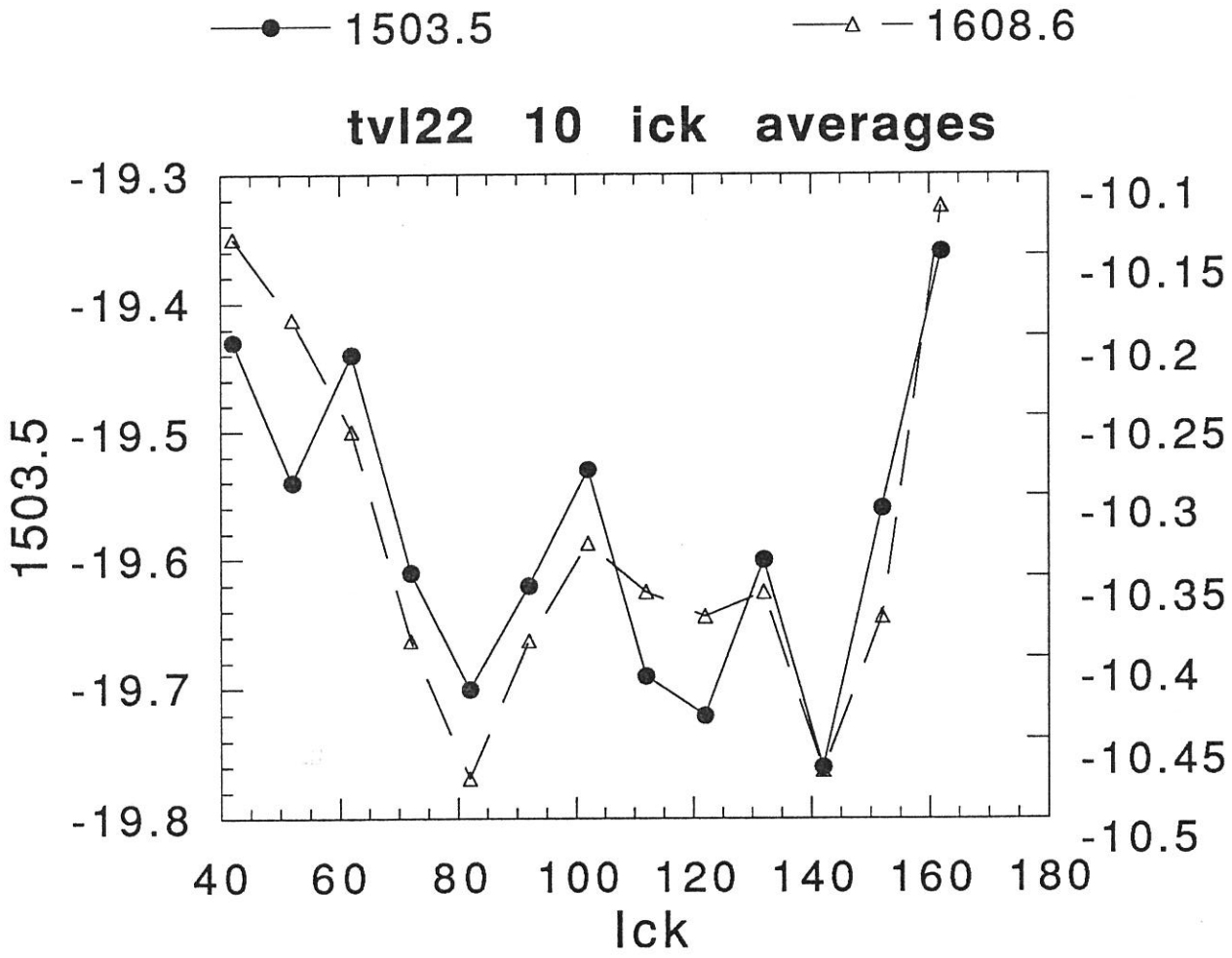
1503.5
1608.6
tvl22 10 ick averages
-19.3
-19.4
-19.5
-19.6
-19.7
-19.8
1503.5
-10.1
-10.15
-10.2
-10.25
-10.3
-10.35
-10.4
-10.45
-10.5
40
60
80
100
120
140
160
180
Ick

Fig. 3-28

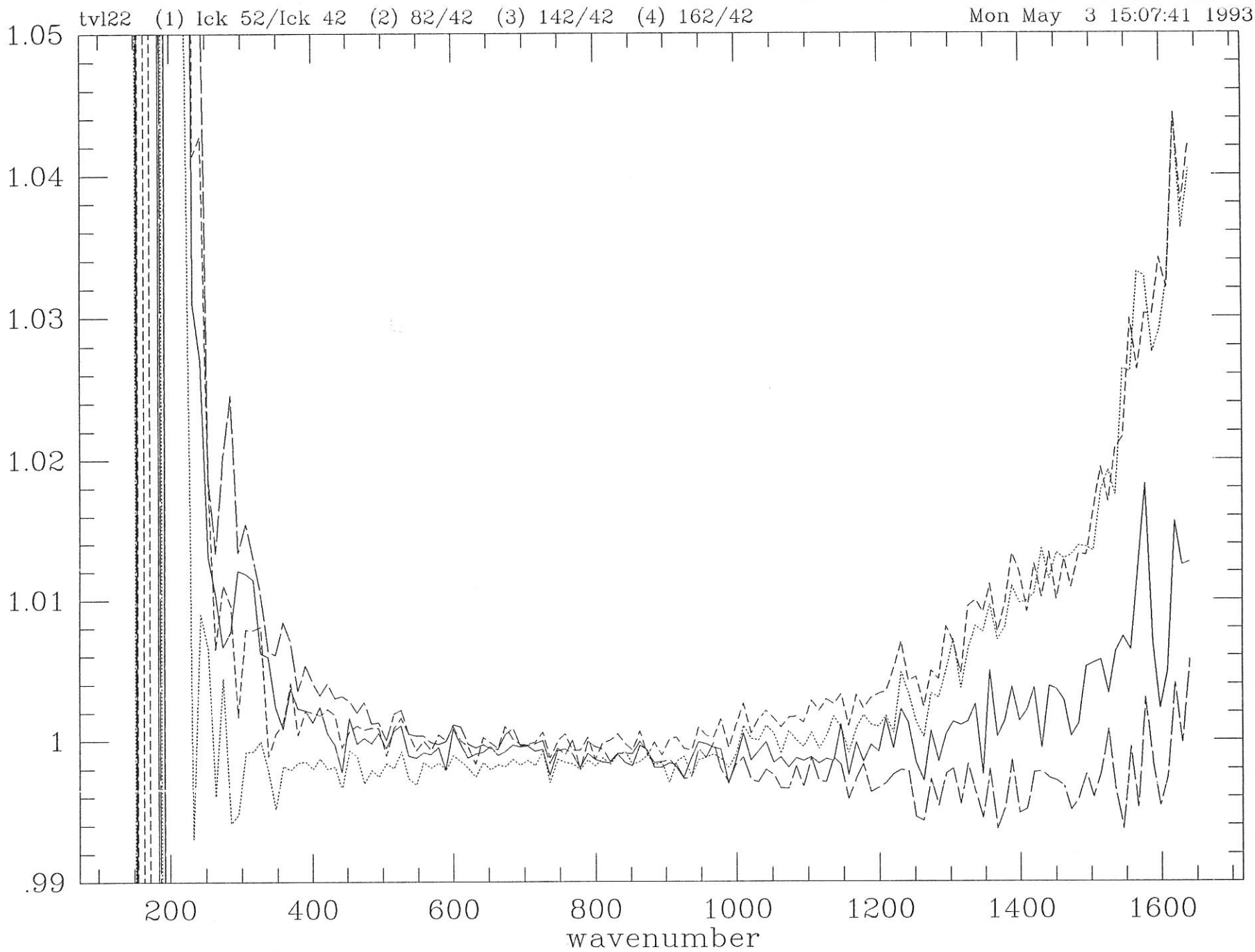
tvl22 (1) Ick 52/Ick 42 (2) 82/42 (3) 142/42 (4) 162/42
Mon May 3 15:07:41 1993
1.05
1.04
1.03
1.02
1.01
1
.99
200
400
600
800
1000
1200
1400
1600
wavenumber

Fig. 3-29

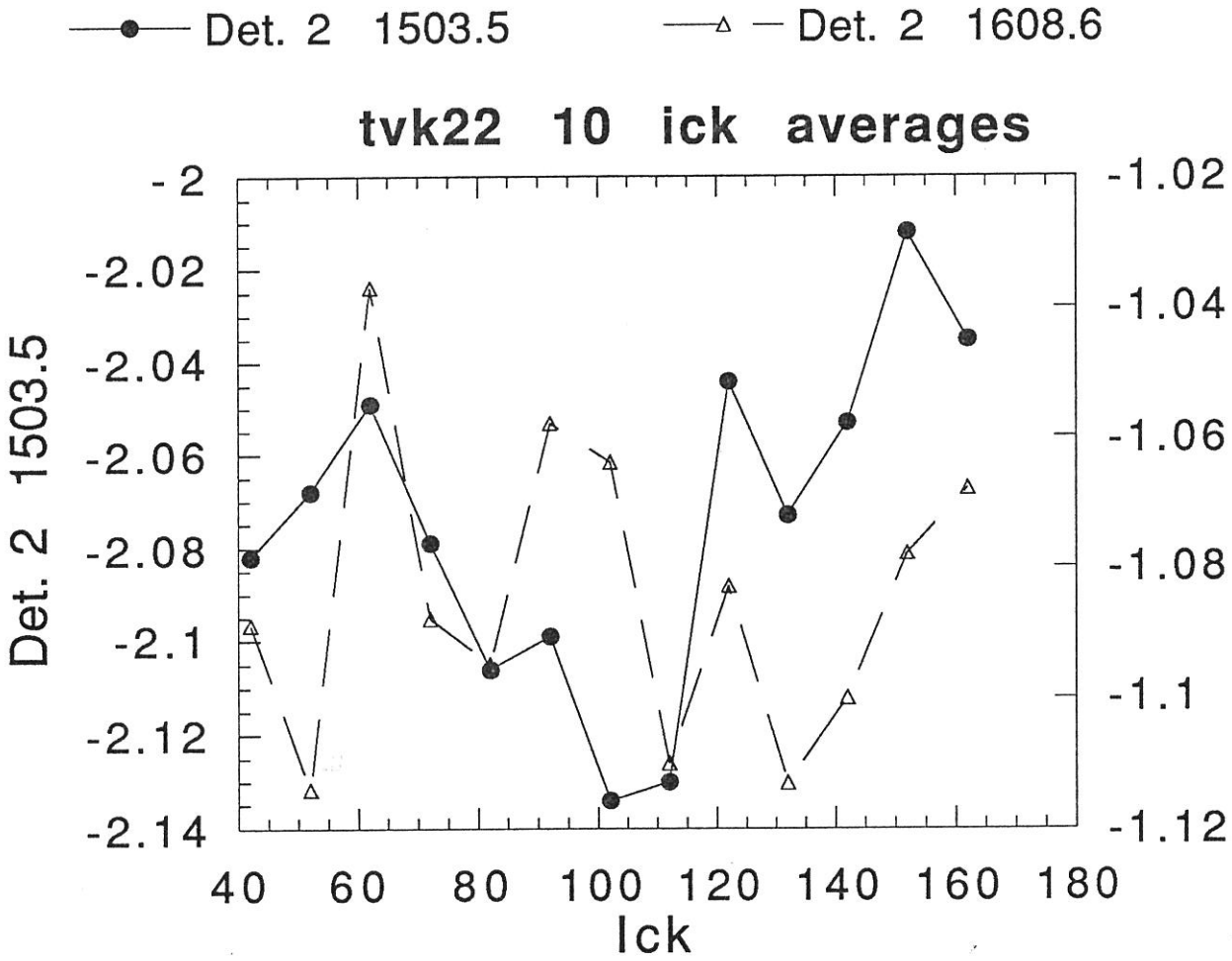
Det. 2 1503.5
Det. 2 1608.6
tvk22 10 ick averages
Det. 2 1503.5
-2
-2.02
-2.04
-2.06
-2.08
-2.1
-2.12
-2.14
-1.02
-1.04
-1.06
-1.08
-1.1
-1.12
40
60
80
100
120
140
160
180
Ick

Fig. 3-30a

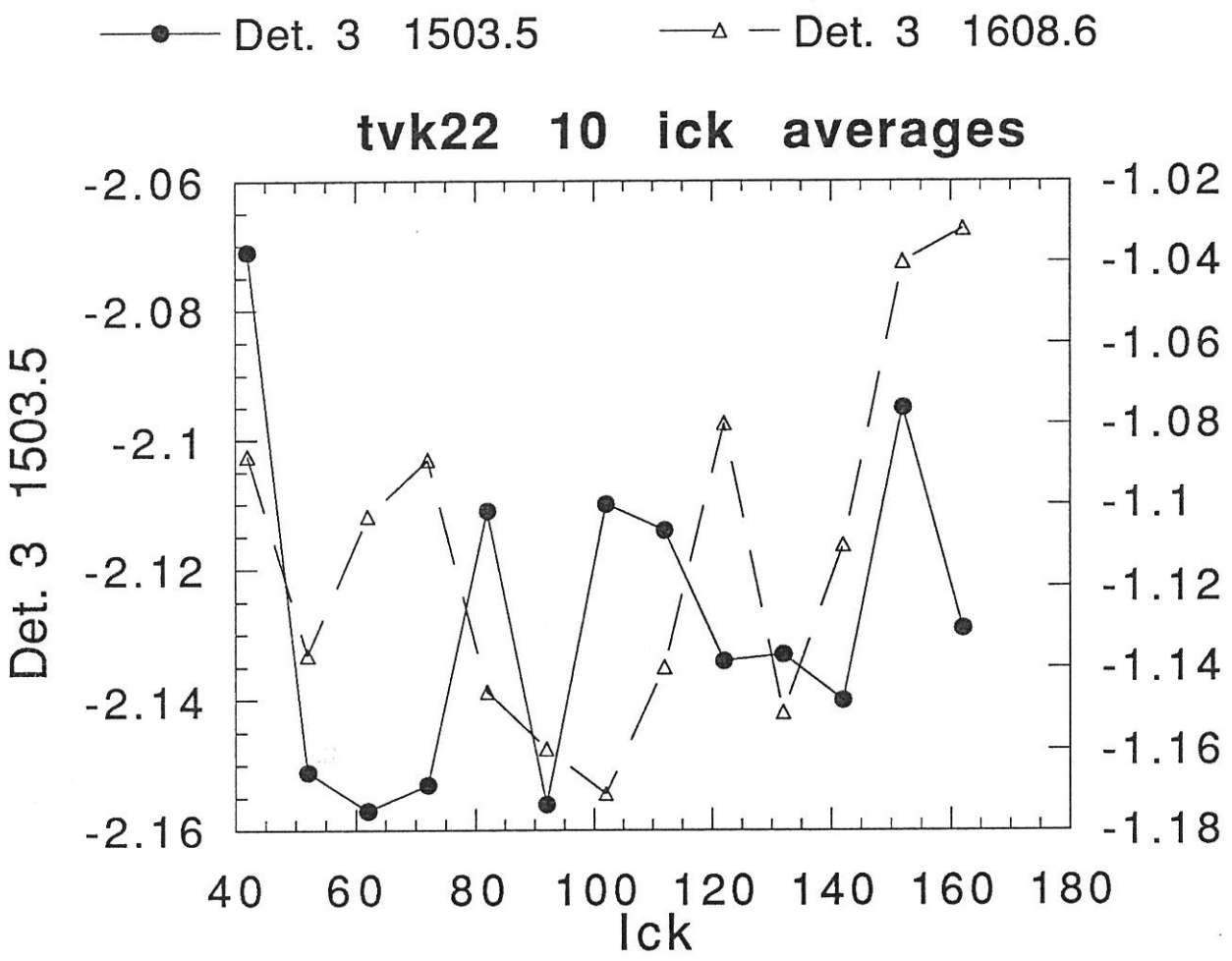
Det. 3 1503.5
Det. 3 1608.6
tvk22 10 ick averages
Det. 3 1503.5
-2.06
-2.08
-2.1
-2.12
-2.14
-2.16
-1.02
-1.04
-1.06
-1.08
-1.1
-1.12
-1.14
-1.16
-1.18
40 60 80 100 120 140 160 180
Ick

Fig. 3-30b

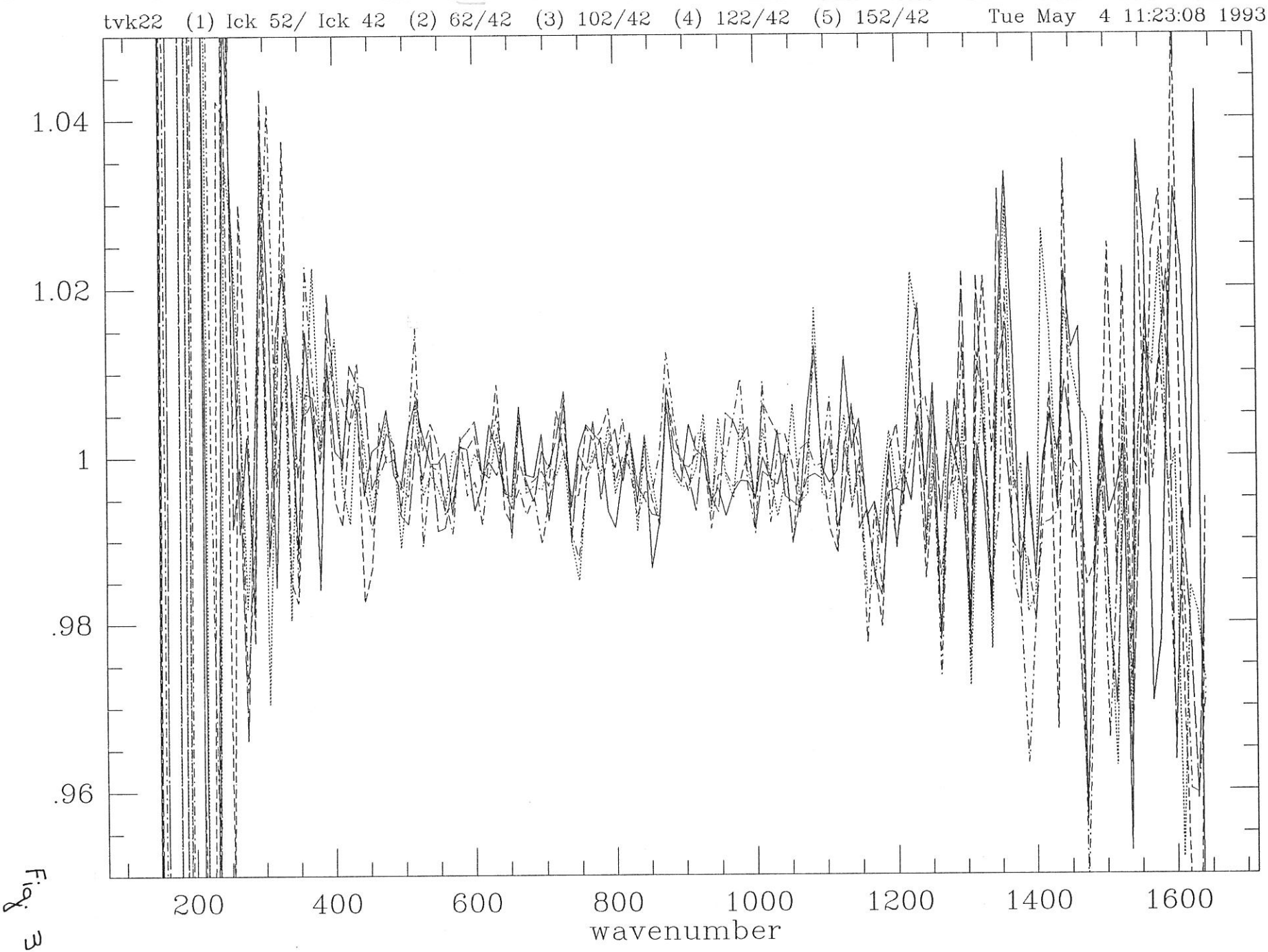
tvk22 (1) Ick 52/ Ick 42 (2) 62/42 (3) 102/42 (4) 122/42 (5) 152/42 Tue May 4 11:23:08 1993
1.04
1.02
1
.98
.96
200
400
600
800
1000
1200
1400
1600
wavenumber

Fig. 3-31

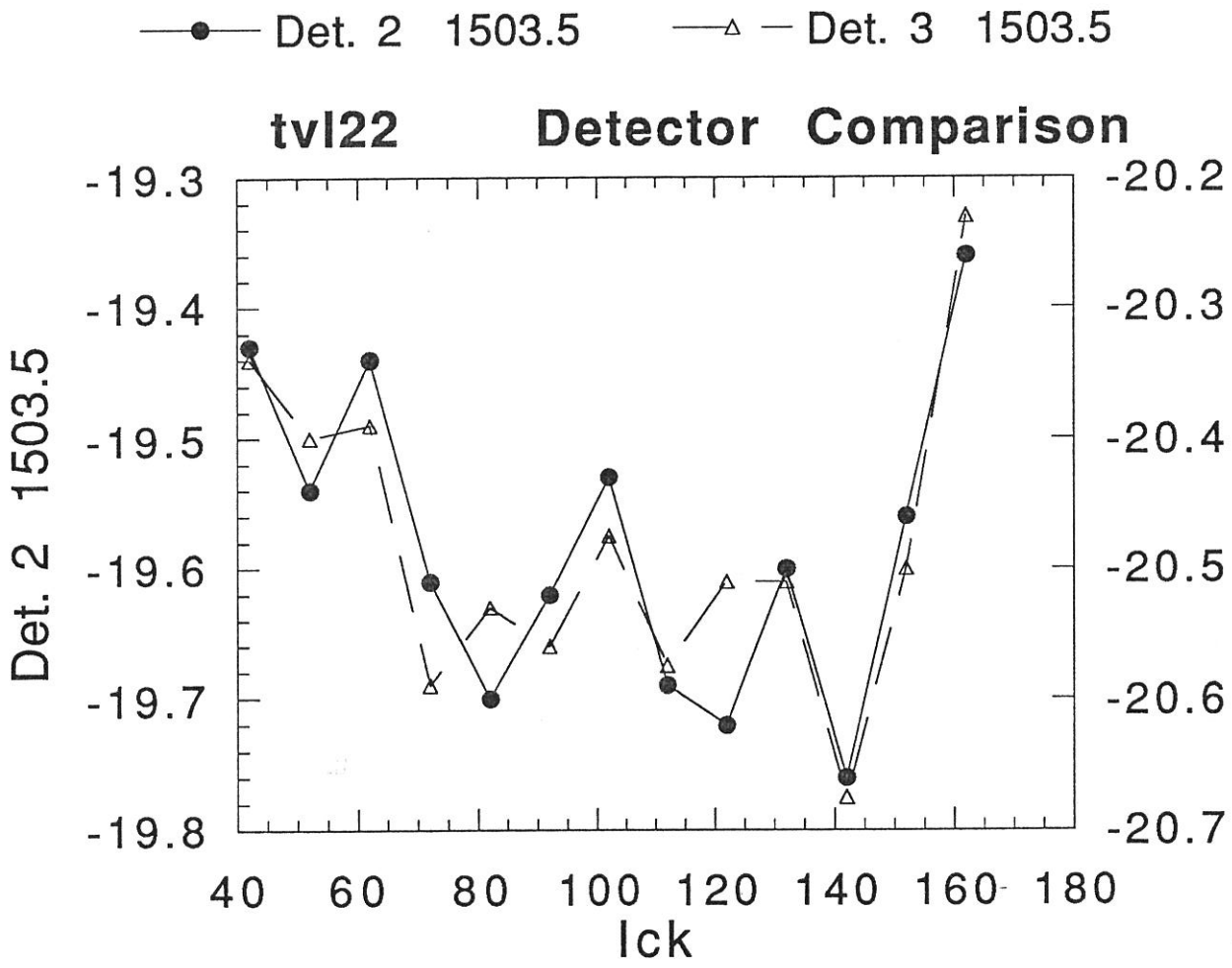
Det. 2 1503.5
Det. 3 1503.5
tvl22 Detector Comparison
Det. 2 1503.5
-19.3
-19.4
-19.5
-19.6
-19.7
-19.8
-20.2
-20.3
-20.4
-20.5
-20.6
-20.7
40 60 80 100 120 140 160 180
lck

Fig. 3-32a

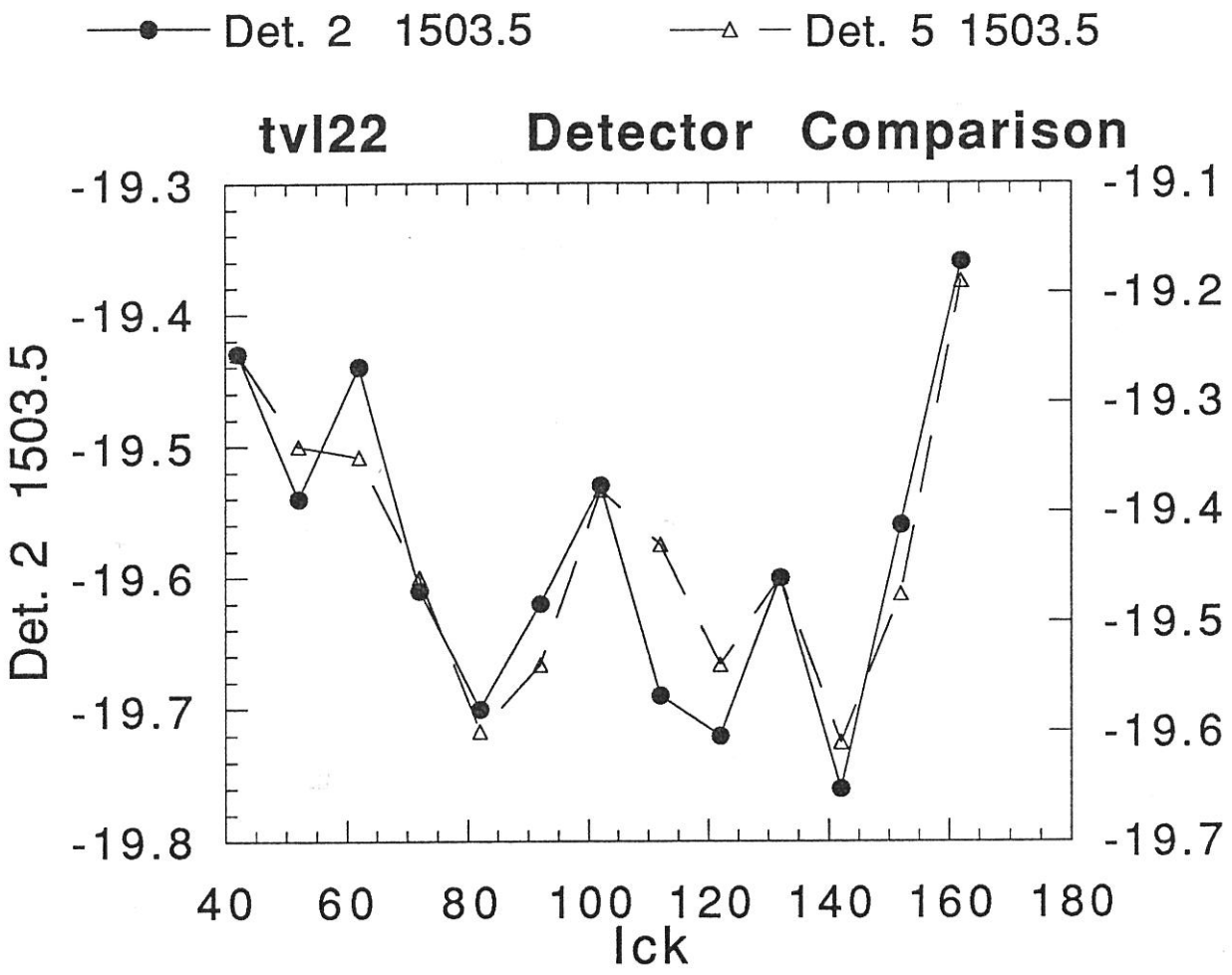
Det. 2 1503.5
Det. 5 1503.5
tvl22 Detector Comparison
Det. 2 1503.5
-19.3
-19.4
-19.5
-19.6
-19.7
-19.8
-19.1
-19.2
-19.3
-19.4
-19.5
-19.6
-19.7
40
60
80
100
120
140
160
180
Ick

Fig. 3-32b

$CAL/archive/inst_resp/rsp_reg.tbl vectors [85 18]

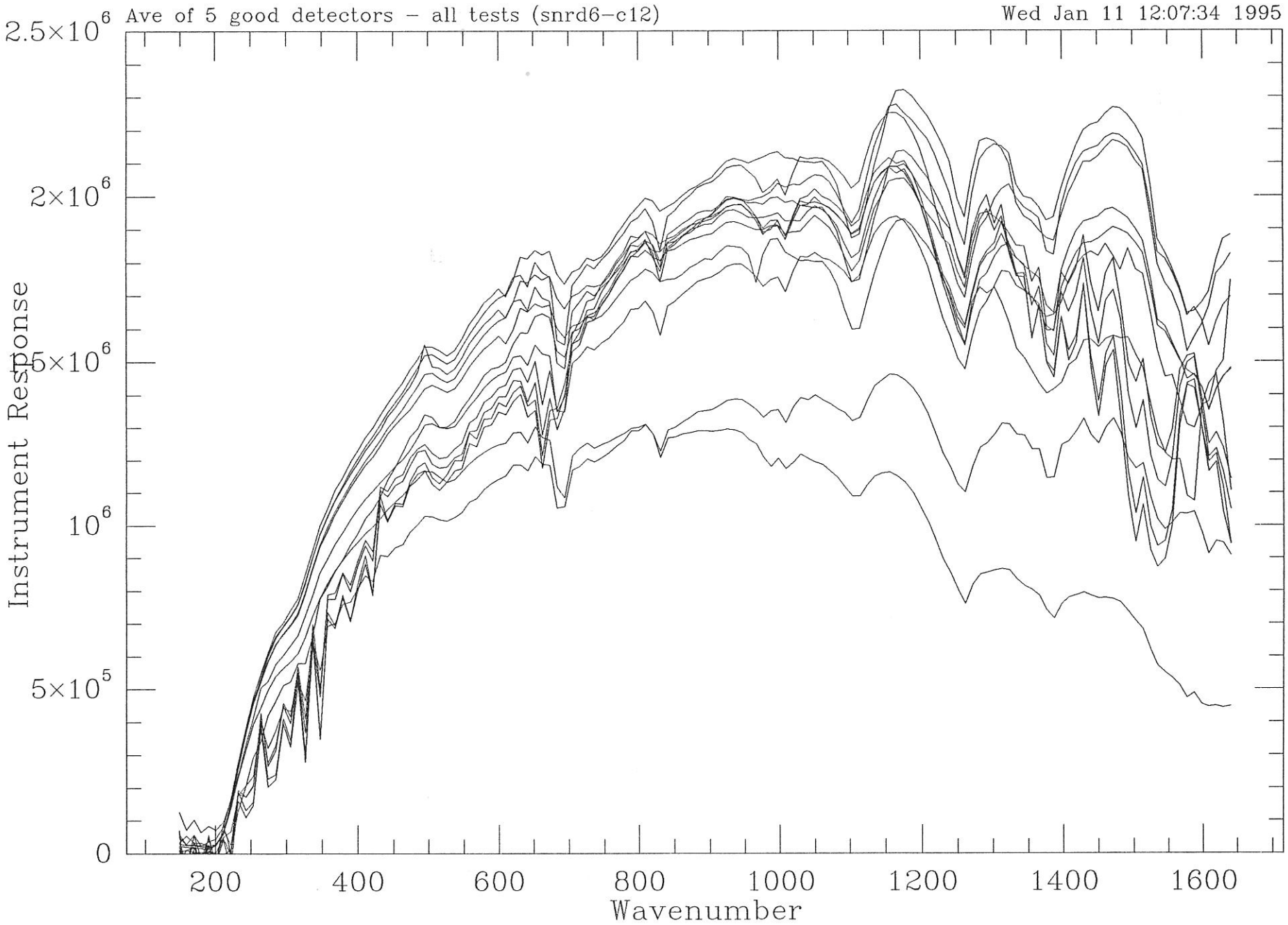

Fig. 4-1

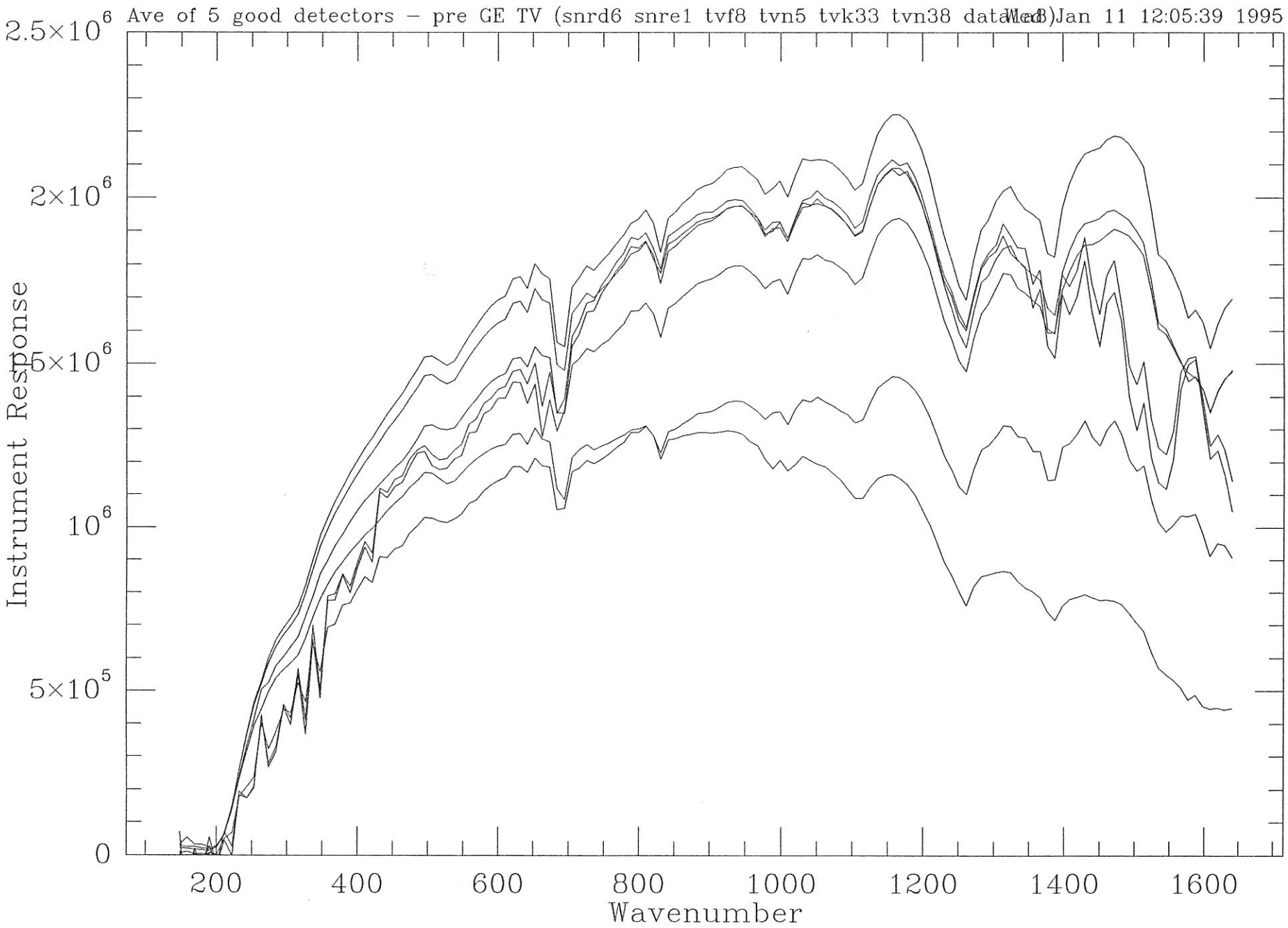
Ave of 5 good detectors – pre GE TV (snrd6 snre1 tvf8 tvn5 tvk33 tvn38 data3)Wed Jan 11 12:05:39 1995
2.5×10^6
2×10^6
5×10^6
10^6
5×10^5
0
Instrument Response
200
400
600
800
1000
1200
1400
1600
Wavenumber

Fig. 4-29

resp-sng.tod

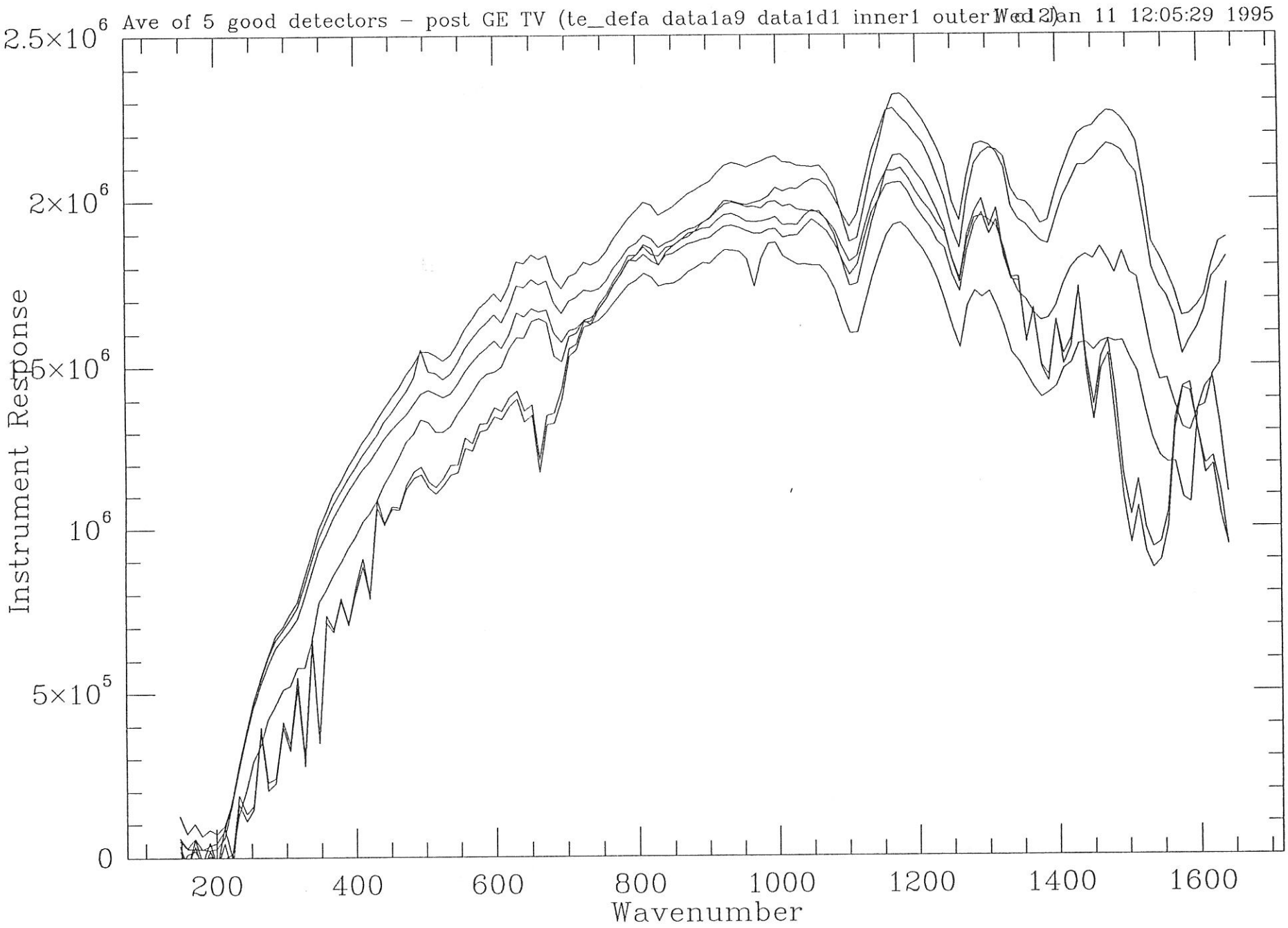

Fig. 4-25

resp - sng. tvz

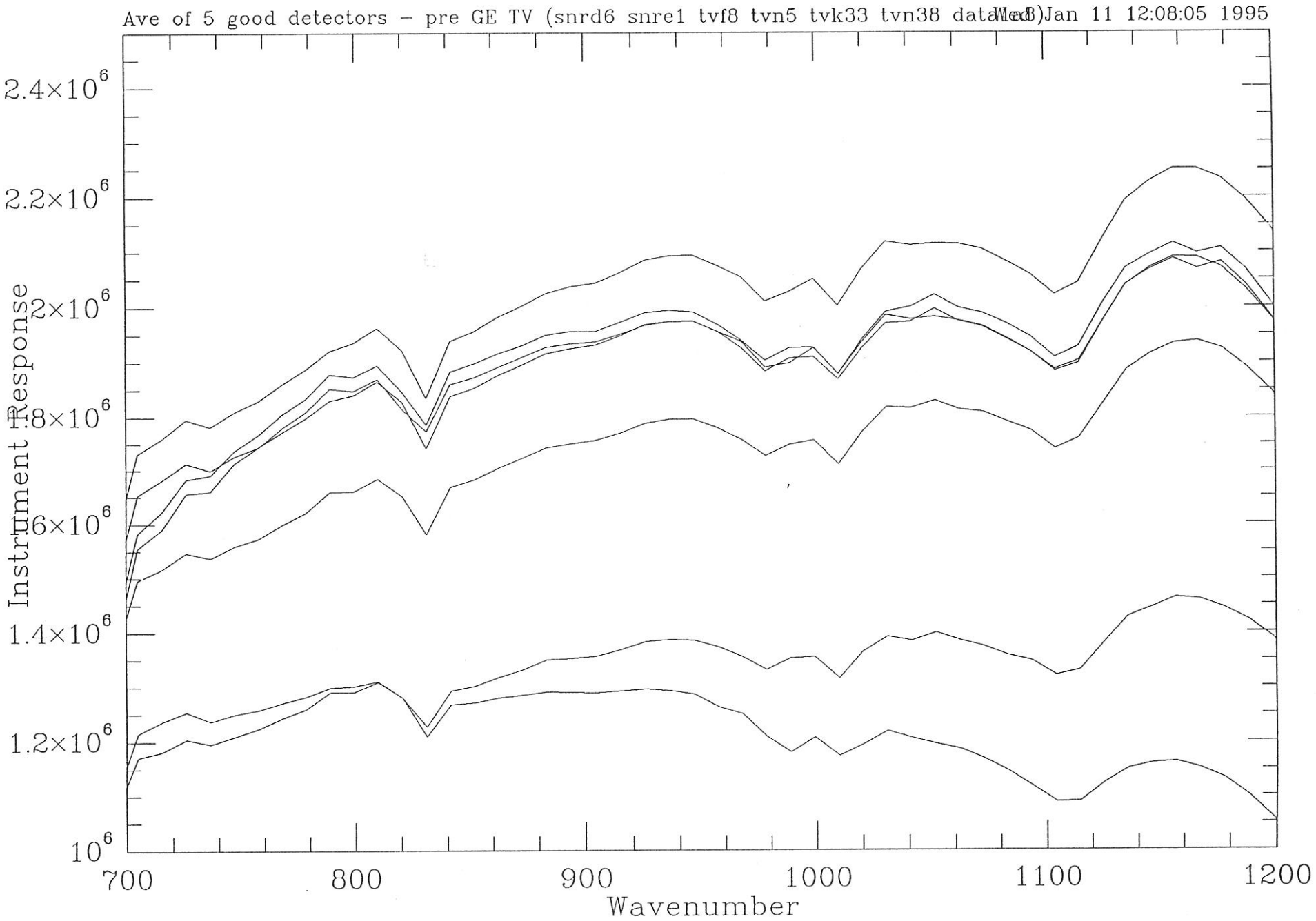

Fig. 4-3a

resp_sng.idb

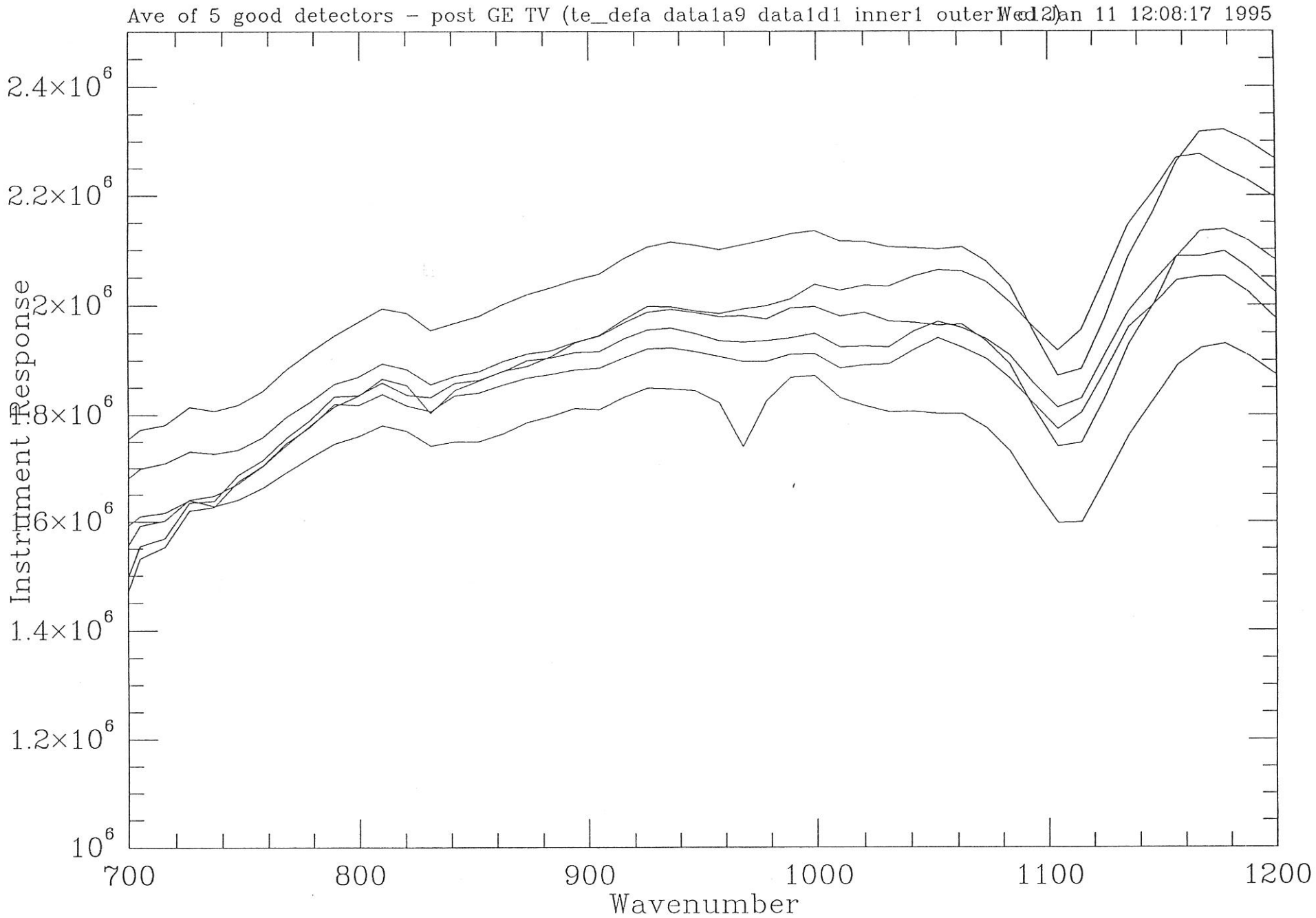

Fig. 4-30

resp_svg.tdb

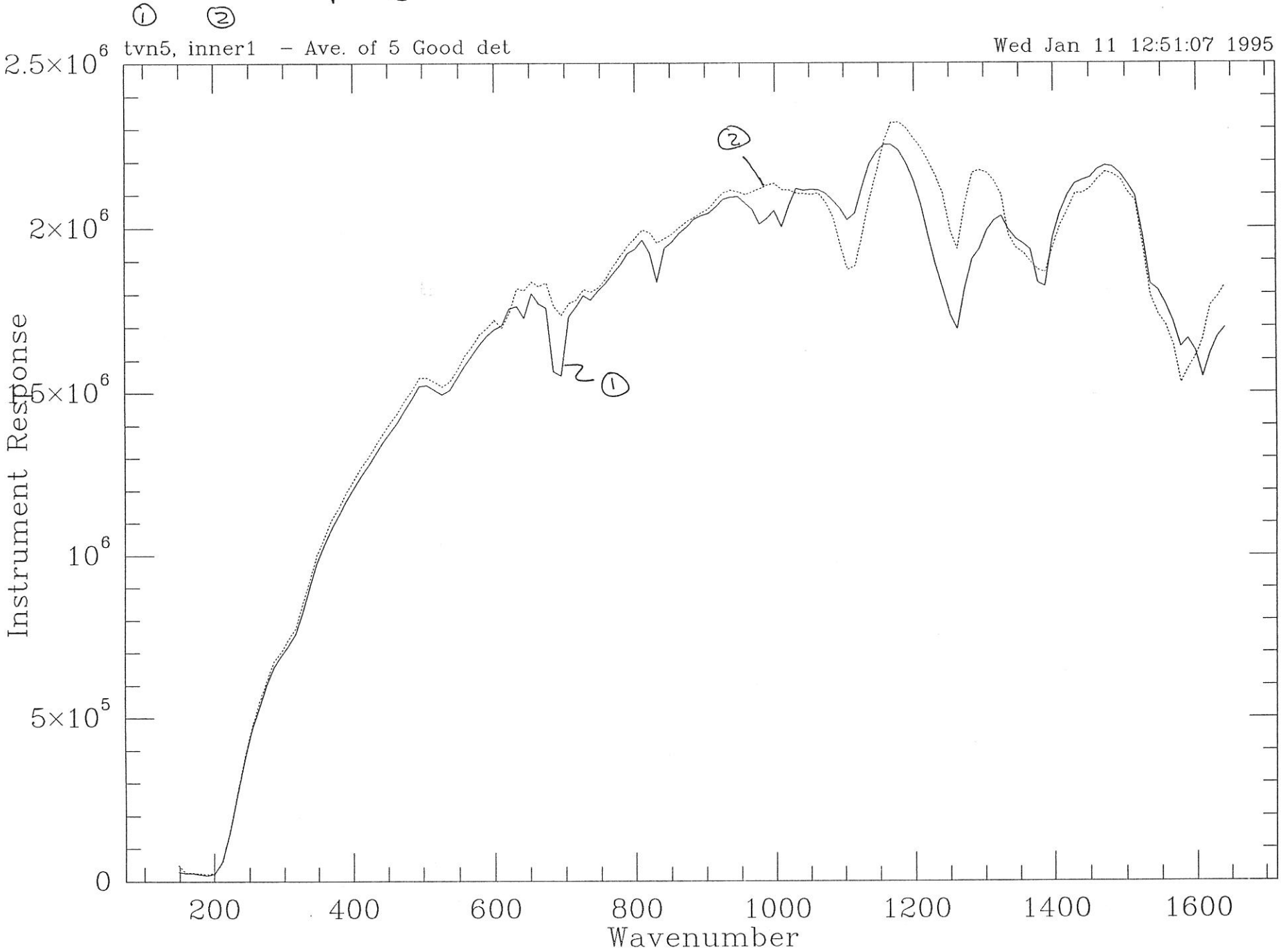

Fig. 4-4